



NUI MAYNOOTH

Ollscoil na hÉireann Má Nuad

AN INVESTIGATION OF REMOTE NON-CONTACT
PHOTOPLETHYSMOGRAPHY AND PULSE OXIMETRY

Kenneth Gerard Humphreys

DIP EE, B.Sc.(Eng.), M.Eng.Sc.

A thesis submitted to the
National University of Ireland
for the degree of
Doctor of Philosophy

August 2007

Department of Electronic Engineering
Faculty of Science and Engineering

Head of Department: Dr. F. Devitt

Supervisors: Dr. Tomás E. Ward and Dr. Charles M. Markham

ABSTRACT

This thesis presents an investigation of non-contact remote pulse oximetry and photoplethysmography. A thorough description is given of the technique of pulse oximetry along with some physiological effects and some characteristics of light-tissue interaction that underlie pulse oximetry. A device is then described that is capable of capturing two photoplethysmograph (PPG) signals simultaneously in a multiplexed fashion. The device is comprised of a complementary metal oxide semiconductor (CMOS) camera and a dual wavelength array of light emitting diodes (LEDs) (760 nm and 880 nm). By alternately illuminating a region of tissue with each wavelength of light and detecting the backscattered light with the camera at a rate of 16 frames per second per wavelength, two PPG signals are simultaneously captured. This process forms the basis of pulse oximetry. A methodical investigation of the comparability of the camera-based device with a conventional clinical contact device is presented. The camera-based device is demonstrated to provide a comparable PPG waveform and measure of pulse rate and a description is given of how, with the inclusion of a calibration procedure, such a device could be used to estimate arterial oxygen saturation (S_pO_2). Some aspects of PPG signal acquisition that are unique to a camera-based device are highlighted and camera-based capture is shown to introduce both tractable complications and the potential for additional utility beyond that of a conventional contact device. Additionally this thesis describes a concept for camera-based reflection tomography with the potential to yield structural information about shallow vasculature and tissue morphology. Lastly this thesis describes areas of further work in relation to the development of clinically useful camera-based pulse oximetry, and areas of further research concerning the potential of camera-based photoplethysmography as an investigative tool.

DECLARATION

I hereby declare that this thesis is my own work and has not been submitted in any form for another award at any university or other institute of tertiary education. Information derived from the published or unpublished work of others has been acknowledged in the text and a list of references is given.

Signed: _____

Date: _____

ACKNOWLEDGEMENTS

I would like to express my appreciation to my supervisors Dr Tomás Ward and Dr Charles Markham: Tomás for his indefatigable enthusiasm and piquancy, and Charles both for his technical input and for his opportune perspectives on the research process, especially during Tomás' sabbatical. This research was conducted in the Department of Electronic Engineering at NUI Maynooth and I would like to take the opportunity to thank the administrative, technical, and academic staff, as well as the postgraduate researchers of the department. This research was funded by Science Foundation Ireland as part of a Terahertz imaging project conducted in the Department of Experimental Physics at NUI Maynooth. I would like to thank the members of the Terahertz optics group and in particular the project's principal investigator Prof. J. Anthony Murphy. Thanks are due to Mr Christopher Soraghan for his help in obtaining LED emission spectra.

This document was created using Microsoft® Word 2000 and MathType™ 5.0; citations and referencing were managed using EndNote® 7; with the exception of figures depicting frames captured by the camera, all images in this document were produced by Matlab® 7 (R14) or were drawn in Microsoft® Word 2000.

CONTENTS

TITLE PAGE	I
ABSTRACT	II
DECLARATION	III
ACKNOWLEDGEMENTS.....	IV
CHAPTER 1 INTRODUCTION	1
1.1 Motivation.....	2
1.2 Objectives.....	3
1.3 Contributions of this thesis	3
1.4 Outline of thesis	4
CHAPTER 2 SCIENTIFIC BACKGROUND.....	6
2.1 Oxygen transportation.....	7
2.1.1 Dyshaemoglobins and fetal haemoglobin.....	11
2.2 Light absorption and scattering in tissue.....	12
2.2.1 Light absorption in tissue—the Beer-Lambert law	13
2.2.2 Light attenuation—the modified Beer-Lambert law.....	14
2.3 Light transport in tissue	16
2.3.1 Light absorption	16
2.3.2 Light scattering.....	17

2.3.3	Monte Carlo simulation of light propagation	17
2.4	Summary	26
CHAPTER 3 PULSE OXIMETRY		27
3.1	Contemporary history of pulse oximetry	28
3.1.1	The Clarke electrode and the transcutaneous PO_2 sensor	33
3.1.2	The CO-oximeter.....	35
3.2	Theory of pulse oximetry.....	37
3.2.1	Light absorption for pulse oximetry	39
3.2.2	Deriving arterial oxygen saturation	42
3.2.3	The need for calibration.....	46
3.3	Operation of a clinical device	49
3.3.1	Light emitting diodes.....	49
3.3.2	Photodetectors and amplifiers.....	54
3.3.3	Signal processing.....	55
3.3.4	Probes	57
3.3.5	Calibration of pulse oximeters.....	59
3.4	Limitations and applications of pulse oximetry	62
3.4.1	Accuracy and errors.....	62
3.4.2	Limitations.....	65
3.4.3	Applications.....	67
3.5	Chapter summary	69
CHAPTER 4 DESIGN CONSIDERATIONS		70
4.1	Choice of source	70
4.1.1	Safety guidelines	71
4.2	Choice of detector (camera technology)	73
4.2.1	CCD image sensors	75
4.2.2	CMOS image sensors	77
4.2.3	Choosing between CMOS and CCD	79

CHAPTER 5	INSTRUMENT DESCRIPTION AND PERFORMANCE	82
5.1	System overview	83
5.2	Hardware description	84
5.2.1	The camera	84
5.2.2	Illumination	87
5.2.3	Timing signals	95
5.2.4	Replicating aspects of a clinical device	96
5.3	Image analysis	102
5.3.1	Extracting AVI files	103
5.3.2	Boxes and their analysis	104
5.3.3	Identifying PPG containing regions	105
5.4	Testing and performance of device	109
5.4.1	Experimental protocol	109
5.4.2	Displaying a PPG	111
5.4.3	Measuring pulse rates	115
5.4.4	Deriving S_pO_2 from a camera-based device	122
5.5	Analysis of aspects of device's performance	127
5.5.1	Effect of ROI size on plethysmograph characteristics	128
5.5.2	Detection of inverted PPG signals	132
5.6	Achievable separation of tissue and camera	138
5.6.1	Monte Carlo simulation	139
5.6.2	Probabilistic model of tissue-camera separation	143
5.7	Chapter summary and discussion	153
CHAPTER 6	A CONCEPT FOR NON-CONTACT CAMERA-BASED BACKSCATTER TOMOGRAPHY	157
6.1	Description of concept	160
6.2	Forward modelling and reconstruction	163
6.2.1	Forward model	163

6.2.2	Algebraic reconstruction	165
6.3	Discussion	169
CHAPTER 7 DISCUSSION AND FUTURE WORK.....		171
7.1	A synopsis of the contributions of this thesis.....	171
7.2	Future work.....	173
7.2.1	Further research into camera-based pulse oximetry	173
7.2.2	Investigation of camera-derived PPG signals.....	173
7.2.3	Development of a clinically useful device	174
7.2.4	Investigation of single camera-based tomography	175
7.3	Concluding remarks.....	175
APPENDIX A		177
APPENDIX B		181
REFERENCES		184

CHAPTER 1

INTRODUCTION

It is fair to say that pulse oximetry has, since its invention in the nineteen seventies, revolutionised anaesthesia and critical care. The technique provides a robust and non-invasive means of accurately estimating arterial oxygen saturation—which is the amount of oxygen that arterial blood *is* carrying compared to the amount it *could* carry, expressed as a percentage. The provision of an estimate of arterial oxygen saturation yields a critical insight into the health and well being of a patient and provides a useful addition to the accepted four vital signs: heart rate, blood pressure, respiration rate, and temperature.

The technique of pulse oximetry is based on near infrared (NIR) spectroscopy and requires capturing at least two photoplethysmograph (PPG) signals at two different wavelengths of light—a photoplethysmogram being a trace of the peripheral arterial pressure waveform obtained by optical means. The ability to capture and display a PPG signal as well as to derive the pulse rate has greatly extended the clinical and investigative usefulness of pulse oximeters, which today are employed in many diverse applications.

Pulse oximeters originally operated by transmission of light through small extremities typically fingers, ear lobes, the bridge of the nose, and less commonly the toes. Such locations are easily accessible but in the case of fingers and toes, suffer from the disadvantage that in cases of trauma, surgery, shock, and hypothermia (or even mild cold), the circulation to the peripheries is immediately

reduced, making *pulse* oximetry difficult or impossible. Sensors were soon developed that operated using diffuse reflected light, making possible measurement from any part of the body surface, and in the process further extending the applications of pulse oximetry and photoplethysmography.

This thesis describes an investigation of both the feasibility and practicalities of remote non-contact pulse oximetry, specifically a camera-based embodiment. It is hoped that such capabilities might further extend the uses of the technique.

1.1 MOTIVATION

Pulse oximetry and photoplethysmography are currently employed in a wide variety of applications, in routine and critical clinical applications, and in surgical, investigative, diagnostic, and experimental applications. A key factor in the emergence of so many applications was the development of reflectance-based probes that made measurement possible from any point on the body surface. However many more application have arisen that required the development of specialised probes, including: probes to monitor mother and child during child birth, probes to be used endoscopically during surgery, probes to fit in a pilot's ear during aircraft testing, probes to interface with the eye to measure retinal perfusion, and many more besides including ambulatory probes and probes for sports research (see the later discussion of pulse oximetry applications in Section 3.4.3).

The development of non-contact capabilities might make possible and practical new applications of pulse oximetry and photoplethysmography. Applications already exist that might benefit from non-contact pulse oximetry. For example, the use of pulse oximeters (or any metal wire) in conjunction with magnetic resonance imaging (MRI) can result in serious burns to the patient (Dempsey and Condon 2001; Nakamura, et al. 2001). There also exist applications where it is undesirable to make contact with the patient, such as sleep studies, patients in isolation units, immunosuppressed patients susceptible to infection by cross-contamination, and burns patients.

Pyrometers and camera-based technologies already exist capable of non-contact temperature measurement. Conventional pulse oximeters provide an estimate of arterial oxygen saturation, as well as pulse rate and potentially respiration rate. If non-contact pulse oximeter functionality were to be achieved, but

for the illusive non-contact measurement of blood pressure, non-contact vital signs monitoring would be a realistic goal.

The ability to monitor a patient's vital signs by non-contact means is a tantalising prospect, and would likely be well received in both surgical and clinical monitoring environments where efforts are already underway to minimise the amount of cabling and clutter currently associated with patient monitoring. Indeed non-contact vital signs monitoring and non-contact respiration monitoring using microwave radar are topical areas of research (Lohman, et al. 2002; Matsui, et al. 2006; Uenoyama, et al. 2006).

1.2 OBJECTIVES

The broad objective of this thesis is to investigate the feasibility of non-contact pulse oximetry. The functionality that a conventional pulse oximeter possesses (which will be established in Chapter 3) includes the ability to estimate arterial oxygen saturation, display a trace of the peripheral arterial pressure waveform, and measure the pulse rate from that waveform. Thus it is necessary to investigate the feasibility of comparably replicating these functions by non-contact means.

In pursuing this objective a camera-based approach is adopted. Thus a further objective of this thesis is to investigate what, if any, complications or limitations are introduced by a camera-based embodiment of a pulse oximeter? The complement to this objective is to identify any additional utility that a camera-based device might possess, beyond that of a conventional contact device.

Having adopted a camera-based approach, a secondary objective of this thesis is to highlight any potential that camera-based devices might offer in NIR or optical investigations of tissue beyond their current application in tissue oximetry and their application here in determining arterial oximetry.

1.3 CONTRIBUTIONS OF THIS THESIS

The primary contribution of this thesis is the description of a device and method that resulted in the first demonstration of the simultaneous capture of two PPG signals at different wavelength, by remote non-contact means, from deep tissue and from a range of subjects, under realistic environmental and lighting conditions. The

subsequent analysis of the device's performance and the demonstration of its comparability with a conventional device collectively establish the feasibility of (camera-based) non-contact pulse oximetry.

Beyond the investigations of feasibility and comparability, an investigation is presented of some aspects of non-contact and camera-based pulse oximetry and photoplethysmography that are unique to a camera-based device. These analyses highlight previously unreported phenomena that allude to the complications and also the potential additional investigative capabilities of a camera-based device.

Important necessary conditions are established pertaining to the choice of illumination pattern, which if neglected undermine the assumptions upon which the technique of pulse oximetry is based.

A concept for camera-based tomography is described that highlights new avenues of research for camera-based NIR and optical investigations of tissue.

1.4 OUTLINE OF THESIS

This thesis is composed of six subsequent chapters, the subjects of which are outlined here.

Chapter 2 establishes information pertaining to the physiology and anatomy of blood oxygen transportation. This information has importance later in the discussion of pulse oximeter operation, limitations, and accuracy. Chapter 2 also establishes the fundamentals of the Beer-Lambert law and Beer-Lambert based spectroscopy, of which pulse oximetry is a special case. Lastly Chapter 2 describes a Monte Carlo simulation of photon migration in tissue. The simulation is used in Chapter 2 to illustrate the path of light travelling through a turbid medium simulating tissue; knowledge of this path is later used to explain the operation of reflectance pulse oximetry (Chapter 3), to provide the rationale for certain design decisions pertaining to the non-contact device (Chapter 4), and to hypothesise the cause of some phenomena observed during non-contact photoplethysmography (Chapter 5). The Monte Carlo simulation is re-employed later in Chapter 5 to simulate the effect of tissue-detector separation on the received light intensity.

Chapter 3 provides a compendious description of pulse oximetry including the history of the technique, its principles of operation, the practicalities of its implementation, and a discussion of its applications and limitations. As such Chapter 3

provides the constraints, specifications, and objectives for the design of a non-contact device.

Chapter 4 describes design considerations pertaining to the source and detector. For the source these primarily include wavelength, bandwidth, and permissible exposure limits. The detector is ultimately chosen to be a digital camera and the discussion in Chapter 4 is concerned with establishing the desirable characteristics of the camera's sensor and choosing between the two available technologies, charge coupled devices (CCD) and complementary metal oxide semiconductors (CMOS).

Chapter 5 provides a description of the non-contact camera-based device for remote pulse oximetry and photoplethysmography. A detailed account is given of the device's design, construction, operation, and performance. An examination of its comparability with a conventional contact device is presented along with an investigation of some aspects of photoplethysmography that are unique to a camera-based implementation. Some further aspects of the device's performance are investigated by simulation.

In Chapter 6 the topic of discussion changes and a concept for camera-based diffuse optical or NIR tomography is described. The discussion is intended to highlight the potential of camera-based NIR and optical investigations of tissue.

The thesis is concluded in Chapter 7 with a review of the arguments and findings and resulting contributions, as well as a discussion of areas for future work, both in further research and in the development of clinically useful devices.

CHAPTER 2

SCIENTIFIC BACKGROUND

The desire to monitor the oxygenation of body tissues or of the blood is motivated by the importance of oxygen to life. The motivation to measure the oxygenation of both tissue and blood by near infrared spectroscopy (NIRS) stems from the suitability of NIRS to safe, accurate, and non-invasive monitoring, of which much is said later in relation to pulse oximetry. NIRS is made possible by several fortuitous happenstances: tissue is relatively transparent to both red and near infrared light; an important respiratory molecule, haemoglobin, exhibits a useful oxygen dependent change in absorption over the same wavelength range; and the diffuse scattering of light over this range by tissue makes possible the detection of backscattered light—facilitating local tissue oxygenation and arterial oxygen saturation measurement from any point on the body surface—and as this thesis advances, facilitates arterial oxygen saturation measurement from beyond the body’s surface. (Appended to this list of fortuities should be the abundance of suitable silicon-based near infrared sources and detectors.) The discussion that follows in this thesis, the rationale for the methods employed here and the analysis of the operation of the resulting device, as well as the concept for a camera-based tomography system, are based on these premises, and this chapter is intended to act as a primer for that discussion.

Specifically this chapter has three purposes. first a basic description of the physiology and anatomy of oxygen transportation in the body is given. This discussion highlights both the importance and the mechanism of maintaining a

sufficient oxygen supply to body's tissues, and in so doing hints at the motivation for, and means by which, arterial oxygen saturation can be measured—which is the subject of Chapter 3. Second this chapter is intended to provide a thorough discussion of the modified Beer-Lambert law that describes light attenuation in tissue, and upon which near infrared spectroscopy is based. Third the scattering of light in tissue is described and with the aid of a Monte Carlo simulation, the arced path of light travelling between two points on the tissue surface is illustrated, the profile of this path is a key presupposition in the development of a non-contact pulse oximeter and in explaining signals observed using such a device, as well as the concept of camera-based tomography described in Chapter 6. Additionally the Monte Carlo simulation, though it is employed here only as an illustrative tool, is reapplied in Chapter 5 as an investigative tool to characterise the effect of tissue-detector separation.

2.1 OXYGEN TRANSPORTATION

Oxygen is addicting; in its grip are all the mitochondria-rich eukaryotes that learned to depend on it during the past 1.4 billion years. This, the first atmospheric pollutant, is the waste product of stromatolites (formations of algal plankton), which excreted it at least 2.3 billion years ago. Since then, all sediments have been rusted or oxidized. Oxygen is toxic. It rusts a person in a century or less. With oxygen came the danger, and the blessing, of fire. If introduced today, this gas might have difficulty getting approved by the Food and Drug Administration.

(Severinghaus 1987a)

At sea level the pressure of air is defined as 1 atmosphere (1 atm), or 760 mmHg in a mercury barometer, or 101.3 Pascals (Pa) (that is 101.3 N/m²) in the international system of units. Dalton's law of partial pressures states that the total pressure exerted by a gaseous mixture is equal to the sum of the partial pressures of the individual gases comprising the mixture. Under normal conditions oxygen accounts for approximately 21% of air and so has a partial pressure (PO_2) of 0.21 atm (21.3 Pa or 159.6 mmHg).

Air is drawn into the body by the mechanical actions of the lungs and respiratory muscles, under the control of respiratory neurons on the brain stem. Once in the lungs, oxygen from the air, diffuses across the thin boundary formed by the walls of the alveoli, into the oxygen depleted blood returning from supplying oxygen to the body's tissues. The oxygenated blood leaves the lungs and is

distributed by the arteries around the body. Although the arterial blood passes tissue in need of oxygen, diffusion—also the mechanism by which oxygen is passed between the blood and tissue—can only take place over distances of about 1 mm, so the arterial blood loses no oxygen at this point. Arteries branch off into smaller arteries and eventually into arterioles, the walls of which are only one cell thick. At this point oxygen from the blood in the arterioles diffuses into the tissue, while CO₂, the waste product of respiration, diffuses back into the blood. The arterioles meet with venules (which collectively form the capillaries), through which the now deoxygenated blood makes its way back into the veins and back towards the lungs to expel its CO₂ and acquire more O₂.

Blood is composed of about 50% liquid (plasma). Under normal circumstances, Henry's law describes the amount of gas that can be dissolved in a liquid at a given temperature, and that amount is directly proportional to the gas's partial pressure. If oxygen dissolved in blood plasma were the only mechanism by which the blood could transport oxygen around the body, then the plasma would need to be circulated around the body about twenty times faster, just to meet the needs of a resting body. The blood however has a much more efficient means of delivering oxygen around the body: haemoglobin.

Haemoglobin is a respiratory molecule found on red blood cells (erythrocytes). Each erythrocyte has approximately 265 million haemoglobin molecules, and each haemoglobin molecule is capable of bonding with four oxygen molecules (Curtis and Barnes 1989). Haemoglobin can typically carry 19 ml of O₂ per 100 ml of blood, which is about sixty five times that which could be carried dissolved in the plasma alone (Clark 1997).

When a completely deoxygenated haemoglobin molecule obtains its first oxygen molecule, its affinity for oxygen increases, as it does again with the acquisition of each subsequent molecule, until it is saturated. The same is true of the reverse process. This characteristic of haemoglobin gives a sigmoidal shape to the haemoglobin dissociation curve, which relates haemoglobin oxygen saturation (the ratio of haemoglobin molecules with four attached O₂ molecules, to all other haemoglobin molecules) to oxygen partial pressure, PO_2 . Figure 2.1 illustrates the profile of the haemoglobin oxygen dissociation curve, generated using Kelman's formula (1966),

$$SO_2(x) = \frac{a_1x + a_2x^2 + a_3x^3 + a_4x^4}{a_4 + a_5x + a_6x^2 + a_7x^3 + x^4}. \quad (2.1)$$

SO_2 is the oxygen saturation of haemoglobin, the variable x represents the oxygen partial pressure, and a_i are constants defined by Kelman (1966).

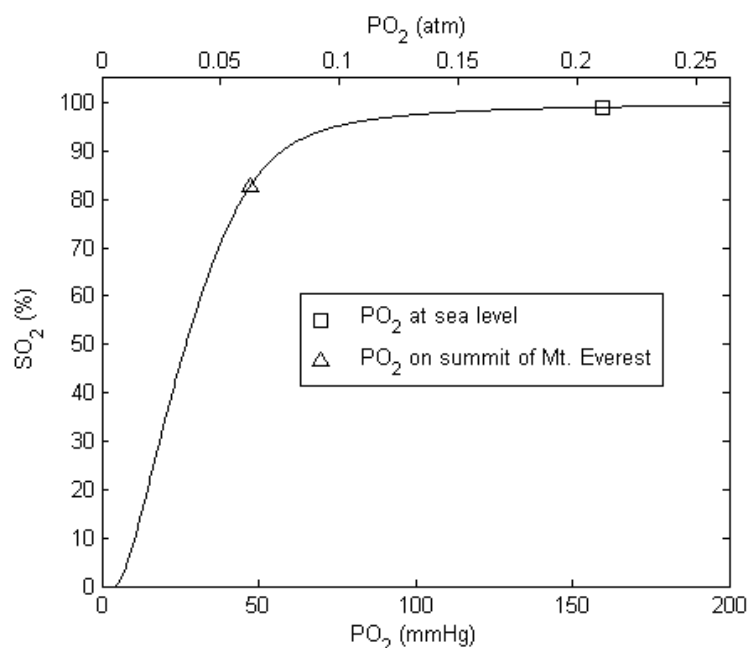


Figure 2.1 Haemoglobin oxygen dissociation curve, generated using the equation described in Kelman (1966). Partial pressure of oxygen is indicated in atmospheres (top axis) and millimetres of mercury (bottom axis).

Figure 2.1 shows the *normal* dissociation curve, that is, for a blood pH of 7.4, carbon dioxide partial pressure (PCO_2) of 40 mmHg, and a temperature of 37 °C. A change in any of these parameters, or a change in the concentration of phosphates in the blood, will cause the dissociation curve to shift (Moyle 1994). Decreasing PCO_2 or temperature, or increasing pH, will cause the curve to shift to the left, resulting in haemoglobin becoming saturated at lower oxygen partial pressures. A change to the contrary in any of these parameters causes the curve to shift to the right. A left-shifted curve, increases haemoglobin's affinity for oxygen, which aids in the uptake of oxygen from the environment but impairs tissue oxygenation—since for the same pressure gradient, less oxygen will diffuse from the blood into the tissue. Fetal haemoglobin has this left-shifted dissociation curve compared to adult haemoglobin, that facilitates obtaining oxygen from the mother but prevents too high an oxygen saturation in the foetus itself, which can be harmful. When breathing an insufficient quantity of oxygen to meet the cellular demand, at high altitudes for example, some cells will switch their metabolism to anaerobic pathways, causing an increase in lactic acid production, resulting in an increase in plasma pH (Moyle 1994). The increasing pH causes a left shift of the dissociation

curve, making the situation worse. A right-shifted curve, conversely, results in decreased affinity, but better facilitates oxygen delivery (Clark 1997).

The actual partial pressure of oxygen present in the alveoli, $P_A O_2$ is less than the ambient oxygen partial pressure of the environment. It is a function of water vapour partial pressure, and of the arterial carbon dioxide partial pressure $P_a CO_2$. The alveolar oxygen partial pressure is given by,

$$P_A O_2 = (P_{\text{ambient}} - P_{H_2O})F_i O_2 - P_a CO_2 \times \frac{\text{Vol. CO}_2 \text{ produced}}{\text{Vol. O}_2 \text{ consumed}}, \quad (2.2)$$

where $F_i O_2$ is the fraction oxygen in the inspired air.

John Scott Haldane, a noted physiologist (and the pioneer of diving decompression theory) commented that *lack of oxygen stops the machine and wrecks the machinery*. The response of individuals to an insufficient supply of oxygen (hypoxia) varies with age and fitness. Within the body the response times of individual tissues and organs also vary. Damage to the cerebral cortex occurs about one minute after the cessation of oxygen supply to it, the liver and kidneys about ten minutes, and skeletal muscle about two hours (Moyle 1994). J.F. Nunn (1987) thus modified Haldane's quote to , *lack of oxygen stops the machine and then wrecks the machinery*.

Haemoglobin has another important property from the point of view of blood oxygen measurement: the colour of haemoglobin changes when it acquires four oxygen molecules. Georg Gabriel Stokes first reported that the coloured substance in blood was the oxygen carrier in 1864. Felix Hoppe-Seyler later crystallised the pigment and coined the name *haemoglobin* (Hb). Hoppe-Seyler observed that when a solution of haemoglobin was exposed to air, it formed a dissociable bond with oxygen, and named this compound *oxyhaemoglobin* (HbO₂). Hoppe-Seyler further observed that Hb was responsible for the absorption of blue and green bands of the solar spectrum. This is why oxygenated blood appears bright red while deoxygenated blood appears blue, however a more useful change in the absorption spectrum of Hb occurs in the near infrared portion of the spectrum (see Figure 3.7) where tissue is translucent—and this facilitates in vivo spectrometry and ultimately pulse oximetry.

2.1.1 DYSHAEMOGLOBINS AND FETAL HAEMOGLOBIN

Oxygen (O₂) is not the only molecule with which haemoglobin can bind, nor is oxygen the only binding agent with which haemoglobin forms a compound that is absorptive of red and near infrared light. A brief description is given here of the other common compounds that haemoglobin forms in blood. They are of relevance to oxygen transportation as these forms of haemoglobin are not able to supply oxygen (dyshaemoglobins), and will later be seen to be of importance in determining the accuracy of blood oxygen measurements (see Section 3.4.1).

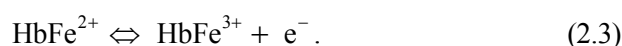
2.1.1.1 CARBOXYHAEMOGLOBIN (COHB)

Carbon monoxide (CO) can also form a bond with haemoglobin to produce a compound Carboxyhaemoglobin (COHb), indeed the affinity of Hb for CO is about two hundred times greater than for O₂. Once bound with haemoglobin however, because of its high affinity, carbon monoxide does not easily relinquish the haemoglobin molecule. From the point of view of oxygen transportation, COHb has the effect of reducing the ability of the blood to carry and supply oxygen.

Haemoglobin bound with carbon monoxide has much higher absorptivity at red wavelengths of light than haemoglobin by itself, and even more so than haemoglobin bound with oxygen. From the point of view of oximetry, COHb levels in excess of those used in calibration (typically < 2% of the total haemoglobin) can cause a large error in the oximetry reading, the cause of which may not be immediately apparent to a user—victims of smoke inhalation, urban dwellers, and indeed heavy smokers can fall into this category (Clark 1997; Moyle 1994; Seidler, et al. 1993; Tungjitkusolmun 1997).

2.1.1.2 METHAEMOGLOBIN (METHB)

Methaemoglobin does not result from the binding of haemoglobin with another gas molecule, but rather, is haemoglobin that has been oxidised, that is, haemoglobin that has lost an electron, and as a result is no longer capable of binding with oxygen. The process can be described as,



Unlike COHb, MetHb occurs naturally and an enzyme system exists for maintaining haemoglobin in its reduced state (HbFe²⁺). Under normal circum-

stances MetHb accounts for less than 0.6% of total haemoglobin, though the concentration varies during the day (Tungjitkusolmun 1997). Its effect on pulse oximetry accuracy is generally less problematic than that of COHb, since MetHb tends to produce an under estimation of blood oxygen content (Moyle 1994), though its effects are difficult to quantify, since its absorption spectrum is strongly pH dependent (Bunn 1986).

2.1.1.3 SULFHAEMOGLOBIN

The irreversible reaction of oxyhaemoglobin and hydrogen sulfide produces sulfhaemoglobin. Sulfhaemoglobin has little effect on oxygen transport as its affinity for oxygen is about one hundred times less than that of unmodified haemoglobin. The absorption spectrum of sulfhaemoglobin is unreported upon, and hence its effects on the accuracy of pulse oximetry are not quantifiable. It is not included in pulse oximetry calibration calculations, though its concentrations in human blood are thought to be sufficiently low as to be insignificant (Clark 1997).

2.1.1.4 FETAL HAEMOGLOBIN

Fetal haemoglobin has a different oxygen dissociation curve compared to normal adult haemoglobin, appropriate to foetal oxygen requirements. It is gradually replaced by adult haemoglobin during the first ten to twelve weeks of life. Its production can be activated pharmacologically in later life, which is useful in the treatment of diseases such as sickle-cell disease. It has a different absorption spectrum to adult haemoglobin, the effects of which are not included in pulse oximetry calibration techniques.

2.2 LIGHT ABSORPTION AND SCATTERING IN TISSUE

This section describes the long established laws and observations that govern the absorption and scattering of light in biological tissue and form the basis of all near infrared spectroscopic techniques, of which pulse oximetry is a special case.

2.2.1 LIGHT ABSORPTION IN TISSUE—THE BEER-LAMBERT LAW

Layers of a substance of equal thickness each absorb the same fraction of an incident beam of light. Thus in a medium consisting of three layers, if the first absorbs $\frac{1}{2}$ of the incident light, the second will absorb $\frac{1}{2}$ the remaining light, as will the third layer, and only $\frac{1}{8}$ of the incident light will emerge from the third layer. This law, derived in the 18th century, is commonly known as the Lambert-Bouguer law, and describes the logarithmic attenuation of light travelling through an absorbing medium. The Lambert-Bouguer can be written as,

$$A = \log_{10} \left(\frac{I_0}{I} \right). \quad (2.4)$$

The dimensionless term A is the light attenuation, given nominal units of optical density (OD), that indicates the order of magnitude of attenuation between the incident light I_0 and the transmitted light I .

In the 19th century August Beer derived a law stating that the optical density of a non-absorbing medium, with an absorbing substance dissolved in it, is proportional to the concentration of the absorbing substance. The combination of these two laws is commonly known as the Beer-Lambert law and can be written as

$$A = \log_{10} \left(\frac{I_0}{I} \right) = \alpha c d, \quad (2.5)$$

where α and c are respectively, the absorptivity¹ and concentration of the absorbing substance, and d is the distance between the points where the light enters and exits the medium.

In cases where there are multiple absorbing substances dissolved in a non-absorbing medium, the combined attenuation due to all the absorbing substance is given by the sum of their individual contributions multiplied by the length of the path travelled by the light, that is,

$$A = [\alpha_1 c_1 + \alpha_2 c_2 + \dots + \alpha_n c_n] d. \quad (2.6)$$

In a typical spectroscopic application, it is required to determine the concentrations of a certain number of substances each of which has a different absorptivity at different wavelengths. The absorptivity as a function of wavelength

¹ Note that α is more correctly the specific extinction coefficient (with units of $\mu\text{molar}^{-1} \text{cm}^{-1}$) and c the concentration in μmolar . The term *absorptivity* is used loosely here since no quantitative data are discussed.

is known for each absorber and the distance d can be measured. Then for different wavelengths of light the attenuation of the medium is measured experimentally. Provided the number of wavelengths used is at least equal to the number of absorbing substances, the concentrations of each of the substances can be found by solving the resulting set of simultaneous equations.

This is the basic premise of all spectroscopic methods of determining tissue oxygen saturation. Tissue might seem apt to this model of attenuation: it is composed largely of water, which can be considered non-absorbing between wavelengths of 200 nm to 900 nm, compared to the absorbers (or chromophores) of interest, Hb and HbO₂. However tissue is also a highly scattering medium. The effect of scattering is to increase the observed light attenuation between two points to a level far greater than can be attributed to absorption alone. Thus the Beer-Lambert law alone is insufficient for determining the concentration of chromophores in tissue.

2.2.2 LIGHT ATTENUATION—THE MODIFIED BEER-LAMBERT LAW

Of the observed attenuation by tissue between two points, absorption accounts for only about 20%, with scattering accounting for the remaining 80% (Elwell 1995). The Beer-Lambert law, equation (2.5), can be modified to take account of the effects of scattering by including an additive term G —the attenuation due to scattering, and a multiplicative term B —the differential path length factor, which when multiplied by the geometric distance d between the source and detector, accounts for the increase in optical path length caused by scattering. Thus the modified Beer-Lambert law can be written as

$$A = \log_{10} \left(\frac{I_0}{I} \right) = \alpha cdB + G. \quad (2.7)$$

The scattering loss G is usually unknown and is dependent on the relative positions of the source and detector, and on the scattering coefficient of the tissue under investigation. As a result of the unknown term, the modified law cannot be used in the same way as the original law, to generate simultaneous equations yielding quantitative values for the sought concentrations. Instead the equation (2.7) is used in a differential form in which the scattering loss is considered to be constant for a given source and detector position. A measurement is made at a particular wavelength yielding attenuation A_1 corresponding to concentration level c_1 . Some

time later, the concentration of the chromophore has changed to c_2 ; another measurement is taken yielding attenuation A_2 . Provided the loss due to scattering (G), the geometric distance between source and detector (d), and the differential path length factor (B), are the same for each measurement, the change in concentration $\Delta c = (c_2 - c_1)$ can be calculated as

$$\Delta A = (A_2 - A_1) = \Delta c \alpha dB . \quad (2.8)$$

For multiple chromophores measured at wavelength λ , the *differential attenuation* can be written as

$$\Delta A(\lambda) = [\alpha_1(\lambda)\Delta c_1 + \alpha_2(\lambda)\Delta c_2 + \dots \alpha_n(\lambda)\Delta c_n] dB(\lambda) , \quad (2.9)$$

where $\alpha_n(\lambda)$ is the absorption of n^{th} chromophore present in the medium measured at a wavelength λ , and where c_n is the concentration of that chromophore in the medium.

Now in a typical spectroscopic application, the values of absorptivity ($\alpha_1(\lambda) \dots \alpha_n(\lambda)$) are known, the geometric path length (d) is measured or calculated, and the differential path length factor ($B(\lambda)$) and the change in chromophore concentration (Δc) remain unknown. Calculation of the differential path length factor is not trivial; two methods are described by Elwell (1995). The first is a time of flight technique that uses a laser capable of generating picosecond duration pulses and a streak camera capable of measuring the time of arrival of a pulse with great accuracy. The pulse from the laser is projected on a beam splitter. One of the resulting beams is directed to the camera via a series of mirrors forming a time reference. The second beam traverses a tissue sample en route to the camera. The difference in the time of arrival is measured and using the speed of light in a vacuum, the refractive index of tissue and the geometric distance, the differential path length factor is calculated. The second method described by Elwell uses an intensity modulated optical spectrometer. A laser beam is modulated and the phase difference between the light entering the tissue and exiting the tissue is measured. This time, using the speed of light in a vacuum, the refractive index of tissue, the modulation frequency, and the measured phase difference, the differential path length factor is calculated.

By measuring the differential attenuation at least at as many wavelengths as there are chromophores, a set of equations can be constructed, which can be solved simultaneously, to yield the time varying, relative change, in each of the chromophores' concentrations. Though this does not yield the quantitative values

for the concentration of individual chromophores, as the unmodified Beer-Lambert law purported to do, the changes in chromophore concentrations over time are useful nonetheless, and form the basis of many spectroscopic investigations of tissue oxygenation and tissue oxygen consumption. See for example Cope (1991) who describes a spectroscopy system for monitoring cerebral oxygenation of new born infants, Niwayama et al. (2006) and Yuanqing et al. (2002) who describe tissue and muscle oxygenation measuring techniques respectively, and Coyle et al. (2004) who describe motor cortex oxygenation monitoring as a means of implementing a brain-computer interface.

Despite the development of such techniques and devices, modified Beer-Lambert law based spectroscopic monitoring, is in general ill-suited to routine clinical monitoring applications, where the need to establish an estimate of the differential path length, for every patient and for each measurement site, is impractical. Though modified Beer-Lambert based spectroscopy is extendable to the application of pulse oximetry (Humphreys, et al. 2005b; Rolfe 2000), in practice, no clinical device utilises the technique. Section 3.2.1 revisits the subject of light attenuation in tissue and describes how the technique of pulse oximetry eliminates the need to establish the optical path length in calculating arterial blood oxygen saturation.

2.3 LIGHT TRANSPORT IN TISSUE

Section 2.2 described how light travelling through tissue is attenuated by the combined effects of scattering and absorption. This section describes the affect of scattering and absorption on the propagation of light through tissue with the aid of a Monte Carlo simulation; specifically, the proclivity of scattering to cause the bending of light propagating through tissue—making possible the measurement of backscattered light and ultimately non-contact measurements of tissue and blood oxygen saturation.

2.3.1 LIGHT ABSORPTION

Light absorption refers to the loss of photonic energy during interaction with electrons, atoms, and molecules. The energy lost by photons is converted into either heat or into light of longer wavelengths (Splinter and Hooper 2007). Within tissue,

near infrared light is absorbed by molecules that possess an electric dipole moment, typically these are molecules composed of dissimilar atoms and they include carbon dioxide, carbon monoxide, nitric oxide, and water (Reddy 1997). Absorption is wavelength dependent.

The absorbers of principal interest in this study are Hb and HbO₂, a list of the other common absorbers (or chromophores) in tissue and of relevance to this study is given in Section 2.1.1.

2.3.2 LIGHT SCATTERING

Light scattering can be classified into three modes of light-particle interaction: Rayleigh scattering, Mie scattering, and Raman scattering. The occurrence of Rayleigh or Mie scattering is determined principally by the ratio of the wavelength of the incident light (λ) to the dimensions of the scattering particle. Rayleigh scattering occurs when λ is much larger than the dimensions of the scattering particle and Mie scattering when the dimensions are comparable. Both Rayleigh and Mie scattering are elastic and cause a change in the trajectory of the scattered photon only. Raman scattering by contrast describes a phenomenon in which the trajectory of the scattered photon is altered, but in addition the interaction causes the emission of light, usually with longer wavelength, from the scattering particle (Splinter and Hooper 2007).

Mie scattering is predominant in light interaction with biological tissue. The interaction closely approximates geometrical optics. The cross-section of the scattering particle and the angle of incidence of the photon are used to determine an anisotropy factor g , which is the probability that the photon will be scattered in a solid angle θ .

2.3.3 MONTE CARLO SIMULATION OF LIGHT PROPAGATION

A Monte Carlo simulation of light propagation through a homogenous scattering medium is presented here. The simulations are instructive in establishing the most probable path along which a beam of photons travels between the injection point and the detection point. Knowledge of the likely path taken by a beam of photons is necessary to explain the means by which contact and non-contact pulse oximetry and photoplethysmography acquire pulse signals from tissue. The profile of the

photons path also provides rationale for design considerations pertaining to positioning of source and detector, and a means of explaining some of the phenomena associated with non-contact camera-based photoplethysmography.

The propagation of optical radiation in tissue is most often described using radiation transfer theory, which ignores wave-like phenomena such as interference. The radiative transfer equation formulates the radiance of light in a medium in terms of absorption and differential scattering coefficients (the derivation of which has been provided by many authors—see for example Splinter and Hooper (2007)). The equation can be solved analytically for simple geometries, however it is most commonly solved by various numerical methods including, but not limited to, Monte Carlo analysis, random walks (Bonner, et al. 1987), and finite element analysis (Arridge, et al. 1993). Of these techniques, Monte Carlo analysis is perhaps the most versatile and commonly used, lending itself to complex tissue geometries. The disadvantage of the Monte Carlo method is that it is computationally intensive and time consuming. The technique provides a simulation of light propagation rather than a direct solution to the radiative transfer equation, and as such requires the simulation of a large number of photons to produce accurate results, with the accuracy increasing in proportion to the square root of the number of photons used (Patterson, et al. 1990). Nonetheless, Monte Carlo simulations are commonly found in investigations of light-tissue interaction and near infrared spectroscopy, see for example: Hiraoko et al. (1993) on investigations of optical path length; Okada et al. (1997) on investigations of light propagation in the adult head for spectroscopy; Fukui et al. (2003) on investigation of light propagation in both adult and neonatal heads; Strangman et al. (2003) on the effects of differential path length factor and optical cross-talk as sources of error in NIR spectroscopy; Reuss (2005) on the comparability of homogeneous and multi-layer models of tissue for reflectance pulse oximetry; and Niwayama et al. (2006) on tissue oxygen measurement.

Figure 2.2 displays the flowchart of the Monte Carlo simulation program used here. The flowchart and the description of its functions that follows, are based on those described by Prahl et al. (1989) and Splinter and Hooper (2007). The method described here utilises a variance reduction technique known as *implicit capture*, in which a group or packet of photons, rather than an individual photon, is propagated through the medium. Upon its launch, each packet is given the same weight; at each tissue interaction location, a portion of the packet's weight is lost due to absorption and the remainder of the packet scattered in accordance with the optical properties of the medium. Packets continue to propagate in the medium until their weight falls

below a certain threshold value, or until they are backscattered from or transmitted through the medium.

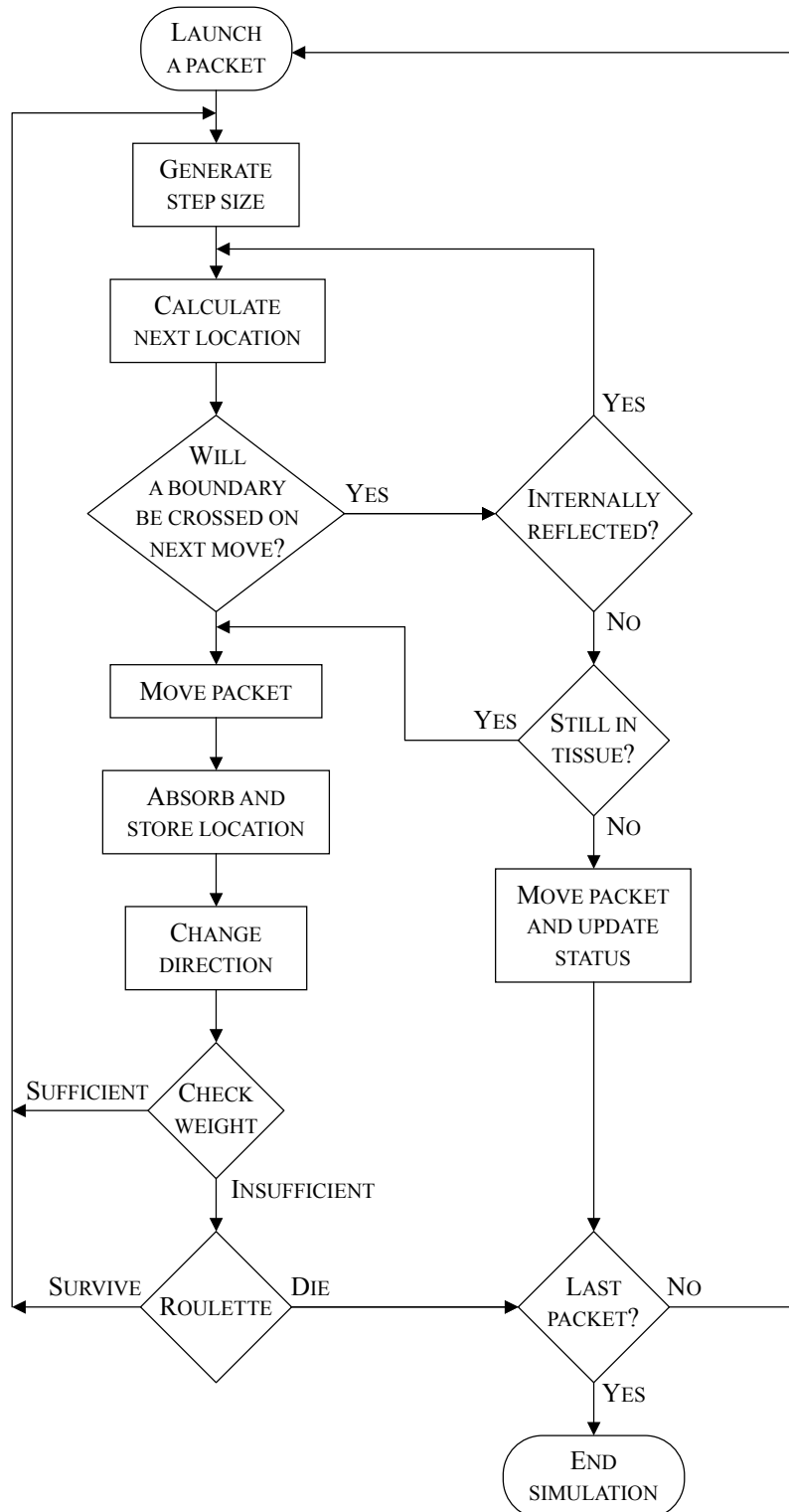


Figure 2.2 Flowchart of Monte Carlo simulation.

Throughout the simulation each packet’s three-dimensional location is recorded as a Cartesian coordinate (x, y, z) . The packet’s current trajectory is

described by three directional cosines (μ_x, μ_y, μ_z); the cosines of the angles made between the packet's trajectory and each of the x, y and z -axes; defined as the dot product of the trajectory vector and a unit vector along each of the x, y and z -axes. The packet's initial position is $(0, 0, 0)$ and its initial trajectory $(0, 0, 1)$. Thus packets are injected at the origin, initially travelling vertically. (When the tissue model comprises one or more horizontal layers, $z < 0$ defines air, $z > 0$ defines tissue, and $z = 0$ defines the air-tissue interface.) In this manner an infinitely narrow beam of photons is simulated.

Attenuation coefficients due to absorption, μ_a , and due to scattering, μ_s , are defined respectively as the mean number of absorption and scattering events encountered by a photon per millimetre. A total attenuation coefficient, μ_t , is defined as the sum of μ_a and μ_s . Thus the mean step size that a photon travels without interacting with the medium, the mean free-path length Δs , is described by,

$$\Delta s = \frac{1}{\mu_t} = \frac{1}{\mu_a + \mu_s} . \quad (2.10)$$

The discussion of the Beer-Lambert law in Section 2.2.1 noted that light travelling in tissue is attenuated exponentially, thus the probability density function that describes the distribution of Δs is also exponential and is proportional to $\exp(-\mu_t \Delta s)$. A step size with such a density function is generated by,

$$\Delta s = \frac{-\ln \xi}{\mu_t} , \quad (2.11)$$

where ξ is a random variable uniformly distributed between zero and one.

Having generated an appropriate step-size Δs , a packet is moved to its new location by updating its (x, y, z) Cartesian coordinates. The new coordinates $(x_{new}, y_{new}, z_{new})$ are given by,

$$\begin{aligned} x_{new} &= x + \mu_x \Delta s \\ y_{new} &= y + \mu_y \Delta s \\ z_{new} &= z + \mu_z \Delta s . \end{aligned} \quad (2.12)$$

At its new location the packet's weight, w , is reduced by a fraction μ_a/μ_t , such that the packet's new weight w_{new} , is given by,

$$w_{new} = \frac{\mu_a}{\mu_a + \mu_s} w . \quad (2.13)$$

The location of the absorption and the new weight of the packet are recorded. The remainder of the packet is scattered.

The scattering trajectory is defined by two angles: an azimuthal angle ϕ and a longitudinal angle θ . The azimuthal angle is uniformly distributed over the range 0 to 2π , and is hence given by,

$$\phi = 2\pi\xi, \quad (2.14)$$

where ξ is again a random variable uniformly distributed between zero and one.

The longitudinal angle θ , is not uniformly distributed and is calculated using the Henyey-Greenstein phase function² defined as,

$$\cos \theta = \frac{1}{2g} \left\{ 1 + g^2 - \left[\frac{1 - g^2}{1 - g + 2g\xi} \right]^2 \right\}. \quad (2.15)$$

The term g , was defined earlier as the anisotropy factor. The term ξ is a random variable uniformly distributed between zero and one. When $g = 1$ scattering is predominantly forward, as g tends towards zero, scattering tends towards isotropic scattering. If scattering is truly isotropic then $g = 0$, and the longitudinal angle is instead calculated as,

$$\cos \theta = 2\xi - 1. \quad (2.16)$$

A photon with a current trajectory defined by the directional cosines (μ_x, μ_y, μ_z) will, after being scattered in a direction (θ, ϕ) , have a new trajectory (μ'_x, μ'_y, μ'_z) , given by,

$$\begin{aligned} \mu'_x &= \frac{\sin \theta}{\sqrt{1 - \mu_z^2}} (\mu_x \mu_z \cos \phi - \mu_y \sin \phi) + \mu_x \cos \theta \\ \mu'_y &= \frac{\sin \theta}{\sqrt{1 - \mu_z^2}} (\mu_y \mu_z \cos \phi + \mu_x \sin \phi) + \mu_y \cos \theta \\ \mu'_z &= -\sin \theta \cos \phi \sqrt{1 - \mu_z^2} + \mu_z \cos \theta. \end{aligned} \quad (2.17)$$

If the current trajectory of the photon is close to vertical, say $|\mu_z| > 0.99999$, then equation (2.17) should be replaced by,

² Henyey and Greenstein (1941) characterised the scattering of light in interstellar dust clouds, by developing an expression for the angular dependence of light scattering by small particles. The identity they developed (which describes the probability density function of an angle as a function of the anisotropy of the scattering medium) is now commonly used to describe the scattering of light in biological tissues.

$$\begin{aligned}
 \mu'_x &= \sin \theta \cos \phi \\
 \mu'_y &= \sin \theta \cos \phi \\
 \mu'_z &= \frac{\mu_z}{|\mu_z|} \cos \phi.
 \end{aligned}
 \tag{2.18}$$

Where a packet's trajectory crosses a boundary between regions of different refractive indices, be it tissue and air or two different tissues, there is a possibility that the packet will be internally reflected with a probability proportional to the angle of incidence. For simple models comprised of parallel layers of tissues, the angle of incidence θ_i , of the packet can be calculated as,

$$\theta_i = \cos^{-1} \mu_z.
 \tag{2.19}$$

The angle of transmission, θ_t , can be calculated using Snell's law,

$$\theta_t = \sin^{-1} \left(\frac{n_i}{n_t} \sin \theta_i \right),
 \tag{2.20}$$

where n_i and n_t are respectively, the refractive indices of the medium from which, and towards which, the packet is travelling.

The probability of internal reflection is given by the Fresnel reflection coefficient $R(\theta_i)$,

$$R(\theta_i) = \frac{1}{2} \left[\frac{\sin^2(\theta_i - \theta_t)}{\sin^2(\theta_i + \theta_t)} + \frac{\tan^2(\theta_i - \theta_t)}{\tan^2(\theta_i + \theta_t)} \right].
 \tag{2.21}$$

Whether the packet is reflected or not is determined by a random number uniformly distributed between zero and one, ξ , such that reflection occurs if,

$$R(\theta_i) < \xi.
 \tag{2.22}$$

Finally it is desirable to cease propagating packets with small remaining weight, as they contribute little to determining the distribution of photons within the medium. Eliminating all packets with less than a threshold weight violates the conservation of energy principle, thus packets with a weighting less than a threshold are subjected to a Roulette process—surviving packets have their weight reset to the maximum and continue propagating.

A Monte Carlo routine based on the description given here and the flowchart depicted in Figure 2.2 was implemented in Matlab[®] (MathWorks Inc.). Figure 2.3 displays the results of a simulation of one million launched packets through a homogenous medium with the optical properties described in Table 2.1. The plot

shows the locations where backscattered photons emerged from the medium. Superimposed on Figure 2.3 are circles concentric on the injection point (0, 0). Each annular region between adjacent circles encloses the same area as that enclosed by the inner circle.

Parameter	Value
μ_a	0.2 mm ⁻¹
μ_s	1.3 mm ⁻¹
g	0.9
Refractive index of tissue	1.3
Minimum packet weight	0.1
Roulette survival probability	0.1

Table 2.1 Optical properties of tissue as used in Monte Carlo simulation.

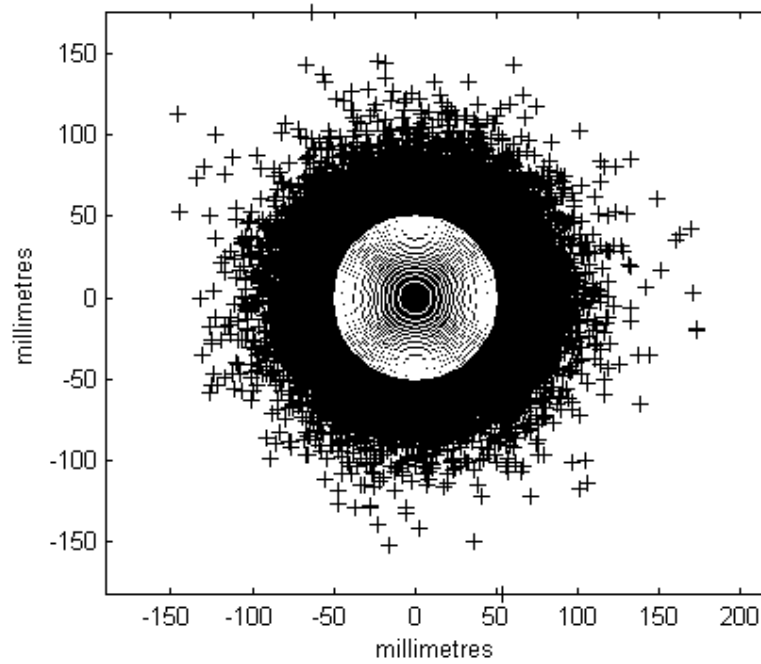


Figure 2.3 Emergence of backscattered photons injected at the point (0, 0) with concentric circles each enclosing equal area.

Figure 2.4 displays a plot of the number of backscattered packets emerging in each annular region, versus radial distance from the injection point. Figure 2.5 displays the cumulative weight of all packets contained in each annular region versus the radial distance from the injection point (where the cumulative weight is the sum of the variable weight that each packet retains upon its emergence from the tissue, which is proportional to the received light intensity). As described earlier (see Section 2.2) the emergent light intensity decreases exponentially in all directions with increasing distance from the source.

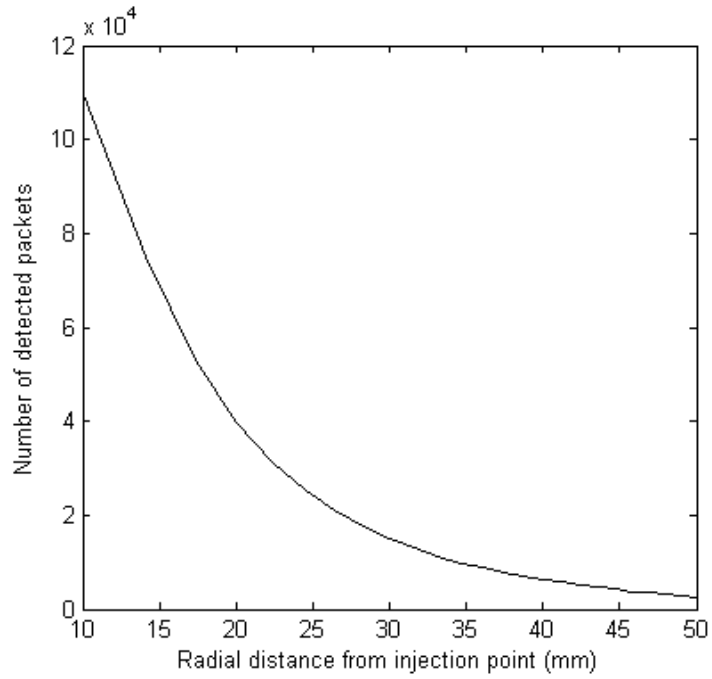


Figure 2.4 Number of emerging packets versus radial distance from injection point (one million photons launched).

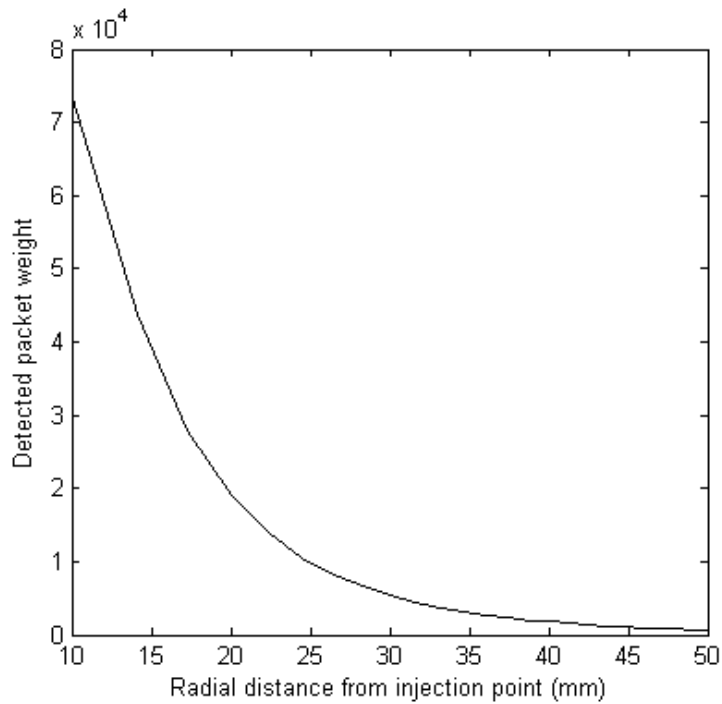


Figure 2.5 Cumulative weight of emerging packets versus radial distance from injection point.

The probable path taken by a photon travelling between a given injection and emergence point, can be predicted to some degree for a medium of known optical characteristics and geometry. Figure 2.6 displays the path taken by all photons that

emerged within a radius of 10 mm of the location (15, 15, 0), in a simulation of one hundred thousand packets using the same optical properties given in Table 2.1.

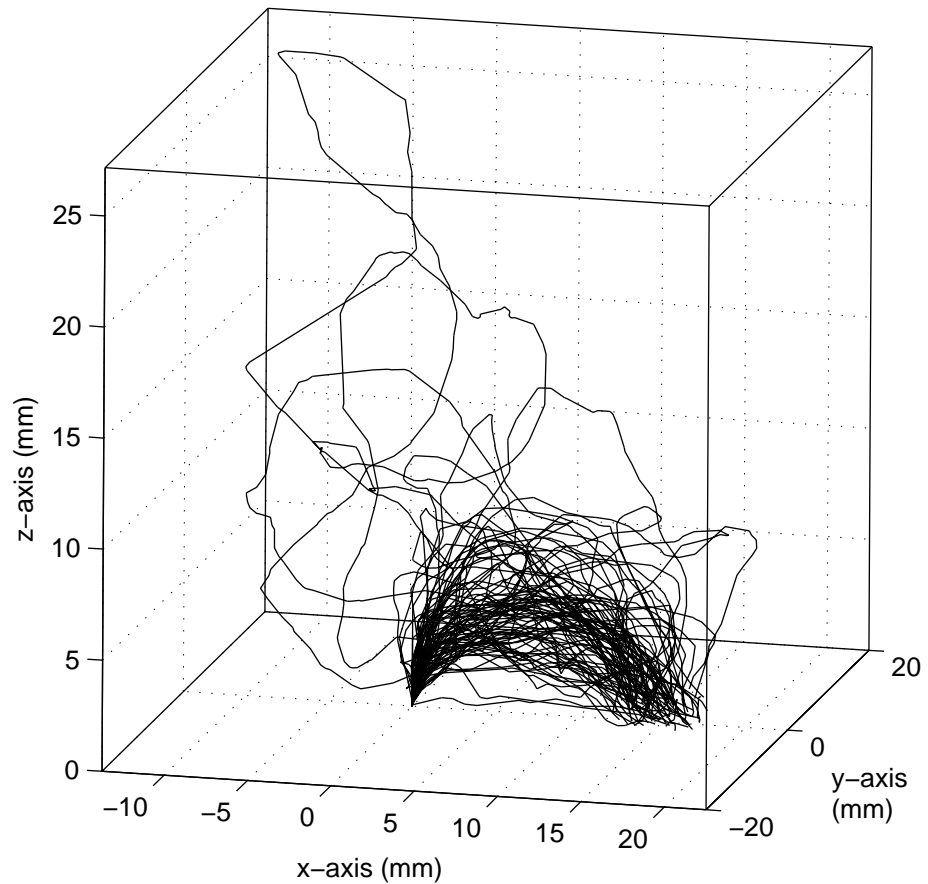


Figure 2.6 Path taken by photons travelling between the injection point and the emergence area.

The photons travel in an arc between the injection point and the emergence area, forming a three dimensional shape that is ubiquitously referred to in the literature as an *optical banana*. The proportions of this banana within a given medium depend on the separation of the injection and emergence point, or the separation of source and detector points in an actual application, with the penetration depth of the light increasing as the source-detector separation increases.

Note that in order to use a Monte Carlo simulation to characterise a medium in terms of absorption, scattering, or light fluence, it is necessary to divide the volume into discrete volumes—voxels. Each time an absorption event takes place, the appropriate absorption quantity is added to the corresponding voxel. As the voxel size is reduced, the granularity of the modelled volume is increased, giving better resolution. However greater granularity results in smaller sampling of the photon distribution, and consequently greater uncertainty. Lower granularity conversely

provides less resolution but higher certainty of the distribution of light fluence, absorption, or scattering within a voxel. Thus to achieve accurate results with a Monte Carlo simulation, a large number of photons must be launched.

The number of photons used to generate the optical paths in Figure 2.6 is insufficient to characterise the transport of light in a medium in general, and the photon paths are intended only to illustrate the effect. (It is impracticable to store or display the paths of very many photons.)

Furthermore, the above simulations characterise the response of the medium to an infinitely narrow beam of photons. To simulate a realistic beam of incident photons one of two techniques can be employed. Either the beam profile may be convolved with the beam source function, or the initial location of the photons may be varied randomly, with a distribution defined by the source profile.

2.4 SUMMARY

This chapter has presented a short overview of oxygen transportation, light attenuation in tissue, and light transportation in tissue. The mechanism of oxygen transportation is important to the method of pulse oximetry and will be shown in Chapter 3 to affect the choice of wavelengths for a device and, in the case of functional and dysfunctional haemoglobins, to affect both the accuracy of the device and the actual measured quantity.

The Beer-Lambert model of absorption and scattering of light in tissue (which are collectively observable as attenuation) is the basis of pulse oximetry and Chapter 3 will build on this discussion in describing the method of pulse oximetry.

The *banana-shaped* path taken by light travelling between two points on the tissue surface has ramifications for the choice of source and detector geometry, both in a conventional contact device and especially in a non-contact device. Knowledge of the shape of this path is used in Chapter 5 as the rationale for choosing the relative position of the source and detector, and is referred to again in Chapter 6 to describe the concept of camera-based diffuse tomography.

The Monte Carlo simulation is employed again in Chapter 5 to investigate the effects of tissue-detector separation on the received light intensity.

CHAPTER 3

PULSE OXIMETRY

The technique of pulse oximetry is rooted in the Beer-Lambert based spectrometry described in the previous chapter. This chapter details the application of the principles of Beer-Lambert based spectrometry to the specific application of arterial blood oxygen saturation monitoring. This chapter has two principal objectives. First it is intended to provide the reader with a thorough explanation of the principles and technologies that form the basis of all variants of pulse oximetry. Second, following this discussion, a description is given of some of the technical problems faced by pulse oximeter designers and manufacturers. Some solutions to common problems are reviewed. The prominence given to the various aspects of clinical device design during this discussion, is not necessarily indicative of their importance to the performance of clinical devices—for example, no consideration is given to the microprocessor, though it is arguably the most important component of a pulse oximeter and is the greatest variable among manufacturers. Rather, the discussion that follows is intended to elucidate aspects of pulse oximeter functionality, which a novel device must emulate comparably, and aspects of pulse oximeter operation that are negated, obviated, or complicated, by a non-contact implementation.

3.1 CONTEMPORARY HISTORY OF PULSE OXIMETRY

An electrical engineer ultimately invented pulse oximetry, though the extent to which it has since been reported upon in biomedical and electronics literature belies the fact that pulse oximetry properly belongs to the physiological field of blood gas analysis. Pulse oximetry owes its existence to fundamental investigations by natural philosophers, physiologists and physicians over three centuries. This brief discussion focuses only on the *recent* history of the subject, and then only on the protagonists and their inventions, which led directly to the present day clinical monitoring technology. The technology used in oximetry has varied markedly with the era in which developments took place, and to a large extent, development in oximetry took place as a result of technological development in other fields. Only passing reference is made to those technologies here, though the concomitant complexities of cumbersome sources, non-linear detectors, and weak amplification, should be borne in mind when considering the pace and magnitude of achievements.

Gas has been extracted from blood for centuries, initially by vacuum, and the constituent gases and their quantities identified with ever increasing precision for the last 150 years (Severinghaus 1987a). Though it has been possible to measure the tension (partial pressure) of oxygen in blood by various means for some time, the impetus for optical measurement was the discovery that the electron emission from cesium cathodes was sensitive to light. This ultimately led to the development of barrier layer photocells; semi-conductive barriers to electrons that become conductive when light is incident upon them. Ludwig Nicolai made the first steps towards modern oxygen saturation measurement in 1931. Using a mercury vapour light and a rotating filter wheel to produce blue and green light, a vacuum photoelectric cell detector, and a vacuum tube amplifier, Nicolai occluded the circulation in his hand and derived curves for the decrease of HbO₂ and increase in Hb over time. Nicolai's associate, Kurt Kramer, then made the first report of precise oxygen saturation measurement of blood both in cuvettes and flowing blood in 1934 using an incandescent light and barrier photo cell (Severinghaus 1987a). Building on their work, in 1935 another German physician, Karl Matthes, produced the first device to continuously measure oxygen saturation in humans, by transillumination of the ear (Severinghaus and Astrup 1986d).

The next important development was the outbreak of World War II in 1939. Military aircraft at the time were not pressurised and at high altitudes, where

oxygen partial pressure is low, aviators sometimes lost consciousness (see Section 2.1). Scientists involved in the British war effort, notably Lord Adrian, professor of physiology at Cambridge University, had begun developing oxygen delivery systems sensitive to altitude and activity. Adrian wrote to the American physiologist Glenn Millikan asking for help with the task. Millikan was at the time a lecturer at Cambridge, though had been visiting his parents in the United States at the outbreak of war in Europe, and had subsequently remained there. Millikan was well primed to take on the task; he had obtained his PhD for a thesis on a dual-wavelength colourimeter, he had worked in Germany prior to the outbreak of war, and in 1936 had been visited by Kramer and adopted the use of the barrier layer photocell. Between 1940 and 1942, Millikan and his colleague Pappenheimer were principally responsible for developing a lightweight and practical aviation ear oximeter, which became known as the Millikan ear oximeter, and incidentally coined the term *oximeter*.³ The device was first presented in 1941 (Millikan, et al. 1941). Millikan and his colleagues had arranged for the device's production and successfully incorporated a servo that controlled the supply of oxygen to an aviator's mask. The device initially used an incandescent battery operated light, and red and green gelatine filters. The use of green light was common at the time due to the high absorption at this wavelength in the haemoglobin spectrum. Millikan had shown the light detected at this wavelength to be independent of oxygen saturation and thus useful as a reference wavelength. However just prior to publishing this in *Review of Scientific Instruments* in 1942, the device manufacturer informed Millikan that the ear was so opaque to green light and transparent to infrared light, that the green filter and its photocell had in fact, fortuitously, been responding primarily to infrared light. The paper was corrected in time and became the first report of red and infrared light in oximetry (Millikan 1942).

Although Millikan had been working in the United States, the United States military only became interested in the technology when they learned that the German Luftwaffe already had such a device (Severinghaus and Astrup 1986d). Despite having access to much of Matthes' work (he had been a prodigious author producing twenty papers on oximetry between 1935 and 1944), the United States had failed to produce a working device. However after V-E Day, the United States Army recovered Kramer (then an SS officer) from a Russian prisoner of war camp.

³ The term *oximeter*, though likely derived from the words *oxygen* and *meter*, is now used to refer exclusively to oxygen measuring devices based on the principle of spectrometry—that is optical methods of determining oxygen saturation.

Kramer was brought to the United States to help perfect the technology—which he did.

Millikan was killed in a rock climbing accident in 1947, though the tremendous efforts that he and others had expended during the war found new application in the emerging field of respiratory physiology. By 1950 some sixty six publications existed that described uses of the Millikan ear oximeter (Severinghaus and Astrup 1986d). It is important to note, that at this point oximeters, though they sought to measure arterial oxygen saturation, could not discern the contributions to their readings from arterial blood, venous blood and scattering and absorption by tissue. Thus while oximeters of the time could indicate a change in saturation and could provide a reading proportional, even close to, the arterial oxygen saturation, they could not provide absolute readings. An important improvement to the Millikan oximeter was made by Wood and Geraci (1949), building on the work of Squire (1940), when they introduced an inflatable balloon with which the ear could be made bloodless to provide an initial zero reading. This technique removed the components due to scattering and absorption by tissue to the arterial oxygen saturation reading, though did not remove the contribution from venous blood.

At this point the ear oximeter was still dependent on barrier layer photocell detector technology. It was not possible to measure the output current of these devices without causing a drop in voltage that decreased the devices' sensitivity. Furthermore the devices' output current varied with time and temperature (Severinghaus 1987a; Severinghaus and Astrup 1986d). At about this time Leland Clarke invented his oxygen electrode, which measured the oxygen partial pressure in a gaseous mixture or the oxygen tension in a solution. Soon this device made possible transcutaneous oxygen partial pressure measurement and as a result a paradigm shift occurred in blood oxygen measurement, physiologists and physicians began thinking of blood oxygen content in terms of partial pressure rather than saturation (Severinghaus and Astrup 1986b). The use of oximetry began to decline, a trend that continued until the development of silicon semiconductor detectors and high gain solid-state amplification techniques.

The next important milestones in the development of pulse oximetry came in the nineteen sixties. Previous oximeters had typically used two wavelengths of light, one sensitive to oxygen saturation and one insensitive. In this manner it had not been possible to discern the contributions of the various species of haemoglobin to the saturation reading (see Section 2.1.1). This problem was tackled with the introduction of the eight-wavelength ear oximeter by surgeon and inventor Robert

Shaw around 1964. This device (constructed from a broadband halogen lamp, optical fibres and photodiode detector—though still utilising a rotating filter wheel to produce multiple wavelengths) was bought and marketed by Hewlett-Packard. It was widely used in physiological research (Moyle 1994), however due to its expense and the large size of the ear piece, it was seldom used for clinical monitoring (Severinghaus and Astrup 1986d). Though it was never intended for clinical monitoring, another important development at this time was the CO-oximeter, the operation and importance of which is discussed later.

The final step in the emergence of pulse oximetry came in the nineteen seventies, when the Japanese engineer, Takuo Aoyagi, realised that by isolating the pulsatile component of the received light intensity, the long sought oxygen saturation of the arterial blood could be distinguished from all the other components of the detected light intensity. Aoyagi had actually been trying to measure blood flow and was initially concerned with removing the unwanted pulsatile component when the realisation occurred (Aoyagi 1992, 2003; Aoyagi and Miyasaka 2002). Aoyagi and his colleagues built the first prototype device between 1973 and 1974. However prior oximeters had never been widely used in clinical applications and in the decade that followed, few foresaw the potential of pulse oximetry. Severinghaus and Honda (1987) attributed the enormous interest that eventually developed to the multi-qualified engineer, physician, and physiologist, William New, and engineer, Jack Lloyd, who together founded the company Nellcor Incorporated. New recognised the potential for pulse oximetry in all applications where a patient is unable to regulate their own oxygen supply. However with the success and worldwide interest that followed came a lucrative medical instrumentation market, and with that came patents and litigation (a decorous description of which, is provided by Severinghaus and Honda (1987)).

The discussion here highlights the impetus and developments that directly contributed to the invention of pulse oximetry. Also of significance to the modern technology were the contributions to reflectance oximetry of Zijlstra (1953; 1958) and his mentor Brinkman.

For an historical overview of the subject of blood oxygen measurement, and its parent subject, blood gas analysis, the interested reader should refer to the works of Severinghaus and Astrup (1985a; 1985b; 1986a; 1986b; 1986c; 1986d) and Severinghaus and Honda (1987). An even more comprehensive and well-narrated treatise of the subject is to be found in the epic, essay-style paper of Severinghaus (1987a). For an insight into the early development of the technology, and transcripts

of symposium discussions between early protagonists (including Severinghaus, Wukitsch, Tremper and others) the interested reader should refer to Payne and Severinghaus (1986).

The taxonomy of the field of blood gas analysis is depicted in Figure 3.1. It is apt to think of pulse oximetry as the culmination of the development of the *in vivo* oximeters. Its displacement of all other methods of *in vivo* oxygen measuring in clinical environments, and the re-reversion of clinical and experimental thinking, from terms of oxygen partial pressure back to oxygen saturation, is now a matter of historical record. However, until the emergence of commercial pulse oximeter devices in the nineteen eighties, oximeter technology faced stiff competition from chemical methods (particularly the invasive Clarke electrode) and the transcutaneous oxygen partial pressure sensor. A short discussion of the construction and operation of this device is included below. An appreciation of the Clarke electrode's operation is instructive in understanding the revolution that pulse oximetry brought to clinical oxygen monitoring, and the comparative robustness of the pulse oximeter.

Also included below is a short description of the aforementioned CO-oximeter. Though the CO-oximeter is a cuvette-based technique that was neither intended nor used for *in vivo* monitoring, it has however, become the gold standard of laboratory blood oxygen measurement, and is central to the calibration procedure (see Section 3.3.5) of both conventional pulse oximeters and the novel non-contact technique described in this thesis.

On the subject of the non-contact device described in this thesis and its classification within the taxonomy described in Figure 3.1, it could be argued that it is either the direct descendant of pulse oximetry or perhaps a separate genus of *in vivo* oximeters, the non-contact oximeter.

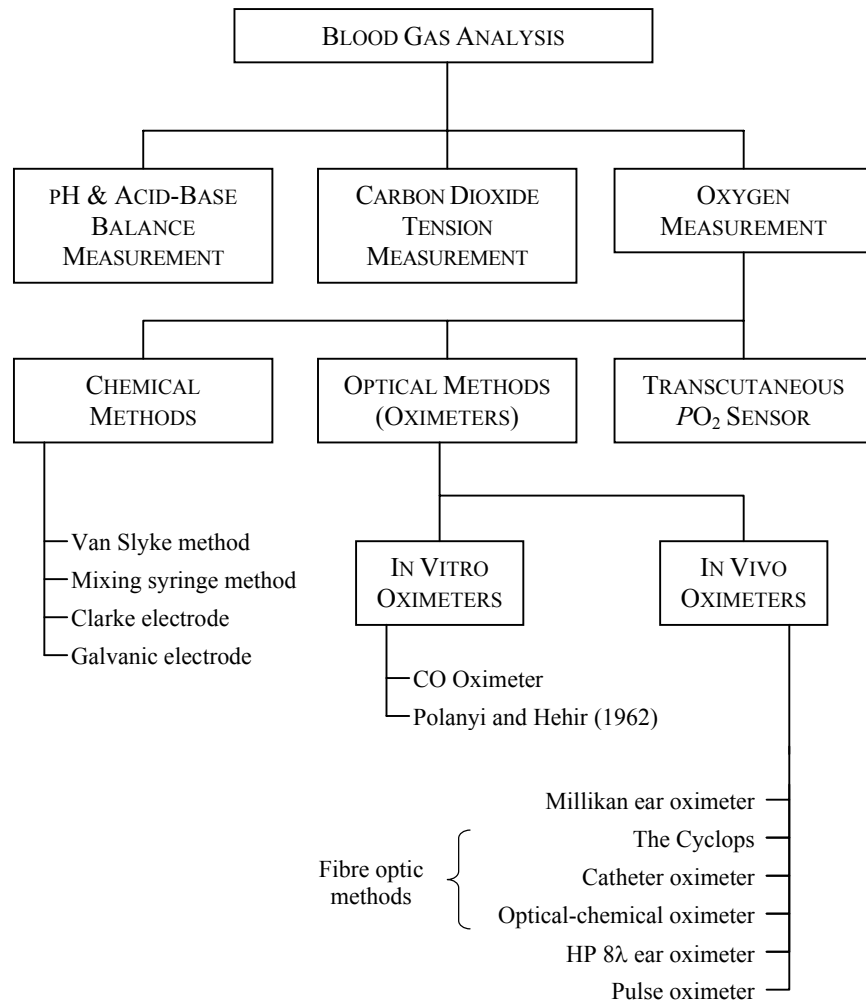
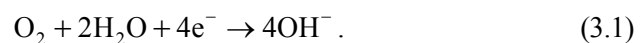


Figure 3.1 Taxonomy of the field of blood gas analysis.

3.1.1 THE CLARKE ELECTRODE AND THE TRANSCUTANEOUS PO_2 SENSOR

Leland Clarke invented the Clarke electrode in October 1954, assembling the first electrode from glass, platinum and silver wire, and a potassium chloride solution, wrapped in a polyethylene film (Severinghaus 1987a). The electrode measures the partial pressure of oxygen (PO_2) using the principles of oxidation and reduction. When oxygen is dissolved in an aqueous solution and exposed to a voltage of approximately 0.6 V the following reaction occurs (Farmer 1997),



The principle of the electrode is illustrated in Figure 3.2. Since the potassium chloride solution provides everything for the reaction except O_2 , the amount of O_2 dissolved in the solution determines the amount of current that flows between the anode and cathode.

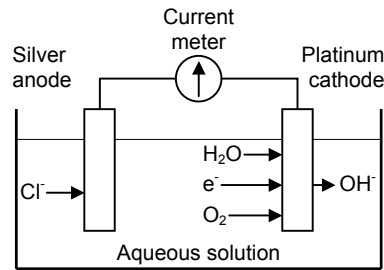


Figure 3.2 Principle of operation of the Clarke electrode.

The actual electrode is arranged in a cylindrical fashion, and is used to measure PO_2 of blood solutions in vitro, and when miniaturised, can be attached to the end of catheter and placed inside an artery to provide in vivo measurement. Clarke's electrode stills forms the basis of most laboratory blood gas analysers (Shapiro, et al. 1989), and is also commonly used in the food industry, beer and wine production, aviation, soil chemistry, and sewage management (Severinghaus 1987a).

The Clarke electrode, mounted upon a catheter, is however an invasive means of monitoring blood oxygen, and the electrode found its greatest clinical use in its less invasive guise, as the transcutaneous PO_2 sensor. The transcutaneous PO_2 sensor is depicted in Figure 3.3. Under normal circumstances, PO_2 of blood near the skin's surface is atmospheric (0.21 bar or 157 mmHg), however hyperaemia (increased blood volume) of the skin can cause the PO_2 of the blood near the surface to approach the arterial oxygen partial pressure, P_aO_2 . This excess oxygen near the skin's surface then diffuses out through the skin and can be detected using the Clarke electrode. Hyperaemia can be introduced by abrasions, drugs and creams, or, as in the case of the transcutaneous PO_2 sensor, by heating. The transcutaneous PO_2 sensor consists of a Clarke electrode with a heating element and a thermistor for temperature control. The skin is heated to between 43 °C and 44 °C, the optimum temperature for achieving the desired transcutaneous effect with minimum skin damage. The sensor must be periodically moved to avoid burns, particularly with infants.

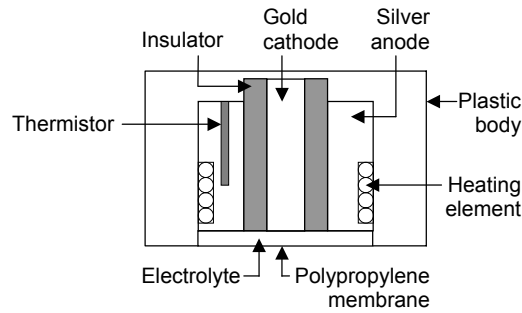


Figure 3.3 Transcutaneous PO_2 sensor.

The sensor has some advantages over a pulse oximeter; for example, it will continue to produce a valid output in the presence of anaemia, which a pulse oximeter will not do. However among its drawbacks are that it requires skin and electrode preparation, a warm-up time of several minutes, requires recalibration, reports low PO_2 if poorly placed, and requires some operator skill (Barker and Tremper 1984; New 1985; Severinghaus 1987b). Most of these requirements are obviated by pulse oximetry, which despite some limitations (see Section 3.4.2) provides less invasive, safer, and more robust clinical monitoring of oxygen saturation, with the added benefits of heart rate monitoring and display of the peripheral arterial pressure waveform.

3.1.2 THE CO-OXIMETER

The term *CO-oximeter* was coined but not copyrighted by Instrumentation Laboratories Inc. who produced the first device in 1966 (Moyle 1994). CO-oximeters are spectrometers designed to analyse haemolysed blood samples using the Beer-Lambert law (see Section 2.2.1) to determine the concentrations of the four most common species of haemoglobin; reduced haemoglobin (Hb), oxyhaemoglobin (HbO_2), carboxyhaemoglobin (COHb), and methaemoglobin (MetHb).

A typical CO-oximeter analyses small samples of heparinised and haemolysed blood. That is blood to which an anticoagulant has been added, and in which the red blood cells have been destroyed (often by ultrasound), releasing haemoglobin into the plasma. Blood samples are maintained at 37°C . Placing either slits or interference filters in front of a broadband light source generates several monochromatic wavelengths of light, which are used to illuminate the blood sample. The light is usually in the visible range between 500 nm and 700 nm.

Typically a photodiode is used as a detector. Since the test solution contains only absorbers, the optical path length can be easily measured. The incident light intensity can be obtained for each wavelength by means of a reference beam. Determining the concentration of the absorbers is therefore, a straightforward matter of applying the Beer-Lambert law for the case of multiple absorbers (Moyle 1994).

CO-oximeters are susceptible to error. The presence of scattering impurities in the blood sample, such as cell fragments remaining from the haemolysis process or lipids, invalidate the presuppositions on which the Beer-Lambert calculations are based. CO-oximeters that use few wavelengths of light can be susceptible to error in the presence of fetal haemoglobin, in which case an overestimation of COHb is produced (Zwart, et al. 1981). Some CO-oximeters attempt to compensate for this by using as many as seventeen wavelengths (Farmer 1997). Figure 3.4 depicts a schematic representation of the IL-282 CO-oximeter. The IL-282 uses four wavelengths of light that it produces by rotating four interference filters mounted on a wheel controlled by a stepper-motor.

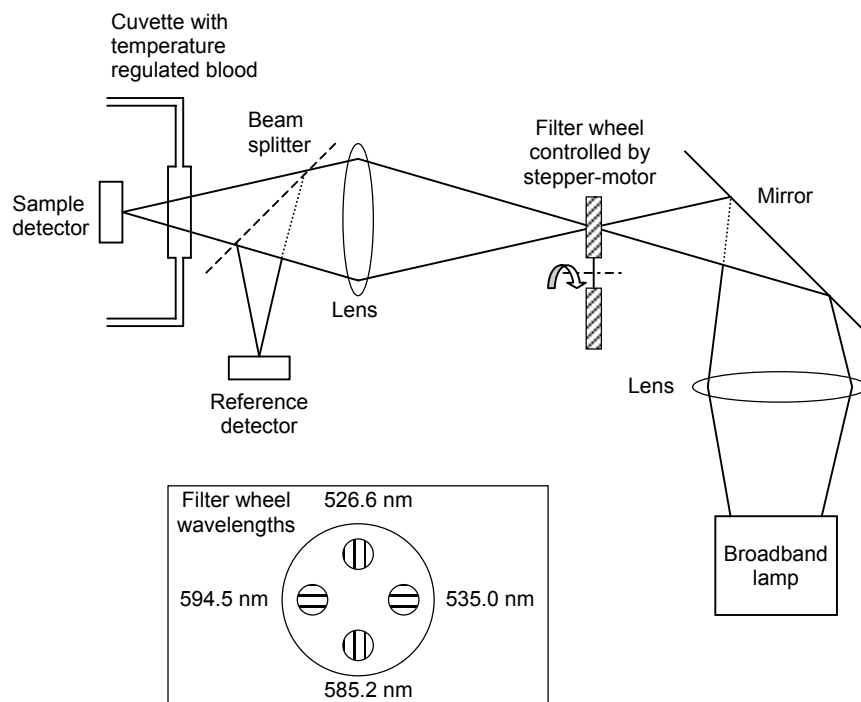


Figure 3.4 Schematic depiction of the Instrument Laboratories IL-282 4-wavelength CO-oximeter.

3.2 THEORY OF PULSE OXIMETRY

If red or near infrared (NIR) light is transmitted through tissue, the received light at a detector will capture a slowly varying attenuation due to reflection from the skin, scattering by tissues such as muscle, bone and fat, and absorption due to tissues such as muscle, bone, fat and venous and arterial blood. The received light intensity will also capture a faster pulsatile attenuation component that is due to the pulsation of arterial blood. Figure 3.5 depicts the components of light attenuation in tissue and indicates the relative contributions of each.

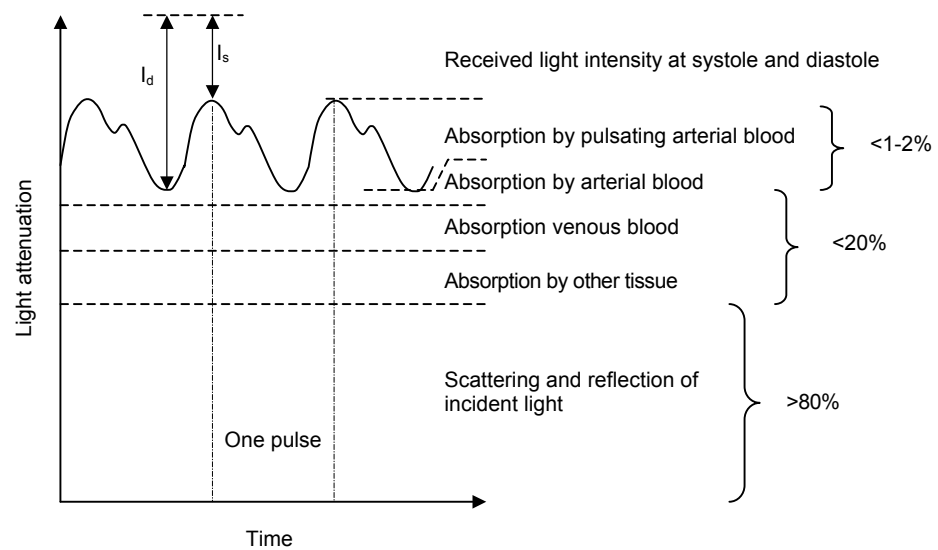


Figure 3.5 Components of attenuation in the detected light exiting tissue.⁴

The pulsatile component of the absorption is specifically caused by the peripheral arterial pressure waveform, a plot of this waveform is known as a plethysmogram, or a photoplethysmogram (PPG) if measured by optical means. Figure 3.6 depicts the arrangement of erythrocytes in an artery at various stages during the cardiac pulse. At systole (peak pressure) the cells are packed tightly together and are orientated such that their long axes are perpendicular to the direction of flow. At diastole (low pressure), the cells are less densely grouped and are rotated such that their long axes are parallel to the direction of flow. These effects combine to produce maximum absorption (minimum transmittance) of light

⁴ Wukitsch et al. (1988) state that an arterial pulsation accounting for 3% of the signal amplitude can be considered normal and 10-11% considered high. Ohmeda pulse oximeters display a *low-signal* warning when the signal's pulsatile component falls to 0.2% (Wukitsch 1987; Wukitsch, et al. 1988).

during systole and minimum absorption (maximum transmittance) at diastole (Liebman, et al. 1962; Visser, et al. 1976).

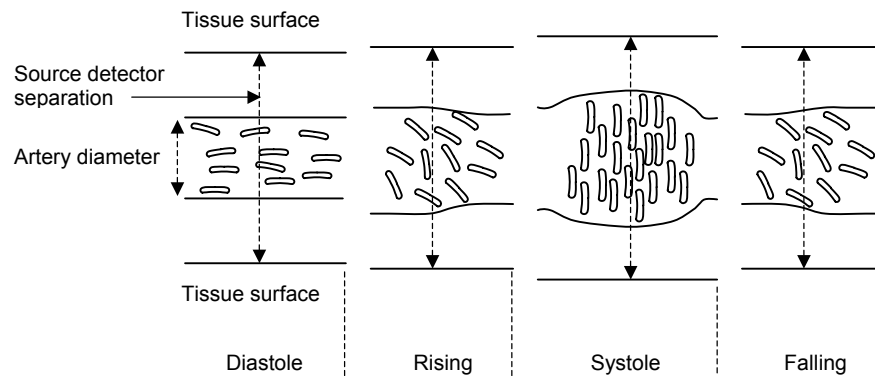


Figure 3.6 Arrangement and orientation of erythrocytes (red blood cells) during the cardiac pulse.

During the discussion of the modified Beer-Lambert Law (see Section 2.2.2) several parameters were identified that must be calculated in order to establish the relative concentrations of absorbing chromophores in a scattering medium. These parameters were enumerated: the incident light intensity at each wavelength; the received light intensity at each wavelength—and by implication the detector's sensitivity to each wavelength; the optical path length; and the differential path length factor that accounts for the increase in path length due to scattering. Two methods of estimating the differential path length factor were described, both of which required a significant amount of instrumentation. The optical path length for a transmission geometry is relatively easily calculated, however, for a reflection geometry it is somewhat more difficult (see Section 2.3.3 and the *optical banana* displayed in Figure 2.6). Calculation of the incident light intensity also requires quantification of the reflection from the surface, which is a function of the angle of incidence and hence also of the light source's emission profile. A clinical oximeter operating on the principle of the modified Beer-Lambert law would need to establish each of these parameters for all wavelengths, for each patient and for each measurement location. If probe movement were an issue, each parameter would need continuous updating. Pulse oximetry however eliminates all these parameters from the estimation of arterial blood oxygen saturation.

3.2.1 LIGHT ABSORPTION FOR PULSE OXIMETRY

Pulse oximetry is a special case of the Beer-Lambert based spectroscopy described in Section 2.2. This section describes the set of conditional assumptions that enable the technique of pulse oximetry by eliminating the incident light intensity and the position and wavelength dependent optical path length as variables from the Beer-Lambert model.

3.2.1.1 ELIMINATION OF INCIDENT LIGHT INTENSITY AND OPTICAL PATH LENGTH AS VARIABLES

The level of absorption due to tissues such as bone, muscle, fat and venous blood, varies slowly with respect to the pulse. Let this baseline absorption have absorptivity α and optical path length d . Let the pulsing arterial blood have absorptivity α_A and path length Δd (and note that Δd varies slightly as the blood pulses). The light emerging from the baseline component I_b , can be written as a function of the incident light intensity I_0 , as

$$I_b = I_0 e^{-\alpha d}. \quad (3.2)$$

The light emerging from the pulsatile component I_p , can be written as

$$I_p = I_b e^{-\alpha_A \Delta d}. \quad (3.3)$$

Substituting equation (3.2) into equation (3.3) yields the light emerging from the pulsatile component as a function of the incident light intensity,

$$I_p = I_0 e^{-(\alpha d + \alpha_A \Delta d)}. \quad (3.4)$$

The transmittance of the arterial component can be defined as the ratio of the light emerging from the arterial component and the light incident on the arterial component; which is the light emerging from the baseline component. Therefore the arterial transmittance $T_{\Delta A}$ is given by

$$T_{\Delta A} = \frac{I_p}{I_b} = \frac{I_0 e^{-(\alpha d + \alpha_A \Delta d)}}{I_0 e^{-\alpha d}}. \quad (3.5)$$

The I_0 terms cancel out leaving the arterial transmittance as a function of the pulsatile component's absorptivity and path length only.

$$T_{\Delta A} = e^{-\alpha_A \Delta d} \quad (3.6)$$

Note that the absorptivity of the pulsatile component is innate to the received light attenuation signal (refer to Figure 3.5 where I_s represents the transmittance at systole and I_d represents the transmittance at diastole). Any device employing this principle is unaffected by fluctuations in the incident light intensity and is effectively self-calibrating (Wieben 1997). It now remains to remove the variable Δd from the calculations.

Taking the natural logarithm of the arterial transmittance yields

$$\ln(T_{\Delta A}) = \ln(e^{-\alpha_A \Delta d}) = -\alpha_A \Delta d. \quad (3.7)$$

Now by comparing the ratio of the arterial transmittance measured at two wavelengths, a ratio R_{OS} can be calculated such that,

$$R_{OS} = \frac{\ln(T_{\Delta A}(\lambda_1))}{\ln(T_{\Delta A}(\lambda_2))} = \frac{-\alpha_A(\lambda_1) \Delta d(\lambda_1)}{-\alpha_A(\lambda_2) \Delta d(\lambda_2)}. \quad (3.8)$$

Now the variable distance Δd (the optical path length over which arterial absorption takes place) can be considered independent of the wavelength at which it is measured if two conditions are met. First, the path of light through the artery should be free of scattering events, since scattering can be wavelength dependent and increases the optical path length beyond the geometric distance. This is not strictly true of whole blood. However, the diameter of arteries in the limbs are small (typically the radial artery is approximately 3 mm, the ulnar 2.5 mm, and the digital arteries 1.6 mm (Fazan, et al. 2004)), and the mean number of scattering events for near infrared light travelling in blood is of the order of $1 - 2 \text{ mm}^{-1}$. So provided that the two measurement wavelengths experience a similar number of scattering events per millimetre, the first condition is approximately met. The second condition is that the geometrical distance between the source and detector is the same at each wavelength. In practice, both sources are located close together and at some distance from the artery, a common detector, also at some distance from the artery, is used for both sources, such that the difference in Δd arising from source positioning is negligible. Thus the second condition is also met and Δd can be considered approximately independent of wavelength—though the first of several conditions pertaining to the choice of wavelengths has been imposed. Equation (3.8) reduces to

$$R_{OS} = \frac{\ln(T_{\Delta A}(\lambda_1))}{\ln(T_{\Delta A}(\lambda_2))} = \frac{\alpha_A(\lambda_1)}{\alpha_A(\lambda_2)}. \quad (3.9)$$

3.2.1.2 CHOICE OF WAVELENGTHS

It is now required to choose wavelengths λ_1 and λ_2 such that the ratio R_{OS} in equation (3.9) is proportional to the arterial oxygen saturation. The precise definition of *arterial oxygen saturation* entails some detail and will be discussed in due course (see Section 3.4.1). For the present a limited but didactic definition will suffice. Arterial oxygen saturation, S_pO_2 , is the ratio of oxyhaemoglobin to total haemoglobin. That is,

$$S_pO_2 = \frac{HbO_2}{HbO_2 + Hb} \times 100\%. \quad (3.10)$$

Where the subscript p denotes the arterial oxygen saturation as measured by a pulse oximeter.

It is now necessary to choose λ_1 and λ_2 such that one wavelength is most strongly absorbed by oxyhaemoglobin (HbO_2) and the other by reduced haemoglobin (Hb).

Figure 3.7 depicts the absorption of Hb and HbO_2 across a portion of the visible and near infrared electromagnetic spectrum. It can be seen in Figure 3.7 that Hb and HbO_2 have different absorption across the entire portion of the spectrum except at 805 nm, termed the *isobestic* point. Below the isobestic point, absorption is principally due to Hb , while above the isobestic point most absorption is due to HbO_2 . The most commonly used wavelengths in pulse oximetry are 660 nm (red) and 940 nm (infrared) (Wukitsch, et al. 1988). There are several reasons why these wavelengths have become prominent. The difference in absorption between Hb and HbO_2 is greatest at 660 nm below the isobestic point, thus absorption measured at this wavelength will be largely proportional to the concentration of Hb only. Above the isobestic point the difference is greatest above 970 nm, however from approximately 950 nm and upwards, the absorption of light by water increases sharply (Elwell 1995) making the use of these wavelengths impracticable. At 940 nm, absorption by water is sufficiently low, and both the Hb and HbO_2 absorption curves are relatively flat. Their flatness is useful. The peak emitted wavelength of an LED can vary somewhat from the specified value. Additionally, the peak emitted wavelength can drift during operation. The relative flatness of both the Hb and HbO_2 absorption curves in this region, serves to insulate the calculations from variances in the peak emitted wavelength of the infrared LED, since movement left or right of 940 nm does not cause a significant change in absorption of either species of haemoglobin. Contrast this with 660 nm, where the Hb curve has a steep

slope. Consequently, calculations are very sensitive to variance of the red LED wavelength, especially at low saturations where Hb is the dominant absorber. (See Section 3.3.1, and refer to de Kock et al. (1991) and Pologe (1987).) There are reasons, discussed later, for choosing alternative wavelengths, notably in the presence of low oxygen saturations (see Section 3.4.1.2 and Mannheimer et al. (1997)), though another compelling reason to choose 660 nm and 940 nm is that light emitting diodes have been commonly available—and thus economical to purchase—at these wavelengths for some time.

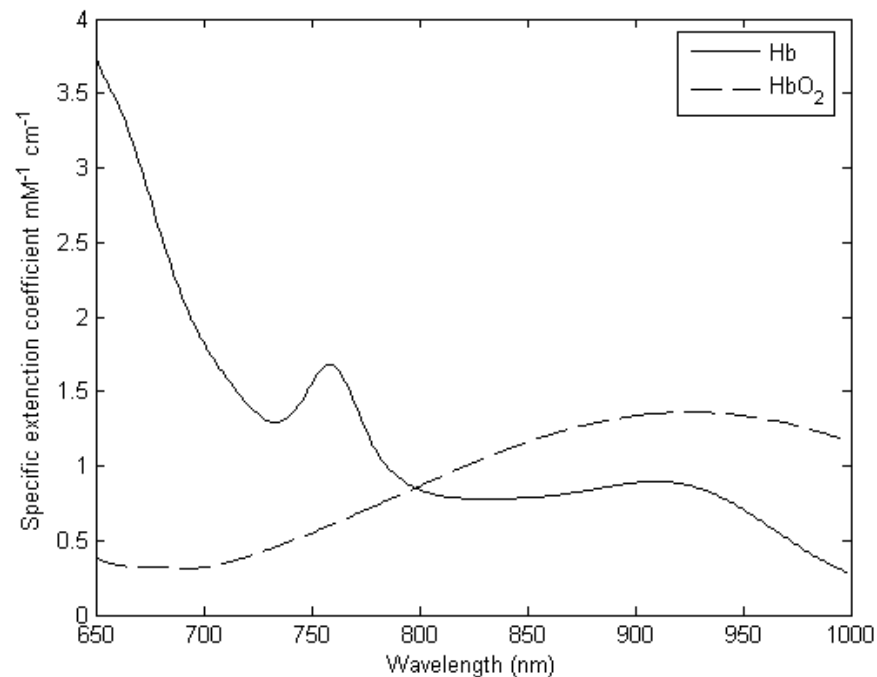


Figure 3.7 Absorption spectra of reduced (Hb) and oxyhaemoglobin (HbO₂).

3.2.2 DERIVING ARTERIAL OXYGEN SATURATION

Having recorded the intensity of light emerging from tissue at two wavelengths, and establishing that each has a pulsatile component, that is a PPG, it is necessary to calculate the variable R_{Os} from the two PPG signals by implementing equation (3.9). Though ultimately each device manufacturer implements this based on their own research, two methods are commonly used (Palreddy 1997). They are the *peak and valley* method and the *derivative method*.

3.2.2.1 THE PEAK AND VALLEY METHOD

Cheung et al. (1989b) first described the peak and valley method of deriving R_{OS} in a US patent application.

Figure 3.8 depicts a red and infrared PPG signal, the signals obtained by monitoring the intensity of light emerging from tissue. Note that the PPG signals appear inverted compared to the attenuation-derived waveform depicted in Figure 3.5.

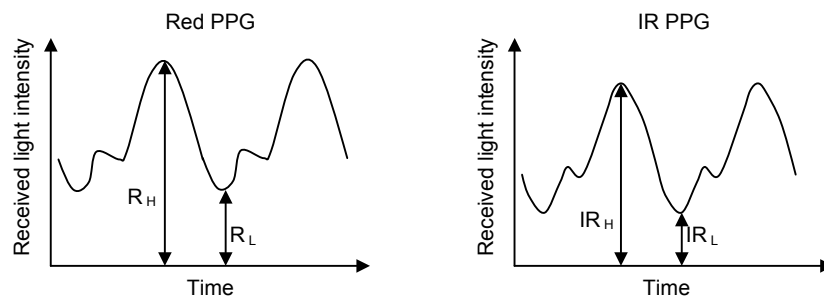


Figure 3.8 Received light intensity from the red (R) and infrared (IR) LEDs over time.

Here the signal peaks correspond to diastolic pressure where the volume of blood between the source and detector is lowest and the erythrocytes are aligned with their long axes parallel to the direction of flow. Thus attenuation is at its lowest and transmittance at its highest. As before, R_H represents the baseline transmittance at the red (R) wavelength, the transmittance in the presence of scattering and absorption by skin, muscle, bone, fat, venous blood and the absorption due the normal volume of arterial blood. The difference between R_H and R_L , represents the reduction in transmittance due to the pulsation of the arterial blood. The natural logarithm of the quotient of R_L and R_H , is the term defined earlier in equation (3.7) as the natural logarithm of the arterial transmittance,

$$\ln(T_{\Delta A}(\lambda_R)) = -\alpha_A(\lambda_R)\Delta d(\lambda_R) = \ln\left(\frac{R_L}{R_H}\right). \quad (3.11)$$

Similarly for the infrared (IR) PPG,

$$\ln(T_{\Delta A}(\lambda_{IR})) = -\alpha_A(\lambda_{IR})\Delta d(\lambda_{IR}) = \ln\left(\frac{IR_L}{IR_H}\right). \quad (3.12)$$

Equation (3.9) defined R_{OS} as the ratio of these terms,

$$R_{OS} = \frac{\ln\left(\frac{R_L}{R_H}\right)}{\ln\left(\frac{IR_L}{IR_H}\right)} = \frac{\alpha_A(\lambda_R)}{\alpha_A(\lambda_{IR})}. \quad (3.13)$$

Since the numerator and denominator of the ratio R_{OS} , are themselves, ratios of the *valleys* and *peaks* of the red and infrared PPG signals respectively, the variable R_{OS} is commonly referred to as the *ratio of ratios*.

3.2.2.2 THE DERIVATIVE METHOD

The peak and valley method has intuitive appeal. The method closely resembles the reasoning used to explain the concept of pulse oximetry and to develop the R_{OS} variable. The peak and valley method provides perfectly valid *measurements* of R_{OS} , however it has limitations that make it incongruous with clinical *monitoring* requirements.

Peaks and valleys in the arterial pressure waveform occur only once per heartbeat, thus R_{OS} can be calculated only once per heartbeat by the peak and valley method. As heart rate varies so does the rate at which R_{OS} is calculated. Such a dependency is unacceptable in a clinical monitoring device. The problem is compounded by signal processing requirements. To mitigate the affects of spurious R_{OS} values resulting from artefacts in the PPG waveforms,⁵ it is desirable that the current displayed oxygen saturation be in some way derived from a moving weighted average of the previous calculated values. Under these conditions, the displayed output saturation value is delayed by several heartbeats, each with a variable period.

Device manufacturers each implement their own particular solutions to this problem—some of which are to be found by searching patent claims—however the underlying method upon which these solutions are based in the *derivative method* (Palreddy 1997). Like the peak and valley method, the derivative method is based on applying the Beer-Lambert law to the PPG signals present in the detected light intensity, I_1 . I_1 can be described in terms of the constant incident light intensity I_0 , as,

⁵ Artefacts in the PPG can result from motion, momentary direct coupling of the source and detector, ambient light interference, or any other of a number of biological factors such as muscular contractions in the region of the probe.

$$I_1(t) = I_0 e^{-\alpha(\lambda)L(t)}. \quad (3.14)$$

In this instance, α is defined as the relative (rather than specific) extinction coefficient and encompasses the concentration of the chromophore. L is the path length of the light through the arterial blood and varies as a function of the arterial pressure waveform, as before it will be assumed approximately equal for both wavelengths. The rate of change of the detected light intensity with respect to time is given by,

$$\frac{dI_1(t)}{dt} = I_0 e^{-\alpha(\lambda)L(t)} \left(-\alpha(\lambda) \frac{dL(t)}{dt} \right), \quad (3.15)$$

therefore,

$$\frac{dI_1(t)}{dt} \frac{1}{I_1} = -\alpha(\lambda) \frac{dL(t)}{dt}. \quad (3.16)$$

The measured light intensity I_1 , contains both the desired PPG component and the large DC offset. However the derivative of I_1 is equal to the derivative of the PPG component alone. Thus the ratio of, the ratio defined in equation (3.16), for two wavelengths, red (R) and infrared (IR), call it R' , is given by,

$$R' = \frac{(dI_R/dt)/I_R}{(dI_{IR}/dt)/I_{IR}} = \frac{-\alpha(\lambda_R)}{-\alpha(\lambda_{IR})}. \quad (3.17)$$

This is the variable defined in equation (3.13) as the *ratio of ratios*, that is, R_{OS} . For a uniformly sampled discrete time signal, the time domain derivative of a signal I , is approximately given by,

$$\frac{dI(t)}{dt} \approx I(t_2) - I(t_1). \quad (3.18)$$

Note that if t_2 and t_1 are chosen to be the peak and valley of the local PPG signal respectively, then the *derivative* method reduces to the *peak and valley* method.

Potratz (1994) described a variation of the derivative method of calculating R_{OS} in a US patent, intended for noise reduction. A limited description of the means by which the Ohmeda clinical pulse oximeters perform R_{OS} calculation is provided by Wukitsch (1987) and by Wukitsch et al. (1988). The Ohmeda system calculated the change in received light intensity (ΔI) at each wavelength thirty times per second. From these ΔI_R and ΔI_{IR} , the ratio R_{OS} was calculated and converted to

instantaneous oxygen saturation values S_pO_{2i} . A moving weighted average of ten S_pO_{2i} values at a time is used to update the displayed S_pO_2 value, which is updated every three seconds. Wukitsch noted that the values of ΔI_R and ΔI_{IR} obtained close to the inflection points of the PPG waveforms are less accurate than those obtained during the rising part of the waveform, and as such are assigned a lower weighting. Wukitsch and his co-authors were, at the time, Ohmeda employees and did not describe how the device determined these weights.

Though Wukitsch does not state the cause of the inaccuracies near the inflection points, they are to be expected on two accounts. First, the change in light intensity over a given sampling period will be least in the region of the inflection points, as the rising arterial pressure slows, temporarily remains static, and then begins decreasing, and vice versa at the next inflection. Since the device has fixed measurement accuracy, the error associated with very small values will be proportionately greater. Second, the corresponding measurements of ΔI_R and ΔI_{IR} are not made simultaneously but rather in a multiplexed fashion. While the arterial pressure is rising steadily, the PPG waveform has relatively fixed slope, and sampling the R and then the IR waveform introduces little error. This is not true at the inflection points, where the slope may be positive at one sample instant and negative at the next. (Section 5.4 revisits this in relation to the performance of the non-contact camera based device described later.)

3.2.3 THE NEED FOR CALIBRATION

The method by which pulse oximetry operates and the exclusion of the variance in path length and incident light intensity as variables from the calculation seem to obviate calibration. To a large extent this is true, the isolation of the PPG signal eliminates the contributions to the attenuation of the detected light that result from reflection from the skin's surface, and the relatively static attenuation due to absorption and scattering by muscle, bone, fat, venous blood and other tissues. However the change in attenuation that occurs over the duration of the cardiac pulse, due only to arterial blood, is itself composed of both absorption and scattering. The varying absorption (discussed above) was attributed to a rotation of the biconcave erythrocytes and the increase in blood volume (that is more densely packed erythrocytes) at systolic pressure. The erythrocytes, on which the absorbing haemoglobin species are located, have a diameter of approximately 700 nm (Wieben 1997). This is sufficiently close to the wavelength of the interrogating light

to cause Mie scattering. In addition, the populous erythrocytes are suspended in plasma, each of which has a different refractive index, and so light is scattered by the erythrocyte-plasma interface. The probability of scattering occurring at the interface is determined not just by the respective refractive indices, but also by the angles of incidence and transmission of the light (see Section 2.3.3). To compound the complexity of this scattering, the erythrocytes and plasma are constantly pulsing between the source and detector with the orientation of the erythrocytes alternating with the pulse. In addition the magnitude of this effect varies with oxygen saturation as the various species of absorbing haemoglobins become more or less numerous—not to mention patient-to-patient variances such as anaemia (deficiency of erythrocytes or haemoglobin) and sickle-cells (characterised by abnormally shaped red blood cells). A further consideration is the bandwidth of the light sources: the calculations assume monochromatic sources, the measurement of the emission spectra of the LEDs in the non-contact device (presented in Section 5.2.4.2) indicates the degree to which this assumption may be invalid.

For illustrative purposes, a comparison is made here, of the theoretically predicted and empirically observed, variance of attenuation at two wavelengths with arterial oxygen saturation (S_aO_2). For simplicity, assume that the only species of haemoglobin present are oxyhaemoglobin HbO_2 , and (reduced) haemoglobin Hb . Thus when S_aO_2 is 100%, HbO_2 accounts for all of the haemoglobin and Hb accounts for none; at 50% S_aO_2 , they each account for half the haemoglobin; at 0% S_aO_2 , Hb accounts for all haemoglobin and so on. Using the common red and infrared wavelengths of 660 nm and 940 nm respectively, the specific extinction coefficients (α) of Hb and HbO_2 are: $\alpha_{Hb, 660} = 3.4408$, $\alpha_{Hb, 940} = 0.7874$, $\alpha_{HbO, 660} = 0.3346$, and $\alpha_{HbO, 940} = 1.3520$, each with units $mMolar^{-1} cm^{-1}$ (from the values reported by Cope (1991), see Figure 3.7). The absorption due to arterial blood at each wavelength can be calculated using the equations,

$$I_{660} = I_{0,660} e^{-(\alpha_{Hb,660} \times C_{Hb} + \alpha_{HbO,660} \times C_{HbO})}, \quad (3.19)$$

$$I_{940} = I_{0,940} e^{-(\alpha_{Hb,940} \times C_{Hb} + \alpha_{HbO,940} \times C_{HbO})}. \quad (3.20)$$

The variable C denotes the relative concentrations of either Hb or HbO and varies between 0 and 1 as S_aO_2 varies. The sum of the relative concentrations of both wavelengths is thus always 1. The optical path length is omitted from the calculation using the earlier argument that it is approximately equal for both

wavelengths. The incident light intensity I_0 , is set to be the same for each wavelength, thus the ratio of red to infrared arterial absorbance is given by,

$$R_{OS} = \frac{\ln(I_{660})}{\ln(I_{940})}. \quad (3.21)$$

The resulting curve is plotted in Figure 3.9 as the solid line. Also plotted in Figure 3.9 is the empirically observed change in the ratio of the absorbance at the same two wavelengths, as reported by Wukitsch et al. (1988). The empirical change in absorption with S_aO_2 is linear. The empirical and theoretical graphs are in relatively close agreement while oxygen saturation is above 37%, however below this saturation⁶ the empirical observation increasingly underestimates the arterial oxygen saturation. At high saturations, a small measurement error might be tolerated, since decisions regarding the patients' management would likely not be affected. However at low saturations, decisions regarding a patient's management are critical and device error in this region of operation could be extremely consequential.

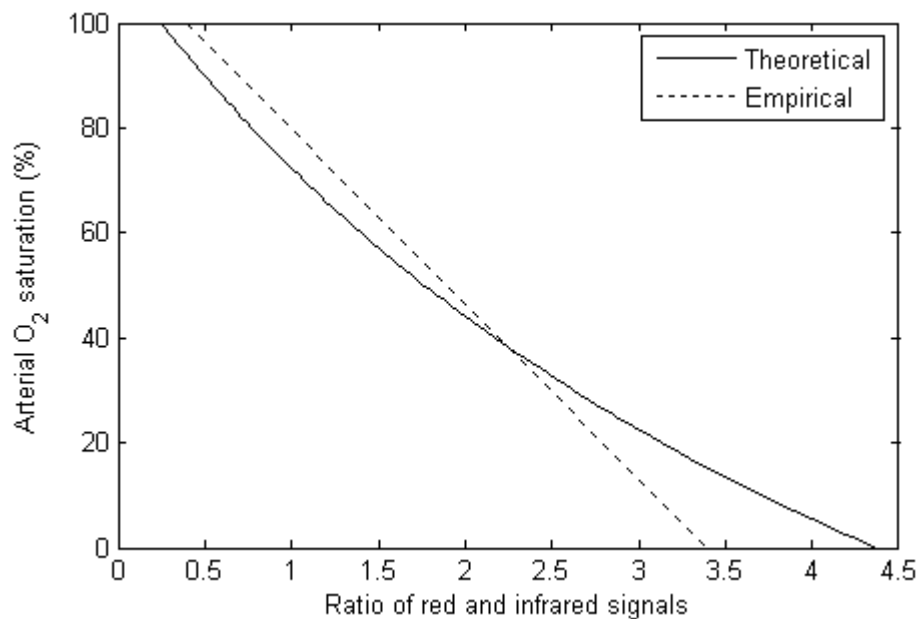


Figure 3.9 Deviation of theoretically predicted and empirically observed, red/infrared ratio variance as a function of oxygen saturation.

⁶ Wukitsch et al. do not state how data pertaining to low oxygen saturations are obtained. Presumably it is by extrapolation or in vitro calibration techniques, since it is unacceptably dangerous to desaturate a human subject below 85% due to the risk of hypoxic brain damage (Moyle 1994). Note that Schowalter (1997a) suggests that a saturation as low as 60% is achievable. Some studies have been made of pulse oximeter performance at low saturations using hospitalised patients already exhibiting very low saturation, see Kelleher (1989) for a summary of such studies.

For this reason, several studies have been conducted investigating the applicability of various absorption and scattering models to pulse oximetry. Steinke and Shepard (1986) studied the multiple scattering model developed by Twersky (1970). Marbel et al. (1994) also studied this topic but reached the conclusion that such models could not replace clinical calibration studies.

Some equations have been developed that relate measured R_{OS} to S_pO_2 using clinically derived constants. Mendelson and Kent (1989) derived the curve,

$$S_pO_2 = \frac{k_1 - k_2 R_{OS}}{k_3 - k_4 R_{OS}}. \quad (3.22)$$

Where $k_1 \dots k_4$ are clinically determined constants.

Fine and Wienreb (1995), report the use of a quadratic polynomial curve by Ohmeda and Radiometer pulse oximeters, of the form

$$S_pO_2 = k_1 + k_2 R + k_3 R^2. \quad (3.23)$$

Where $k_1 \dots k_3$ are again, clinically determined constants

The use of lookup tables is a popular alternative, as multiple conversion curves can be stored to accommodate variances in the interrogation wavelength (Moyle 1994; Wieben 1997).

3.3 OPERATION OF A CLINICAL DEVICE

3.3.1 LIGHT EMITTING DIODES

All clinical pulse oximeters utilise light emitting diodes (LEDs) as light sources (Bourgeois 1997). LEDs produce light by electroluminescence, which is highly efficient compared to other forms of light emission such as photoluminescence or high-temperature emission. The fact that LEDs are so suited to the application is a result of the convergence of several parameters. First, LEDs emit light with wavelengths over a range of approximately 700 nm from violet (about 400 nm, just below indigo and blue) in the visible range to the near infrared. This band of emission overlaps the near infrared window into tissue (Jobsis-vanderVliet 1999) and coincides with suitable peaks in the absorption spectra of Hb and HbO₂ (Elwell 1995).

Manufacturers commonly specify the following parameters of LEDs: peak emitted wavelength, bandwidth, beam angle, forward voltage, forward current and corresponding emitted power, power dissipation, reverse breakdown voltage, reverse current, operating temperature, switching times, maximum pulse current as a function of duty cycle and frequency, dimensions, and finally, cost. A thorough explanation of all of these parameters is to be found in many electronics textbooks and handbooks. It is sufficient here to say that the requirements of pulse oximetry do not approach the limits of any of these parameters—with two caveats. First the specified peak emitted wavelength of a light emitting diode, can vary from one device to the next, by an amount sufficient to introduce a significant error in the calculated oxygen saturation percentage. Steps must be taken to account for this. Second, in pulse oximetry, LEDs are placed in direct contact with the skin, often for long periods. LEDs have the capacity to cause burns and their power dissipation must meet certain specifications.

3.3.1.1 VARIANCE IN PEAK EMITTED WAVELENGTH

LEDs produced in bulk from the same material should have the same characteristics including peak emitted wavelength. As with all manufacturing processes, imperfections occur. Pologe (1987) investigated the variance in peak emitted wavelength of LEDs produced in bulk from the same lot at the common wavelengths of 660 nm and 940 nm, and found that the variance can be as much as 15 nm from the specified peak wavelength. This is particularly important at the lower red wavelength, where the absorption spectrum of Hb has a very steep slope.

Figure 3.10 displays the effects on the theoretical ratio of the red and infrared signals, caused by a 15 nm increase in the peak emitted wavelengths of a 660 nm and a 940 nm LED, as the arterial oxygen saturation varies between 100% and 0%. (The values of the Hb and HbO₂ extinction coefficients at these wavelengths were reported by Cope (1991) and the description of how these curves are generated was given in Section 3.2.3.) Note that the deviation of the empirically observed red–infrared ratio from the theoretical variation with arterial oxygen saturation was discussed in Section 3.2.3.

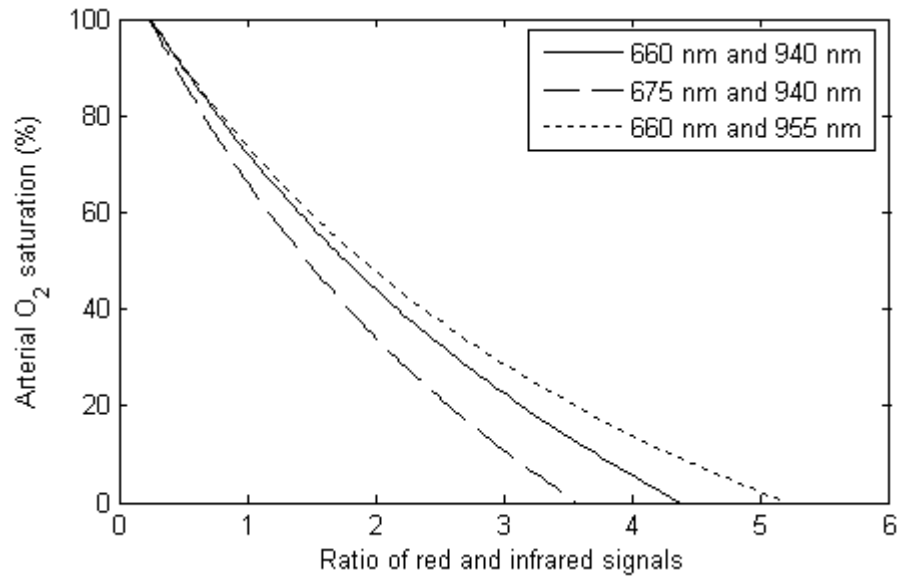


Figure 3.10 Variance in red/infrared ratio caused by a 15 nm increase in peak emitted wavelength, in the red (660 nm) and infrared (940 nm) LEDs.

To compensate for this effect device manufacturers employ one of two strategies. During manufacture, the peak emitted wavelength of each diode is measured using a spectrometer. With the first strategy the manufacturer uses only diodes that are extremely close to the specified wavelength, for example, Hewlett Packard selects diodes that are within ± 1 nm of 660 nm for the red wavelength (Bourgeois 1997). The second strategy used by manufactures is to note the peak emission wavelength of each LED and then to include some way for a device to interrogate a probe upon connection and choose a calibration curve appropriate to the two wavelengths contained in that probe. A common method of performing this, described in patents by New and Corenman (1987; 1988), is to include a resistor in the probe, the resistance of which, indicates the wavelength combinations of the LEDs contained in that probe. When a probe is connected to a device, the device sends a current through the coding resistor and uses the measured voltage drop to determine the resistance and hence the wavelengths.

Each method has its drawbacks—selecting only LEDs that meet the criteria diminishes the cost saving of bulk buying, while the addition of an extra component and the associated additional functionality required by the coding resistor method have a direct cost. Both approaches require measurement of every purchased LED.

3.3.1.2 DRIFT IN PEAK EMITTED WAVELENGTH

The wavelength of light emitted from an LED is described by,

$$E_g = \frac{hc}{\lambda}, \quad (3.24)$$

where E_g is termed the band gap (or energy gap) in electron volts, h is Planck's constant, c is the speed of light in a vacuum, and λ is the wavelength of emitted light. The physical properties of the material from which the LED is constructed determine the value of E_g . Materials such as gallium arsenide phosphide (GaAsP) and gallium phosphide (GaP) are commonly used to construct LEDs in the visible range with wavelengths from 380 nm to 740 nm, while gallium arsenide (GaAs) is commonly used to produce near infrared wavelengths. Though less common gallium aluminium arsenide (GaAlAs) can be used to produce both visible and near infrared light (Bourgeois 1997).

E_g is also a function of the p - n junction temperature, typically decreasing as temperature increases (Varshni 1967), which, referring to equation (3.24), causes the emitted wavelength to increase. During operation, the pulse oximeter LEDs are alternately pulsed with duty cycles ranging from 2% to 50% depending on the manufacturer (Reynolds, et al. 1991). The resulting average driving current is usually still sufficient to cause heating of the p - n junction. Note that pulse oximeters typically vary the driving current to each LED in proportion to the amplitude of the detected PPG at that wavelength (Bourgeois 1997; Moyle 1994).

In addition to the heating caused by driving current, the effect of ambient temperature can be significant. de Kock et al. (1991) investigated these effects using wavelengths of 660 nm and 950 nm. The maximum shift of peak wavelength due to driving current (at 100% of maximum rated drive current for duty cycle and frequency) was 8 nm for the red LED and 0 nm for the infrared LED. For an increase in ambient temperature from 0 °C to 50 °C, the maximum shift of peak wavelength was 5.5 nm for the red LED and 7.8 nm for the infrared LED. Referring again to Figure 3.10, though the error due to peak wavelength drift during operation is smaller than that resulting from device-to-device peak wavelength variance, it will be significant.

Device manufacturers compensate for this by either placing a temperature sensor in the probe or by directly monitoring the driving current for both LEDs. In both cases, the information is fed back to the device's microprocessor, where an estimate is made of the current LED wavelengths. The device then chooses a new

calibration curve appropriate to the current wavelength combination (Bourgeois 1997).

3.3.1.3 PREVENTION OF BURNS

Several international and national standards have been published pertaining to pulse oximetry: ISO 9919 and ASTM F1415. For the most part these documents specify the parameters, data, and methods of calibration, which the manufacturer should provide or make available on request. Issues such as electrical safety and electromagnetic interference are also covered, as well as descriptions of alarms that devices should provide. For the most part these documents are of limited use to pulse oximeter designers. The American Food and Drug Administration requires that the temperature of the contact region between the probe and the skin not exceed 41 °C. The pertinent LED parameter is the specified thermal resistance, which is defined as the increase in *p-n* junction temperature (T_J) above the ambient temperature (T_A), per unit of power dissipation (P_D), with units of °C/W. In the event there is no heat sink, it is given by,

$$R_{TH} = \frac{(T_J - T_A)}{P_D}. \quad (3.25)$$

Typically, LEDs used in pulse oximeters possess a sufficiently low R_{TH} and low average driving current to pose no significant risk (Bourgeois 1997). Moyle (1994) noted that although there had, as of 1994, been several reports of pulse oximeter probes causing burns, especially in small children, these were most likely not caused by thermal emissions from LEDs; rather Moyle suggests that these were pressure necroses caused either, by the probe being too tight, or by poor perfusion of the skin under the probe. Note however that some specialised pulse oximetry and tissue oximetry applications utilise higher performance LEDs with highly dissipative metal cases, which may be necessitated by a demand for deeper tissue penetration, beyond the normal requirements of pulse oximetry. Such systems have the potential to cause thermal injuries and care should be taken to ensure compliance (see Coyle (2005) as an example of such a system).

3.3.2 PHOTODETECTORS AND AMPLIFIERS

One of the hindrances to early oximetry was the lack of suitable detectors. While the photocells used by early oximeters were sensitive across the wavelengths now used in pulse oximetry, those devices produce a varying resistance in response to changes in incident light intensity. Their response is highly non-linear and slow. In addition they are temperature sensitive. The magnitude of the change in resistance produced by incident light is very large, typically between $100\ \Omega$ and $100\ \text{M}\Omega$ between dark and illuminated conditions (though Schowalter (1997b) states that it can be as large as 10^{14}), which makes incorporating them into instrumentation circuitry challenging. They are also unsuitably large with diameters of 5 mm to 25 mm.

Modern pulse oximeters have a range of alternative devices available. Shottky diodes provide ultra fast response times, though are typically used in ultraviolet sensing applications. Avalanche photodetectors (APDs) use an avalanche multiplication effect to provide very high sensitivity. APDs are suited to specialised applications where detected light levels are low (see Coyle et al. (2004) as an example of such). However APD response time is comparatively slow and the large reverse bias required for their operation creates a large electric field that may preclude the use of APDs in some clinical situations (Pallas-Areny and Webster 1991). Phototransistors possess some characteristics favourable to pulse oximetry, notably they can provide built-in current amplification, yielding a light-to-current conversion ratio that can be hundreds of times greater than a similar photodiode. Phototransistors were used in early pulse oximeters (Schibli, et al. 1978) though their comparatively large dark currents and non-linear sensitivity over the range useful in pulse oximetry ultimately saw them replaced by photodiodes as the sensor of choice (New and Corenman 1987).

Photodiodes offer good linearity between incident light and output current when connected in a photoconductive mode, at a reasonable cost. The only challenger to their dominance is the integrated circuit (IC) detector. IC devices can incorporate a photodiode and transimpedance amplifier, to produce an output voltage that varies linearly with incident light intensity. By placing the initial amplification stage so close to the source, IC detectors can achieve excellent noise performance. The principal drawback to the IC detector is that the component itself is several times the price of a photodiode and requires extra wires. Its size may also be a limiting factor in some applications.

3.3.3 SIGNAL PROCESSING

The extent and complexity of signal processing employed by individual commercial devices varies among manufacturers. However signal processing invariably consists of sampling, de-multiplexing of the signals from each channel, and analogue to digital conversion—each of which is also of relevance to a non-contact device.

3.3.3.1 SAMPLING

Device manufacturers employ various sampling and timing strategies, though invariably, they each contain an ambient light sample during which neither LED is energised. This ambient light level is later subtracted from the signal.

Figure 3.11 depicts the output of the photodiode from an Ohmeda pulse oximeter. The system uses a three-state clock in which, the red LED is pulsed, followed by the infrared, followed by a period of the same length in which neither diode is energised (Pologe 1987).

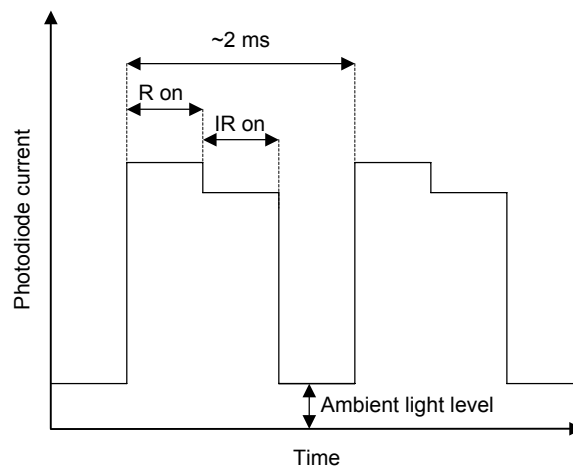


Figure 3.11 Ohmeda timing diagram: three-state clock, adapted from Pologe (1987).

Figure 3.12 depicts the output from a Nellcor device using a four-state clock in which, the red LED is pulsed, followed by a dark sample, following which the infrared LED is pulsed, followed by a second dark sample. Each period is of equal duration.

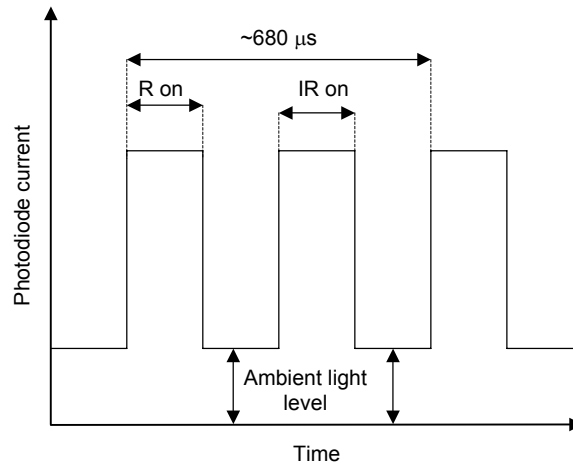


Figure 3.12 Nellcor timing diagram: four-state clock, adapted from Paranjape (1997).

The comparative merits of either sampling strategy or of other sampling strategies are unreported in the literature.

3.3.3.2 DE-MULTIPLEXING

The photo diode detector of the pulse oximeter probe produces a continuously varying output current that is sampled by a sample-and-hold circuit. Since the photodiode's output current contains information from both the red and infrared channels, the signal is first de-multiplexed to produce two separate red and infrared signals. Each signal is then low-pass filtered to remove any high frequency switching noise (Paranjape 1997).

3.3.3.3 ANALOGUE TO DIGITAL CONVERSION

Note that the detected light intensity consists of a pulsatile, and non-pulsatile component that varies slowly compared to the pulsatile component. Recalling the discussion of Section 3.2, both of these components are required for the calculation of the arterial oxygen saturation. However it is also important to measure the pulsatile PPG component as accurately as possible (see Section 3.2.2.2 on the inaccuracy of R_{OS} readings obtained near the inflection points). Thus the maximum utility of the analogue to digital conversion (ADC) quantization range would not be obtained were the captured light intensity signals to be quantized directly, since a large part of the quantization range would be used up by the almost stationary DC offset. Therefore, prior to ADC the DC component is removed, its magnitude

digitised and stored, such that it can be added back to the signal prior to later calculations where it is required. The matter was first described in a US patent by Cheung et al. (1989a). (Whether this remains a problem for contemporary clinical devices, with access to modern ADCs, is questionable, it is however pertinent to the camera-based device described later, where limited quantization range will be shown to be consequential.)

3.3.4 PROBES

The discussion so far in this chapter has alluded principally to transmission of light through tissue, in practice, pulse oximeter probes can operate by transmittance or reflectance—though the use of the word *reflectance* is a little misleading as the sensor is actually detecting what is more accurately described as backscattered light. The term reflectance is an anachronism that dates from the nineteen fifties, prior to studies of light propagation in tissue, it remains in use in relation to pulse oximetry (see Section 2.3.3). Within the category of reflectance probes, probes may also be reusable or disposable.

3.3.4.1 TRANSMITTANCE PROBES

In the case of a transmittance probe, the two LEDs and the photo diode are housed in a clip designed to fit around a finger or toe, the bridge of the nose, or the earlobe. The photodiode is located on one side of the clip with the two LEDs side by side on the other side of the clip directly opposite the detector. The clip itself serves to shield the detector from ambient light and to maintain good contact between the optical elements and the tissue. The only significant variable in transmission probes is the force applied by the clip. This varies with manufacturer and model. If the force exerted by the probe is significant, the blood underneath the probe may clot and if the force is insufficient motion artefacts may increase (Reddy 1997).

The advantage of transmittance probes is that they are reusable indefinitely and have the lowest associated cost per usage. Their disadvantages include the aforementioned risk of clotting, their tendency to reduce circulation in the region of the probe over time, and the risk of cross contamination. Indeed cleaning of the probe is required between patients, and their use is not recommended for infectious patients or patients with high risk of infection, such as neonates or immuno-

suppressed patients. As such, transmittance probes are best suited to short term monitoring, typically less than four hours (Reddy 1997).

3.3.4.2 REFLECTANCE PROBES

Early investigations into measurements in a reflection geometry were conducted by Brinkman and Zijlstra, who produced a commercially available reflectance oximeter for measurements from the forehead—the Cyclops—as early as 1950. Detailed studies were subsequently published by Zijlstra (1953; 1958). The idea of reflectance (backscatter) based oxygen saturation measurement marked a significant advancement in non-invasive measurement, ultimately making possible measurement from any part of the body surface.

In the case of disposable probes, which are invariably reflectance probes, the probe is adhesive. For reusable reflectance probes some variety of adhesive wrap is used (Reddy 1997).

The mechanisms of back scattering of light in tissue were discussed in Chapter 2. The two variables of concern in the design of reflectance probes are the source and detector separation and the photosensitive area of the detector—or indeed the number of detectors and their arrangement.

As the source and detector separation increases, so does the penetration depth of the detected light. A greater penetration depth and longer optical path, illuminates a larger vascular bed, and increase the likelihood of detecting a suitable PPG. However, for a given incident light intensity, as the source and detector separation increases the detected light intensity decreases.

Mendelson and Ochs (1988) investigated the effect of using three photodiode detectors, arranged symmetrically around the two LEDs. This effectively tripled the photosensitive area of their detector and allowed proportionately larger PPG signals to be detected for a given source and detector separation. Reddy (1997) stated that the same effect could be obtained by using a photodiode with three times the area. This is likely inaccurate, as a single detector with an enlarged area could not be positioned such that the extra area is equidistant from the source. Since the detected light intensity decreases with increasing radial separation of the source and detector, the extra area of the larger photodiode would receive increasingly less back scattered light as it becomes distant from the sources, compared with the case of three detectors arranged symmetrically. However, a case will be presented later in

this thesis, for favouring one large continuous detection area rather than multiple symmetrically arranged discrete locations (see Section 5.5.2), particularly where the source and detector separation is considerable.

3.3.5 CALIBRATION OF PULSE OXIMETERS

Recall from the discussion in Section 3.2.3, that while the technique of pulse oximetry removes the unwanted contributions of absorption and scattering by tissues other than the arterial blood, scattering by the arterial blood itself, causes the empirically observed ratio of absorption at two wavelengths to differ from that predicted by theory (see Figure 3.9). For this reason it is necessary to derive empirical calibration curves that map the observed ratio of absorption at two wavelengths to the actual value of arterial oxygen saturation. Calibration can be performed *in vivo* or *in vitro*.

3.3.5.1 IN VIVO CALIBRATION

In vivo calibration was until 1993 the only method used to calibrate pulse oximeters (Moyle 1994). *In vivo* calibration typically takes place in a hospital environment using informed and consenting, non-smoking, healthy volunteers as human test subjects. Subjects are fitted with an indwelling arterial cannula placed in the radial artery. An initial arterial blood sample is taken and tested to ensure that only normal adult haemoglobin is present and that each subject's background levels of carboxyhaemoglobin and methaemoglobin are within normal limits. Typical values are $\text{MetHb} < 1\%$ and $1\% < \text{COHb} < 2\%$ (Moyle 1994; Schowalter 1997a; Wukitsch, et al. 1988). A CO-oximeter is used to determine the oxygen saturation of the blood samples precisely. The subjects breathe air or oxygen-enriched air until their arterial blood samples show 100% saturation. The subjects' arterial oxygen saturation is gradually and incrementally reduced by replacing the oxygen in their breathing gas with nitrogen, and pausing at each step to allow time to equilibrate. When the device under test indicates a stable reading, an arterial sample is immediately taken and analysed by the CO-oximeter. The data from each device are plotted against each other to yield a graph with oxygen saturation on the vertical axis and ratio of absorption at two wavelengths on the horizontal axis (see Figure 3.9). A lookup table is then constructed to perform an exact mapping of the R_{OS} readings from the device under test to the corresponding S_aO_2 level, or, a

transform equation is constructed that generates a best fit to the plotted graph. This process must be repeated for every LED wavelength combination that the manufacturer intends to use in their probes.

There are several reasons why *in vivo* calibration is unsatisfactory. The principal reason is that because it is unsafe to desaturate a human test subject below 85% (due to the aforementioned risk of hypoxic brain damage), the data that result from *in vivo* calibration pertain only to high oxygen saturations—where the need to ascertain accurate oxygen saturation readings is least. The mapping of R_{OS} to S_aO_2 for lower saturations must be extrapolated.

3.3.5.2 IN VITRO CALIBRATION

In vitro calibration methods can be divided into those that use blood or haemoglobin solutions and those that do not. Methods that do not use blood or haemoglobin solutions can generally provide only one reference saturation point, which limits their utility. Though the appeal of a blood free device is such that several attempts have been published—see Munley (1989) for a pragmatic example—the consensus however, is that versatile *in vitro* methods require a blood or haemoglobin solution (Reynolds, et al. 1992).

Several blood-based *in vitro* techniques have been described in the literature and in patents, ranging in complexity from Yount's (1989) wedge-based technique to the comprehensive system described by Reynolds et al. (1992). The system described by Reynolds et al. is depicted in Figure 3.13. It serves as a good example of the tasks and components involved.

The system uses whole blood to which the anticoagulant heparin has been added. A computer controlled peristaltic pump circulates the blood around a closed loop with minimum damage to the erythrocytes, mimicking the pulsatile blood flow of the arteries. A gas-mixing pump provides a mixture of O_2 , N_2 and CO_2 , in user defined proportions. The CO_2 is necessary to maintain the correct pH and realistic carbon dioxide partial pressure. Gas diffuses into and out of the blood through an oxygen membrane, which provides a large permeable interface area with gas on one side and a thin film of blood on the other, mimicking the alveolar function of the lungs. The probe of the pulse oximeter under test is attached to a phantom finger in which the blood is circulating. A sample port provides an extraction point for blood samples, which are subsequently analysed by a CO-oximeter. The computer, using

parameters fed-back from a second, modified pulse oximeter, varies and controls the gas mixture and rate of peristaltic displacement, to simulate the desired heart rate and arterial oxygen saturation.

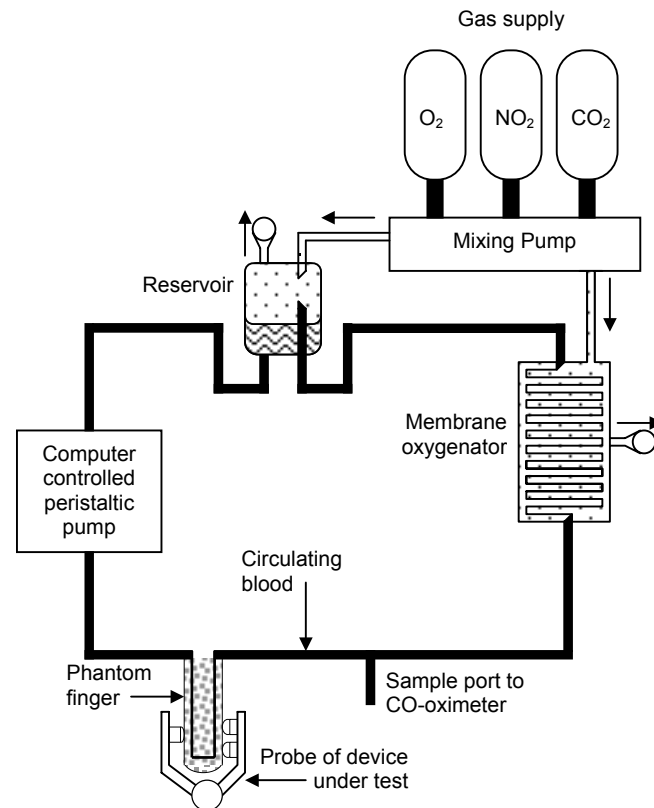


Figure 3.13 Apparatus for in vitro calibration of pulse oximeters (Reynolds, et al. 1992).

The construction of the phantom finger, to which the probe of the device under test is attached, is an important factor. The phantom should possess similar absorptive and scattering properties to a real finger and in addition, should exhibit a similar variance in volume to a real finger, when exposed to the artificial pulse. A system similar to that of Reynolds et al. was developed by Vegfors et al. (1993), though with a greater emphasis on the phantom finger.

3.4 LIMITATIONS AND APPLICATIONS OF PULSE OXIMETRY

3.4.1 ACCURACY AND ERRORS

In Section 3.2.1.2 the saturation quantity, S_pO_2 , displayed by a pulse oximeter was defined as the ratio of oxyhaemoglobin to total haemoglobin. This definition is imprecise and in need of revision. The quantity defined in equation (3.10) is in fact the *functional* arterial oxygen saturation, defined as,

$$\text{Functional } S_aO_2 = \frac{HbO_2}{HbO_2 + Hb} \times 100\%. \quad (3.26)$$

The functional oxygen saturation ignores species of haemoglobin that are present in the blood but not available for oxygen transportation. The percentage oxygen saturation of all haemoglobin in the blood is termed the *fractional* oxygen saturation, and is given by,

$$\text{Fractional } S_aO_2 = \frac{HbO_2}{HbO_2 + Hb + HbCO + MetHb} \times 100\%. \quad (3.27)$$

It is important to note that pulse oximeters measure neither of these quantities, but rather measure the absorption of light at two wavelengths and use empirically derived calibration tables to map the ratio of the absorption at each wavelength to either the fractional or functional saturation. Since pulse oximeters are calibrated using a CO-oximeter, which measures at least the four quantities in the denominator of equation (3.27), CO-oximeters can measure either functional or fractional saturation. Thus a pulse oximeter can display an estimate of either the fractional or functional oxygen saturation; it is up to the manufacturer to explicitly state which parameter their particular device is estimating.

It is important to remember that regardless of the manufacturer's goal to measure fractional or functional saturation, the device will display neither of these quantities, since, invariably, the patients' blood pH and background levels of dyshaemoglobins will differ from those of the calibration subjects'—and perhaps significantly since a patient is presumably in a state of illness when monitoring commences. Moyle (1994) stated that the quantity displayed by a pulse oximeter, S_pO_2 , is best thought of and referred to, as *the oxygen saturation as displayed by a pulse oximeter*, since it is variable between devices and unavoidably inaccurate in either case to a varying degree.

With this in mind, how good is a pulse oximeter's estimation of arterial oxygen saturation, and how useful is it?

Pulse oximeter performance is rated by its *accuracy*; the systemic error or bias associated with the method; and, its *precision*; the reproducibility of the measurement or the variation of the random error associated with the measurements. The CO-oximeter is the *gold standard* against which pulse oximeter performance is calibrated and compared. (CO-oximeter manufacturers (IL 482) report precisions as high as 0.5% (Tungjitkusolmun 1997).) It is obviously desirable that the magnitudes of these parameters are as small as possible—however in clinical practice it is generally acceptable for a device to exhibit a 95% confidence limit of $\pm 3\%$ (Tungjitkusolmun 1997), though its accuracy will be determined by several factors relating to the patient's condition.

Some of the other factors affecting pulse oximeter accuracy are summarised below. They are naturally of great interest to clinicians and competing device manufacturers alike.

3.4.1.1 DYSHAEMOGLOBINS AND FETAL HAEMOGLOBIN

The affects of dyshaemoglobins and fetal haemoglobin beyond their normal background levels are multifarious. Any increase in their levels causes an increase in the denominator of the fractional saturation defined in equation (3.27). Their overall effect on the displayed S_pO_2 value is determined by the haemoglobin specie's absorption spectrum and the wavelengths of light used by the pulse oximeter.

A discussion of their individual affects on S_pO_2 is to be found in Moyle (1994), Reynolds et al. (1993), and Tungjitkusolmun (1997).

3.4.1.2 SATURATION, PERFUSION, AND OTHER FACTORS

Perhaps the most crucial relationship to quantify is the variance in pulse oximeter error as a function of oxygen saturation. This is typically specified for regions of oxygen saturation. In the region of high saturation (greater than 97.5%) the statistical parameters pertaining to a pulse oximeter's performance are difficult to establish accurately. Since pulse oximeters never display saturations greater than 100% the accuracy and precision of their measurements in this region are biased

(Clayton, et al. 1991a). However patients in this saturation range are in no immediate danger.

Pulse oximeters have reliable performance in the region of normal saturation (90% to 97.5%). This is the easiest region in which to obtain in vivo calibration data. In a study of thirteen commercial devices Webb et al. (1991) found that eight devices had absolute mean errors of less than 1% and a standard deviation of less than 2%, while in the remaining five devices these figures were 2% and 3% respectively. Taylor and Whitman (1988), reported a mean bias of +2.8% for five commercially available devices in the saturation range 80% to 100%.

At low saturations (less than 80%) pulse oximeters are most susceptible to errors. Recall from Section 3.3.5 on calibration that it is unethical and dangerous to repeatedly desaturate volunteers to these levels during in vivo calibration. Thus many of the calibration curves are extrapolated in this region. The absorption spectrum of the most abundant absorber at these saturations, Hb, is steep at the common red wavelength of 660 nm, making devices particularly susceptible to wavelength variances at these saturations (see Section 3.3.1). Webb et al. (1991) also reported the use of intensive care patients exhibiting low saturations to test the same thirteen devices. The results varied among manufacturers, though absolute values of bias and precision decreased in all devices. Two devices, a Datascope Accusat and a Nonin 8604, had biases within 1.7% of each other for normal saturations, which increased to 15.9% for low saturations.

Mannheimer et al. (1997) conducted the first study aimed at improving pulse oximeter performance in the crucial low saturation range. They used both Monte Carlo and photon diffusion numerical models to simulate the affect of wavelength on oximetry accuracy at low saturations. They concluded that wavelengths of 735 nm and 900 nm provide the best trade-off between low saturation accuracy and the need to equilibrate the fractional change in path length experienced by both wavelengths (see Section 3.2.1.1).

Since pulse oximeters require an arterial pulse, low perfusion can be problematic. Poor perfusion and a concomitant reduction in peripheral arterial pulsations can result from hypothermia, vasoconstriction, hypotension, or cardiac arrest. Another interesting complication can result from venous congestion, where blood is accumulated within an organ. The resulting backpressure can introduce pulsations into the venous blood, which cause that blood to contribute to the pulse oximeter reading. Since venous blood is considerably less rich in oxygen, the

resulting S_pO_2 values are lower than the true value (Tungjitkusolmun 1997). This phenomenon is also the basis for venous oximetry, in which, an artificial pulsation that is discernable from the natural arterial pulsation, is introduced to the venous blood. When combined with pulse oximetry, venous oximetry has the potential to yield local tissue oxygen consumption data in a relatively non-invasive manner (Chan, et al. 2003).

Some further factors that can introduce error are: motion artefacts, optical interference, intravenous dyes, nail polish, activity, and the presence of dried blood.

3.4.1.3 ACCURACY AND PROBE LOCATION

Some consideration should also be given to the location of the pulse oximeter probe. Under certain conditions, principally rapid desaturation, the accuracy can vary with probe location. It has been known for some time that PPG signals captured from the finger differ significantly compared to those captured from the ear. Nijboer and Dorlas (1985) demonstrated that changes in pressure during induction, maintenance, and recovery from anaesthesia, are greater when recorded from the finger, and hence should preferably be measured from the finger.

In relation to pulse oximetry, Severinghaus et al. (1989) found that ear and forehead probes generally had a much faster response to changing S_aO_2 values than finger probes. Young et al. (1992) conducted a significant study of this phenomenon at the Royal Air Force Institute of Aviation Medicine. They measured the response times of thirteen pulse oximeters from ten manufacturers using twenty-six probes (thirteen ear and thirteen finger probes) to a 10% step reduction in arterial oxygen saturation. Ear probes showed a faster response than finger probes.

In relation to poor perfusion, Clayton et al. (1991b) showed that finger probes have superior performance to either ear, nose or forehead probes, and recommended their use in poor perfusion situations.

3.4.2 LIMITATIONS

J. Severinghaus at the conclusion of a considered history of the entire field of blood gas analysis (to which he himself made significant contributions in carbon dioxide measurement) said of pulse oximetry:

Pulse oximetry is arguably the most important technological advance ever made in monitoring the well-being and safety of patients during anesthesia, recovery and critical care.

(Severinghaus 1987a)

J. Moyle however, promulgated this caveat, enjoining users against complacency:

The reputation of the technique of pulse oximetry can be maintained only if its limitations are always borne in mind. Currently this is not the situation and the indicated value of S_pO_2 is relied on totally by most users.

(Moyle 1994)

Beyond the technical and circumstantial constraints discussed above, two inherent factors largely account for the limitations of the technique. They should be borne in mind equally by the clinician managing a patient and by the researcher seeking to find new applications.

The first is pulse oximetry's ability to monitor oxygen delivery, be it too much or too little. Lack of oxygen at a cellular level is termed *hypoxia*. Hypoxia can be further categorised into four groups: hypoxic hypoxia (arterial Hb oxygen saturation is low), anaemic hypoxia (Hb concentration is low—but may be well saturated), stagnant hypoxia (low cardiac output or vessel occlusion), and histotoxic or cytotoxic hypoxia (oxygen is delivered but cells are unable to utilise it). Of these categories, pulse oximetry can measure and indicate only one—hypoxic hypoxia—though a device may produce readings during instances of other types of hypoxia. Thus a patient may be globally or locally hypoxic despite S_pO_2 readings to the contrary.

Also on this point, pulse oximetry is insensitive to the delivery of too much oxygen—*hyperoxia*. Excess oxygen can be toxic, leading to either central nervous system (CNS) toxicity (that can result immediately upon exposure to very high oxygen partial pressure, typically greater than 1.6 atm (United States Navy 1994)), or pulmonary oxygen toxicity (that can result from prolonged exposure to oxygen partial pressures above 0.5 atm (Moyle 1994), common in intensive care). This limitation of pulse oximetry is important in monitoring patients receiving supplementary oxygen, particularly premature babies and neonates, who can suffer retinopathy, resulting in blindness, if their arterial oxygen saturation is allowed to go too high (Moyle 1994).

The second limitation of pulse oximetry is that it requires a pulse. Though it is desirable to monitor the oxygen saturation of a patient experiencing cardiac arrest, or, exhibiting an irregular pulse, low perfusion, or low blood volume (hypo-

volaemia), this is exactly when pulse oximetry either, is precluded in the case of cardiac arrest, or should be treated sceptically in the remaining cases. Indeed Moyle (1994) states that all pulse oximeters should display a PPG, and that the indicated S_pO_2 value should not be relied upon unless the displayed PPG bears a strong resemblance to an arterial pressure waveform complete with dichrotic notch.⁷

It is worth noting that the limitations of the technique of pulse oximetry apply equally to both existing clinical devices and to any future non-contact device that is based on the principle.

3.4.3 APPLICATIONS

The clinical applications of pulse oximetry in medicine are as important as oxygen is to life. This may seem an overstatement, but as more and more pulse-oximeters are coming into use, more and more hypoxaemic events are being seen as precursors of pathological events.

(Moyle 1994)

The scientific and medical literature is filled with examples of studies in which pulse oximetry has been either the subject or an investigative tool. There are numerous calls for, and statements that, pulse oximetry should become a standard technique in monitoring patients where their own ability to regulate breathing is diminished by either illness or medical treatment. However, the volume of publications on the subject, suggests that pulse oximetry has already been adopted as a standard in these situations. Indeed it has been suggested in several fields of medicine that pulse oximetry should become, or is already being used as, a fifth vital sign (Mower, et al. 1998; Mower, et al. 1997; Neff 1988).

In addition to its common functions pulse oximetry has been used surgically to assess the viability of bowel tissue and in so doing, to discern recoverable from irrecoverable levels of ischaemia of bowel tissue (DeNobile, et al. 1990). A list of other uses to which pulse oximetry has been put since its inception, includes but is not limited to the following:

- Assessing the perfusion of extremities and transferred tissue during illness, after injury or surgery, and after reattachment (Lindsey, et al. 1991).

⁷ The dichrotic notch is the inflection in the falling edge of the PPG that results from a momentary back flow of blood caused by the abrupt closure of the aortic valve. See Figure 3.5.

- In emergency medicine as a quick indicator of the likelihood of desaturation as a cause of malaise and to monitor the effectiveness of cardio pulmonary resuscitation.
- In dentistry where sedation or anaesthesia is used and to indicate the perfusion and viability of dental pulp (Schmitt, et al. 1991).
- In monitoring sleep apnoea and generally in sleep studies.
- In continuous assessment of sick neonates—to whom high saturation may also be dangerous.
- In monitoring the health of pilots of high performance aircraft and in monitoring the effects of commercial aircraft cabin pressure on passengers.
- Monitoring both mother and child during childbirth.
- Computer controlled oxygen weaning.
- Cerebral oxygen measurement through the eye and measurement of the saturation of the retina—which is important in monitoring the progress of diseases such as diabetes.
- Veterinary medicine.

Key to many of these applications, for example, monitoring the saturation of mother and child during childbirth (Chung and McNamara 1993), measuring retinal and cerebral saturation (de Kock, et al. 1993) (which unlike peripheral circulation is not affected by shock, hypothermia, or haemorrhage), and measuring oesophageal saturation (Kyriacou, et al. 2002; Kyriacou, et al. 2003) in patients under going thoracic surgery (and who consequently have very low peripheral circulation), has been the development of new and different probes apt to the particular needs of the monitoring situation.

It should also be noted that many applications of pulse oximetry are in fact utilising only the ability of a pulse oximeter to a display a PPG. For example, compromised extremities or transferred tissue (such as skin, muscle flaps, and digits) can be assessed using two probes, one on a healthy limb and the other on the compromised extremity or transferred tissue.

3.5 CHAPTER SUMMARY

This chapter has reviewed the principles of pulse oximetry and highlighted some aspects of commercial device design and construction. Commercial devices employ numerous sophisticated digital signal-processing techniques and are comprised of both a microprocessor and specialised instrumentation electronics. Though the degree of sophistication varies among commercially available devices, the process of capturing two PPG signals simultaneously at two different wavelengths is fundamental to all conventional pulse oximeters, and equally so to a non-contact device. As a further point on the importance of capturing a PPG, while this chapter has emphasised how a PPG signal is captured by a pulse oximeter and how arterial oxygen saturation is subsequently determined, the ability of a pulse oximeter to also display a PPG signal is an integral part of the device's clinical usefulness. The pulse rate (which is determined from the PPG signal) and the profile of the waveform itself, when interpreted in conjunction with the arterial oxygen saturation, greatly enrich the capabilities of a pulse oximeter, as both a monitoring and diagnostic tool.

The aspects of clinical device design that have been highlighted—particularly choice of source and detector, source and detector separation, reflection-based pulse oximetry, and sampling strategy—will be prominent themes in the design considerations for a remote non-contact device (Chapter 4), and will be shown to have a strong bearing on the performance of such a device (Chapter 5).

Additionally this chapter has highlighted some of the uses and inherent limitations of the technique of pulse oximetry, as well as the importance of the technique in its primary application. The current diversity of applications in which pulse oximetry is employed and particularly its use in anaesthesia, surgery and patient monitoring (with which it has become synonymous), are in stark contrast to the needs that spurred its development—an example of Diamond's adage that in contradiction to the popular saying, *invention is often the mother of necessity* (Diamond 1997).

Together these areas of discussion provide a useful insight into the functionality that a novel device must possess as well as defining the levels of accuracy and precision that a novel device must approach. The description of the limitations of pulse oximetry is instructive in delineating the capabilities and desired functionality of a remote camera-based pulse oximeter from existing camera-based tissue oxygenation monitoring techniques utilising similar technologies, however with markedly different design requirements.

CHAPTER 4

DESIGN CONSIDERATIONS

This chapter outlines considerations pertaining to the choice of source and detector in a remote non-contact pulse oximetry (or photoplethysmography) application. This chapter is concerned primarily with identifying suitable technologies for use as a source and detector, while the details of the system used in this study are presented in Chapter 5, along with analyses of both the components' performance and the system's performance. This chapter also summarises the existing safety guidelines pertaining to exposure to near infrared light.

4.1 CHOICE OF SOURCE

Section 3.2.1.2 described the three constraints on the choice of illumination wavelength imposed by the technique of pulse oximetry. They were that the wavelengths should fall within the optical window into tissue, that the two wavelengths should be on opposite sides of the Hb/HbO₂ isobestic point, and that each wavelength should have a similar differential path length factor.

In addition the nature of a remote camera-based system requires that the optical density of the tissue and the emitted power at each wavelength should be sufficient to allow the detection of PPG signals at each wavelength, while

maintaining an illumination intensity that is safely within the maximum permissible exposure for that wavelength.

The formulation of the theory describing light attenuation by tissue assumed monochromatic light sources. In practice monochromatic light is difficult to produce within the power, size, and safety constraints of a clinical environment—as is very narrow-band light. While some light emission at wavelengths other than the desired wavelength can be accommodated, it is required as a minimum that the two sources have no significant emission at common wavelengths, which can lead to cross talk between the haemoglobin species.

There are three categories of light sources that meet these criteria: light-emitting diodes (LEDs), laser diodes, and broadband sources (used in conjunction with optical filters).

Lasers meet all of the criteria except safety, where their coherent light makes them hazardous particularly to the eyes and especially in the near infrared where the projected light is invisible to the naked eye.

Broadband sources (such as tungsten or halogen lamps) used in conjunction with optical filters do not easily lend themselves to quickly alternating the emitted wavelength (though such a source was utilised in the earliest reported studies of camera-based non-contact photoplethysmography by Blažek et al. (2000) while an annular ring of LEDs was used by Hülsbusch and Blažek (2002)).

Laser diodes are generally suitable though they are relatively large and often require optical fibres to couple them to the tissue. By comparison LEDs are small and relatively inexpensive. When used with inbuilt lenses LEDs can be arranged to create various illumination patterns. The only drawback of LEDs in their application to non-contact pulse oximetry is that light from an LED is emitted over a wide angle. Even with the incorporation of a lens this limits the distance at which the light source can be located from the tissue under investigation.

Other than the choice of illumination method the only other design consideration pertaining to the light source is safety.

4.1.1 SAFETY GUIDELINES

The mechanisms by which light can cause damage to biological tissue include thermal, acoustic, optical (electric breakdown), and photochemical interactions

(ICNIRP 1996). The occurrence of each type of interaction is governed by the wavelength of light and the duration of the exposure. For example, pulses less than approximately 0.1 ms can lead to acoustic damage caused by rapid local expansion of heated tissue, pulses of less than a nanosecond can cause optical breakdown and plasma formation, while lengthy exposures (greater than 10 s) to very short wavelengths can cause photochemical damage (ICNIRP 1996)—sun burn being an example. The wavelengths used in pulse oximetry fall into the category visible and IRA light, defined by the International Commission on Non-Ionizing Radiation Protection (ICNIRP) as 400 nm to 1400 nm.

Although there are no definite boundaries between injury mechanisms, certain mechanisms predominate according to the spectral region and exposure duration (ICNIRP 1997). The pulse durations used in pulse oximetry (see Section 3.3) are considerably longer than the threshold at which tissue damage can occur either by acoustic or optical breakdown mechanisms. Within the visible-IRA range, photochemical damage is predominant over thermal damage only in the wavelength range 400 nm to 700 nm. Above 700 nm thermal damage is predominant with injury to the skin resulting from temperature rises exceeding 45 °C (ICNIRP 1997). LEDs in pulse oximeters are widely considered safe from a radiation perspective; most absorption in tissue at these wavelengths is due to blood, which is constantly circulating. Indeed the primary cause of heating of the skin in pulse oximetry is heat conduction from the *p-n* junction, discussed in Section 3.3.1.3. Bozkurt and Onaral (2004) conducted a study of skin heating resulting solely from semiconductor junction heating. They found the temperature increase in skin due to the semiconductor junction to be in the range 1 °C to 10 °C. Both Bozkurt and Onaral and Ito et al. (2000) place the temperature increase due to near infrared light absorption alone at less than 0.5 °C. The risk of burns caused by semiconductor junction heat conduction is obviated by a remote non-contact application.

Guidelines exist for both incoherent broadband light sources (ICNIRP 1997) and coherent monochromatic laser sources (ICNIRP 1996, 2000), though narrow-band LEDs belong to neither category. With the advent of high power LEDs and their widespread use have come calls for the development of safety standards specific to LEDs (Horak 1999). ICNIRP (1997) recommends adherence to broadband safety guidelines when evaluating the safety risk posed by LEDs; in contrast, the International Electrotechnical Commission (IEC) includes LEDs in its safety guidelines for laser products (British Standards 1994). The IEC guidelines are more conservative and specify the following maximum permissible exposure (MPE) of

skin to coherent light in the range 700 nm to 1400 nm (exposure time t , $10^3 \text{ s} < t < 3 \times 10^4 \text{ s}$),

$$\text{MPE} = 2000 \times 10^{0.002 \times (\lambda - 700)} \text{ [W/m}^2\text{]}. \quad (4.1)$$

Individual LEDs generally do not exceed this exposure limit—though an array of high power LEDs utilising lenses may have the potential to do so. The compliance of the array used in this study is discussed in Section 5.2.2.3.

4.2 CHOICE OF DETECTOR (CAMERA TECHNOLOGY)

Various silicon semiconductor based detectors are used in near infrared spectroscopy applications. The band gap of silicon (the energy required by an electron to move from the valance band to the conduction band) is approximately 1.12 eV. Thus incident light with a wavelength shorter than approximately 1107 nm has sufficient energy to induce conduction, making such detectors well suited to tissue oximetry and pulse oximetry applications.

Within tissue oxygenation studies and particularly imaging based studies, the charged coupled device (CCD) is the detector of choice. A CCD is effectively an array of either photodiodes or photogates. In dedicated near infrared spectroscopic systems, tissue is illuminated by a broadband source. Detected light is coupled to the spectrometer by a fibre bundle where it is projected at a prescribed angle of incidence onto a diffraction grating (or prism). Light is diffracted from the grating (or refracted from the prism) at an angle that is a function of its wavelength; thus different wavelengths of light fall on different parts of the CCD array and the intensity of each can be measured separately (Lerner 2006). Such systems are suited to measuring the oxygenation of small regions of immobile tissue. Two such techniques are described by Irwin (1995) and Stranc (1998), which describe the use of tissue oxygenation and perfusion monitoring to assess the viability of tissue during plastic surgery.

CCDs have also been employed as detectors in camera-based systems to measure regional variation in tissue oxygenation. Sowa et al. (1997), Sowa et al. (1999a; 1999b), Sowa et al. (2001), and Attas (2001), present studies on tissue hydration and oxygenation during surgical procedures and following burns using both a spectrometer and a non-contact CCD-camera-based system. To acquire images at various wavelengths, broadband sources were used to illuminate the

tissue and either fixed wavelength or liquid crystal tuneable filters of variable centre wavelengths were placed in front of the camera lens. The studies were interested in establishing the value of tissue oxygenation and hydration monitoring as indicators of tissue viability.

The development of non-contact camera-based tissue oxygenation imaging systems seem—in name at least—similar to the goal of non-contact camera-based pulse oximetry. However unlike tissue oxygenation, arterial oxygen saturation does not vary regionally, thus there is little merit to arterial oxygen saturation imaging with the intent to observe variation (refer to the discussion of oxygen transportation in Section 2.1). A camera-based system does however, through its optics, offer the ability to observe a significant area of tissue, while preserving the possibility of compensating for motion.

Though a camera-based approach is suited to the task of non-contact pulse oximetry, the nature of pulse oximetry, as opposed to tissue oximetry, places significantly different demands on the camera. Changes in tissue oxygenation occur over several minutes (Sowa, et al. 1997); arterial oxygen saturation changes are more rapid (see Section 3.3.4) and the technique of pulse oximetry requires the capture of two pulse signals simultaneously. Non-contact camera-based pulse oximetry requires that near infrared spectroscopy be performed at faster frame rates than are necessary in camera-based tissue oximetry. The technique of pulse oximetry also requires narrow band (ideally monochromatic) light sources. Neither the frequency response nor the time-domain response of the liquid crystal tuneable filters used in the above studies is sufficient for use in pulse oximetry. Since a silicon-based camera sensor has no inherent means of differentiating the intensity due to incident light of different wavelengths, a camera-based system must resort to the conventional pulse oximetry method: alternately illuminate tissue with two separate sources at different wavelengths and construct a multiplexed output from the detector.

The requirements of a camera for use in remote non-contact pulse oximetry are thus: that it be sufficiently sensitive to measure the difference in absorption (received light intensity) at two wavelengths of light (detector quantum efficiency and signal to noise ratio); that it be capable of capturing frames at a rate sufficient to monitor the pulse component of the change in absorption at both wavelengths in a multiplexed fashion (frame rate); that it be capable of quantizing these data to a useful resolution (bits per pixel); that it have sufficient dynamic range; and that it be

capable of imaging a sufficiently large region of tissue that the observation of a PPG signal at each wavelengths is probable (frame size).

Collectively these requirements can be grouped into two conflicting demands of the imaging sensor: high sensitivity and accuracy, and high data rate. Although CCD sensors have been the incumbent technology in scientific digital imaging applications since its inception, the conflicting requirements of sensitivity and speed that arise here, warrant the inclusion for consideration of CCD's competing technology—complimentary metal oxide semiconductors (CMOS).

4.2.1 CCD IMAGE SENSORS

Figure 4.1 depicts three common CCD sensor architectures: full frame, interline transfer, and frame transfer. The full frame CCD sensor is the original format and consists of an array of adjacent pixels. Each pixel consists of one photodiode or one photogate. During an exposure incident photons with sufficient energy cause photoelectrons to accumulate in the pixels upon which they are incident. At the end of the exposure the charge from every pixel in the array is readout sequentially via a buffer row in a process that manufacturers often refer to as a *bucket brigade*. The charges from the last row of the array are transferred to the buffer row by reducing the voltage in the last row and simultaneously increasing the voltage in the buffer row. The charges in each of the above rows are moved to the row directly beneath in the same manner. The charges in the buffer are then shifted horizontally towards the amplifier. This *coupling* of charges is what gives the technology its name. At the amplifier the charges from the accumulated photoelectrons are converted to voltages. When each column of the buffer row has been emptied the next row from the array is moved down. The arrows in Figure 4.1 depict the path taken by the charge collected in one pixel on its way to the amplifier.

The sequential manner in which charge is read from a full frame CCD array means that the readout time is long, and during readout the pixels are still accumulating charge from the incident light. This causes the appearance of vertical stripes in the captured image, emanating from bright parts of the image, known as smearing, which can only be avoided through the use of a mechanical shutter that halts exposure almost simultaneously across the array. This is of no concern in still photography but is impractical in video applications.

Smearing can be avoided by the use of an interline transfer layout. In such schemes a small channel of light-shielded pixels are placed between each column on the array. At the end of an exposure the accumulated charge in each pixel is transferred to the adjacent shielded pixel thus ending the exposure. In addition it is possible to conduct the readout of the previous frame during the exposure of the current frame, thus increasing frame rate. The impunity from smearing and increased frame rate however come at the expense of *fill factor*—that is the ratio of the optically sensitive area to the total area of each pixel is reduced. By reducing the fill factor the sensitivity of the array is reduced.

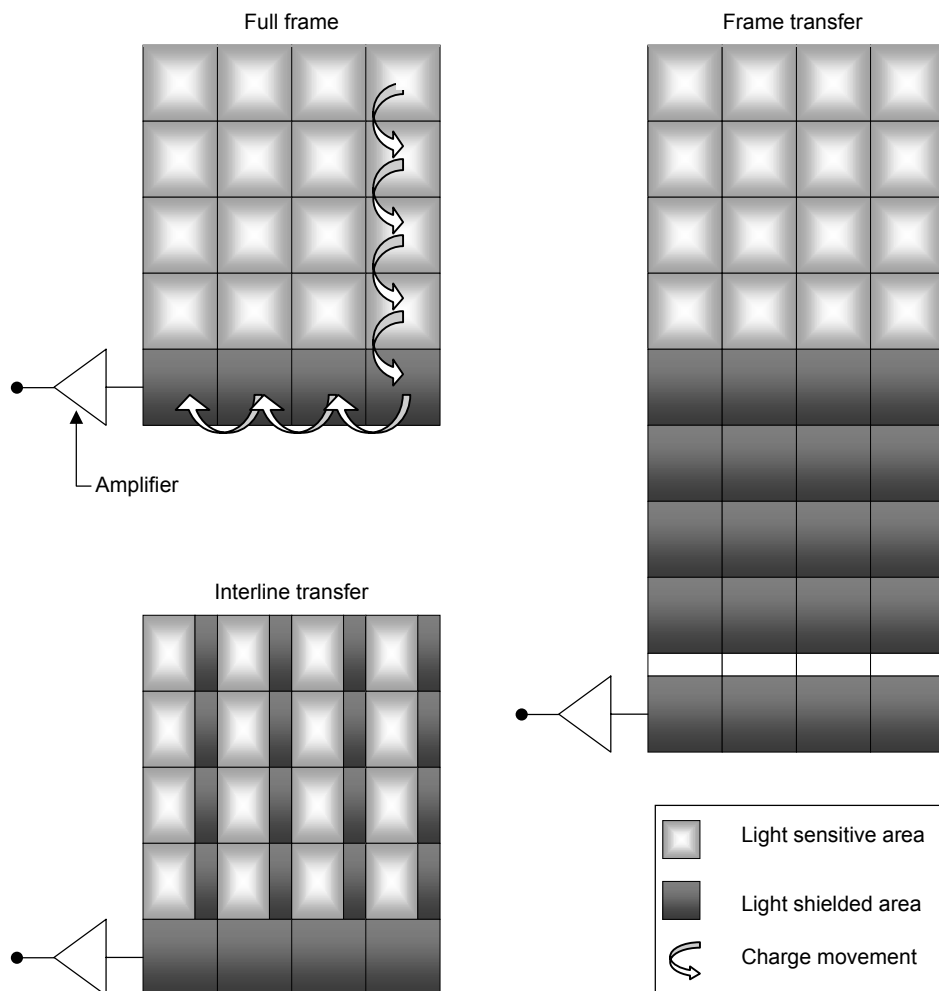


Figure 4.1 Three common CCD image sensor architectures.

An alternative is the frame transfer CCD architecture, in which a second array of light-shielded pixels is attached to the sensing array. At the end of an exposure the charge from the sensing array is transferred to the shielded array. During the next exposure the charge from the shielded array can be readout in the conventional

way via a buffer row. Frame transfer architectures achieve frame rates and levels of smearing mitigation higher than those of full frame architectures but lower than those of interline transfer architectures. Their advantage over interline transfer architectures is that fill factor and thus sensitivity is not compromised—their disadvantage is that they require almost twice as much space and power.

An important characteristic of an image sensor's performance that incorporates several physical characteristics of the sensor itself is its dynamic range—the ratio of a pixel's saturation level (its full-well capacity) and its threshold level (the minimum incident light required to produce an output signal in excess of the noise floor). The threshold is determined by the characteristics of the material from which the sensor is constructed, the fill factor, and the amount of noise producing circuitry surround the image sensor. Saturation level is determined by the size of the pixel and in the case of CCDs, the penetration depth of the electric field that couples the pixels. When a CCD pixel becomes saturated any additional accumulated charge spills over into adjacent pixels, an effect known as blooming. Unlike smearing, which is characterised by vertical stripes, blooming causes streaks to spread out radially from bright points in the image.

All forms of CCD sensor read every pixel in the array serially, thus charge to voltage conversion and amplification are performed by a single amplifier. Large array sizes and high frame rates place a heavy burden on this amplifier, which must have an extremely high bandwidth. The amplifier's bandwidth is a limiting factor in some CCD applications.

4.2.2 CMOS IMAGE SENSORS

Figure 4.2 depicts a schematic of a CMOS image sensor. Each pixel of a CMOS sensor is composed of an optical sensing area (photodiode or photogate) and an optically insensitive area comprised of between one and five transistors. Between each row and column of a CMOS sensor are optically insensitive metal tracks. The fill factor of a CMOS sensor is thus always less than 100%.

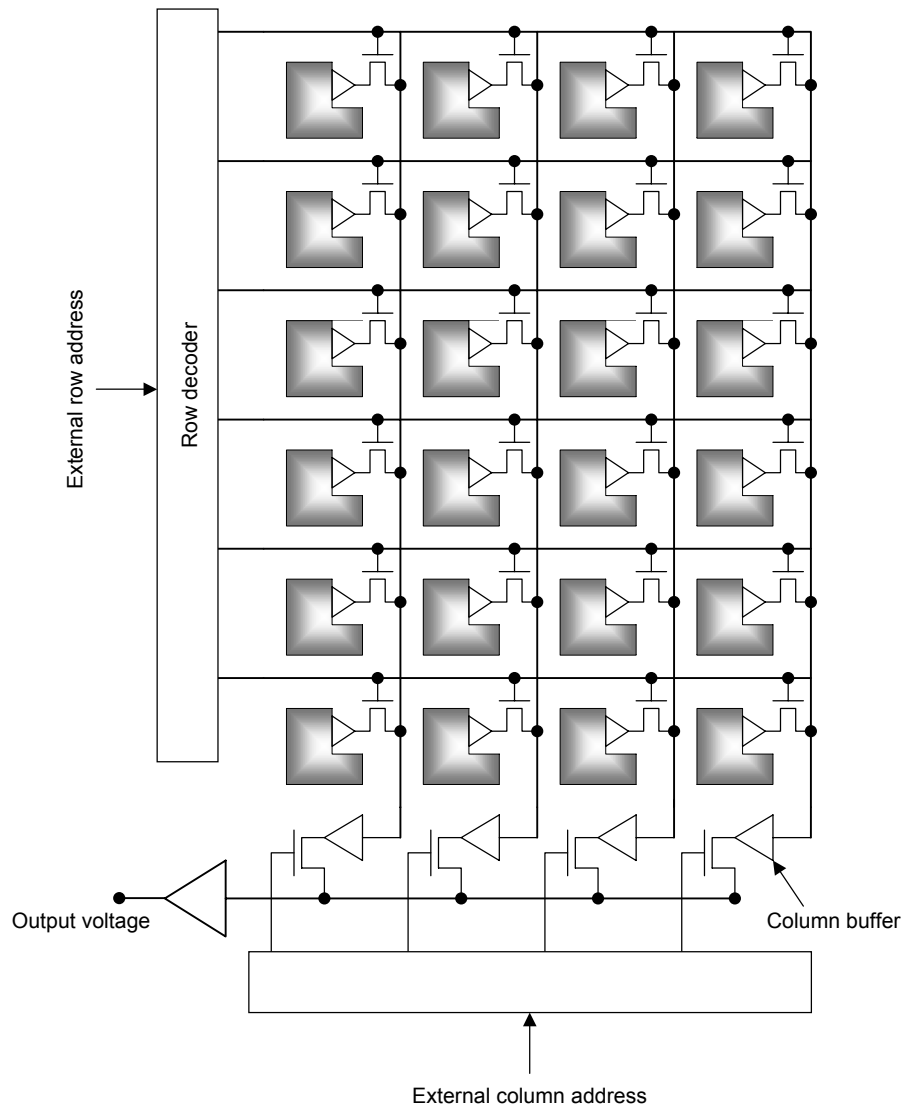


Figure 4.2 Schematic of generic CMOS image sensor architecture.

CMOS sensors also contain a row and column decoder. During the readout process any pixel or any group of pixels can be selected arbitrarily by their row and column address. Unlike CCD sensors, the accumulated charge in each pixel of a CMOS sensor is converted to a voltage and possibly amplified within the pixel.

The original CMOS sensors contained only one transistor per pixel and were referred to as passive or 1T sensors. With just one transistor per pixel, 1T devices could provide arbitrary readout from the array but no amplification and thus suffered from low signal to noise ratios. Additionally they are subject to the same smearing effects during readout as full frame CCD sensors. They are now obsolete.

Modern CMOS sensors have active pixels containing a minimum of three transistors (3T). Charge collection and accumulation, charge to voltage conversion, and amplification all occur within the pixel. Immediate amplification of the signal

improves their SNR, though at the expense of fill factor and thus sensitivity and dynamic range. To reduce the impact of extra components per pixel on fill factor manufacturers switched to finer lithography wafer fabrication processes (typically 0.25 μm , 0.18 μm , or less). This increased cost and ultimately led to the need for manufacturing processes dedicated to CMOS image sensor production; CMOS imagers had originally shared production processes with standard memory and logic production processes giving them a cost advantage over CCD sensors, which have always required customised processes. (Indeed the erudite reader may have already noted the similarity between dynamic random access memory and the CMOS sensor depicted in Figure 4.2.)

In-pixel amplification also gives rise to a phenomenon known as *fixed pattern noise*. This results from slight variations in the amplifiers across the array. Fixed pattern noise must be corrected by image processing.

Though 3T devices offer acceptable SNR for many applications they are subject to smearing of the image during readout in video applications. A certain amount of smearing is acceptable in some consumer applications though not in most scientific or industrial applications. The addition of a fourth or fifth transistor per pixel (4T and 5T) can provide such functions as electronic global shuttering and correlated double frame shuttering (in which the dark current or pixel thermal noise is subtracted from the recorded value for each pixel).

4T and 5T devices have significantly better SNR and dynamic range than 3T devices.

4.2.3 CHOOSING BETWEEN CMOS AND CCD

CCD sensors have traditionally offered good sensitivity, good SNR, good uniformity, and good dynamic range by virtue of their inherently high fill factor and full well capacity. CMOS sensors have typically lagged CCD in each of these areas but have traditionally been capable of higher frame rates and lower power consumption. Figure 4.3 depicts the relative positions of the various CCD and CMOS architectures in relation to some of these parameters.

Manufacturers are constantly improving the performance of both technologies within both of their traditionally strong and weak areas. Many manufacturers provide highly specialised devices that utilise cooling of the sensor, anti-reflective coatings to minimise reflection losses, rear illumination to minimise transmission

loss, micro-lenses over each pixel to mitigate the effects of diminished fill factor, and various other techniques.

Though both technologies have become associated with various specialised applications, for example CCD with spectroscopy and CMOS with machine vision, non-contact pulse oximetry is a new application and the choice of technology is not obvious, requiring both sensitivity and speed.

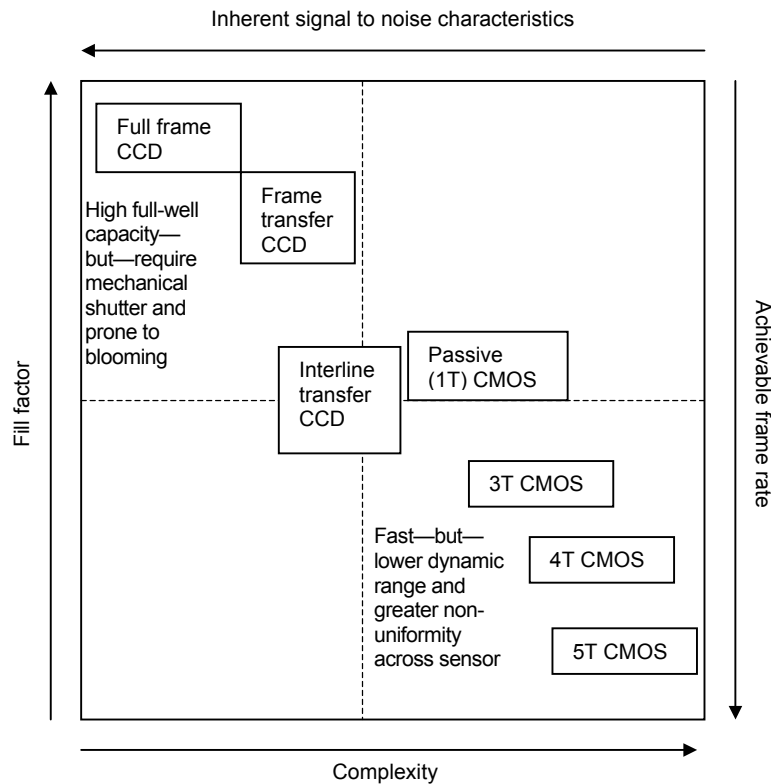


Figure 4.3 Comparison of the characteristics and tradeoffs associated with various CCD and CMOS architectures.

CCD undoubtedly provides the greater sensitivity; the quantum efficiency of a CCD pixel benefits from the larger fill factor. The sensitivity of a sensor is also a function of the SNR. CMOS sensors have a greater amount of noise producing circuitry mounted on the chip. Sensitivity is important to this application as tissue is optically dense and light may have to traverse several centimetres before re-emerging at greatly reduced intensity.

Quantization range and dynamic range are also important to non-contact pulse oximetry. In conventional contact pulse oximetry the variation in received light intensity due to the pulse may under normal circumstances be as little as 1% of the total received light intensity (see Section 3.2). The camera's ability to record such a variation in both brightly and dimly illuminated areas of the image is determined by

its dynamic range. CCD sensors provide better dynamic range by virtue of higher sensitivity during low levels of illumination and larger full well capacity during high levels of illumination. Both technologies can provide sufficient quantization levels for non-contact pulse oximetry—that is sufficient to characterise the profile of the PPG waveform.

To choose between CCD and CMOS it is necessary to prioritise the camera requirements of non-contact pulse oximetry. Sensitivity is a desirable characteristic of all detectors, however pulse oximetry does not require the sensitivity of tissue oximetry methods, which endeavour to quantify the concentrations of individual chromophores. Provided the tissue is sufficiently well illuminated either CCD or CMOS cameras can provide sufficient sensitivity to detect a PPG waveform by non-contact means. Thus the overriding consideration in choosing an image sensor is the ability to achieve a frame rate sufficient to sample two PPG waveforms in a multiplexed fashion while providing a suitable frame size.

As a constraint on the minimum frame size, a suitable size means that the combination of the number of pixels per frame and the magnification produced by the system's optics, provide sufficient sensitivity to capture a PPG signal, while imaging an area of tissue sufficiently large that the observation of a PPG signal is probable. As a constraint on the maximum frame size, suitable size means that the achievable frame rate should not be unduly diminished by an excessive number of pixels per frame.

CMOS sensors generally offer higher frame rates than comparable CCD sensors and crucially, possess the capability of varying the frame size—allowing even higher frame rates.

This capability is paramount in non-contact pulse oximetry, in both offline processing and especially in real-time processing. For this reason a CMOS image sensor was adopted in this study.

CHAPTER 5

INSTRUMENT DESCRIPTION AND PERFORMANCE

This chapter is intended to serve two purposes. First, the chapter details the construction and operation of a novel non-contact remote camera-based device; capable of capturing two PPG signals simultaneously—the prerequisite for pulse oximetry. The non-contact system described here is based on the principles and methods of conventional pulse oximetry, described in detail in Chapter 3. The components of the system, principally an array of LEDs and a CMOS camera, were designed and chosen respectively, in accordance with the considerations, constraints, and requirements that were discussed in Chapter 4. The second purpose of this chapter is to present a methodical investigation of the comparability of measurements from the non-contact camera-based device with those from a conventional contact device. Conventional devices perform three core functions: monitor S_pO_2 , monitor pulse rate, and display a plethysmogram; the comparability of the camera-based device is examined in regard to each of these functions. The examination is intended to establish both the feasibility of such a device and to identify important inherent differences between conventional pulse oximetry and a camera-based technique.

Additionally this chapter presents an investigation of some aspects of photo-plethysmography that are unique to a non-contact implementation. The observation

of *inverted* PPGs by non-contact means is described, a phenomenon that is, in the least a curiosity, and may be a hint to the potential utility of a non-contact device beyond that of a conventional device. A possible explanation of the phenomenon is formed from the known characteristic path of light propagating in tissue (described in Chapter 2) and from the absorptive characteristics of the pulsing arterial blood (described in Chapter 3).

Finally this chapter attempts to address the effect of increasing distance between the device and the tissue under investigation. The achievable tissue-device separation is ultimately a function of the system's optics, the camera's characteristics, and the type of source and its characteristics. However some predictions of the decrease in detected light intensity with increasing separation can be made, with knowledge of the characteristics of the backscattered light emerging from the tissue. A simplified probabilistic model of the effect of tissue-camera separation is developed here, based on a priori knowledge of the distribution of photon trajectories emerging from the region of interest. The prediction by the model is compared to results from a Monte Carlo simulation (described in Chapter 2) of a three-layer tissue model and is shown to provide a prediction comparable to the simulation results.

5.1 SYSTEM OVERVIEW

The principal components of the device are illustrated in Figure 5.1, in an arrangement that is indicative of a typical experimental set-up. The main components of the system are the camera, the array of LEDs, and the optical filter. Also depicted in Figure 5.1 is the relative timing of the system, and the arrangement of the two wavelengths of LEDs relative to each other on the illumination array. Light from the LED array alternately illuminates the tissue under investigation at wavelengths of 760 nm and 880 nm. By monitoring the backscattered light emerging from the tissue using the camera, through image analysis, a PPG signal can be obtained at each wavelength. The two resulting multiplexed PPG signals are then separated and processed by a personal computer (PC) off line (not shown) to yield the desired physiological measurements (the pulse rate and the shape of the peripheral arterial pressure waveform) and to measure the ratio of arterial absorption at each wavelength of light.

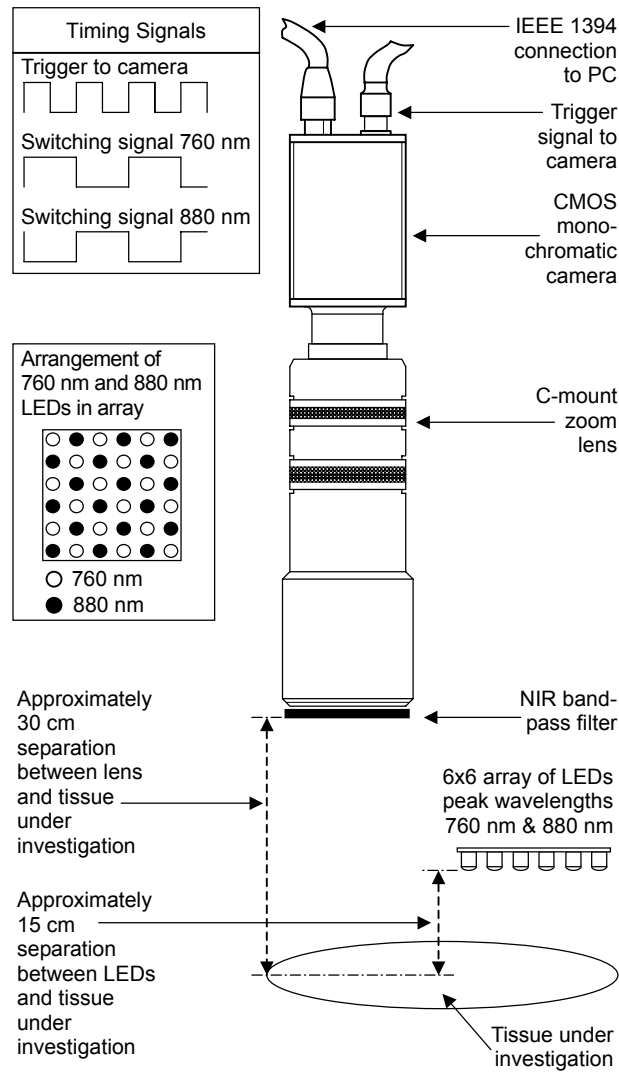


Figure 5.1 Overview of the principal components of the non-contact system.

5.2 HARDWARE DESCRIPTION

5.2.1 THE CAMERA

In accordance with the design specifications pertaining to the sensor, enumerated in the previous chapter (see Section 4.2), a CMOS camera was chosen for this application. The camera (PixelINK PLA-741, IIDC 1.3/DCAM compatible) utilises a $\frac{2}{3}$ inch monochromatic CMOS sensor (8.576 mm \times 6.912 mm, 11.01 mm diagonal). The sensor has 1280 \times 1024 square pixels of length 6.7 μ m.

The camera uses an IEEE 1394-interface connection. Pixels can be encoded using 8 bits or 10 bits.

The camera is configured to operate using a global or synchronous shutter, such that, upon generation of an internal trigger, or upon receipt of an external trigger, the camera exposes the entire sensor for a predefined amount of time—the exposure time. At the end of the exposure, the camera simultaneously reads out the charge accumulated by each pixel, within a user-defined region of interest (ROI), thus ensuring that each pixel has been exposed for precisely the same duration, and for precisely the same period of time.

5.2.1.1 SENSITIVITY

Silicon is sensitive to wavelengths between approximately 1100 nm (in the near infrared) and 400 nm (violet in the visible spectrum). At wavelengths longer than 1100 nm, incident photons lack sufficient energy to overcome the silicon energy band gap, while wavelengths shorter than 400 nm do not penetrate silicon sufficiently deeply to produce photoelectrons.

Manufacturers often specify their detector's sensitivity using a graph of quantum efficiency (QE) as a percentage versus wavelength. The QE parameter incorporates other attributes of the sensor such as pixel area and fill factor, however it excludes the SNR performance of the chip. A more useful figure of merit, which incorporates the sensor's SNR, is the amount of charge produced in excess of the device's noise floor per unit of incident light—usually expressed in units of A/W. The CMOS detector used in this application has a sensitivity of 0.091 A/W at 760 nm and 0.055 A/W at 880 nm.

5.2.1.2 MAXIMUM ACHIEVABLE FRAMERATE

The IEEE 1394 standard specifies a maximum data rate of 400 Mbits/s. This sets an upper limit for the maximum achievable frame rate. For raw data the camera's output data rate is given by,

$$\text{Bits per second} = (\text{Bits per frame}) \times (\text{Frames per second}), \quad (5.1)$$

where the number of bits per frame is given by,

$$\text{Bits per frame} = (\text{Frame Width} \times \text{Frame Height}) \times (\text{Bits per pixel}). \quad (5.2)$$

Thus for a given frame size and number of bits per pixel, the maximum achievable frame rate is limited by the IEEE 1394 maximum data rate. However

equations (5.1) and (5.2) do not take account of the readout time associated with each frame. The maximum achievable frame rate of the camera is a function of readout time, which in turn is proportional to the frame size (or the user defined ROI). The inclusion of the readout time imposes a lower limit on achievable frame rate than the IEEE 1394 bandwidth. The maximum achievable frame rate F_M , is thus given by,

$$F_M = \frac{1}{\text{Exposure time} + \text{Readout time}} \text{ (frames/second)}. \quad (5.3)$$

Thus the camera's maximum data rate D_M , is given by,

$$D_M = (\text{Bits per frame}) \times F_M \text{ (bits/second)}, \quad (5.4)$$

which, due to readout time, is always less than 400 Mbits/s.

Operating at frame rates approaching the maximum achievable rate can result in dropped frames, which are difficult to detect during operation, and can go unnoticed during image analysis. A dropped frame has the potential to critically impair the de-multiplexing of the PPG signal from each wavelength during the image analysis process. It is desirable to avoid dropped frames completely, or at least to detect them in the event of their occurrence.

In an attempt to eliminate dropped frames, a safe maximum frame rate F_{SM} , was empirically established for several frames sizes. To accomplish this, two LEDs were placed side by side within the camera's field of view. LED₁ received a square wave driving current, with period T_1 and 50% duty cycle. LED₂ received a square wave driving current, synchronised with LED₁, but with period $T_2 = 2 \times T_1$, also with 50% duty cycle. The camera was externally triggered by a square wave voltage signal, to capture a frame upon receiving a rising edge. The rising edge of the voltage signal was synchronised with the rising edge of the driving current to LED₁. In this manner the two LEDs flash in a four-state binary sequence. The camera was fixed in place such that the LEDs always flash in the same place in each of the recorded frames. A dropped frame is observable as it causes the LEDs to flash out of their correct binary sequence. In this manner up to four sequential dropped frames can be detected. The resulting values of safe maximum frame rate for pixel resolutions of 640×480 and 320×240 are tabulated in Table 5.1 and Table 5.2 respectively.

Resolution	Exposure time (ms)	Ideal maximum frame rate (frame/s)	Maximum achievable frame rate (frames/s)
640×480	10	100	49
	12	83	45
	14	71	41
	16	62	38
	18	55	35
	20	50	33
	22	45	31
	24	41	29
	26	38	27
	28	35	26
	30	33	25

Table 5.1 Empirically derived maximum achievable frame rates at a pixel resolution of 640×480 with global shutter. Defined as the maximum frame rate that resulted in 0 dropped frames per 10,000 captured frames.

Resolution	Exposure time (ms)	Ideal maximum frame rate (frame/s)	Maximum achievable frame rate (frames/s)
320×240	10	100	76
	12	83	66
	14	71	58
	16	62	52
	18	55	47
	20	50	43
	22	45	40
	24	41	36
	26	38	34
	28	35	33
	30	33	30

Table 5.2 Empirically derived maximum achievable frame rates at a pixel resolution of 320×240 with global shutter. Defined as the maximum frame rate that resulted in 0 dropped frames per 10,000 captured frames.

5.2.2 ILLUMINATION

Illumination is provided by an array of thirty-six GaAlAs LEDs—eighteen with a peak emission wavelength of 760 nm and eighteen with a peak wavelength of 880 nm. The 880 nm LEDs (Opto Diode Corp. OD880-L) emit 17 mW at a forward current of 100 mA. The 760 nm LEDs (Opto Diode Corp. custom wavelength L-package) emit 10 mW at the same forward current. Both types of LED are housed in a TO-46 gold-plated casing, with in-built glass lenses and a specified full width half

maximum (FWHM) beam angle of 30° . The LEDs are mounted on a printed circuit board (PCB) along with two transistors that activate each wavelength of LED. A schematic of the array showing the relative positioning of the two wavelengths of LEDs is depicted in Figure 5.2. The various aspects of the array's design and operation are discussed separately below.

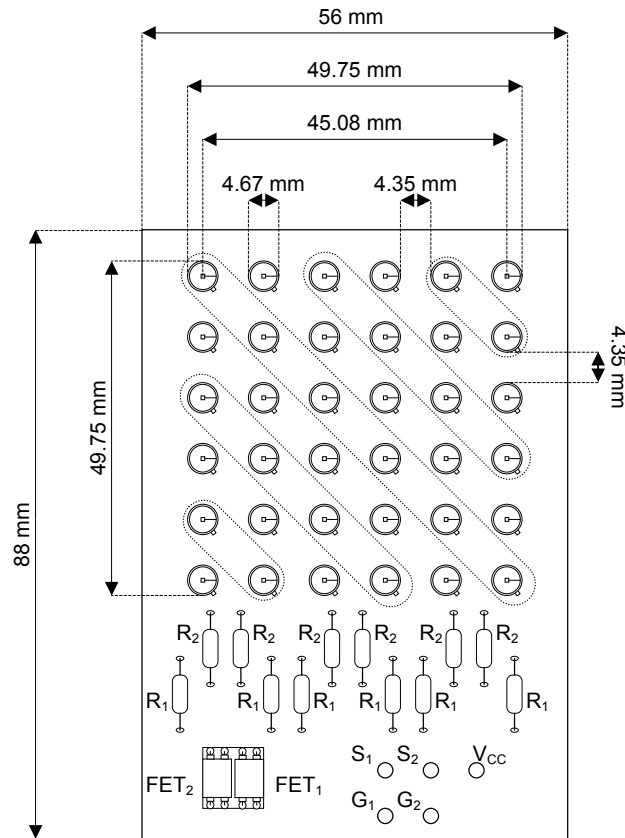


Figure 5.2 Schematic of the illumination array showing the arrangement of the 760 nm LEDs (surrounded by dotted outline) and the 880 nm LEDs, along with ancillary components.

5.2.2.1 CHOICE OF WAVELENGTH

The criteria for choosing the wavelengths of the two light sources were enumerated in Section 3.2.1.2 and extended in Section 4.1: one wavelength either side of the Hb/HbO₂ isobestic point; each wavelength should have a similar differential path length factor; and, the optical density of the tissue at each wavelength should be sufficient to allow the detection of signals at each wavelength, without exceeding the maximum permissible exposure for that wavelength.

The wavelengths selected for this application were 760 nm and 880 nm. This choice was based in part on the prior work of Coyle et al. (2003) and Coyle et al.

(2004), which demonstrated the capture of PPG signals by contact reflectance over several centimetres of tissue using these wavelengths. Early investigations of the feasibility of a camera-based approach (Humphreys, et al. 2005a; 2005b; 2005c) further indicated the suitability of these wavelengths for use with the camera described earlier (Section 5.2.1).

In particular, the choice of 760 nm as opposed to the more conventional pulse oximetry wavelength of 660 nm, places the lower wavelength just inside the near infrared band, making the use of a commonly available band pass filter possible, and thus excluding much unwanted ambient light. Within the region of the near infrared spectrum that lies below the Hb/HbO₂ isobestic point, the region in the vicinity of 760 nm is particularly apt to the technique of pulse oximetry due to a hump in the Hb extinction curve, which causes a marked and desirable difference in the absorption by Hb and HbO₂ (refer to Figure 3.7). The total absorption by blood at this wavelength is considerably less than at 660 nm. Note however that by selecting a wavelength at the peak of the hump in the Hb extinction curve, quantitative measurements of oxygen saturation are made vulnerable to error. Any drift in the peak emitted wavelength of the 760 nm LEDs or deviation among individual components would significantly alter the relative absorption by Hb and HbO₂ (see Section 3.3.1). The performance of the LEDs in this regard is described in Section 5.2.4.

The difference in absorption by Hb and HbO₂ at 880 nm is broadly similar to—though less than—the difference at the conventional wavelength of 940 nm. The sensitivity of the camera's CMOS sensor however is approximately 45% less at 940 nm than at 880 nm.

5.2.2.2 ILLUMINATION PATTERN

Various illumination patterns were tested, including an annular pattern of LEDs directed circumferentially around the camera's field of view, and a small bright spot adjacent to the camera's field of view (see Humphreys et al (2005b; 2005c)). The most successful pattern for obtaining signals from deep tissue, proved to be a large, brightly illuminated area, adjacent to the camera's field of view.

There are compelling reasons for preferring a small brightly illuminated spot (ideally a point source) to any other illumination pattern and in particular the technique of pulse oximetry implicitly precludes the use of an annular light source.

However an explanation of this point is deferred until the conclusion of this chapter (Section 5.7), at which point it is discussed in conjunction with several other aspects of the device's performance and some aspects of photoplethysmography and pulse oximetry that are unique to a camera-based implementation.

The illumination pattern created by the array depicted in Figure 5.2 varies with distance from the array. The manufacturer specifies a FWHM beam angle of 30° for both types of diode. Measurements of this parameter suggested a FWHM beam width of 32° for both wavelengths of LEDs. Using the FWHM parameter, the diameter of a diodes' half-maximum intensity beam d , at a distance x from the diode, is given by,

$$d = 2x \tan\left(\frac{\angle_{\text{FWHM}}}{2}\right). \quad (5.5)$$

Using the measured FWHM angle of 32° , and the geometry of the array specified in Figure 5.2, the illumination pattern of the 760 nm LEDs, at a distance of 15 cm, from a flat surface, was computed, as the superposition of the illuminated spot from each of the eighteen individual 760 nm LEDs. The resulting illumination pattern is illustrated in Figure 5.3. At a distance of 15 cm, each diode projects a half-maximum intensity spot of diameter 8.6 cm. The brightness of the image in Figure 5.3 is proportional to the number of diodes coincident on that region. The maximum height and width of the illuminated area is 131.10 mm. The illumination pattern generated by the 880 nm LEDs is identical but rotated by 90° .

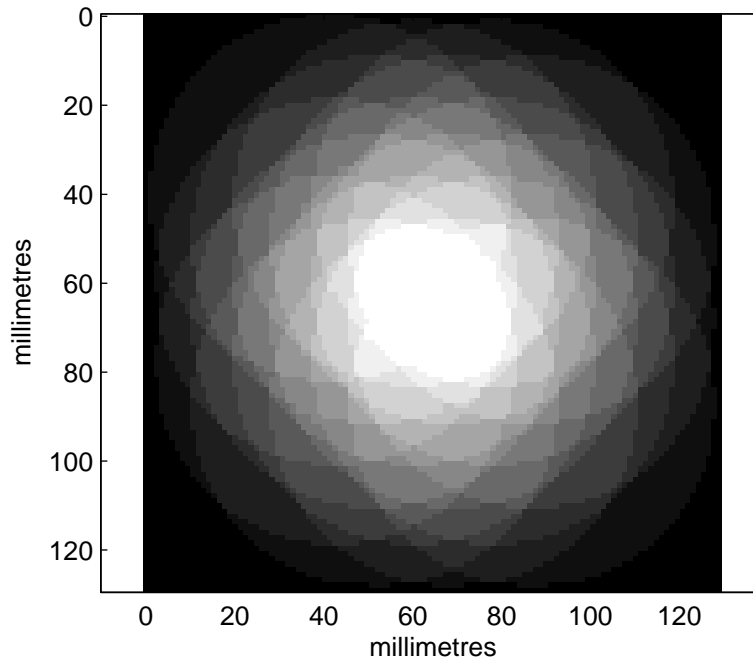


Figure 5.3 Computed illumination pattern resulting from the superposition of the eighteen 760 nm LEDs depicted in Figure 5.2, at a distance of 15 cm from the array.

It is important to consider the profile of the illumination pattern when further evaluating aspects of the system's performance.

5.2.2.3 COMPLIANCE WITH MAXIMUM PERMISSIBLE EXPOSURE

The compliance of single LEDs in conventional contact pulse oximetry is well established (see Section 3.3.1), however this study utilises an array of LEDs and it is the compliance of the array as a whole that is investigated here. The various standards pertaining to LED safety and maximum permissible exposure (MPE) were discussed in Section 4.1.1. The most conservative applicable limit for skin exposure, specified by the International Electrotechnical Commission (IEC), for coherent light sources in the range 700 nm to 1400 nm (British Standards 1994) was given in equation (4.1),

$$\text{MPE} = 2000 \times 10^{0.002 \times (\lambda - 700)} \text{ [W/m}^2\text{]}.$$

The limit is applicable for exposure durations between 1000 s to 30000 s.

For 760 nm, equation (4.1) imposes a limit of 2.6 KW/m², or 260 mW/cm². For 880 nm, the imposed limit is 450 mW/cm². In evaluating the compliance of the illumination array with the MPE limits, the effects of multiple LEDs coincident on the same region of tissue should be taken into account. The intensity profile of the

illumination pattern created on a flat surface, parallel to the array, at a distance of 15 cm, is depicted in Figure 5.3. Taking 15 cm as the nominal distance from tissue under investigation, at which the array will be placed during operation, a contour map of the intensity profile depicted in Figure 5.3 was computed, and is depicted in Figure 5.4.

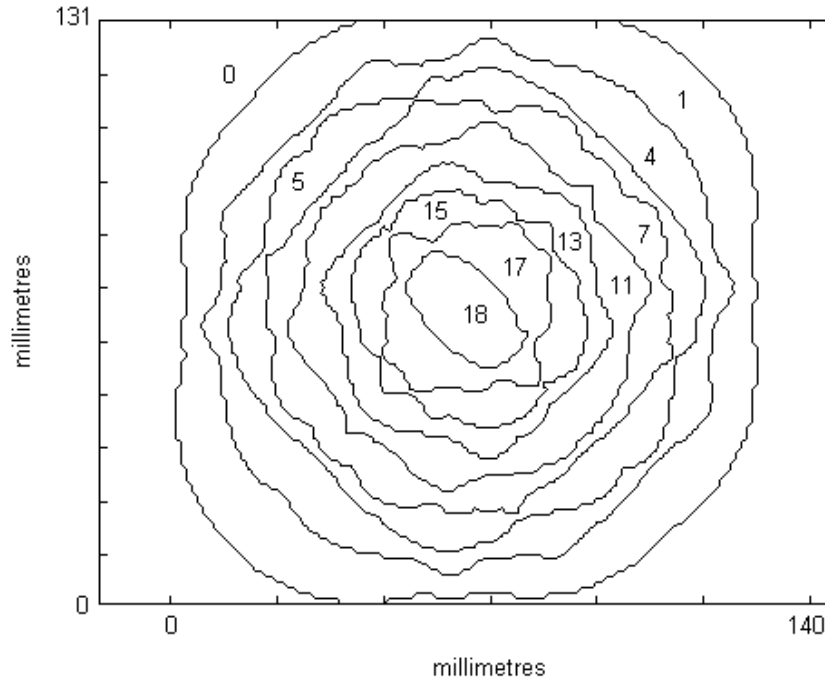


Figure 5.4 Contour map of illumination pattern intensity profile depicted in Figure 5.3. Contour lines mark regions where the specified numbers of LEDs are coincident—that is where their FWHM spots overlap at a distance of 15 cm from the array.

The entire illuminated area fits inside a square of dimensions 132×132 mm—an area of 174.2 cm^2 . However within that area, the intensity is non-uniform—indeed 30 cm^2 receive no illumination (that is less than half the maximum intensity of one LED). The intensity of only one LED illuminates a continuous region around the edge of the pattern, while moving towards the centre of the pattern, the projected spots of several LEDs begin to overlap. There is a region in the centre of the pattern where all eighteen 760 nm LEDs are coincident. The tissue in this central region experiences the greatest exposure.

Using the data mapped in Figure 5.3 and Figure 5.4, the area of the central region where all 760 nm LEDs are coincident, was calculated to be 4.7158 cm^2 . The specifications for the 760 nm LEDs, state a typical power output of 10 mW. Assuming the worst case, in which all LEDs are located centrally over the region, at a distance of 15 cm, for a FWHM beam angle of 32° , each diode could provide a

radiant power density of $172.1524 \mu\text{W}/\text{cm}^2$. The entire region in Figure 5.4 upon which all eighteen LEDs are incident, would therefore receive a collective exposure of 14.6130 mW , or an exposure per unit area of $3.0987 \text{ mW}/\text{cm}^2$. The 880 nm LEDs have a specified typical emitted power of 17 mW , and under the same conditions would deliver a collective exposure of 24.8241 mW , to the central region of Figure 5.4, and an exposure per unit area of $5.2678 \text{ mW}/\text{cm}^2$.

Thus the maximum possible radiant power delivered by the LED array per square centimetre at 760 nm and 880 nm, represent just 1.19% and 1.17% respectively, of the maximum permissible exposures at those wavelengths.⁸ As was discussed earlier, the actual emitted power of the array will be mollified by the requirement of pulse oximetry that both wavelengths of LEDs operate on a 50% duty cycle or less (see the discussion of signal processing by a clinical device in Section 3.3.3). Furthermore, the LEDs are not monochromatic; their maximum emitted power is not in fact concentrated at one wavelength but rather spread over a range of wavelengths (see Figure 5.8 and Figure 5.9 below), further diminishing the hazard. Finally the MPE limit recommended by the IEC refers to coherent light exposure, while LEDs produce incoherent light.

5.2.2.4 LED DRIVING

The LEDs are placed in series in groups of three, each group in series with a small value resistor to limit the current. Both wavelengths of LED are limited to a maximum driving current of 100 mA. The 880 nm LEDs have a forward voltage of 1.54 V at a forward current of 90 mA. Owing to their shorter emission wavelength (see Section 3.3.1), the 760 nm LEDs have a forward voltage of 2.01 V at the same forward current. Figure 5.5 depicts a schematic of the LED driving circuit. The LEDs are arranged in the same pattern as that indicated in Figure 5.2.

⁸ In Section 5.2.4.2 it will be shown that the actual peak emitted wavelength of the 880 nm LEDs is closer to 860 nm. Recalculating the MPE at 860 nm, the array is found to produce 1.26% of the MPE.

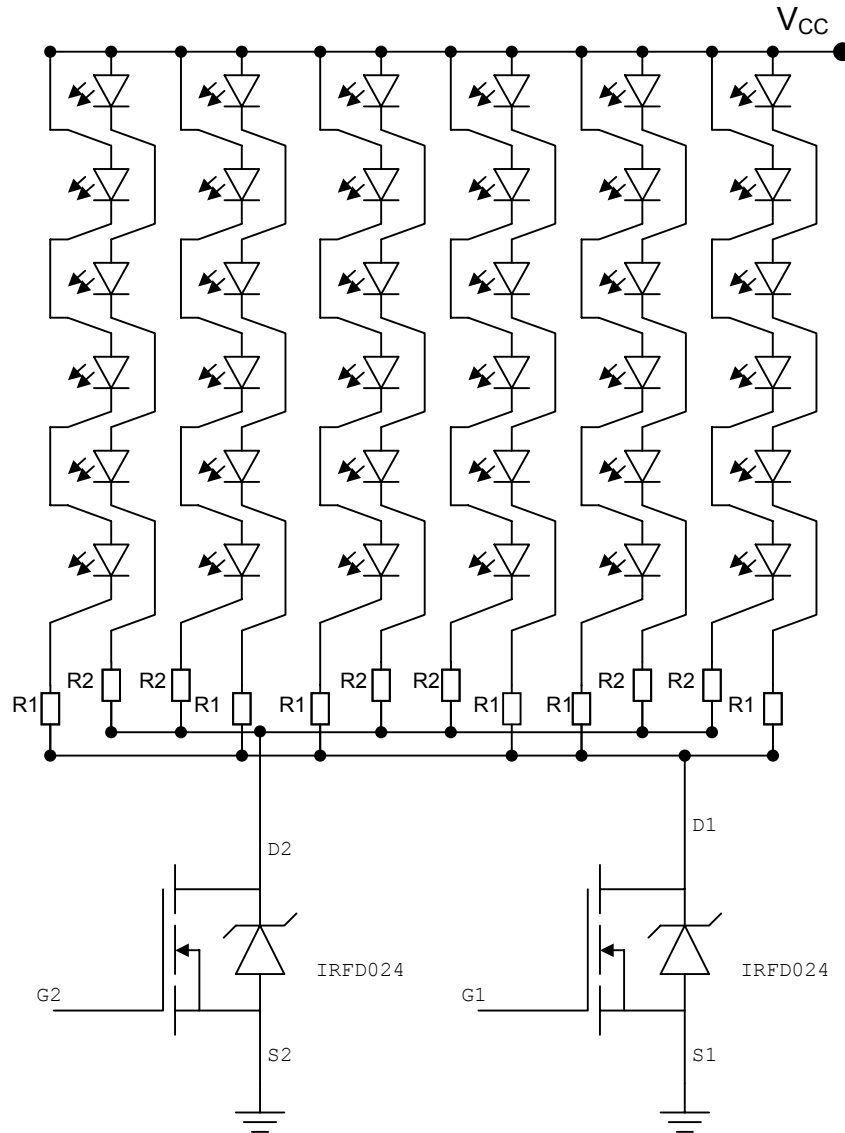


Figure 5.5 Schematic of LED driving circuit. V_{CC} is set at +6 V, R_1 is 14 Ω and R_2 is 4.7 Ω . The two transistors are n-channel enhancement type, power MOSFETs, with a maximum drain current rating of 2.5 A.

A suitable signal applied to the gate of either transistor energises the eighteen diodes at that wavelength. The transistors used are metal-oxide semiconductor field-effect transistors (MOSFETs), rated to a maximum continuous drain current of 2.5 A. The MOSFET channels are fully conductive when their gate-source voltage exceeds 3.7 V. Since the MOSFETs are alternately activated with 50% duty cycle, the maximum instantaneous current due to either wavelength of LED is 1.8 A. The circuit's rail voltage V_{CC} , is +6 V, thus the circuit requires a maximum continuous power of 10.8 W.

This circuit is intended exclusively for use in non-contact illumination. The outer metal case of the LEDs is electrically connected to the anode, thus for safety,

also produces a signal S' that is the inverse of S . The signal S is used to activate the 880 nm LEDs and the signal S' to activate the 760 nm LEDs. The 880 nm signal is also fed to an AND gate acting as a buffer, which drives an 880 nm indicator LED, the purpose of which is discussed below.

The camera is triggered by the clock signal after it has been fed through an AND gate. The gate serves two functions: first when connected as shown in Figure 5.6 it isolates the camera from fluctuations in the clock signal level; and second the connection from the AND gate to V^+ can be replaced by a connection to a master trigger step that synchronises the initiation of a capture sequence by the camera with a second device.

Figure 5.7 depicts the relative timing of the various signals. The response time of the camera, the LEDs, the transistors, the flip-flop, and the AND gates, are all of the order of microseconds, whereas a typical frame length is of the order of tens of milliseconds. Thus the response times of all the components are negligible compared to the duration over which a frame is integrated. In the event that a master control signal is required, to either initiate a capture sequence by the camera or to synchronise the system with another measurement device, the rising edge of the master control step acts as the initial trigger. During such operation, the clock signal AND the master control step signal, forms the trigger signal to the camera.

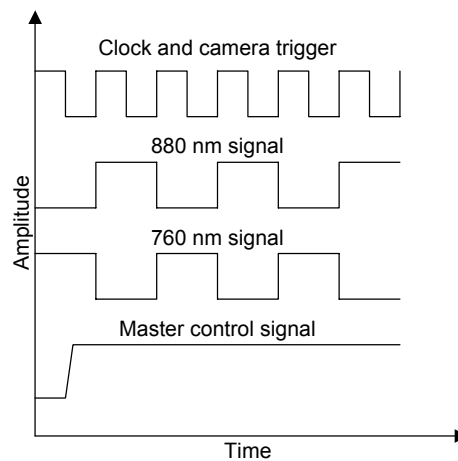


Figure 5.7 Relative timing of triggering signals to the camera, the indicator LED, and to both wavelengths of LEDs on the illumination array.

5.2.4 REPLICATING ASPECTS OF A CLINICAL DEVICE

In Section 3.3 several aspects of a conventional contact device's operation were emphasised; among them were: ambient light interference; compensation for the

variance in the peak emitted wavelength of LEDs; compensation for drift in peak emitted wavelength of LEDs caused by increased p - n junction temperature; obtaining maximum utility from the analogue to digital quantization process; and maintaining a sufficient signal level at the detector. These topics are revisited here and the practicability of the conventional contact device's countermeasures and solutions to each are evaluated in the context of the non-contact camera-based device.

5.2.4.1 AMBIENT LIGHT INTERFERENCE

Section 3.3.3.1 described the approach of clinical pulse oximeters to mitigating the effects of ambient light. This invariably comprises sampling the ambient light while the LEDs are off and subtracting the level from the adjacent samples during which the LEDs are on. The ratio of ambient samples to data samples and the sampling rate vary widely among manufacturers, though all clinical devices sample at a rate far greater than the frame rates achievable with a camera-based non-contact device.

The camera-based system's susceptibility to ambient light interference can however be mitigated to some degree by the inclusion of a bandpass filter. Figure 5.1 depicts such a filter placed directly in front of the camera's lens. The filter used is a Hoya RT830 near infrared glass band pass filter, centre wavelength 830 nm, half maximum pass band 570 nm to 1090 nm.

The inclusion of a dark frame in the camera-based system's sampling sequence is of course possible, however as will be discussed in Section 5.4, achieving the maximum possible frame rate is paramount to a camera-based device's accuracy—at least within the range of frame rates currently achievable.

5.2.4.2 VARIANCE IN LED PEAK EMITTED WAVELENGTH

Limitations of the manufacturing process cause the actual peak emitted wavelength of LEDs to differ from the design wavelength, even among components produced from the same lot. The accuracy of the technique of pulse oximetry is conditional on the use of two precisely known monochromatic wavelengths. In practice two narrow-band light sources with precisely known peak emission wavelengths suffice. Manufacturers compensate for inter-device variation in peak emitted wavelength by either selecting only LEDs with specific wavelengths or noting the actual

wavelengths and compensating for the discrepancy during the calibration process (see Section 3.3.1).

The non-contact technique requires multiple LEDs of both wavelengths to provide sufficient illumination. Thus the possibility of compensating for discrepancy in peak emitted wavelength between LEDs is precluded. The remaining—more costly—option for the non-contact device is ensuring each individual LED used has the correct peak emitted wavelength, for both wavelengths.

Figure 5.8 displays an overlay of the normalised emission spectra of the eighteen 760 nm LEDs used in the illumination array. (Measured using Ocean Optics Inc. S2000 spectrometer.) The vertical dashed line at approximately 758 nm indicates the mean peak emission wavelength.

Figure 5.9 displays the same data from the 880 nm LEDs. The mean peak emitted wavelength for the 880 nm LEDs is 858 nm.

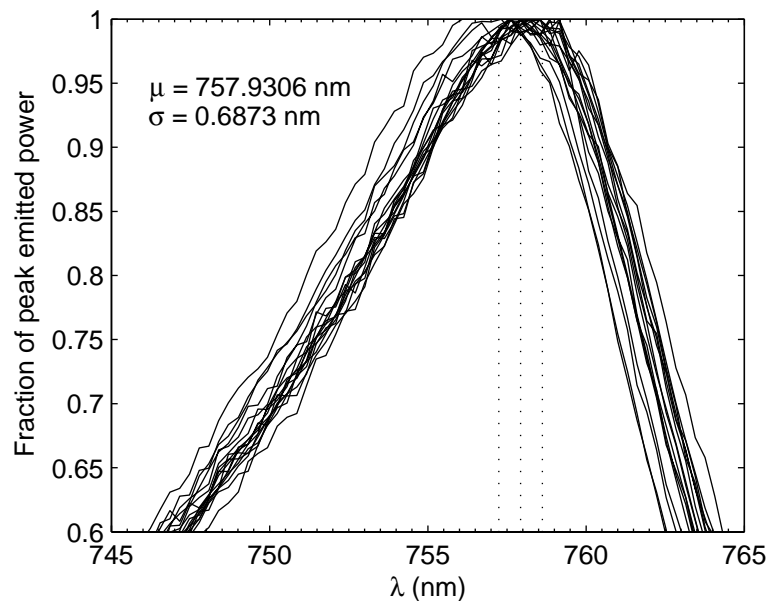


Figure 5.8 Normalised peak emitted wavelength of the eighteen 760 nm LEDs. (Mean peak emission wavelength 758 nm.)

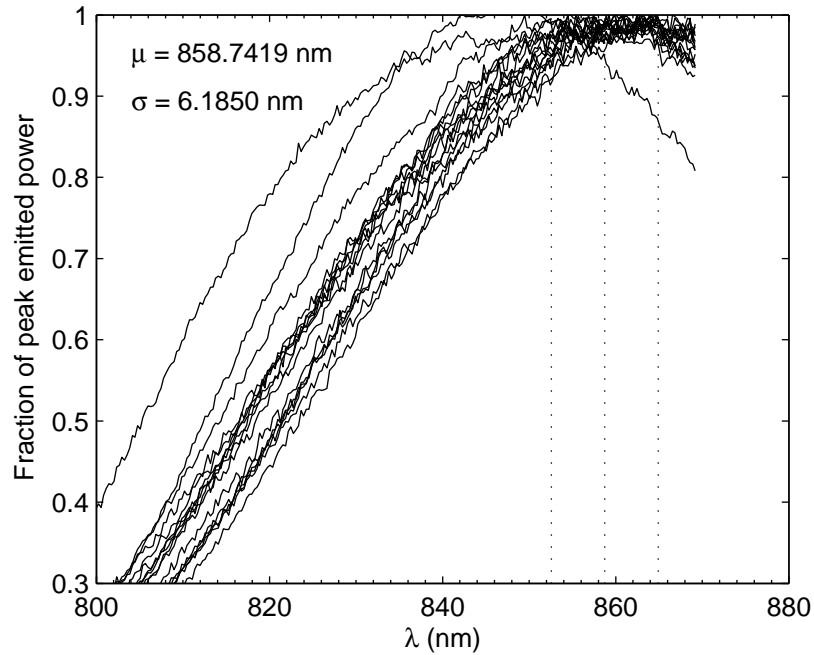


Figure 5.9 Normalised peak emitted wavelength of the eighteen 880 nm LEDs. (Mean peak emission wavelength 858 nm.)

In comparing the characteristics of the two types of LED, the 880 nm LEDs can be seen to exhibit a much greater deviation from their design wavelength as well as a greater variance in peak emitted wavelength between individual diodes than the 760 nm diodes. (Indeed the continued use of the label *880 nm* LED is questionable.) Owing to the profiles of the HbO₂ and Hb extinction curves (Figure 3.7), pulse oximetry is more sensitive to deviation in the peak emitted wavelength of the 760 nm LEDs; where the Hb curve exhibits a large inflection. Referring to Figure 3.7, the 2 nm deviation in peak emitted wavelength of the 760 nm LEDs would correspond to a change in the absorptivity of Hb and HbO₂ of +0.45% and -2.07% respectively. The 22 nm deviation in the 880 nm LEDs would correspond to a change in absorptivity of Hb and HbO₂ of -5.49% and -6.77%. Since it is the change in the ratio of absorption of the two haemoglobin species that is consequential, the 2 nm shift in the 760 nm LEDs would in fact be more detrimental to quantitative estimates of S_pO_2 than the 22 nm shift in the 880 nm LEDs.

5.2.4.3 DRIFT IN PEAK EMITTED WAVELENGTH

The causes of drift in peak emitted wavelength during operation were described in Section 3.3.1.2. Both ambient temperature and driving current affect the *p-n* junction temperature of the diode, altering the amount of additional energy required by an electron to cross the junction and hence altering the emitted wavelength.

To quantify the drift in peak emitted wavelength of the LEDs during operation, two sets of spectra were obtained. The first set was measured immediately after the array had been energised, at a driving current of 60 mA with a 50% duty cycle to each diode. The driving current was then increased to 110 mA and the spectra measured again after ten minutes of continuous operation at 50% duty cycle. The results are plotted in Figure 5.10. The 760 nm LEDs exhibited a shift in mean peak emitted wavelength of 3.5 nm and the 880 nm LEDs 0.7 nm. These observations are similar to those reported by de Kock et al. (1991).

Commercial pulse oximeters compensate for drift in peak emitted wavelength by either placing a temperature sensor in the probe or by monitoring the LED driving current. In either case the peak emitted (red and infrared) wavelengths' dependence on either parameter is predetermined and the appropriate calibration tables are chosen by the device during operation to match the current estimate of peak emitted wavelengths.

Either approach is applicable to a non-contact device, though as will be discussed in the next section, LED driving current need not be variable in the case of a camera-based system.

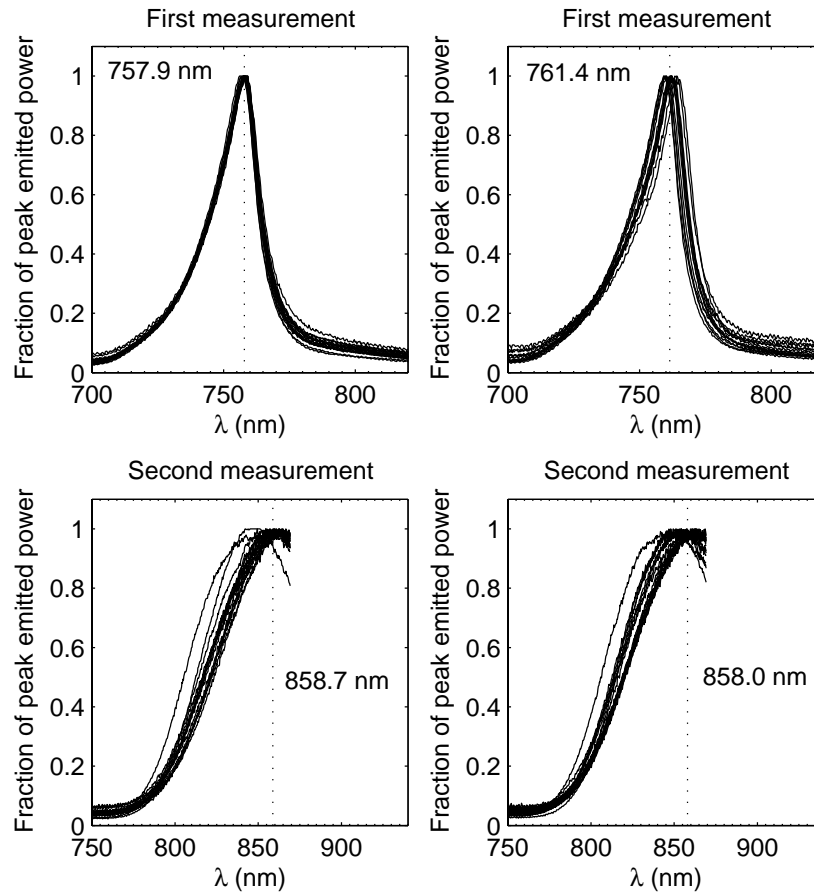


Figure 5.10 Drift in peak emitted wavelength of all LEDs on the illumination array after ten minutes at high driving current.

5.2.4.4 OPTIMISING PULSE SIGNAL LEVEL AND QUANTIZATION

At start up a conventional clinical pulse oximeter incrementally increases the driving current to the LEDs until a sufficient pulse signal is detected at each wavelength. This enables identical pulse oximeter probes to be used on the entire range of subjects, regardless of an individual's size or skin colour, and without ever saturating the photodiode detector. During operation the LED driving current is continually adjusted to maintain signal level and prevent saturation.

Control of the signal level in the camera-based system need not be limited to control of the light source. The combination of the digital camera and its optics form a highly configurable detector. While providing a constant illumination level, sufficient to detect signals across a broad range of subjects, saturation of the detector can be avoided by varying the lens aperture and the duration of the camera exposure. Amplification of weak signals is made possible by the CMOS chip's in-built circuitry.

Having obtained suitable pulse signals commercial devices also attempt to maximise the utility of the ADC process by removing the DC offset from the analogue signal prior to quantization (see Section 3.3.3.3). This makes the full quantization range available to encode the important pulse component of the received light intensity.

Since a camera produces a digital signal in response to a continuously varying light intensity, there is no opportunity to remove the resulting DC component prior to quantization by signal processing means. However the offset can be reduced somewhat by carefully varying the camera's lens aperture such that the mean received light intensity is just below the current intensity at the troughs of the PPG waveform (Wieringa, et al. 2005). If employed in conjunction with the sensor's onboard amplifier the technique has the potential to improve the quantization of the PPG signal.

In the experiments that are described below (Section 5.4) this technique is not employed however; since the base level of the PPG signal can vary significantly over relatively short observation periods, it would be necessary that the lens aperture be continuously varied to maintain the effect.

5.3 IMAGE ANALYSIS

Image analysis takes place offline using Matlab[®]. Successive frames of the tissue under investigation, illuminated alternately by light with wavelengths of 760 nm and 880 nm, are saved to a PC in Full Frame (uncompressed) Audio Video Interleave (AVI) media container format—the merits and demerits of which are discussed shortly. Image analysis comprises: separation of the multiplexed frames into two separate sequences of frames, one illuminated at 760 nm and one at 880 nm; and the division of each frame, from both sequences, into smaller rectangular regions apt to searching for PPG signals.

Synchronisation between the camera and the illumination array is maintained by means of an 880 nm indicator LED that pulses synchronously with the 880 nm LEDs on the array, with reduced intensity. The indicator LED is coupled to an optical fibre, the other end of which is positioned in a corner of the camera's field of view.

5.3.1 EXTRACTING AVI FILES

Since it is not required to play back the recorded video file the utilisation of the AVI format is an inefficient use of storage resources compared to a raw data format. The uncompressed or Full Frame AVI format stores each frame in *truecolor* format, in which three numbers are used to represent every pixel in a video frame. These numbers indicate the red, green, and blue colour intensities of that pixel. However the camera, being monochromatic, produces only one 8-bit number per pixel that represents the intensity of each pixel on a grey scale with 256 levels. The *truecolor* format triplicates the 8-bit number produced by the camera and saves it to each of the red, green, and blue fields of that pixel. Thus for a grey scale image, the *truecolor* format is three times as large as the raw data. For small numbers of frames, the AVI structure also produces a header chunk that is significantly larger than the collective size of the individual raw data headers, making AVI less than three times as efficient for small numbers of frames. For larger numbers of frames, the AVI format converges towards three times the size of the raw data. The advantage of the AVI format is that it collects all the data from a period of monitoring into just one file—rather than thousands of small files. At the start of image analysis only one of the identical red, green, or blue fields need be processed while the rest are discarded. This is simple matter of indexing in Matlab and need not add to the processing delay. So long as memory and storage space permit, the use of the AVI format in offline processing is not restrictive.

Figure 5.11 depicts the structure of the resulting frames. One of the red, green, or blue layers of each frame is selected, and by identifying the state of the indicator LED, *on* or *off*, the illumination wavelength of each frame is determined. The frames are then divided into two separate sequences for further processing. To decide whether the indicator LED is on or off, the mean value of intensity of that corner of the video is determined over ten frames. If the intensity of that region in any individual frame then exceeds a certain threshold, say $1.25 \times$ mean value, the indicator LED is determined to be on, and if it is less than a low threshold, say $0.8 \times$ mean value, the LED is determined to be off. If neither threshold is passed, the mean is recalculated using a different region of the video, or the thresholds moved closer together.

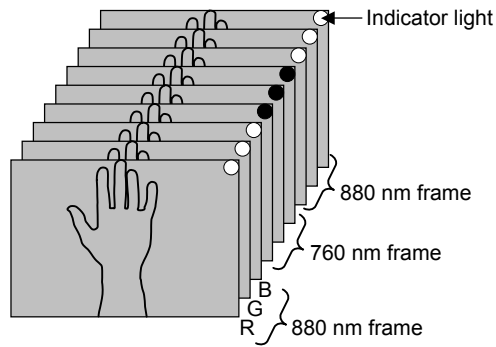


Figure 5.11 Depiction of the identical, red (R), green (G), and blue (B) layers of successive frames in the AVI file—only one of which need be selected per frame. The status of the indicator light indicates the wavelength at which the tissue was illuminated during that frame.

5.3.2 BOXES AND THEIR ANALYSIS

After generating a sequence of frames illuminated by the same wavelength, each frame is analysed by dividing it into boxes, or rectangular regions comprised of adjacent pixels. The mean values of these boxes are determined for every frame, and a matrix constructed such that each frame adds a new row to the matrix, while the mean value of each box within a frame resides in a column of the matrix. Thus a particular column of the matrix records the time-varying mean value of the pixels in a particular box, as they vary from frame to frame. Where backscattered light emerging from the tissue and captured by the camera, has traversed an artery, a PPG may be detectable. Where a PPG is detectable at both wavelengths, within the same box, over the same period of time, the prerequisite for pulse oximetry is met. Figure 5.12 depicts a sample PPG signal obtained in this manner during an early trans-illumination experiment at one wavelength (805 nm).

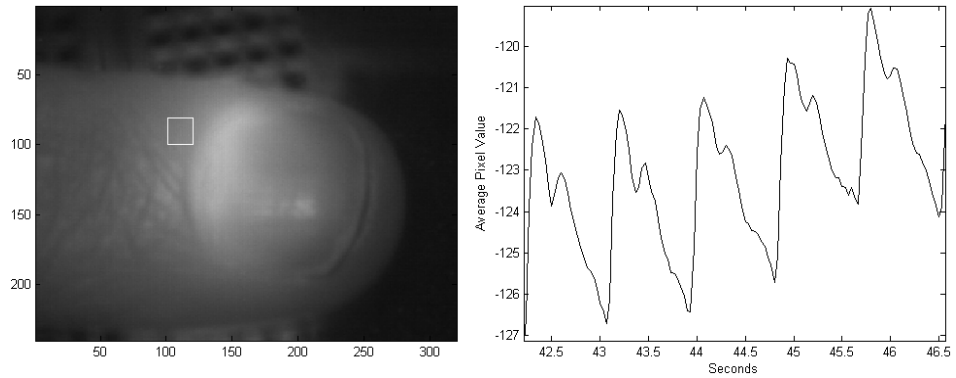


Figure 5.12 Sample PPG obtained by transmission illumination of the index finger at 805 nm. The white square of dimensions 20×20 pixels in the left image indicates the area of the video where the signal was observed. (Note the PPG signal has been inverted.)

5.3.3 IDENTIFYING PPG CONTAINING REGIONS

A PPG signal can be observable in a single pixel or in the sum or average of a group of pixels. Regardless of the area of the region of interest (ROI) most ROIs in the video frame will not possess a strong PPG signal at both wavelengths (some portions of the video will contain the indicator LED signal and some others may not be displaying tissue). It is desirable to have an automatic means of identifying ROIs with strong PPGs at both wavelengths. Two methods of identifying PPG containing ROIs were used during this study; both assume the average pulse rate during the observation window is known, either from a second device or from pre-processing.

The first method takes the signal from each ROI and identifies all the inflection points. This can be efficiently achieved by differencing adjacent samples of the signal x to form an approximate derivative \dot{x} ,

$$\dot{x}[n] = x[n+1] - x[n]. \quad (5.6)$$

Each place where the sign of $\dot{x}[n]$ differs from the sign of $\dot{x}[n+1]$ signifies an inflection point at the n^{th} sample. The number of these inflection points is counted. Referring to Figure 5.12, a PPG signal free from noise and other artefacts has four inflection points per pulse (or two per pulse if the dichrotic notch is not visible in the waveform). When the number of counted inflection points per second is within a certain threshold of four times the pulse rate, that ROI is deemed to contain a PPG at that wavelength. Noisy signals have many more inflection points and are rejected.

Though this method is simple, it is computationally efficient and is not prone to false positives. Figure 5.13 displays an image of the index and middle finger from the right hand of twenty-six year old male subject. Each finger is trans-illuminated by an 805 nm LED. Superimposed on the frame are 20×20 pixel ROIs in which PPG signals were detected using the inflection point method (from Humphreys et al. (2005a)).

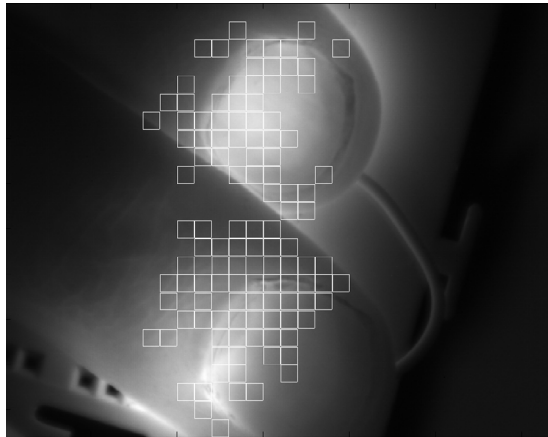


Figure 5.13 ROIs containing PPG signals identified by the inflection point method.

The inflection point method is however susceptible to false negatives in the presence of noisy signals. As such it is most suited for use with transmission illumination schemes.

PPG signals at multiple wavelengths, obtained in a multiplexed fashion, from deep tissue, and in a non-contact reflection geometry, are weaker, sampled at a lower rate (because of both multiplexing and the need for a longer exposure time), and are consequently less well defined than that depicted in Figure 5.12. To identify ROIs containing PPG signals in such videos a simple spectral method was developed and employed during this study.

A matrix containing the time-varying signal from each ROI is constructed as described in Section 5.3.2. The mean value of the signal from each ROI is subtracted to remove the DC offset and its Fourier spectrum calculated. A region of the spectrum is defined from 0.2 Hz up to 1.9 times the pulse rate (in Hertz), which excludes the low frequency Mayer wave and vasomotion, and the first harmonic of the pulse frequency. Within this region a smaller region is defined from 0.5 times the pulse rate up to 1.5 times the pulse rate that allows for pulse rate variability over the observation window. A figure of merit is then calculated for each ROI, defined as the area under the Fourier spectra in the smaller pulse-rate-centred region, divided

by the area under the Fourier spectra in the larger region. The process is depicted in Figure 5.14, which shows data from a thirty-three year old male subject with a mean pulse frequency of 1.2 Hz (72 pulses per minute).

Figure 5.14 depicts a portion of the Fourier spectrum indicating the two previously defined regions (top plot). The figure of merit is calculated as the area of the black portion divided by the sum of the areas of the black and grey portions. The figure of merit for all ROIs is plotted in the bottom plot of Figure 5.14, with a circle marking the merit value for this example. The middle plot shows the PPG signal associated with this ROI.

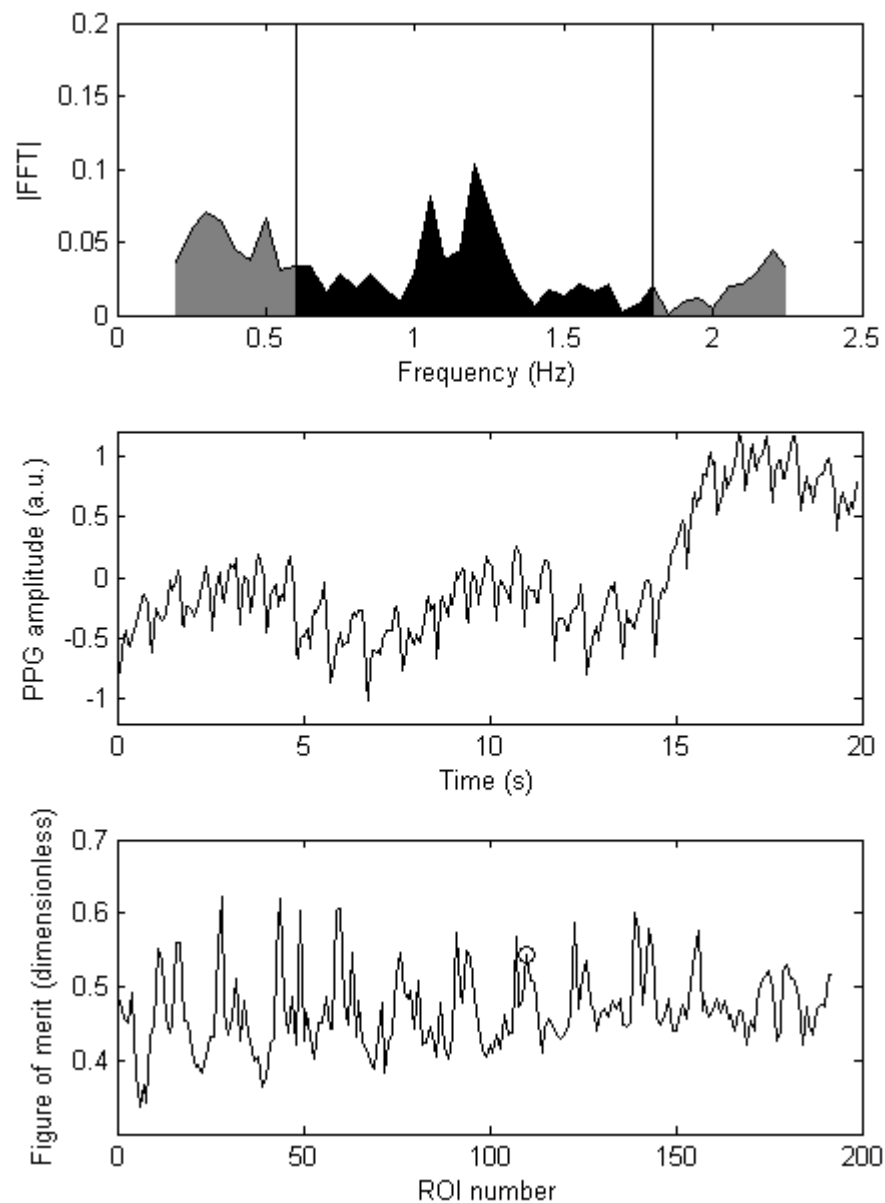


Figure 5.14 Spectral method of identifying ROIs containing PPG signals—depicting a good PPG signal.

Figure 5.15 depicts the spectrum, figure of merit, and resulting PPG from an ROI with a poor associated figure of merit. In this instance though a small component is visible at the pulse frequency in both the time-domain and the frequency-domain, in both domains the signal exhibits greater energy at predominantly lower frequencies.

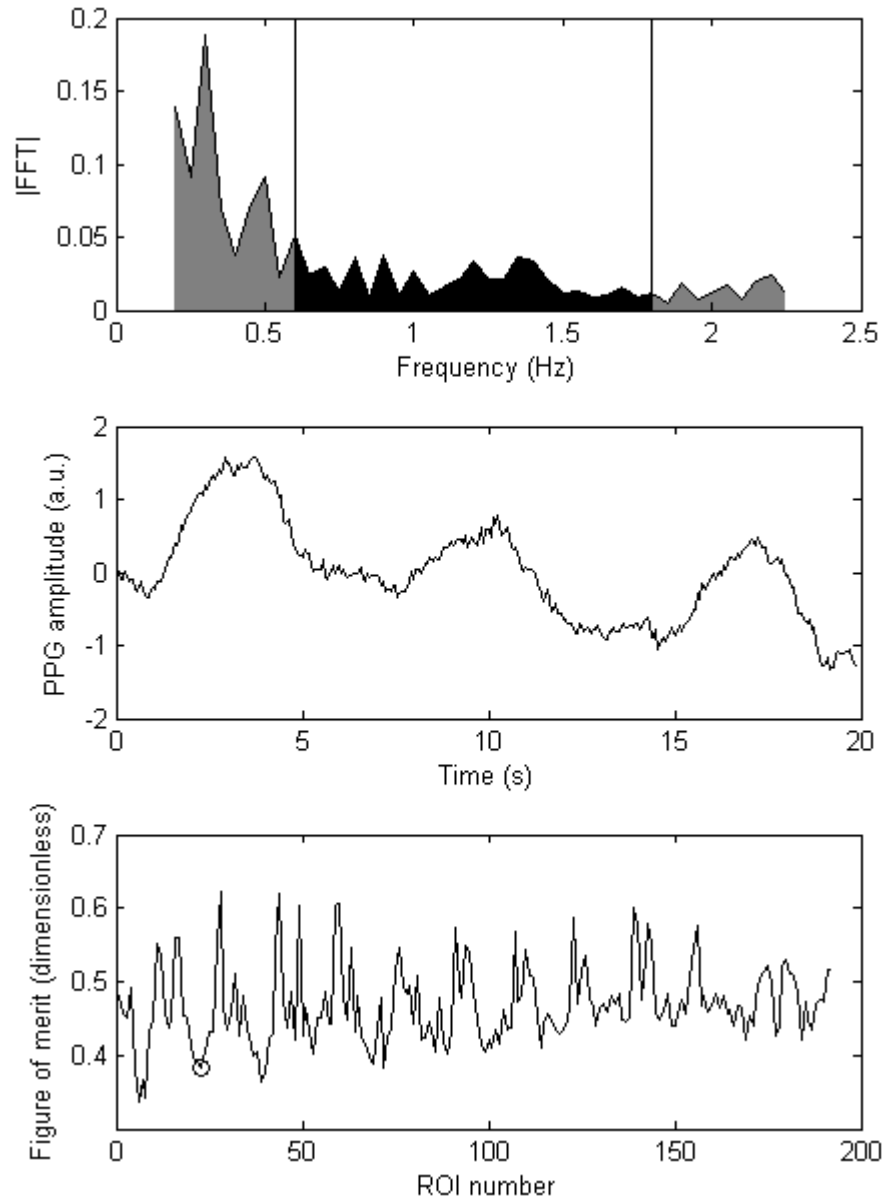


Figure 5.15 Spectral method of identifying ROIs containing PPG signals—depicting a poor PPG signal.

ROIs with strong PPG signals tend to be spatially grouped in certain regions of the video frame (discussed later in Section 5.5). Thus the figure of merit from each ROI, when converted to a 1D vector from its 2D matrix form, exhibits a periodicity that corresponds to the spatial location of signal containing ROIs. The decrease in

magnitude of the figure of merit with increasing ROI number in Figure 5.14 and Figure 5.15, is a result of increasing distance from the light source and the concomitant decrease in received light intensity.

Neither of these methods is suited to a real-time implementation—the former being too susceptible to false negatives in the presence of noise and the latter being too computationally intensive—they are however well suited to off-line processing of videos. The task of quickly and accurately identifying ROIs is key to a real-time implementation and is deserving of further investigation.

5.4 TESTING AND PERFORMANCE OF DEVICE

This section describes the apparatus and experimental protocol used to test the non-contact device. For the non-contact device to provide an acceptable substitute for a conventional device in any application, it must provide comparable measurements to a conventional device. *Comparable*, from a clinical perspective means that decisions regarding the management and treatment of a patient would not alter depending on the instrument used to assess the patient. For the case of a pulse oximeter, the three primary indicators of a patient's health provided by the device are the patient's arterial oxygen saturation S_pO_2 , the patient's pulse rate, and a display of the patient's peripheral arterial pressure waveform—a PPG. Collectively these parameters are used to assess the effectiveness of the patient's cardio pulmonary system, the oxygen content of the arterial blood being indicated by the S_pO_2 value, and the combined effectiveness of the cardiac pump and arterial delivery system, being indicated by the pulse rate and PPG waveform (see Chapter 3). Any novel non-contact pulse oximeter should provide comparable measurements of all of these parameters. Furthermore though a non-contact device will undoubtedly be subject to extra constraints by virtue of its position, remote from the tissue under investigation, the device should nonetheless be capable of obtaining measurements from a broad subject base and under realistic operating and environmental conditions.

5.4.1 EXPERIMENTAL PROTOCOL

Experiments were conducted using ten informed subjects (ten Caucasian, nine male, and one female) aged between 21 and 45 years (mean 31.70 years and

standard deviation 6.37 years). Subjects were seated in an upright position with their right arms resting, volar side upwards, on a cushioned bench. A conventional reflection mode PPG sensor with a wavelength of 805 nm (BioPac UIM100C) was connected to the subjects' right index fingers. A conventional contact pulse oximeter (Nellcor 660 nm/940 nm probe – Welch Allyn device) was connected to the subjects' left index fingers.

The camera was positioned and focused manually such that an area of the volar side of the forearm close to the wrist was occupying most of the image. The LED array was positioned so as to illuminate an area on the proximal side of the imaged area, at a distance of approximately 15 cm from the tissue surface. Figure 5.16 illustrates the relative position of the illuminated and imaged area. Overhead fluorescent lighting was present during all of the experiments (mains supply 50 Hz).

Over several sets of preliminary experiments on small numbers of test subjects, using both the system described here and variations of the system (described in Humphreys et al. (2005a; 2005b; 2005c)), PPG signals were captured from various parts of the body surface. Reflection mode PPG signals were obtained from the sole of the foot, the palm of the hand, the fingertips, the ankle, the forearm, and the neck. The forearm was chosen as the region of interrogation for this experiment because of the ease with which the apparatus can be repeatedly positioned to obtain similar measurements from multiple test subjects of varying physical size. Whilst other observation sites on the body and are undoubtedly of interest, as are other observation positions, for example a reclined and supine position, observing the forearm in a seated position represents a more practical and comfortable protocol from the point of view of the volunteers, given the decidedly experimental rather than clinical environment in which the experiments took place.

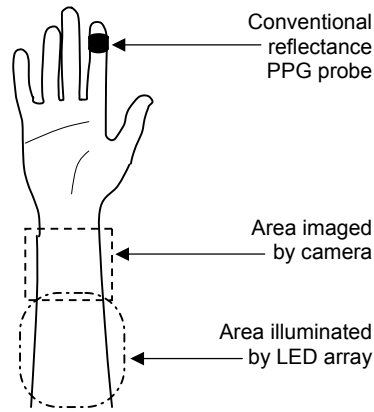


Figure 5.16 Relative position of the imaged and illuminated regions of tissue.

Once stable and normal pulse rate and S_pO_2 readings were indicated by the pulse oximeter, a trigger was sent to the camera-based system and the PPG data acquisition system, simultaneously initiating a 20 s capture of data by both devices.

The camera was configured to capture 640 frames, at resolution of 640×480 pixels, with a 20 ms exposure time. The camera was triggered externally at a rate of 32 frames/s (refer to the maximum achievable frame rate data in Table 5.1). The LED array was correspondingly switched at 16 Hz (see Figure 5.7).

The LED array was activated for several minutes prior to each experiment to allow the LEDs reach their stable operating temperature and wavelength (see Section 5.2.4 for timing signals).

All subjects were asked to sit motionless and to breathe normally during the experiments.

5.4.2 DISPLAYING A PPG

Early commercially available pulse oximeters used in clinical monitoring incorporated an electro cardiograph (ECG)—as do many patient-monitoring suites available currently. Though the pulse period could be and indeed was estimated from the PPG waveform, the heart rate was also calculated from the distinctive R-peak of the QRS complex of the ECG waveform. Both of these measurements of heart rate were displayed and users often employed a rule of thumb: the displayed S_pO_2 values should only be relied upon if the heart rate indicated by the electrical ECG signal and the pulse rate indicated by the PPG signal were within one to two beats per minute of each other (Wukitsch, et al. 1988). This rule of thumb served to

alert users of instances where a PPG signal was poor; likely due to probe placement but possibly due to a serious deterioration in the patient's condition; pulse oximetry requires only a weak pulsatile signal rather than a pulse to produce some S_pO_2 value, though it is likely erroneous in the former case.

The need for an extraneous corroboration of the validity of the pulse signal, on which the S_pO_2 values are based, is obviated if the device is capable of displaying the arterial pressure waveform on which it is currently basing its calculations. Thus, by a pulse oximeter displaying a PPG waveform, the experienced user can evaluate the validity of the current pulse rate and S_pO_2 values.

In addition, the displayed PPG trace gives the user a quick indication of the cardiac rhythm and of any changes in its regularity. When the PPG trace is not normalised, it will indicate any sudden changes in cardiac output or hypovolaemia.

Furthermore, the shape of the peripheral arterial pressure waveform, and notably the prominence of the dichrotic notch, can provide diagnostic information about the health and compliance of the vasculature (Joyce, et al. 1990).

For these reasons it is important that the camera-based device be capable of capturing a suitable PPG signal. (Separate to the pursuit of pulse oximeter functionality the ability to capture spatially resolved PPGs is important to the device's independent investigative capabilities.)

Figure 5.17 displays non-contact PPG signals captured at 760 nm and 880 nm by the remote camera-based system, and also a contact PPG signal captured using a finger probe at 805 nm (200 Hz sampling rate).⁹ The signals were captured from a 45-year-old male test subject imaging an area similar to that depicted in Figure 5.16 with a tissue-camera separation of approximately 30 cm. Note that although clear pulses are visible, the dichrotic notch is not well defined in either of the non-contact signals, and not discernable in the contact signal. For this subject, a 0.5 Hz high pass filter has been applied to the contact PPG signal, while the non-contact PPG signals are the result of the image analysis described in Section 5.3.2 only, to which no further signal processing has been applied.

⁹ The non-contact PPG signals in Figure 5.17 and Figure 5.18 have been orientated such that their amplitude is proportional to light absorption rather than received light intensity. The contact device utilises this format by default—the non-contact signals are orientated such for ease of comparison only.

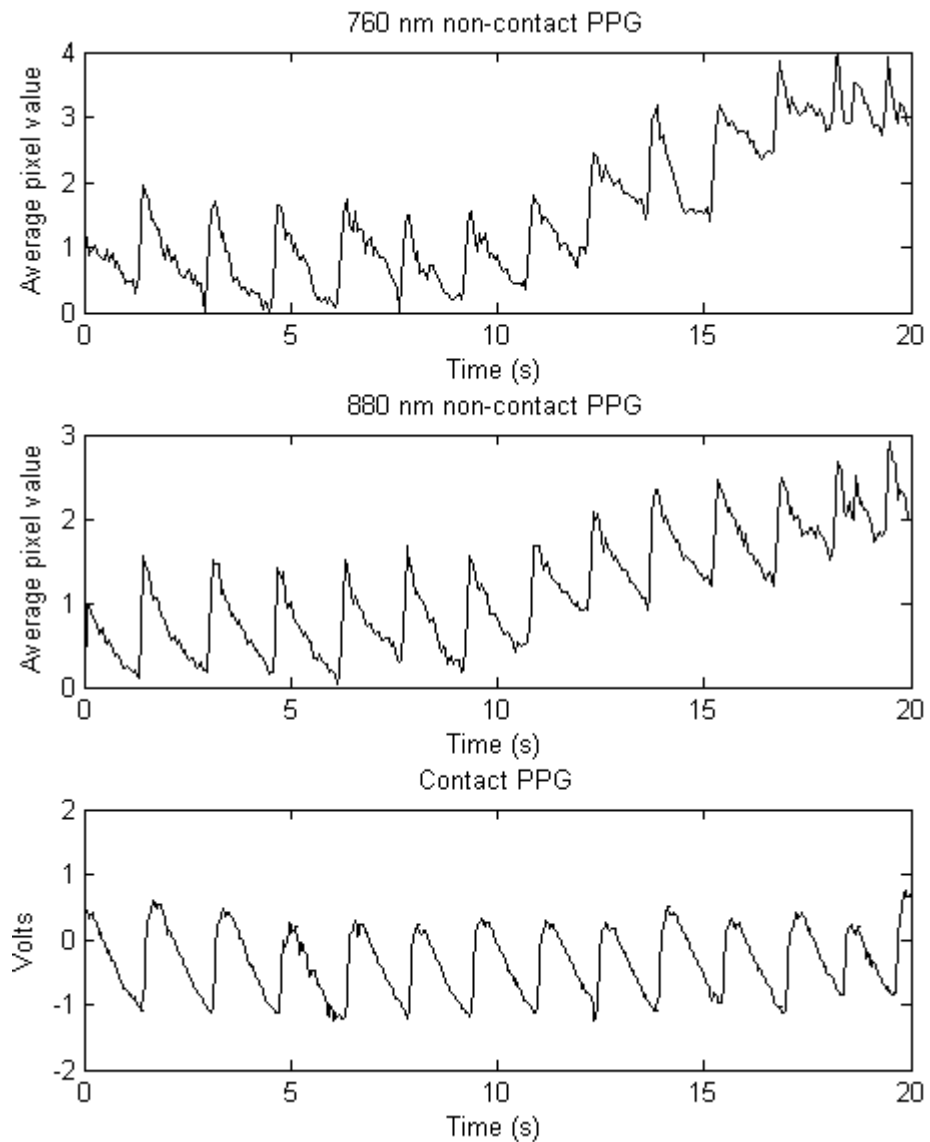


Figure 5.17 PPG signals captured simultaneously by the camera-based, non-contact device at 760 nm and 880 nm, and from the conventional contact probe (on the finger) at 805 nm, from a 45-year-old male test subject.

Figure 5.18 displays the same data captured from a 21-year-old male test subject, in which the pulses complete with dichrotic notch are clearly visible in all three signals. The contact PPG signal, for this subject, is unfiltered. The non-contact PPG signals again, represent the output of the image analysis described in Section 5.3.2.

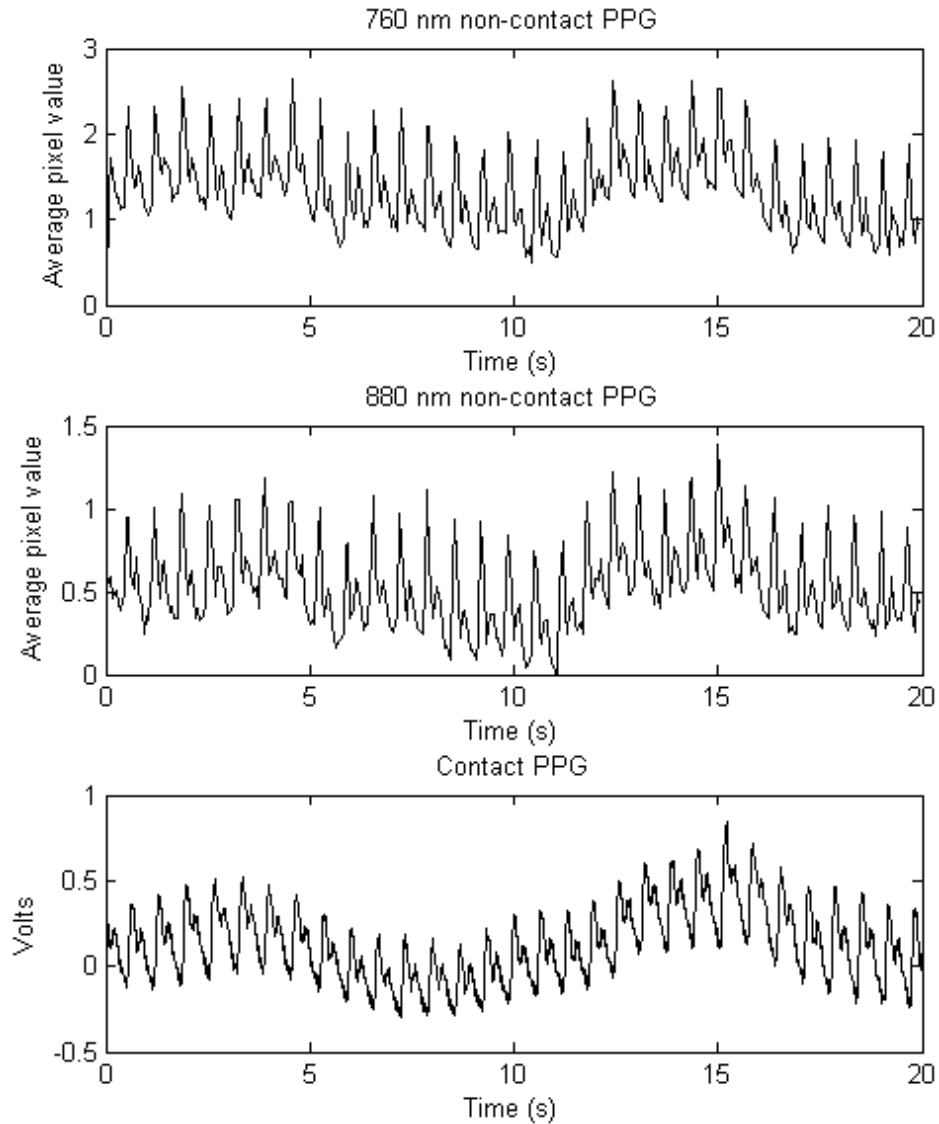


Figure 5.18 PPG signals captured simultaneously by the camera-based, non-contact device at 760 nm and 880 nm, and from the conventional contact probe (on the finger) at 805 nm, from a 21-year-old male test subject.

In addition to the pulse component, a lower frequency oscillation can be seen in the PPG signals (except the high pass filtered contact PPG in Figure 5.17). This component is partially due to respiration. The component is more clearly visible in the frequency domain. Figure 5.19 displays the Fourier spectra of the PPG signals plotted in Figure 5.18. The component due to respiration can be seen in each of the spectra as a peak at 0.35 Hz, prominent in both the camera PPG signals, though less so in the contact signal. The pulse component is visible as the distinctive peak at 1.5 Hz and its first harmonic can be seen at 3 Hz. The low frequency Mayer waves

and vasomotion can be seen between 0 Hz and 0.1 Hz¹⁰ (it is particularly evident in the time-domain contact PPG plot as the smooth undulation with a period slightly longer than 10 s in Figure 5.18).

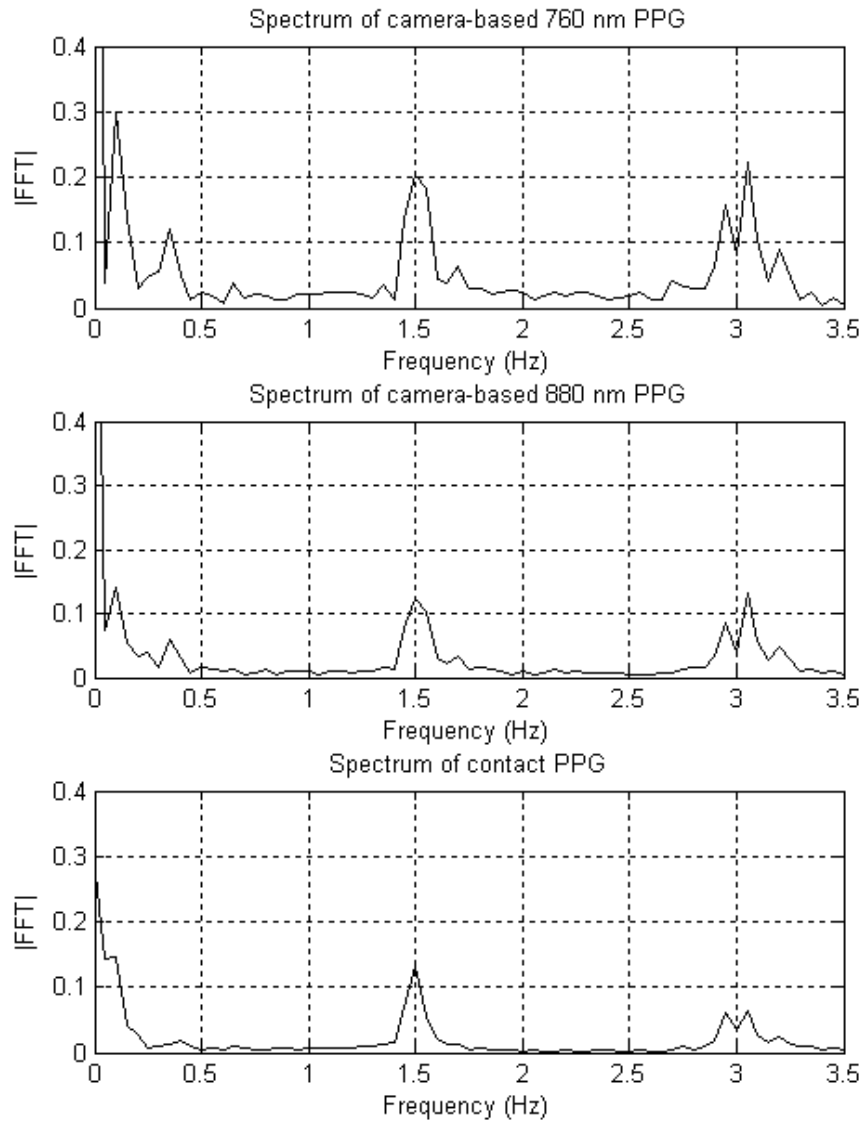


Figure 5.19 Fourier spectra of the PPG signals plotted in Figure 5.18, from a 21-year-old male test subject.

5.4.3 MEASURING PULSE RATES

The next important purpose of a commercial pulse oximeter is to measure the pulse rate, a vital sign (Mower, et al. 1998; Mower, et al. 1997). In Section 5.4.2 reference

¹⁰ The Mayer waves are oscillations in arterial pressure at frequencies lower than respiration that are coupled with the activity of the sympathetic nervous system (Julien 2006). Vasomotion refers to small and slow changes in vascular diameter generated within the vascular wall. Though both phenomena are well documented their respective physiological causes remain elusive.

was made to early clinical devices that incorporated an ECG. The ECG signal can provide a measurement of *heart rate*, while a pulse oximeter—utilising a photoplethysmograph—provides a measurement of the *pulse rate*. These two parameters should agree closely, but may vary a little, since the rate at which pulses pass by a sensor in the peripheral arterial vasculature is affected by the transit time, the compliance of the vasculature, and the musculature that lies between the probe site and the heart. The need to ensure close agreement between the ECG indication of heart rate and the pulse oximetry indication of pulse rate, as an indication of the validity of S_pO_2 values, was ultimately obviated by the incorporation of a plethysmographic display. It is thus necessary to ensure that a measure of pulse rate provided by the non-contact device agrees sufficiently closely with that produced by the conventional contact plethysmogram, that the two devices can be used interchangeably for this purpose.

A useful method of assessing the agreement between two devices or techniques is the Bland-Altman method (Altman and Bland 1983; Bland and Altman 1986). The Bland-Altman method is a particularly popular tool for assessing agreement between two clinical devices, where both devices exhibit a certain amount of measurement error.¹¹ It is preferable to other commonly employed methods, for example Student's *t-test*, in that it is fundamentally a graphical method, which can compare the accuracy, precision, and bias between two devices or methods, without requiring assumptions to be made about the normality of the data's distribution. Indeed insufficient data are available here to reliably ascertain the normality of their distribution by usual means (for example a Shapiro-Wilk or Kolmogorov-Smirnov test). The Bland-Altman method is to be preferred to the use of a correlation coefficient, as it inherently identifies bias between the devices.

To obtain a pulse rate measurement for each of the test subjects over the 20 s observation window, the Fourier spectra of the contact, and 760 nm and 880 nm non-contact, PPG signals were calculated and the peak frequency of the cardiac component noted. Figure 5.20 shows a scatter plot of the pulse rate measurement from the conventional contact finger probe, versus the measurement from the camera-based non-contact device. The non-contact 760 nm measurements are

¹¹ On a serendipitous note: the second paper Bland and Altman published on this method (1986)—which appeared in the *Lancet* and can be credited with bringing the technique to the attention of the clinical community—assessed, as an example, the agreement between the *new technique* of pulse oximetry and the established CO-Oximeter, as a means of determining arterial oxygen saturation.

plotted as circles and the 880 nm measurements as crosses. Where the circles and crosses align the non-contact measurements agree at both wavelengths for that subject. Also plotted in Figure 5.20 is the line $x = y$, where data points lie along this line, there is perfect agreement between the two devices. Deviation from the line indicates disagreement, an underestimation of pulse rate by the non-contact device when the plotted point is to the left of the line, and an overestimation when the point is to the right of the line.

It is worth noting that the measurements by the two devices will be perfectly correlated if the points in the scatter plot lie along *any* straight line; only along the line $x = y$ however, do the two devices agree.

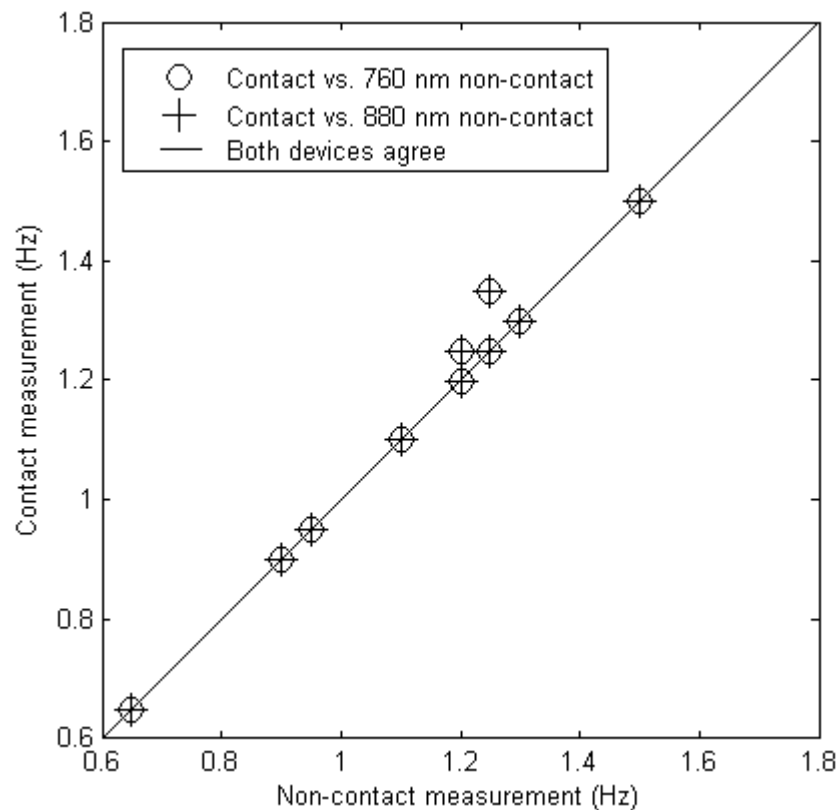


Figure 5.20 Scatter plot showing the non-contact device's measurement of pulse rate at two wavelengths, versus the contact device's measurement, for each subject. Also plotted is the line $x = y$, where both devices are in perfect agreement about the measurement. From Humphreys et al. (2007).

Examining Figure 5.20 it can be seen that for eight subjects, both devices are in perfect agreement. However, for two subjects the non-contact device recorded a lower pulse rate than the conventional device. Since the two devices are in agreement for higher, intermediate, and lower pulse rates, and since both devices

agree for other measurements in this range, it is reasonable to presume that the disagreement for these two subjects is not systemic to either device.

Having established that both devices produce largely agreeable pulse rate measurements over the range of pulse rates exhibited by the test subjects, it remains to establish if the two devices agree sufficiently closely that one device is substitutable for the other in making clinical measurements. This can be assessed using a Bland-Altman plot and analysis.

Figure 5.21 is a Bland-Altman plot, showing the mean of the measurements by the two devices on the horizontal axis, versus the difference between the measurements by the two devices (contact – non-contact) on the vertical axis.

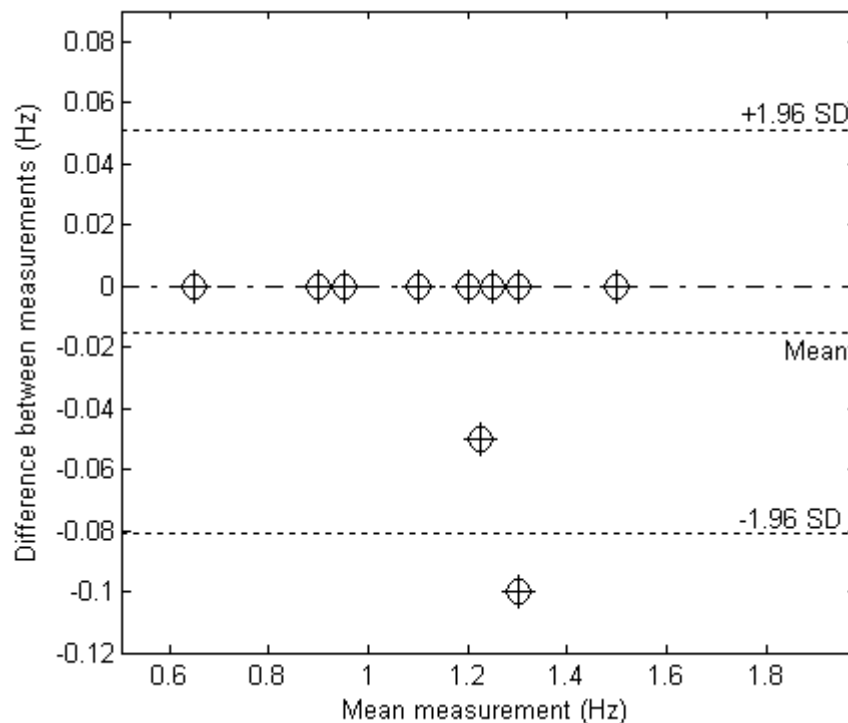


Figure 5.21 Bland-Altman (mean versus difference) plot showing the mean pulse rate measurement by the two devices versus the difference between their measurements. Non-contact measurements at 760 nm are plotted as circles and 880 nm as crosses. Also shown are the mean (-0.0150 Hz) and ± 1.96 standard deviations (0.0337 Hz) about the mean. From Humphreys et al. (2007).

The utility of the Bland-Altman plot is that unlike the scatter plot, it displays disagreement between the two devices as a vertical displacement from the mean measured value of the parameter—which is unknown; the mean of the two measurements is the best available estimate. The mean value of the difference between the two devices is -0.0150 Hz and the standard deviation is 0.0337 Hz. If

the two devices exhibited greater disagreement, Figure 5.21 would make any bias plainly evident.

Assuming that the mean difference between the devices is normally distributed, the 95% confidence interval can be calculated as ± 1.96 standard deviations. (It would take several more samples to establish if the difference is normally distributed; a histogram would quickly show that these samples are not.) Converting the 95% confidence limits from Hertz to pulses per minute, the non-contact camera-based device should be expected to provide a measurement of pulse rate that is within 4.8687 pulses/minute above or 3.0687 pulses/minute below the contact device, for 95% of measurements. This is sufficiently close that the two devices could be used interchangeably, since an indicated pulse rate 5 pulses/minute above or 3 pulses/minute below the estimation of a currently accepted clinical monitoring device, would not affect decisions regarding patient management (Humphreys, et al. 2007).

In practice the pulse period can vary significantly from pulse to pulse, and pulse oximeters use a weighted moving average of the peaks of the PPG waveforms to calculate the displayed pulse rate (Wukitsch, et al. 1988). The use of the peaks of the Fourier spectra in the above analysis has the effect of averaging the individual pulse periods. This does not invalidate the analysis—the analysis is applied to the contact and non-contact device alike—though it limits the number of sample points on which the analysis is based to ten (the number of test subjects). It also limits the range of pulse periods across which the two devices are compared, since the variance in pulse rate of healthy resting adults is conceivably less than the variance in the pulse-to-pulse period of an individual.

To analyse the comparability of the contact and non-contact devices in this regard, the data pertaining to two test subjects were selected. Figure 5.17 and Figure 5.18 depict the slowest and fastest recorded pulse rates among the test subjects respectively. The data from these subjects were further processed to determine the pulse periods of corresponding pulses as measured by the contact device and the camera-based device, at both 760 nm and 880 nm. The pulse period was measured as the distance between adjacent systolic peaks. Analysis of the data pertaining to the two subjects exhibiting the maximum and minimum values of the parameter of interest should identify any relationship that might exist between the bias of the measurement and the value of the measured parameter.

Figure 5.22 depicts a Bland-Altman plot of the contact device’s measurement of pulse period versus the non-contact device’s measurement at 760 nm. Intuitively, it might be expected that the measurements exhibit greater disagreement at higher pulse rates—since the camera achieves a comparatively low 16 samples per second compared to the contact devices 200 samples per second. The analysis shows the opposite trend—disagreement between the contact and non-contact devices increases with increasing pulse period. Figure 5.23 shows that the non-contact measurements at 880 nm exhibit the same trend.

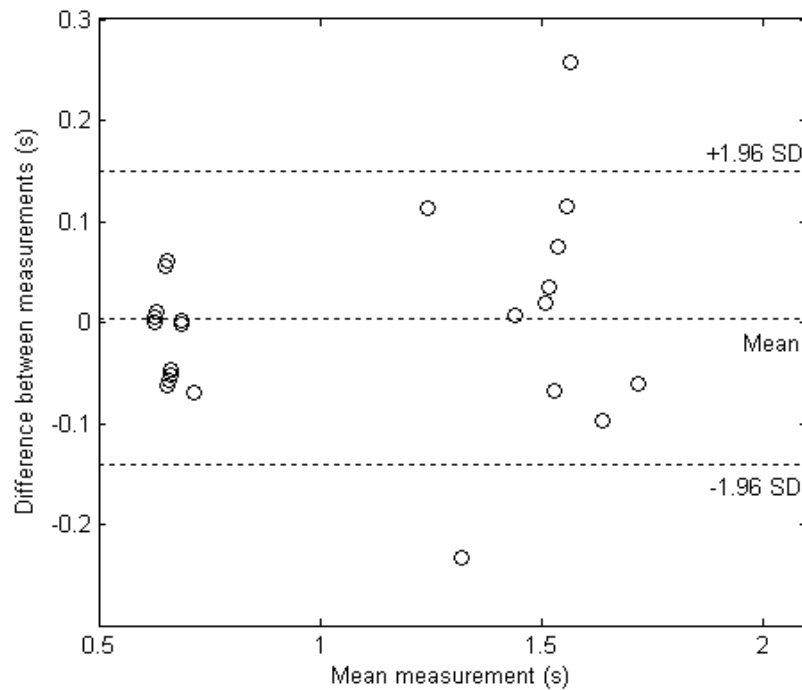


Figure 5.22 Bland-Altman plot of the contact device’s measurement of pulse period versus the non-contact device’s measurement at 760 nm. The data pertain to the two subjects that exhibited the fastest and slowest pulse rates during the experiments. (Mean 0.0043 s and standard deviation 0.0742 s.)

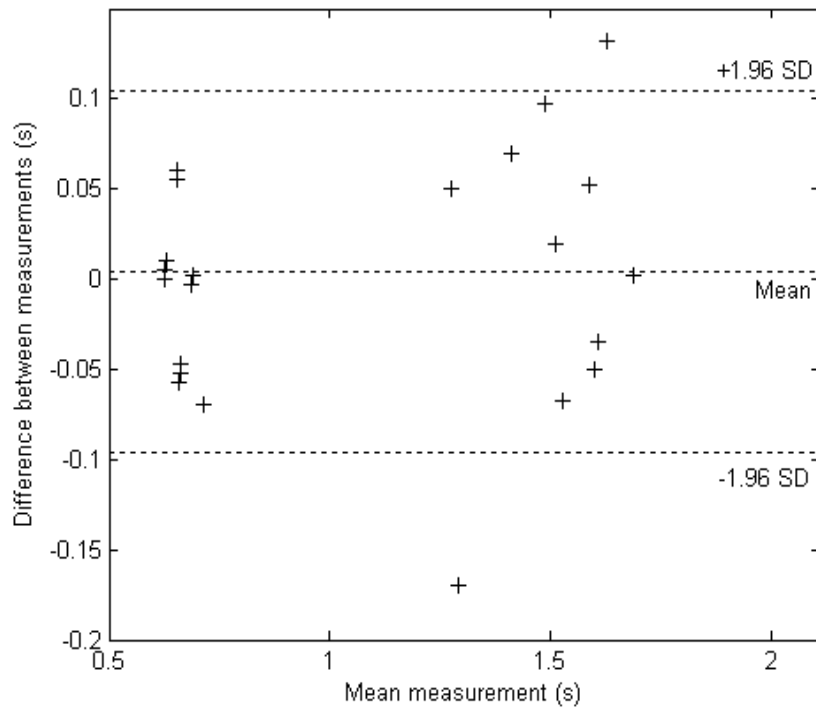


Figure 5.23 Bland-Altman plot of the contact device's measurement of pulse period versus the non-contact device's measurement at 880 nm. (Mean 0.0043 s and standard deviation 0.0510 s.)

For pulse period measurements at 760 nm, the 95% confidence interval is between +0.1497 s and -0.1411 s. (For 880 nm it is +0.1043 s and -0.0957 s.) If this magnitude of disagreement were present between the conventional and camera-based devices, for every pulse measurement, the resulting difference in the reported pulses per minute, for a subject with a pulse rate of 72 beats per minute, would be 63.9931 – 86.6760 beats per minute. This is a significantly greater level of disagreement between the conventional and camera-based technique than was suggested by the analysis of the Fourier spectra measurement of all subjects' pulse rate. With this level of disagreement between the two devices, they could likely not be considered comparable from a clinical perspective. However, some caution should be exercised when interpreting these results.

The disagreement between the devices for large pulse periods is likely a result of the differences in the shape of the contact and non-contact PPG waveforms for this subject (refer to Figure 5.17). The non-contact PPG signals each display pulses in which the systolic peak is consistently to the left of the pulses, which have a sharp profile. The contact PPG signal for this subject exhibits pulses with a more curved profile, on which the position of the systolic peak varies a little from pulse to pulse—in addition to the normal pulse period variation. In addition to being obtained by two different methods, the contact and non-contact PPG signals were

captured from different locations. The effects of probe location on the shape of the PPG waveform and its affect on pulse oximetry were discussed in Section 3.4.1.3, while the combined effects of low sampling rate and camera-based detection on the PPG waveform are the subject of the next section.

There is also a positive aspect of the pulse period analysis that deserves mention. Referring again to the Bland-Altman plots depicted in Figure 5.22 and Figure 5.23, it can be seen that the measurement difference between the two devices does not exhibit a static bias or a varying bias across the pulse period's range. This bodes well for the inherent accuracy of the camera-based technique compared to the contact technique—that is the measure of systemic error or bias. The absolute mean error of the camera-based device is small (0.0150 Hz and 0.0043 s), and correct to four decimal places, both wavelengths yielded the same mean error in both analyses. The standard deviation of the measurement differences from both analyses can be interpreted as an indication of the precision of the non-contact technique compared to the contact technique—that is the degree of reproducibility of the measurements. The analysis of the pulse period measurements suggests the camera-based technique to be less precise for low pulse rates, though as mentioned the shape of the non-contact PPG waveforms likely bear some culpability for this precision. In general, the precision of the system can be improved by higher sampling rates (yielding greater time resolution) and a camera with higher dynamic and quantization ranges.

5.4.4 DERIVING SPO₂ FROM A CAMERA-BASED DEVICE

As discussed in Section 3.2 pulse oximeters estimate arterial oxygen saturation S_pO_2 , by means of an interim variable R_{OS} , the ratio of arterial absorption at two wavelengths, obtained from the PPG waveforms, and then employ empirically derived calibration curves to convert R_{OS} to S_pO_2 . The procedure and apparatus of in vivo calibration and the principle of in vitro calibration were described in Section 3.3.5; both in vivo and in vitro calibration are beyond the purview of this research; this thesis instead focuses on evaluating the suitability of non-contact photoplethysmography to existing calibration methods. In addressing the suitability of non-contact PPG signals for use with existing methods of determining R_{OS} (see Section 3.2.2) two points about camera-based systems should be noted. They are the effects of low sampling rates and the integrative effect of camera-based sampling of waveforms (Humphreys, et al. 2007).

Pulse oximeters typically sample at hundreds of Hertz, allowing over 100 samples per second per wavelength, as well as the sampling of ambient light levels. Camera-based systems will likely never enjoy these frame rates, however at low frame rate (Wieringa et al. (2005) reported frame rates as low as 6.7 frames/s) the error in estimating the instantaneous amplitude of the PPG waveforms can be significant. This is especially true of the *peak and valley* method (Section 3.2.2.1) where sampling before or after the true peak or troughs in the waveform yields a smaller peak-to-peak amplitude than the true value. Low frame rates will also affect the accuracy of *derivative* type algorithms (Section 3.2.2.2). Recall that derivative methods calculate R_{OS} many times per pulse, though the values calculated in the vicinity of the inflection points are inaccurate and need to be weighted as such to prevent spurious values of S_pO_2 . At low frame rates the number of estimates possible during the most reliable, diastolic to systolic rise in the pulse waveform, will be reduced. The problems of low frame rates are compounded by the manner in which a camera samples a time-varying waveform.

The photodiode in a contact device produces a continuously varying output current proportional to the instantaneous incident light intensity, which is converted to a voltage and sampled by a sample-and-hold circuit, as often as once every 2 ms (Section 3.3.3.1). A camera by contrast, exposes its CCD or CMOS sensor for typically tens of milliseconds and then has a short readout time before beginning the next exposure. The value readout at the end of the exposure is however, not an instantaneously sampled value, but rather a charge proportional to the sum of all photons received during the exposure—that is, the camera-derived signal is proportional to the mean light intensity observed during the exposure. Thus none of the points in a camera derived PPG signal are actual sample values of the true signal, but rather they are all values proportional to the sum of the true signal, as observed over several almost contiguous windows. The effect of this *integrative* sampling on a sinusoidal waveform is illustrated in Figure 5.24.

Since the frame duration is constant, the mean value of the integration window is plotted rather than the sum in Figure 5.24, which maintains the scale of the *integrative* waveform. The dashed vertical lines indicate the end of a frame, at which point the mean value of the true waveform (continuous line) between the current vertical line and the vertical line immediately to the left is readout. During periods of increasing amplitude, the mean value is always less than the instantaneous value, and the converse is true during periods of decreasing amplitude. The combined effect of low sampling rate and *integrative* sampling is to

cause the observed waveform to exhibit reduced peak-to-peak amplitude and to appear to lag the sample-and-hold waveform. Figure 5.25 illustrates one period of the synthetic pulse waveform (generated by summing three sinusoids at typical cardiac, vasomotion, and respiratory frequencies and amplitudes) and the corresponding *integrative* waveform. The circles mark the inflection points of the sample-and-hold waveform and the crosses the inflection points of the *integrative* waveform.

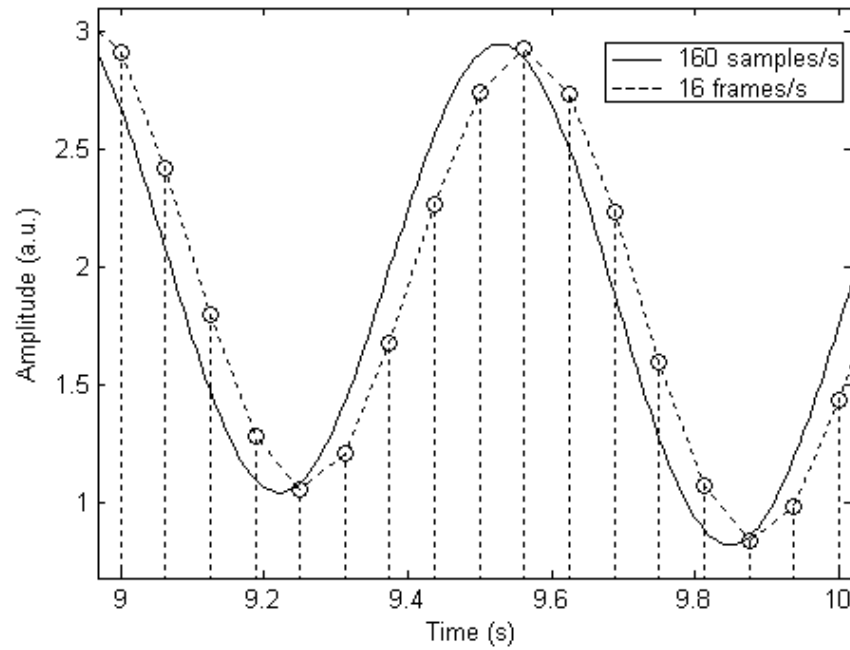


Figure 5.24 Result of camera-based *integrative* sampling (dashed line) at 16 frames per second on a synthetic pulse waveform (continuous line) with 160 samples per second.

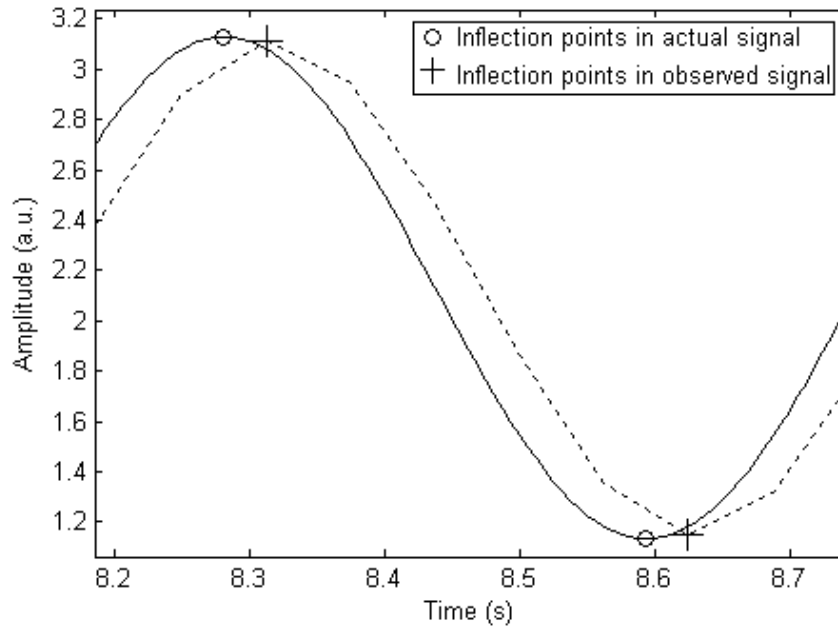


Figure 5.25 Combined effect of low frame rate and *integrative* sampling on the peak-to-peak amplitude of a sample-and-hold synthetic pulse waveform.

The affect that this waveform distortion would have on a *derivative* based method of calculating R_{OS} would depend on the characteristics of the moving weighted averaging of the instantaneous red/infrared ratios employed by the manufacturer (see Section 3.2.2.2). It is reasonable to presume that it would not be beneficial to accuracy. The affect of the waveform distortion on a *peak and valley* based method of calculating R_{OS} can be more readily quantified.

By again constructing a synthetic pulse signal composed of three sinusoids at the typical vasomotion, respiratory, and cardiac frequencies, and with typical proportionate amplitudes, the percentage error in the calculation of R_{OS} values using the *peak and valley* method, was determined for varying oxygen saturation levels and pulse rates. The effect of varying oxygen saturation levels was emulated by varying the ratio of the infrared and red PPG amplitudes linearly between approximately 2.3 and 0.5, which for a red wavelength of 660 nm and an infrared wavelength of 940 nm, correspond approximately to S_pO_2 values of between 100% and 60% (see Figure 3.9 and refer to Wukitsch et al. (1988)). R_{OS} was calculated using equation (3.13):

$$R_{OS} = \frac{\ln\left(\frac{R_L}{R_H}\right)}{\ln\left(\frac{IR_L}{IR_H}\right)}$$

The results of the simulation are summarised in Table 5.3. The discrepancy between the R_{OS} values obtained from the sample-and-hold waveform and the *integrative* waveform vary with both pulse rate and oxygen saturation. The percentage error is largest when both the saturation and pulse rate are at their highest.

The dependence on pulse rate exhibited by the simulation results should be interpreted with some caution. The likely cause of the increased error with increased pulse rate, is the increased slope of the rising (diastolic to systolic) portion of the synthetic PPG waveform, which causes the *integrative* waveform to further lag the sample-and-hold waveform and consequently to underestimate the true peak. In an actual PPG waveform, the slope of the rising edge is proportional to the force of contraction of the heart, which is not particularly dependent on pulse rate—compare the PPG signals plotted in Figure 5.17 and Figure 5.18.

Approx. S_rO_2 (%)	IR:R PPG scaling factor	Pulse rate		
		50	72	100
100	2.32	1.3	1.69	2.58
	1.66	0.69	0.9	1.35
85	1	0	0	0
	0.81	-0.2	-0.28	-0.4
60	0.47	-0.51	-0.73	-1.09

Table 5.3 Simulated percentage error in calculation of R_{OS} due to *integrative* sampling at a frame rate of 16 frames/s, compared to a sample-and-hold waveform sampled at 160 samples/s (Humphreys, et al. 2007).

More credence can be given to the error's oxygen saturation level dependence. As the magnitudes of the red and infrared PPG signals vary with oxygen saturation, so too do the magnitudes of the integration error associated with each. At high saturations the infrared PPG has much larger amplitude than the red PPG, consequently its associated error is larger too. Equation (3.13) defined R_{OS} as the quotient of the red and infrared PPG signals. Thus for high saturations the error associated with the numerator (the red PPG) is comparatively small and the error associated with the denominator (the infrared PPG) is comparatively large. Since a larger error means greater underestimation of the peak-to-peak amplitude, at high saturations R_{OS} is overestimated by a small fraction. At low saturations, the red PPG has larger amplitude than the infrared, thus the reverse is true and R_{OS} is under

estimated by a small fraction—though the comparative difference in the PPG amplitudes is slightly less at low saturations and so the underestimation has smaller magnitude than the overestimation at high saturations. At some saturation level the red and infrared PPG signals will have equal magnitude (approximately 85% for 660 nm and 940 nm), at this saturation level the error associated with each signal is the same and their quotient does not introduce error into the R_{OS} calculation.

Within the range of pulse rate and oxygen saturation level simulated, compared to the contact technique, the camera-based technique produced a maximum overestimation in R_{OS} of 2.6% and a maximum underestimation of -1.1%. If the differences in R_{OS} values summarised in Table 5.3 were translated directly in to S_pO_2 errors, for high saturations, the bias resulting from the camera's *integrative* sampling would cause an over estimation of saturation that is of comparable size to the current clinically accepted accuracy of the contact method: $\pm 3\%$ (see Section 3.4.1). Such an additional error might be of clinical significance.

Fortuitously, the simulation results suggest that integration error decreases with saturation, providing an underestimation in low saturation regions where a patient would be danger.

5.5 ANALYSIS OF ASPECTS OF DEVICE'S PERFORMANCE

A further consideration should be made in performing camera-based non-contact photoplethysmography for pulse oximetry: choosing the size of the region of interest (ROI) within the imaged frame from which the PPG signal is obtained. The size of the ROI and its position relative to the tissue under investigation influences the characteristics of the derived PPG signal.

Section 3.3.4.2 reviewed the design considerations pertaining to reflectance probes in conventional pulse oximeters. In summary, those parameters were the source and detector separation and the surface area of the detector, or in the case of multiple detectors, their arrangement. Mendelson and Ochs (1988) concluded that in the case of contact reflectance pulse oximetry, summing the signals from multiple detectors arranged symmetrically around the sources provided the best PPG signals. Reddy (1997), in reviewing Mendelson and Ochs' work, suggested that a detector with enlarged area would achieve the same results.

In a camera-based system the active area of the detector—the regions of interest within each frame—are almost arbitrarily variable in shape, number,

arrangement, and area. This section investigates the effectiveness of enlarged detector area and multiple detection sites in the camera-based device.

5.5.1 EFFECT OF ROI SIZE ON PLETHYSMOGRAPH CHARACTERISTICS

Unless the PPG signal is obtained from just one pixel a camera-based system inherently utilises multiple detectors, combining their surface area to either sum or average the intensity of the emitted light in the search for PPG signals. For convenience in addressing pixels within the frames, the regions of interest are chosen as contiguous pixels grouped into rectangles, which thus far, have also been square. The shape and size of this area is naturally a variable of interest.

During investigations of the effects of the region of interest's size and shape, some interesting size dependent phenomena were observed, which hint at the additional unforeseen complexity and indeed potential of camera-based photoplethysmographic investigation. For illustrative purposes, a comparison is provided here of the PPG signals that are obtained from one twenty second AVI file, when image analysis is performed using three different sized regions of interest.

Figure 5.26 depicts a sample frame from the 880 nm sequence on which are imposed the square outlines of ROIs with dimensions, 20×20 , 40×40 , and 80×80 pixels respectively. Also visible in each image is the 880 nm indicator light in the top right hand corner. The imaged area corresponds approximately to that depicted in Figure 5.16 (though the orientation is upside down compared to Figure 5.16) and the separation of the camera and tissue is approximately 30 cm. The actual area of tissue that is imaged is a function of the system's optics though the image in Figure 5.26 depicts approximately 16 cm^2 .

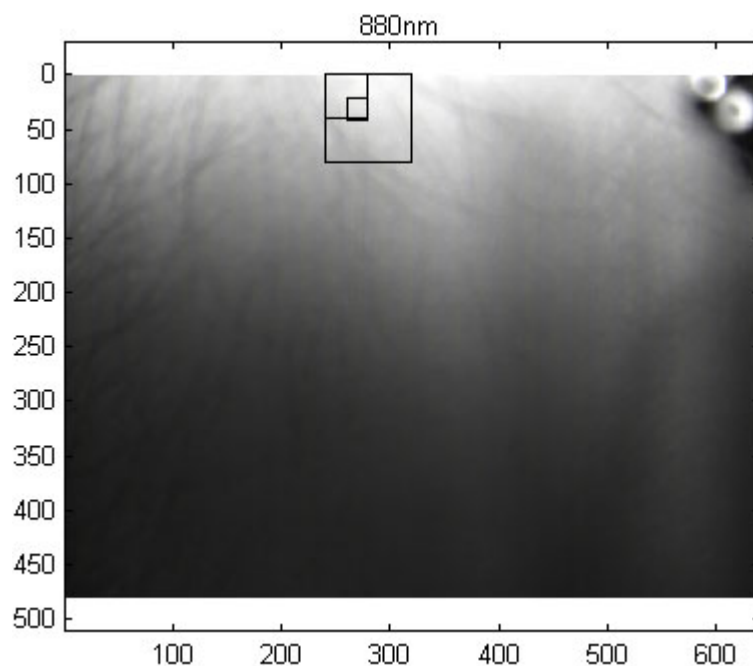


Figure 5.26 A sample frame from the 880 nm sequence showing the locations of a 20×20, 40×40, and 80×80 pixels regions of interest.

Each ROI is centred on approximately the same region of the frame. The PPG signals obtained from each of these regions, at both 880 nm and 760 nm, are plotted in Figure 5.27. Note that in previous plots, the PPG signals have been reorientated such that increasing PPG amplitude corresponds to increasing absorptivity (see Figure 5.17 and Figure 5.18 above). In Figure 5.27 the PPG signals are plotted in their received form; PPG amplitude—the average pixel value within the region of interest—is proportional to received light intensity and inversely proportional to absorptivity. The mean value of each PPG signal has been subtracted so that the pulsatile components of the signals are directly comparable.

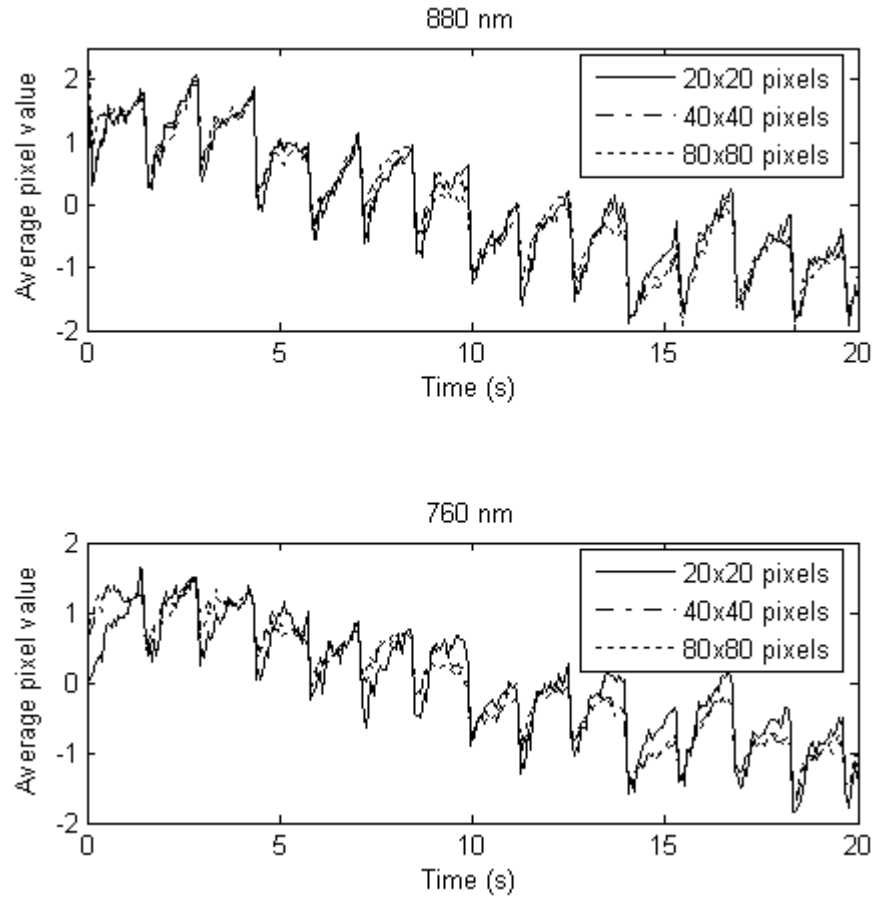


Figure 5.27 PPG signals obtained from similarly positioned regions of interest of different sizes for both wavelengths.

The three PPG signals obtained using different size regions of interest are broadly similar for both wavelengths. They are well aligned during the diastolic to systolic portion of the pulse (the peaks and troughs respectively in Figure 5.27). However the magnified view of the waveforms depicted in Figure 5.28 shows that a significant difference exists in the peak-to-peak amplitude of the PPG signal depending on the size of the region of interest. Converse to the findings of Mendelson and Ochs (1988) and the predictions of Reddy (1997) pertaining to contact reflectance PPG measurement, the detected PPG amplitude diminishes as the area of the detector, the region of interest (the boxes) in this case, increases.

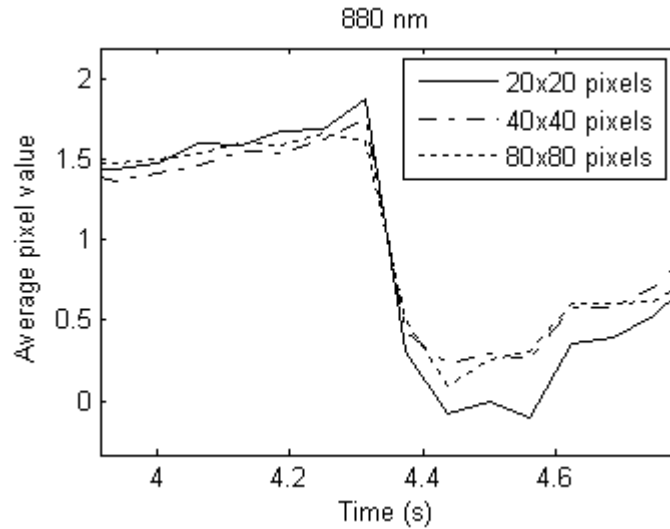


Figure 5.28 Magnified portion of the three 880 nm PPG signals plotted in Figure 5.27, depicting variation in PPG peak-to-peak amplitude due to different size regions of interest.

The magnitude of the effect can be more clearly observed in the frequency domain. The Fourier spectra of the PPG signals plotted in Figure 5.27 are plotted in Figure 5.29. All three spectra share similar peaks, though the amplitudes vary. At the pulse frequency (approximately 0.7 Hz) the enlarged regions of interest result in a reduction of amplitude of approximately 25% at 880 nm and approximately 50% at 760 nm, compared to the peak resulting from the 20×20 pixel region of interest.

The reduction that occurs at the pulse frequency is disproportionately large compared to the other peaks, for example the respiratory peak at approximately 0.4 Hz, which is not affected by region of interest size at 880 nm and minimally affected at 760 nm.

The cause of the PPG amplitude reduction with increasing region of interest size in this instance is a phenomenon that is largely unreported upon in the literature: *PPG inversion*. In some regions of the imaged tissue, the camera-based device captures signals that are the precise inverse of the expected PPG signal. When a region of interest becomes large enough to encompass both a normal PPG and an inverted PPG, the two signals interfere destructively, resulting in a reduction of the detected PPG amplitude.

An examination of the PPG inversion phenomenon and a hypothesis as to the cause are the subjects of the next section.

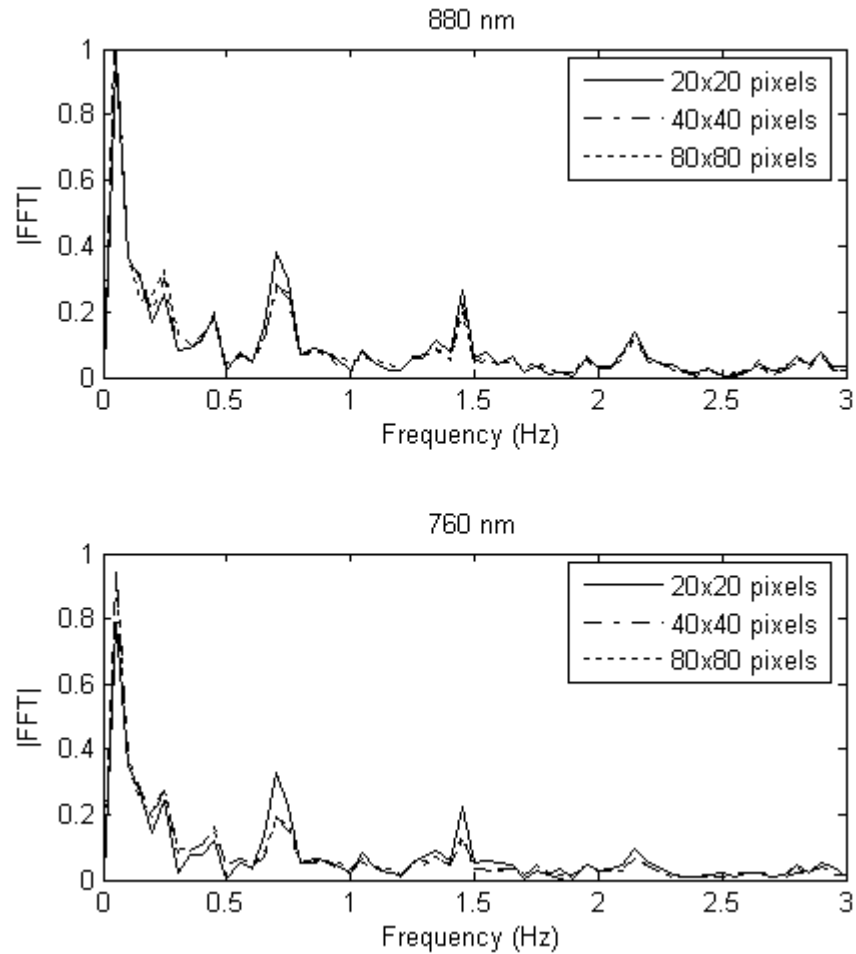


Figure 5.29 Fourier spectra of PPG signals obtained from different size regions of interest.

5.5.2 DETECTION OF INVERTED PPG SIGNALS

When making remote non-contact observations of deep tissue in a reflection geometry the camera-based system routinely detects inverted PPG signals. That is, signals where the peak in the detected light intensity occurs at the systolic peak of the pulse waveform, and the trough at the diastolic trough of the pulse waveform. This is the reverse of the normal situation, where high absorptivity during systole causes low transmittance and a trough in the detected light intensity, the reverse being true of the diastolic portion of the waveform (refer to Section 3.2.1).

Figure 5.30 displays a normal waveform captured by the camera system. The vertical axis displays the average pixel value within the region of interest, which is proportional to the received light intensity.

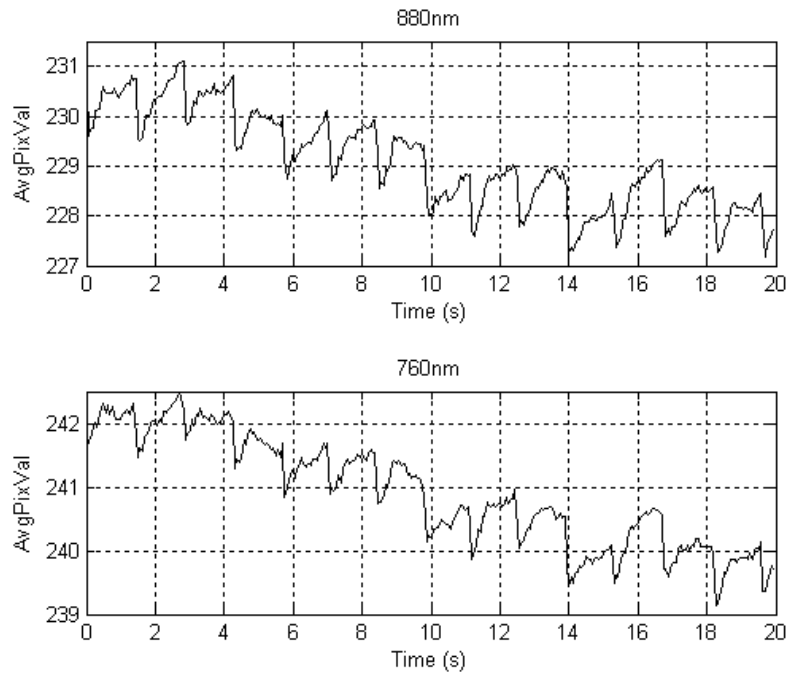


Figure 5.30 Normal PPG waveforms captured from a 40×40 pixel region of interest.

Figure 5.31 displays an inverted PPG waveform captured from a different region of the same AVI file. It can be seen that at both wavelengths the signals share common inflection points, though the signals in Figure 5.31 appear to be the inverse of those in Figure 5.30.

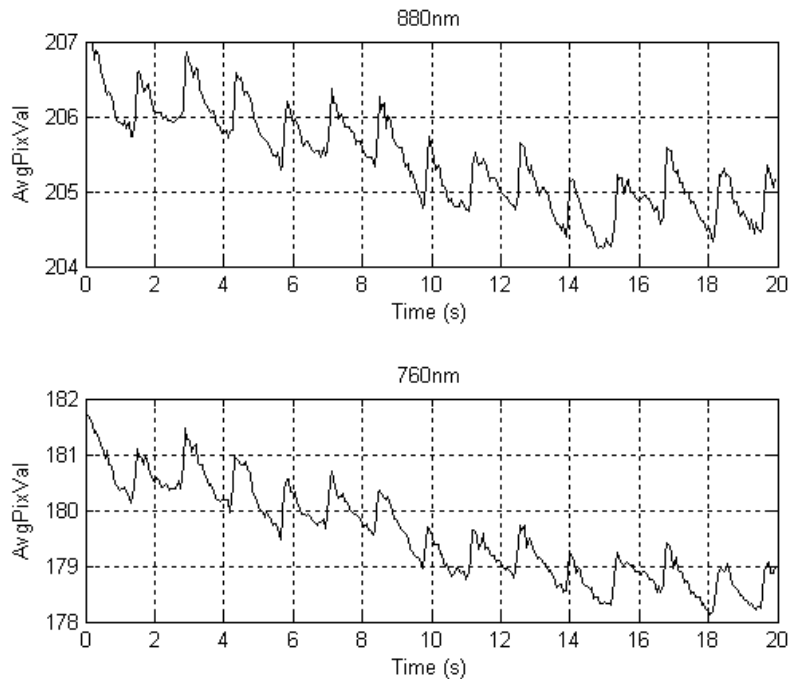


Figure 5.31 Inverted PPG waveforms captured from a 40×40 pixel region of interest within the same AVI as Figure 5.30.

The inverted signals are not subjected here to the scrutiny that the normal PPG signals received earlier; that they are indeed inverted PPG signals seems a reasonable postulation given their similarity to the normal signals (note also the inversion of the dichrotic notch).

Figure 5.32 displays an overlay of the Fourier spectra of the normal and inverted PPG signals at both wavelengths.

Both signals have distinct peaks coincident at the pulse frequency (0.7 Hz) and at its first harmonic. The inverted 760 nm spectrum exhibits a larger peak at the pulse frequency than the normal PPG spectrum and a similar peak at the respiration frequency (0.4 Hz). The inverted 880 nm spectrum has a comparable peak at the pulse frequency and a reduced peak at the respiratory frequency compared to the normal PPG spectrum.

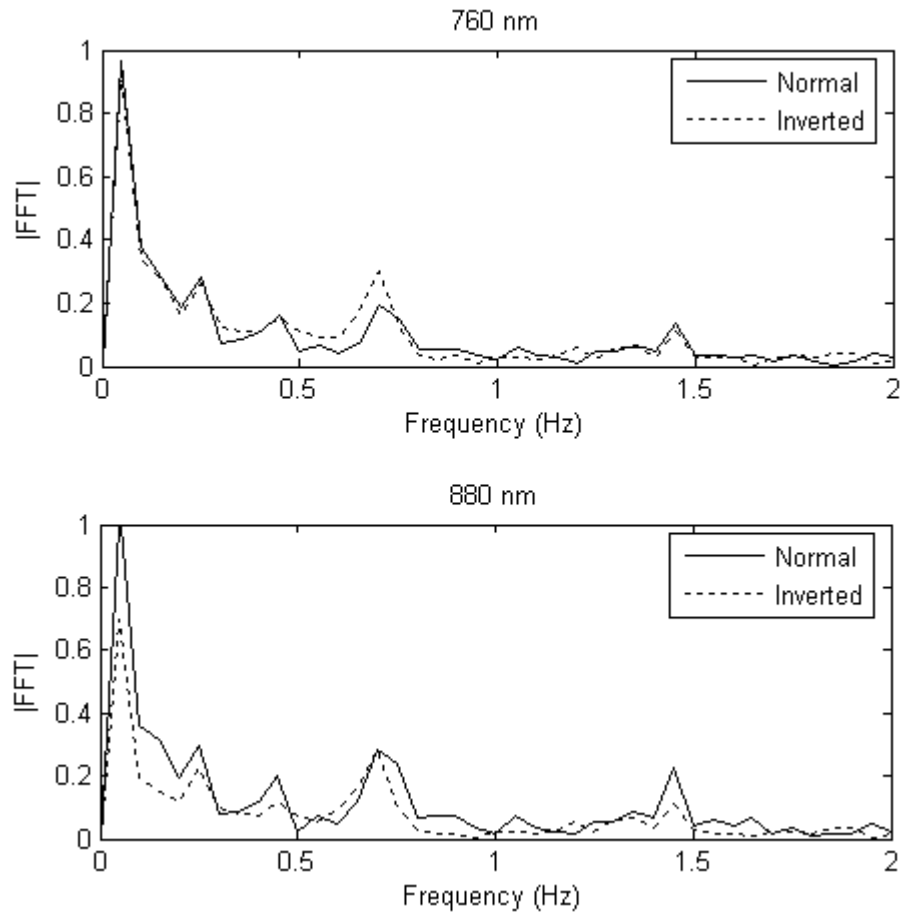


Figure 5.32 Fourier spectra of the inverted and normal PPG signals at both wavelengths.

The inverted PPG signals are most often detected from contiguous regions of the frames. Figure 5.33 displays a sample frame from the 880 nm sequence of an

AVI file. Boxes are superimposed indicating the regions where PPG signals were clearly discernable at both wavelengths. Also indicated in Figure 5.33 are the boxes in which inverted PPG signals were detected at both wavelengths.

Figure 5.34 displays the results obtained from the same AVI file when image analysis is performed using a box size of 40×40 pixels and Figure 5.35 the results from analysis at 80×80 pixels. Note that for the most part between areas with normal and inverted PPG signals, there is region in which no signals are detected. Where light emerging from those regions contains both inverted and normal signals the resulting destructive interference cause no pulsatile component to be detected. Note from Figure 5.30 and Figure 5.31, and from the spectra in Figure 5.32, that the inverted and normal PPG waveforms have comparable pulsatile amplitudes, accounting for typically less than 1% of the quantization range. With reference to the spectra in Figure 5.32 and the spectral method of identifying PPG containing ROIs in Section 5.3.3, inverted PPG signals frequently produce the highest spectral figure of merit for a video file.

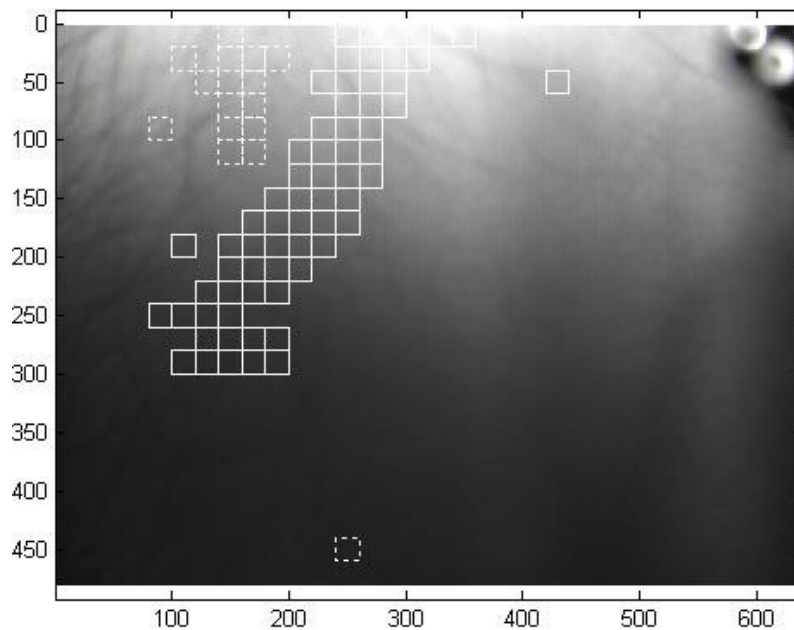


Figure 5.33 Outline of 20×20 pixel regions from which PPG signals (continuous line) and inverted PPG signals (broken line) were discernable at both wavelengths.

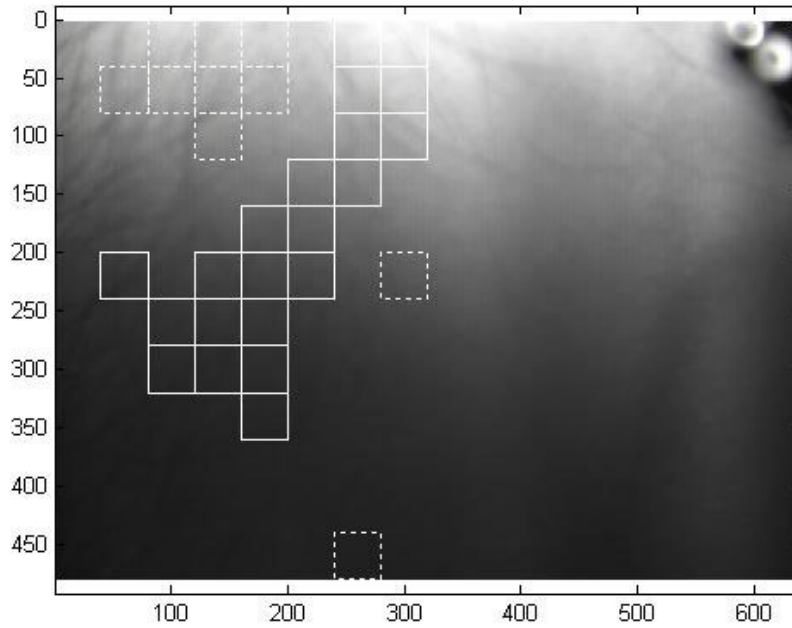


Figure 5.34 Outline of 40×40 pixel regions from which PPG signals (continuous line) and inverted PPG signals (broken line) were discernable at both wavelengths.

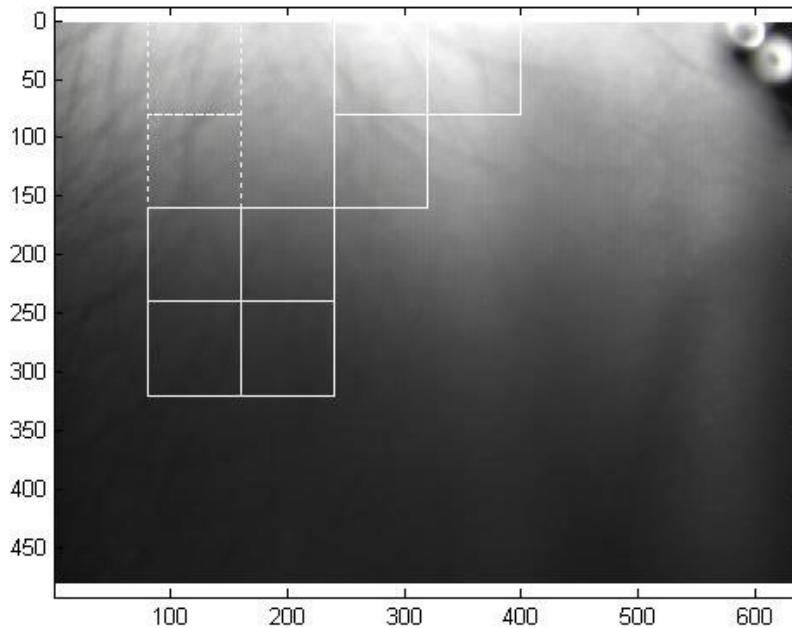


Figure 5.35 Outline of 80×80 pixel regions from which PPG signals (continuous line) and inverted PPG signals (broken line) were discernable at both wavelengths.

This phenomenon is unreported in the literature pertaining to either reflective or transmissive contact pulse oximetry. The phenomenon was reported by Maguire (2004), who encountered it but did not explain it, during a study of reflectance photoplethysmography based pulse transit-time measurement. In the experiment described here in Section 5.4.1, data from three of the ten test subjects exhibited the

phenomenon. The phenomenon was not observed in earlier experiments using a camera-based system to perform detection by either transmissive illumination and detection (Humphreys, et al. 2005a; Humphreys, et al. 2005b), or reflective illumination and detection of small extremities (Humphreys, et al. 2005c).

Figure 3.6 depicted the arrangement of erythrocytes during the various stages of the pulse cycle. At systolic pressure the erythrocytes are densely grouped and orientated such that their long axes are perpendicular to the direction of blood flow. At diastole the erythrocytes are least densely grouped and are orientated such that their long axes are parallel to the direction of blood flow. The direction of arteries within small extremities means that transmission probes cannot be orientated other than to have the path between the source and detector perpendicular to the direction of the artery. Thus for a transmission geometry maximum absorption (minimum transmittance) of light occurs at systole and minimum absorption (maximum transmittance) at diastole. The position of a transmission source and detector and the optical path between them are depicted in Figure 5.36.

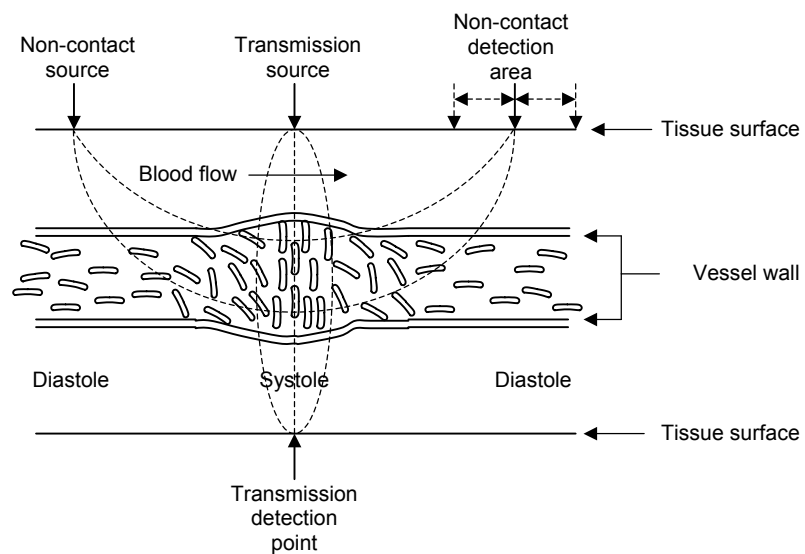


Figure 5.36 Depiction of the arrangement and orientation of erythrocytes in a peripheral artery during the cardiac pulse. Also depicted are the outline of the optical paths between source and detector for a transmission and non-contact reflection geometry (dashed lines). (Not to scale.)

Also depicted in Figure 5.36 are the relative locations of the source and detector for the camera based device. The source and detector separation are significantly greater for the non-contact device and since the signals are obtained from backscattered light, the possibility exists that the optical path between the source and detector will pass axially through an artery, rather than diametrically as

in the transmission case. In this case, during diastole, the erythrocytes are orientated such that their long axes, while still parallel to the direction of blood flow, are perpendicular to the optical path. During systole, the erythrocytes present their short axes to the optical path. This situation results in maximum transmittance (minimum absorption) at systole and minimum transmittance (maximum absorption) at diastole—resulting in a signal that is the inverse of a conventional PPG. The proclivity of camera-based system to capture such signals may be due, in general to the larger source and detector separation than is present in contact probes, and in this instance in particular to the region of tissue being imaged; the forearm is imaged with the axis of alignment between the source and detector parallel to the major arteries (see Figure 5.16). The fact that such inverted signals have not previously been observed with conventional contact reflectance probes might be explained by the smaller source-detector separation. In conventional reflectance contact probes the source-detector separation is limited to just a few millimetres. This has the effect of limiting the penetration depth of the light so that absorption is due to a shallow vascular bed, in which the directions of the smaller arteries do not follow the orientation of the limb. Where the propagation path does intersect axially with arteries, the short source-detector separation limits the axial absorption.

5.6 ACHIEVABLE SEPARATION OF TISSUE AND CAMERA

Naturally a question of interest to remote non-contact pulse oximetry or photoplethysmography, is how far can the light source and detector be located from the tissue under investigation? The achievable separation may determine the uses to which the technique can be put.

Experimentally testing the achievable separation of one particular camera and source combination would be somewhat meaningless. The achievable separation of the system is ultimately a function of the combined characteristics of the system's optics, source, and detector. To experimentally investigate the affect of tissue-source separation would require several types of light source—since LEDs or arrays of LEDs are unsuited to illuminating tissue from distances of more than a few centimetres. Equally to investigate the achievable detector-tissue separation experimentally would require at least a selection of lenses of suitable magnification and optical format for the camera. These results would then pertain only to that camera—which is in itself arguably the most variable component.

Rather than collecting empirical data pertaining to the system described in this thesis, a simplified probabilistic model is developed here. The model attempts to predict the decrease in the number of photons striking the detector as a function of tissue-detector separation and detector area, in response to a monochromatic point source. The prediction by the model is compared to data from a Monte Carlo simulation (see Section 2.3.3) of a three-layer tissue model.

During the course of the discussion that follows, knowledge of the distribution of the photons' trajectories as they emerge from the tissue under investigation, will be seen to be crucial to the accuracy of the prediction by model. As such two models are developed here, one based on a normal distribution and the other based on a uniform distribution.

5.6.1 MONTE CARLO SIMULATION

The Monte Carlo simulation of tissue-detector separation is described first as knowledge of the characteristics of photons emerging from the tissue model is instructive in describing the rationale for the probabilistic models that follow.

A Monte Carlo simulation was conducted using a simple three-layer model of tissue, consisting of parallel layers of skin and fat, with respective thicknesses of 2 mm and 5 mm, and an infinitely deep layer of muscle. Niwayama et al. (2006) describe the optical properties of such a model for similar purposes, which are given in Table 5.4. The same Cartesian coordinate system is used here as that described in Section 2.3.3. The tissue surface is assumed to be the flat x - y plane defined as $z = 0$. Positive values of z denote a position inside the tissue, negative values a position outside the tissue, and $z = 0$ the air-tissue interface. The refractive indices of all tissues are assigned the value 1.3.

Tissue	μ'_s (mm^{-1})	μ_a (mm^{-1})
Skin	1.3	0.02
Fat	1.2	0.002
Muscle	0.6	0.02

Table 5.4 Values of bloodless scattering coefficients (μ'_s) and absorption coefficients (μ_a) for three-layer Monte Carlo model (Niwayama, et al. 2006).

One million photon packets were injected vertically at location $(0, 0, 0)$ constituting a point source. The detector area (with dimensions in millimetres) was defined as the circular region centred at $(15, 15, z)$, with radius 10 mm, where the value of z denotes the separation of the tissue and detector (with $z = 0$ being contact).

At this point a simplifying assumption is made that the detector area, which in practice is the lens face, is a flat surface, and that all incident photons striking the detector surface are detectable (by the camera). This assumption ignores several important physical attributes of both the system's optics and the camera's detector (be it a CMOS or CCD sensor). Firstly the lens will present a convex parabola rather than a flat surface towards the tissue surface, which itself is likely uneven and not parallel to the detector surface. Secondly the glass lens will have a critical angle of incidence, beyond which incident photons will be reflected from the surface rather than refracted by the lens. Thirdly the lens will have a limited ability to focus light from a wide numerical aperture onto the camera's detector. Fourthly, assuming the lens has focused light from a wide numerical aperture onto the camera's detector, the detector may yet be insensitive to light focused from such angles depending on the geometry of the detector and the lens aperture. This may be particularly prevalent in 4/5T CMOS devices, where a stack of optically insensitive components can cast a shadow on the optically sensitive area of each pixel. The problem can be compounded with either CMOS or CCD technology by the presence of micro-lenses over the pixels (refer to the discussion in Section 4.2). The collective affect of these assumptions is to overestimate the number of detectable photons at small tissue-detector separations (since at larger separations photons travelling on wide trajectories will likely not strike the detector area).

Thus under the contact condition ($z = 0$) a detectable photon is considered to be any backscattered photon emerging from the tissue within a 10 mm radius of the point $(15, 15, 0)$.

Once a photon emerges from the tissue its trajectory in air remains unchanged. Thus, using the photon's point of emergence and its directional cosines (defined in Section 2.3.3), a second point on each photon's trajectory can be calculated by equation (2.12), where Δs is now an arbitrary distance,

$$x_{new} = x + \mu_x \Delta s$$

$$y_{new} = y + \mu_y \Delta s$$

$$z_{new} = z + \mu_z \Delta s.$$

From the two points along each photon's trajectory a parametric equation is formed. For each parametric trajectory the point of intersection with each plane to which the detector is moved is calculated, as well as the angle each trajectory makes with the normal to the tissue plane (and all parallel detector planes). Where the point of intersection of a trajectory and the current detector plane is less than 10 mm from the point (15, 15, z), that photon is considered detectable at that distance from the tissue.

Figure 5.37 displays the diverging trajectories of photons emerging from the defined detector region, resulting from the Monte Carlo simulation. The points of intersection of the trajectories with detector planes at 50 mm and 100 mm from the tissue surface are marked by dots. Note that the rectangles imposed on the planes in Figure 5.37 have dimensions of 100 mm by 100 mm.

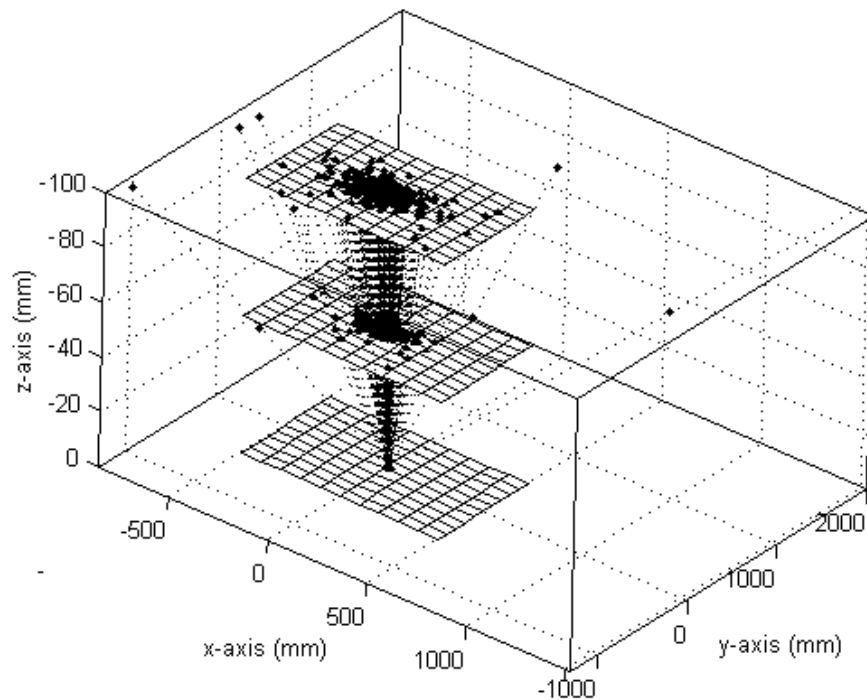


Figure 5.37 Diverging trajectories of photon packets emerging from circular region of three-layer tissue model. Dots mark the points of intersection with parallel planes to the tissue at $z = -50$ mm and $z = -100$ mm.

Figure 5.38 depicts the results of the Monte Carlo simulation showing the decrease in number of detectable photons as a function of tissue-detector separation.

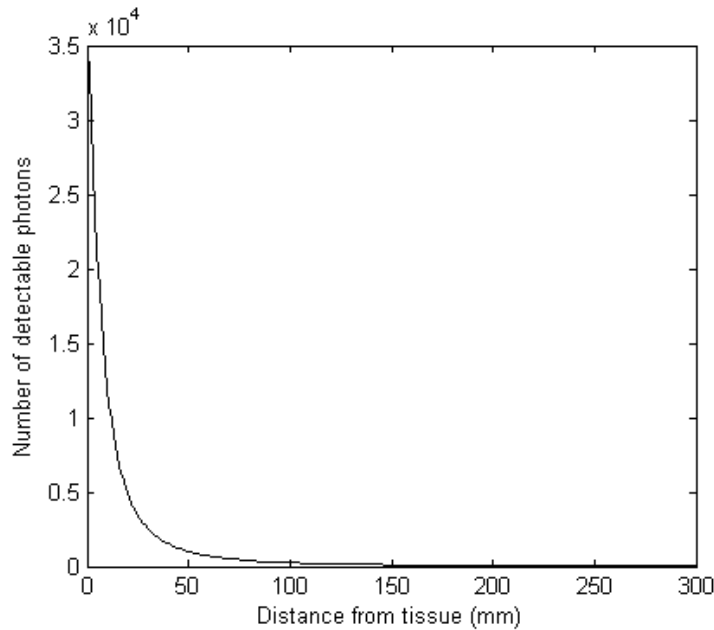


Figure 5.38 Decrease in the number of detectable photons with increasing tissue-detector separation, from Monte Carlo simulation.

The angle that a photon's trajectory makes with a normal vector to the tissue plane ϕ , is in the range $0 \leq \phi < \pi/2$. The angle ϕ is constrained to be less than $\pi/2$ since the photon's final trajectory is the result of the last scattering event before emerging from the tissue. This event takes place a small distance beneath the tissue surface (determined by the mean free path length defined in Section 2.3.3) and thus a trajectory must make an angle greater than zero with the tissue surface (less than $\pi/2$ from the normal) to escape the tissue. Within the tissue, both the uniform azimuthal scattering and the anisotropic forward scattering determine the final trajectory assigned to the photon. The distribution of the trajectories of photons that actually emerge from the tissue is governed by the probability of internal reflection from the air-tissue boundary, which is a function of the refractive index of the medium's final layer, and the Fresnel reflection coefficient (see Section 2.3.3). Thus while it is possible that the angle ϕ take on any value in the range $0 \leq \phi < \pi/2$, the distribution of the continuous random variable ϕ is not uniform. Furthermore whatever the distribution of all emergent trajectories, the distribution of detectable trajectories will be skewed in favour of smaller angles from the normal, since larger angles from the normal will be detectable only if they emanate from a very shallow point in the tissue or from a point located centrally under the detector.

Figure 5.39 displays the probability density function of the angle ϕ for all detected photons from the Monte Carlo simulation, constructed from a frequency

distribution with ninety bins, such that the magnitude of the n^{th} vertical line in Figure 5.39 gives the probability

$$\text{Prob}\left(\frac{\pi}{180}(n-1) \leq \phi < \frac{\pi}{180}n\right). \quad (5.7)$$

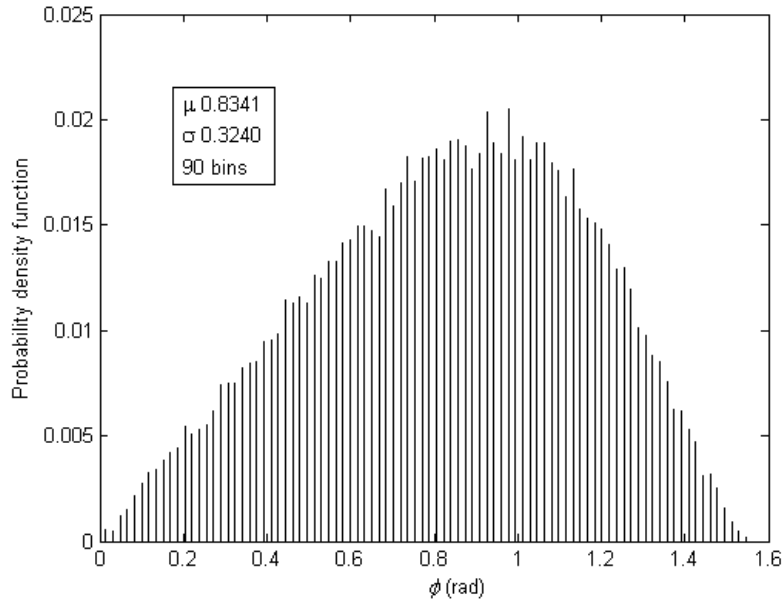


Figure 5.39 Probability density function showing the distribution of the angle between the photon trajectories and the normal to the tissue plane ϕ .

As expected, the distribution can be seen to tail off more gradually to its left side—favouring trajectories that make small angles with the normal to the tissue.

The next section describes two probabilistic models to predict the decrease in the number of detectable photons as a function of tissue-detector separation and detector area.

5.6.2 PROBABILISTIC MODEL OF TISSUE-CAMERA SEPARATION

Predicting the relative number of detectable photons at a given height above the tissue surface, for a given detector area, depends upon correctly modelling the distribution of the detectable photons. Two simplified geometric models are developed here based on a uniform trajectory distribution and a normal trajectory distribution. The predictions by both models are then compared to data from Monte Carlo simulations.

5.6.2.1 UNIFORM CONIC MODEL

Consider an infinitely tall inverted cone, perpendicular to the tissue surface, defined by an angle θ , and emanating from a point p some distance below the tissue surface. The cone is constructed such that its circular cross-section at the tissue surface coincides exactly with the circular area of the detector of radius r , as depicted in Figure 5.40. The angle θ is defined to be the maximum angle that a photon trajectory (ϕ) makes with a normal vector to the tissue plane. Since the cone's surface coincides with the detector area at the tissue surface, the volume of the cone encloses the trajectories of all photons that are detectable under contact conditions. The point p , the apex of the cone located a distance z beneath the tissue surface, is the geometrical projection of where the scattering appears to have taken place when viewed from outside the tissue. In fact the photons are only collinear at the injection point on the tissue surface, and after travelling through the region indicated in Figure 5.40, acquire their ultimate trajectory only a fraction of a millimetre beneath the tissue surface.

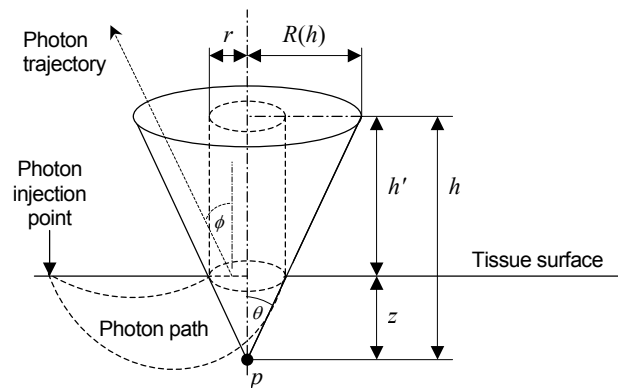


Figure 5.40 Conic model of decrease in number of detectable photons as a function of tissue-detector separation and detector area.

Two assumptions are now made about the distribution of photons emerging from the region of interest. First it is assumed that the points of emergence of the backscattered photons are uniformly distributed throughout the region of interest. In Chapter 2 it was established theoretically and by simulation that the number of backscattered photons emerging from the tissue decreases exponentially with increasing radial distance from the injection point. Thus the assumption that photon emergence points are uniformly distributed over the detector area may be invalid close to the injection point where the exponential profile is steep (refer to Figure 2.4). However referring to Figure 2.4 (which depicts the number of backscattered photons versus radial distance from the source), the assumption

appears reasonable for larger source-detector separations (say greater than 50 mm). Second it is assumed that the angle ϕ itself is uniformly distributed about the normal to the tissue plane. (The invalidity of this assumption can quickly be ascertained with reference to the actual distribution of ϕ depicted in Figure 5.39.)

Now having assumed that the photon trajectories are uniformly distributed about the normal vector to the tissue, and that the emergence points are uniformly distributed over the detector area, the probability of detecting any given photon at a height h' above the tissue surface is given by the ratio of the detector area to the area of the cone's face at h' ,

$$\text{Prob}(\text{detection at } h') = \frac{\pi r^2}{\pi R^2(h', \theta)}. \quad (5.8)$$

Thus if N photons are detectable when the detector is in contact with the tissue, the number of photons detectable at a height h' above the tissue surface $n(h')$, is given by

$$n(h') = \frac{Nr^2}{R^2(h', \theta)} = \frac{Nr^2}{(r + h' \tan \theta)^2}. \quad (5.9)$$

The angle θ is bounded between the same limits as the photon trajectory angle ϕ , thus $0 \leq \theta < \pi/2$. In practice, the assumption of a uniform distribution greatly exaggerates the divergence of the photons (see Figure 5.39) and predicts far fewer detectable photons than the simulation suggests. The inaccuracy of the assumption that the distribution is uniform can be reduced by limiting the range of θ to $0 \leq \theta < \pi/4$. Imposing such a limit on θ excludes many photons emerging on trajectories that form a large angle with the normal—indeed from Figure 5.39 $\text{Prob}(0 \leq \theta < \pi/4)$ is calculated to be 0.4376. However trajectories with a large divergence from the normal to the tissue quickly become undetectable in any event, and the exclusion of such trajectories produces significant prediction error only at small tissue-detector separations. The prediction by the conic model as compared to the Monte Carlo simulation results can be seen in Figure 5.41.

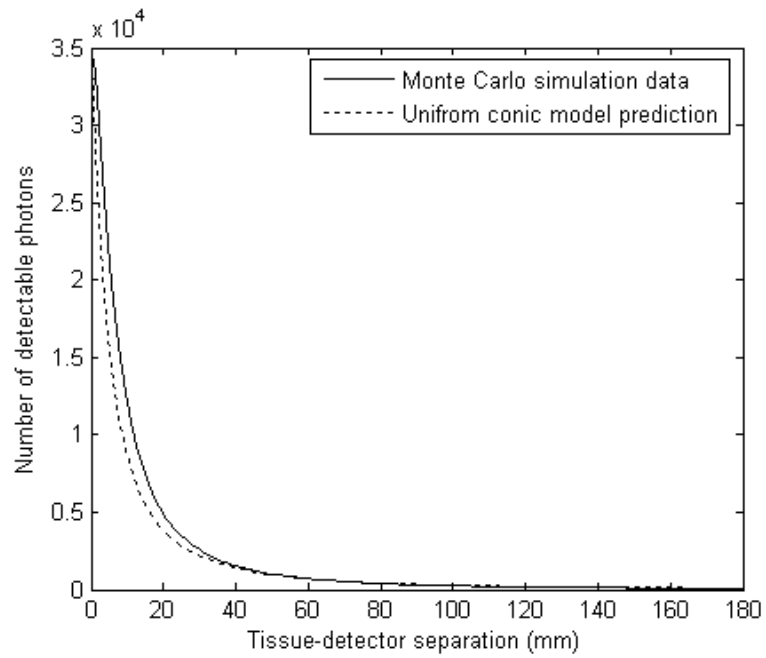


Figure 5.41 Comparison of uniform conic model prediction and Monte Carlo simulation data, showing decreasing number of detectable photons with increasing tissue-detector separation.

The uniform conic model forms its prediction based on assumptions about the distribution of backscattered photon trajectories and on the area of the detector’s lens. For a given system the model may be a useful predictor of achievable tissue-lens separation, however it can also serve as a quick indicator of the effect of varying the lens size. Figure 5.42 displays the predicted effect of increasing lens radius from 5 mm to 50 mm on the relative number of detectable photons.

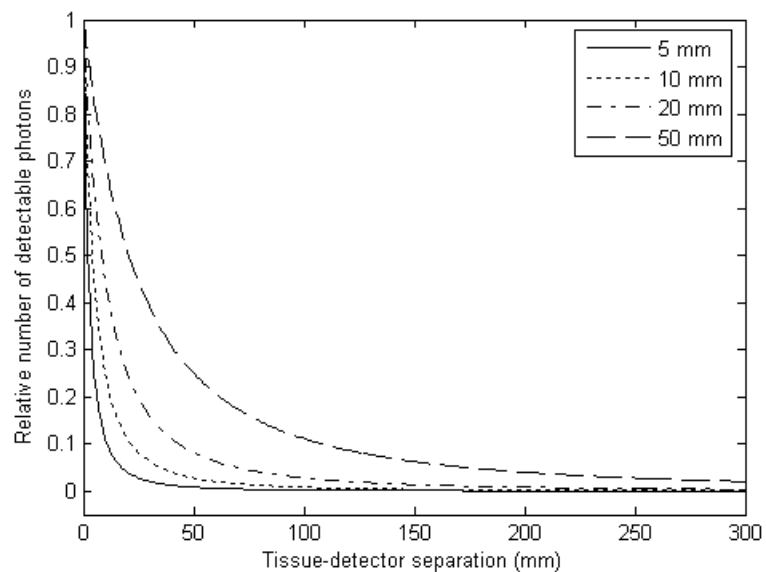


Figure 5.42 Uniform conic model prediction of effect of increasing lens radius on the relative number of detectable photons as a function of tissue-lens separation.

The prediction of the effect of increased lens radius by the uniform conic model was tested against the Monte Carlo simulation data. For a common injection point defined at (0, 0, 0), data were collected from two detector areas, both centred at (30, 0, z) with radii of 10 mm and 20 mm. The results are displayed in Figure 5.43. The model can be seen to have a comparable prediction error for each radius, and converges on the simulation data for separations greater than approximately 60 mm. This result in conjunction with that displayed in Figure 5.41 is significant, as collectively they evaluate the model for varying detector areas, both close to, and at some distance from the injection point. This gives some validity to the first assumption of the uniform conic model that (despite being known to have an exponential distribution) the emergence points of photons within the detector area can be considered uniformly distributed.

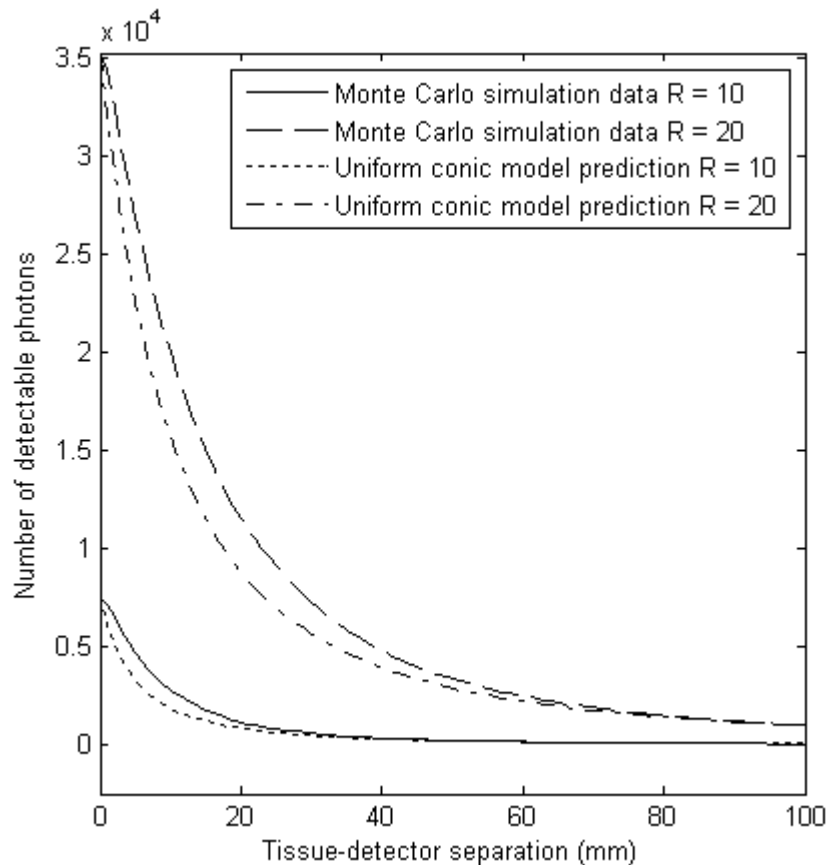


Figure 5.43 Predicted and actual effect of increasing lens radius on the number of detectable photons.

A point worth noting about the relationship between the number of detectable photons and the tissue-detector separation is that the curve is particularly steep for small separations and almost flat beyond a few centimetres. Operating at distances of several centimetres from the tissue surface, the detectable light intensity can be

expected to vary little with small changes in the tissue-detector separation. However at smaller tissue-detector separations, the variation in detected light intensity emanating from the region of interest will be significantly affected by even slight variations in the separation distance. It is in this initial sensitive region that the uniform conic model's prediction deviates most from the simulation data.

5.6.2.2 NORMAL CONIC MODEL

Though it is perhaps easiest to envision applications of non-contact pulse oximetry or photoplethysmography that operate at larger tissue-detector separations, it is conceivable that future applications may also operate close to the tissue surface. A conic model based on a normal distribution of the angle between the photon trajectories and the normal vector to the tissue is described here, which attempts to improve upon the uniform conic model's prediction, particularly in the initial separation region.

For convenience the conic model depicted in Figure 5.40 is redrawn here as a flat elevation view in Figure 5.44. Once again the photons' trajectories are defined by the angle they make with a normal vector to the tissue plane ϕ . While the geometric construction of the cone is as before, an important distinction is made here. In the uniform model the angle θ enclosed the trajectories of all backscattered photons simultaneously. Now θ is defined to be the solid angle enclosing an individual photon's trajectory. Although θ has the same value and distribution as ϕ , the cone formed by θ and emanating from the point p is constructed to intersect the tissue plane through the circumference of the detector area. Thus the cone encloses the photon trajectory with angle ϕ regardless of the point of emergence of the photon, obviating the need for an explicit simplifying assumption about the distribution of the emergence points within the detector area. The point p is located a distance z beneath the tissue surface. The distance z must be sufficiently shallow to accommodate the maximum value of θ , which like ϕ can be arbitrarily close to but less than $\pi/2$. The maximum value of z is thus given by

$$z = \frac{r}{\tan^{-1} \theta_{\max}} . \quad (5.10)$$

As before, the detector radius is denoted by r and the radius of the cone's face at a given height above either the apex (h) or the tissue surface (h') is denoted by R .

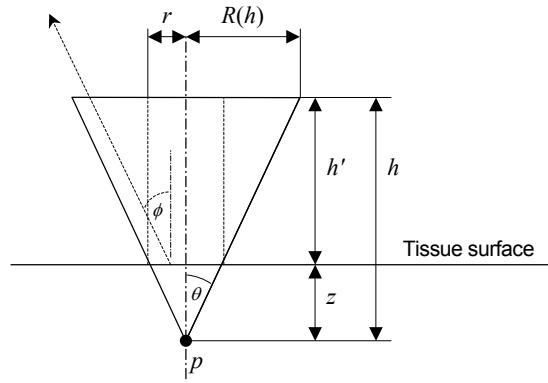


Figure 5.44 Elevation view of 3D conic model depicted Figure 5.40.

For a given detector radius r , the probability that a photon with a trajectory ϕ is detectable at a height h is given by,

$$\text{Probability of detection} = \text{Prob}(R(h) \leq r). \quad (5.11)$$

The radius of the cone's face at a height h is given by,

$$R(h) = (h' + z) \tan \theta. \quad (5.12)$$

Thus the probability of detection at a height h' above the tissue surface can be written as,

$$\text{Probability of detection} = \text{Prob}\left(\theta \leq \tan^{-1}\left(\frac{r}{h' + z}\right)\right). \quad (5.13)$$

Thus from equation (5.13) the probability that a particular trajectory is detectable at a height h' above the tissue surface is given by the cumulative distribution function of the continuous random variable θ , which is also the cumulative distribution function of the continuous random variable ϕ .

Constructing a normal curve with a mean value (μ) of $\pi/4$ radians and a standard deviation (σ) of $\pi/8$ radians produces a bell shaped curve that approximates the distribution of the random variable ϕ (which from the Monte Carlo simulations was found to have actual values of $\mu = 0.8341$ radians and $\sigma = 0.3240$ radians). The curve is depicted in Figure 5.45.

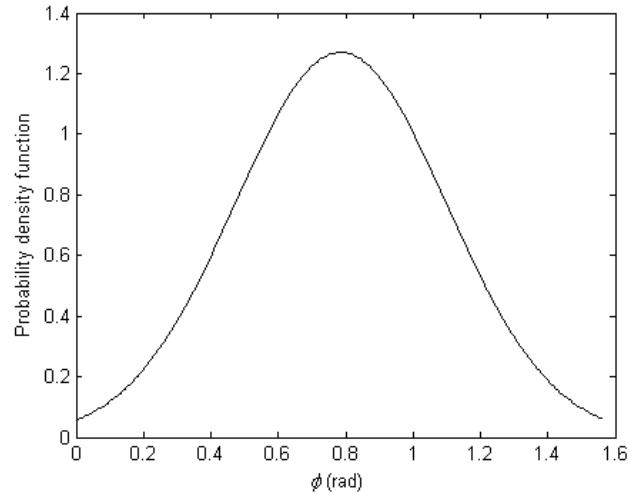


Figure 5.45 Normal probability density function.

The desired cumulative distribution function is obtained by numerically integrating the probability density function. The resulting curve is displayed in Figure 5.46. For comparison the cumulative distribution of the actual Monte Carlo simulation data is also displayed.

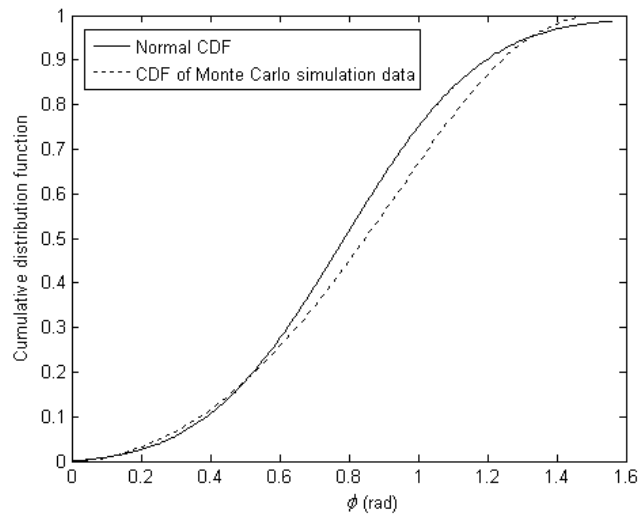


Figure 5.46 Normal cumulative distribution function.

Two points should be noted about using a normal distribution to approximate the distribution of the backscattered photon trajectories. First with reference to Figure 5.39, the distribution of the simulated photon trajectories is asymmetric about its mean value; a normal approximation will be symmetric. The second, more consequential point, is that unlike a true continuous normal random variable, the photon trajectories, although continuous, are limited to the range $0 \leq \phi < \pi/2$. The area under the curve in Figure 5.45 is 0.9850 and only sums to unity as the limits of integration become infinite in both directions. In this sense the curve depicted in

Figure 5.45 is not a probability distribution. As a direct result, the cumulative distribution function depicted in Figure 5.46 has a value of less than one as ϕ approaches $\pi/2$, meaning that the conic model will assign a probability of less than one to the event that all photons are detectable under contact conditions, despite the geometry of the model having been explicitly constructed on this basis.

It now remains to calculate the distance z , which is a function of the largest photon trajectory ϕ that the angle θ must enclose. In practice it is sufficient to choose θ_{\max} to be some angle improbably close to $\pi/2$ (determinable from cumulative distribution function), of the order $19\pi/40$. A comparison of the Monte Carlo simulation data and the normal conic model prediction of the decreasing number of detectable photons is depicted in Figure 5.47.

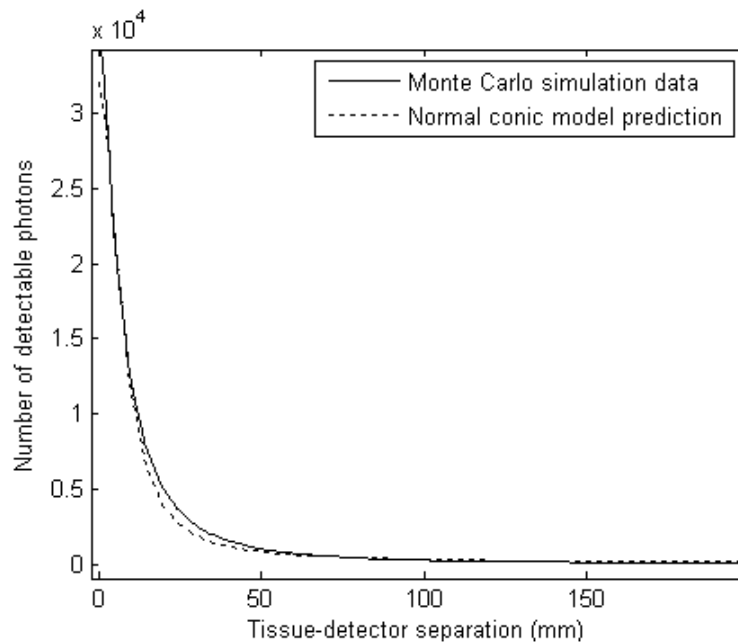


Figure 5.47 Comparison of normal conic model prediction and Monte Carlo simulation data, showing decreasing number of detectable photons with increasing tissue-detector separation.

Apart from the normal conic model's underestimation of contact detection, its prediction rapidly converges on the simulation data. A comparison of both the normal and uniform conic model predictions against the simulation data is depicted in Figure 5.48. The data were collected with an injection point at $(0, 0, 0)$, and a detector area centred at $(15, 15, z)$ with radius 10 mm. The performance of the two models can be compared over three regions distinct regions. For close proximity, say 5 mm to 20 mm, the normal model provides the most accurate prediction. Between approximately 20 mm and 100 mm the two provide comparable

predictions and both are close to the simulation data. For distances greater than 100 mm the uniform model provides the most accurate prediction while the normal model begins to overestimate the number of detectable photons. The steps visible in the normal model prediction at large tissue-detector separations result from the numerical integration of the probability density function, producing discrete samples of the cumulative distribution function.

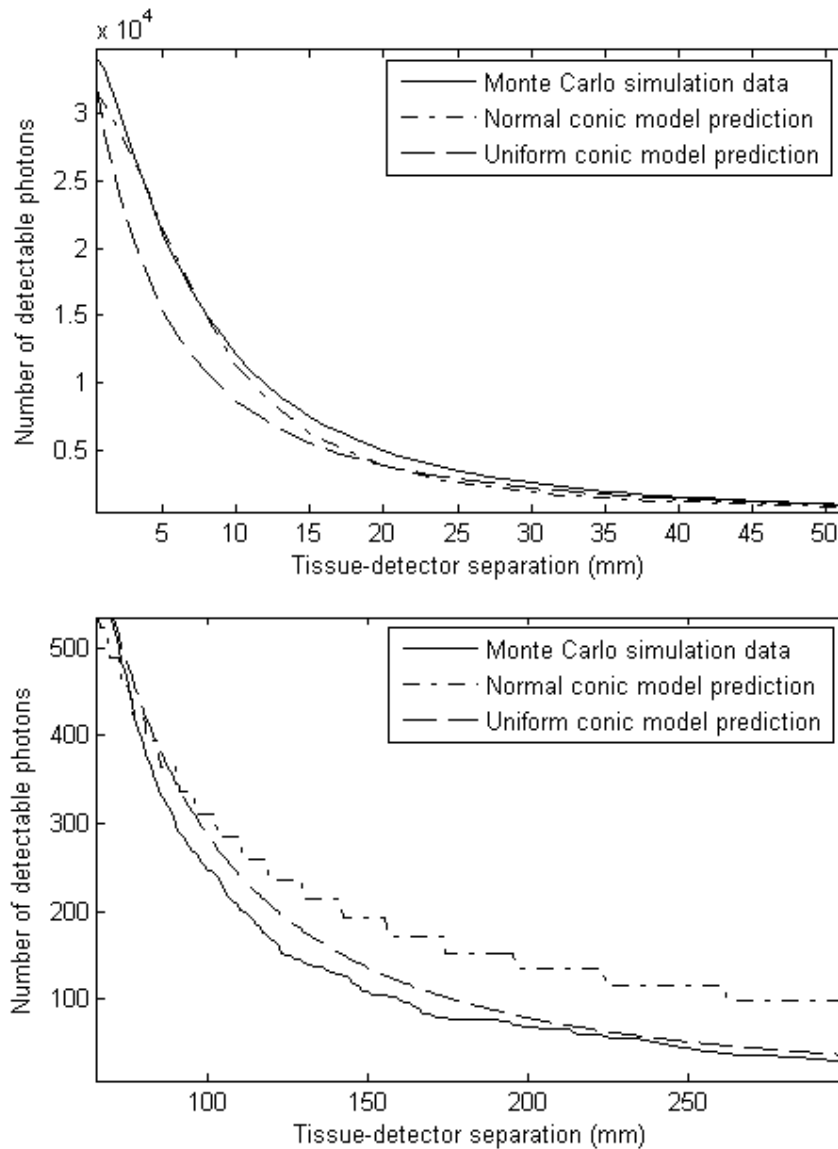


Figure 5.48 Predictions by uniform and normal conic models, and Monte Carlo simulation data, depicting decreasing number of detectable photons with increasing tissue-detector separation.

The performance of both models can be improved upon by replacing the normal distribution with the actual cumulative distribution of the simulation data, which is depicted as the broken line in Figure 5.46.

Rather than pursue further refinement of these models, at this point it is prudent instead to note that knowledge of the backscattered photon trajectories is paramount to the accuracy of any model—as highlighted by the application of the actual cumulative distribution curve to the conic model. While the three-layer tissue model employed here broadly replicates the absorptive and scattering characteristics of tissue, the model lacks the intricate fine structure of real tissue, such as the vascular bed, parenchymal and fascial tissue, hair, as well as an uneven tissue surface. The distribution likely varies with time to some degree, as the pulsing blood causes constant rotation of the scattering erythrocytes and mechanical displacement of the surrounding tissue.

As a final point about the achievable separation of tissue and detector, it should be noted that the probabilistic geometric models described here, and the simulation data against which the models are compared, describe the decrease in the detectable number of *desired* photons—that is the number of photons that emanated from a particular region of interest on the tissue surface. For a circular region of interest, there exists an annular region of surrounding tissue, from which unwanted photons emerge. The number of unwanted photons striking the detector will increase (from zero under contact conditions) as the detector is retracted from the tissue surface. Where those photons have travelled a similar path to those emanating from the region of interest, they may be a serendipitous boon, adding to the signal level. In most instances however those photons will likely add only to the noise level, and in some instances (as was described in Section 5.5.2) the unwanted photons may contain an inverted signal that interferes destructively with the desired signal and simultaneously adds to the noise level.

5.7 CHAPTER SUMMARY AND DISCUSSION

This chapter has presented a study of a remote non-contact camera-based device, capable of simultaneously capturing two PPG signals at different wavelengths in a multiplexed fashion. These PPG signals have been shown to be comparable to a finger PPG signal captured simultaneously by a conventional contact device, both in the characteristics of the waveform and as an indicator of peripheral arterial pulse rate. In so doing, the prerequisite for non-contact camera based pulse oximetry has been met and two of the three core functions performed by a clinical pulse oximeter have been replicated: display of a plethysmogram and measurement of the pulse rate.

The determination of arterial oxygen saturation by the technique of pulse oximetry requires calibration of the device either *in vivo* (which requires a clinical setting as described in Section 3.3.5.1) or *in vitro* (which requires obtaining and artificially oxygenating whole blood as was described in Section 3.3.5.2); both are beyond the purview of this research. This chapter has instead focused on identifying aspects of pulse oximetry (and indeed photoplethysmography) that are unique to a camera-based implementation. Principally the effect of camera-based *integrative* sampling, as opposed to a conventional sample-and-hold method, has been highlighted. In summary both analysis and simulation suggest that *integrative* sampling combined with low frame rates will cause a small (but potentially significant) error in the calculation of the *ratio of ratios* variable (R_{OS}) that is a function of both pulse rate and arterial oxygen saturation.

The ultimate solution to *integrative* sampling error is higher frame rates, since the integrative sample value will converge towards the sample-and-hold value as the integration time becomes shorter. It may be possible to account for *integrative* sampling error during the calibration phase: pulse oximeters currently store calibration curves (which transform R_{OS} values to S_pO_2) pertaining to all combinations of LED wavelengths used in the probes to which the device may be connected; it is conceivable that this could be extended to encompass several pulse rate regions and in so doing account for integrative error.

The effects of camera-based sampling deserve further investigation. The pulse rate exhibits a continuous and natural variability and the camera's sampling instances are not phase locked with the pulse waveform. It may be possible to apply time-domain system identification techniques to correct the problem prior to the calculation of S_pO_2 .

A nuance of camera-based photoplethysmography discussed in Section 5.5.2, which hints at the potential utility of a camera-based device beyond that of non-contact pulse oximetry, is the detection of inverted PPG signals. This phenomenon highlights the sensitivity of a camera-based device to regional variations in the PPG signal. Blažek et al. (2000), Hülsbusch and Blažek (2002) and Wieringa et al. (2005) highlighted the investigative potential of a device capable of spatially mapping variations in the PPG signal. An important caveat about a camera-based device's ability to perform this task should be stated: a signal observed to be emanating from a point on the tissue surface bears little if any information about the point from which it is emerging; rather, the signal principally contains information pertaining to the region of tissue the light has traversed between the point of entry

into the tissue and the point from which it is observed leaving the tissue. The use of a continuous-wave diffuse illumination scheme (Hülsbusch and Blažek employed a ring of LEDs designed to give even diffuse lighting), annular illumination scheme (as employed by Wieringa et al.), or, to a lesser degree, a large spot (as employed in this study), precludes knowledge of the optical path, making it difficult to attribute a particular PPG signal (which is likely due to the superposition of several paths) to a specific region of tissue.

The choice of illumination scheme has ramifications for pulse oximetry as well. Section 3.2.1 described a number of simplifying assumptions upon which pulse oximetry is based, which free it from the constraints that apply to other forms of Beer-Lambert based oximetry. Specifically the wavelength dependent optical path length and differential path length factor are eliminated from the calculations of oxygen saturation by making two assumptions: first it is assumed that both wavelengths encounter a similar amount of scattering and second it is assumed that the geometrical separation of the source and detector are the same for both wavelengths. Collectively these assumptions imply that both wavelengths of light have travelled a similar path between the source and detector. This assumption is likely invalid for any source that does not closely resemble a point source. Where multiple possible optical paths exist simultaneously between an uncontrolled source and the detector point, the detected light must be considered to be due to the superposition of all potential paths. In the case of an annular illumination scheme illuminating an area of tissue surrounding the imaged region, the detected light at the centre of the image would likely have traversed a volume of tissue similar in shape to an inverted umbrella—completely undermining the assumption of similar paths. The next chapter elaborates on this point to describe how a camera used in conjunction with a controllable light source might be employed as a tomographic imager yielding 3D images vascular anatomy.

It is however the contention of this thesis that despite the added complication and complexity of a camera-based implementation, neither *integrative* sampling nor restrictions on the illumination scheme preclude the achievement of full pulse oximeter functionality by non-contact means.

Lastly this chapter has presented an illustrative analysis of the effect of tissue-camera separation on the number of detectable photons compared to the number detectable under contact conditions. A conic model of the detectable number of photons as a function of the distribution of the photons' trajectories, the distance from the tissue, and the lens radius, has been developed, which in the least is

instructive in providing an intuitive understanding of the effects of increasing separation and in predicting the characteristics of regions of non-contact operation.

CHAPTER 6

A CONCEPT FOR NON-CONTACT CAMERA-BASED BACKSCATTER TOMOGRAPHY

The principal subject of this thesis thus far has been the rigorous design, development, and analysis of camera-based non-contact pulse oximetry and photoplethysmography. In this, the penultimate chapter, both the subject and tone of the thesis change somewhat. During the course of this work a number of camera-based biomedical instruments of novel quality were conceived that might yet spawn future research. This chapter contains an extended (though cursory) description of one such concept that is of singular novelty and which exemplifies the potential of camera-based techniques in biomedical investigations. To that end this chapter describes a novel concept for a non-contact diffuse reflection tomographic imaging device, comprised of a controlled light source and a single camera. Such a device could be an independent investigative tool, capable of imaging and mapping tissue morphology close to the body surface, providing complementary information to haemodynamic measurements and perfusion mapping (provided by a camera-based pulse oximeter) or particularly tissue oxygenation mapping measurements (provided by camera-based tissue oxygenation monitoring). Such a device could also conceivably be amalgamated into an NIR non-contact pulse oximeter or non-contact vital signs monitoring device.

The objective of this chapter is to describe the concept of camera-based tomography rather than to establish the feasibility. Some commentary is provided on potentially suitable apparatus and on foreseeable issues that will be associated with any embodiment of the device. However in the interests of brevity this chapter is limited to a description of the concept followed by a presentation of results from a simplified simulation utilising qualitative data. Only superficial reference is made here to technique's mathematical basis and to the area of tomography.

Two examples of camera-based non-contact surface-vascular imaging systems have been developed, the first by Zeman et al. (2004) and the second by Wieringa et al. (2006). The system developed by Zeman et al., which is comprised of a CCD camera and infrared LED ring light source, is intended to provide vein contrast enhancement for phlebotomists in clinical environments. The system captures an NIR image of a region of tissue and then projects an enhanced visible image back onto the same region of tissue, enhancing the contrast of the veins. The system displays the 2D location of vasculature but no depth information. The system developed by Wieringa et al. is stereoscopic, comprised of two CMOS cameras and an LED array providing both visible and NIR (920 nm) light. By combining the multi-spectral stereoscopic images, the system is capable of selectively enhancing superficial blood vessels, and by virtue of its stereoscopic operation, can perceive the depth of the imaged vasculature. Wieringa et al. list the potential clinical applications of such a device: blood withdrawal; vein inspection in dark skin; vein detection through iodine; varicose vein inspection; and nevi pigmentosum inspection.

Chapter 5 highlighted the importance of knowledge of the likely path light has taken through tissue in interpreting the received light intensity as observed at a point on the tissue surface. As an alternative to the stereoscopic system (utilising an uncontrolled light source) developed by Wieringa et al. (2006), it may be possible to construct a device comprising a single camera and a controllable light source that is capable of 3D imaging of the vasculature close to the tissue surface, by utilising diffuse reflection-based—or more correctly backscatter-based—optical tomography.

Tomography refers to imaging by sections and the most common form is X-ray computed tomography, which is used in many applications to form 3D images of the interior structure of an object. X-rays travel in straight lines through tissue though they are absorbed by dense structures. Computed tomography imagers simultaneously transmit multiple X-ray beams through tissue, the beams strike a

detector that measures the spatial variation in absorption. The source and detector are then rotated relative to the imaged object and another set of measurements made. This process results in a large volume of data to which a reconstruction algorithm is applied, resulting in an image of the interior structure of the imaged object. Two common geometries of computed tomography systems are depicted in Figure 6.1, parallel x-rays incident on a flat detector (the original implementation), and a fan beam emanating from a point source and incident on a curved detector.

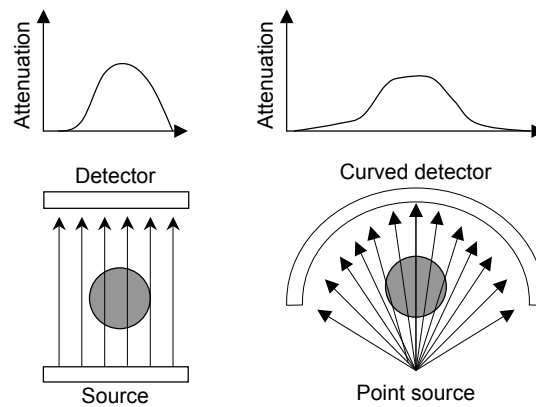


Figure 6.1 Two common source and detector geometries used in X-ray computed tomography.

Optical and NIR light is strongly diffused in tissue and transmission imaging as depicted for X-rays in Figure 6.1 is not generally possible in diffuse optical tomography. Instead the curved path of optical radiation in tissue must be taken into account. In such a system the transmission schemes depicted in Figure 6.1 can be replaced by a geometry as depicted in Figure 6.2.

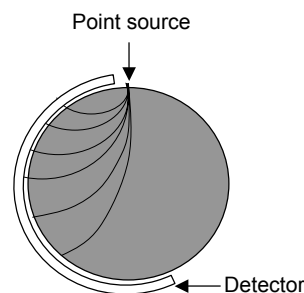


Figure 6.2 Depiction of geometry used in diffuse optical tomography.

The most prevalent biomedical imaging application of diffuse optical tomography is mammography and breast-cancer detection. Though the diffusion of light in tissue makes it difficult to obtain clear optical images of the inside of

biological tissue, the anticipated safety benefits of optical tomography alone (compared to existing X-ray mammography) have spurred research in the area. A comprehensive description of a representative device, its principles, and its capabilities can be found in Colak et al. (1999).

The geometry of the breast necessitates a similar detector geometry, and to that end the system described by Colak et al. (1999) utilises a cup, the walls of which are lined with photodiode detectors. Most of the body surface is however comparatively flat (when viewed in small areas), in this respect a camera may serve as a suitable detector, allowing diffuse optical tomographic reconstruction methods to be employed to form 3D reconstructions of shallow tissue morphology from a 2D camera derived image and multiple purposefully positioned point light sources. The idea is illustrated in Figure 6.3 where the camera images the surface of the tissue and measures the emergent light intensity in response to a point source.

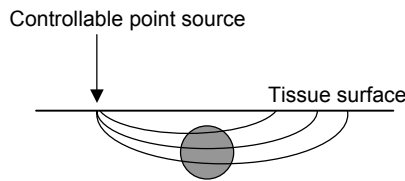


Figure 6.3 Depiction of camera-based tomography concept.

Unlike X-ray tomography where the source and detector are rotated relative to the object, here it is proposed that the camera remain fixed on an area of tissue while the light source is moved across the tissue surface, with each source position generating a different path to each region of the frame. Each region of the frame effectively constitutes a separate detector position and by collating the detected absorption due to many source and detector positions it is proposed to reconstruct a tomographic image of the underlying tissue.

6.1 DESCRIPTION OF CONCEPT

Consider a point source of light perpendicularly incident on the flat surface of a homogenous scattering and absorbing medium. Light from the source enters the medium and is scattered in all directions. Some of the light, having travelled a distance through the medium, is backscattered and detected by the camera, which is observing this region of the medium's surface. Further portions of the incident light

are backscattered from an unobserved area of the surface and a further portion continues to propagate in the medium until it has been absorbed. (The medium is considered infinitely deep and to extend infinitely in the horizontal plane. Furthermore it is assumed that no reflection occurs at the medium's surface.) For a given source position, light detected at a certain position on the medium's surface can be considered most likely to have travelled along a curved path between the source and detector points (refer to the Monte Carlo simulations of such a medium described in Section 2.3.3). The optical characteristics of the medium define the shape of the optical path, while the optical characteristics of the medium in conjunction with the source and detector separation determine the depth of the path. This concept is illustrated graphically in Figure 6.4, in which the most likely paths between five source and detector positions (annotated A – E) are depicted as lines. To illustrate the concept the lines have been arbitrarily chosen as ellipses, defined by a major axis between the source and detector positions and a lower semi-minor axis equal to one third of the major axis' length. Figure 6.4 represents a 2D cross-section of the medium, with the top line representing the medium's surface.

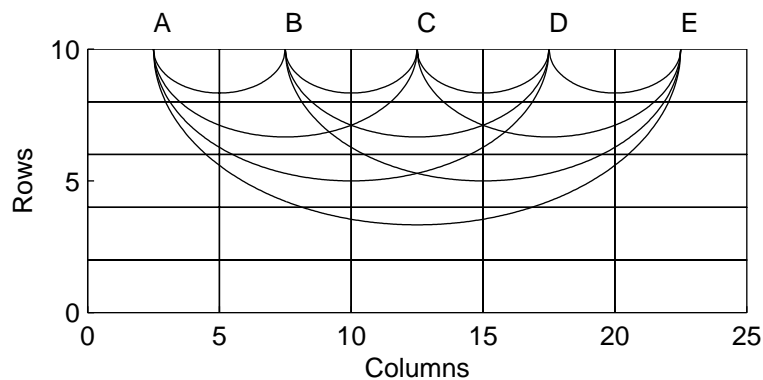


Figure 6.4 Depiction of the most likely paths between five source and detector positions.

Imposed on Figure 6.4 are rectangular voxels used to granularly identify regions of the medium through which the light propagates.

If there are n mutually exclusive source and detector positions (columns of voxels), then the number of possible source and detector groups, choosing one source and detector position at a time, is given by the number of two-element *permutations* of n . Assuming that light is subject to the same attenuation travelling along the path between A and B, as between B and A, the number of unique source and detector groups is given by the number of two-element *combinations* of n ,

$$\text{Number of unique paths} = \frac{n!}{2!(n-2)!} \tag{6.1}$$

The detector locations that form a unique path given a specified source location are enumerated in Table 6.1.

Source position	Detector positions			
A	B	C	D	E
B	-	C	D	E
C	-	-	D	E
D	-	-	-	E

Table 6.1 Unique source and detector positions from available permutations in Figure 6.4.

It is now suggested that the absorption attributable to each voxel along an elliptical path (or a projection in the parlance of tomography) might be determined by the application of existing tomographic algorithms, such that an image of the absorbing structure of the medium can be formed.

With reference to Figure 6.4 it can be seen that many voxels are poorly interrogated by projections, becoming increasingly ill determined with increasing depth, and several are not interrogated at all. This clearly limits the technique to imaging shallow features perhaps the first 2 cm – 3 cm of tissue. While the dependence on backscattered light limits the technique to surface features, it is within the realm targeted by the devices of Zeman et al. (2004) and Wieringa et al. (2006). However within this depth constraint, increasing the number of source and detector positions—that is narrowing the voxels—greatly increases the determinability of shallow voxels. Figure 6.5 depicts the same area as Figure 6.4 now interrogated by three hundred unique projections resulting from twenty-five columns of voxels.

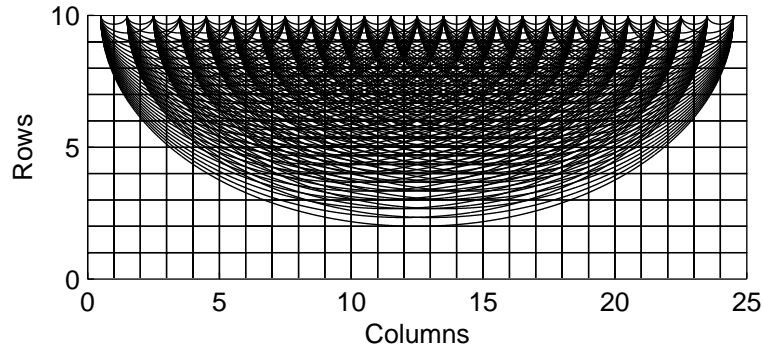


Figure 6.5 Depiction of elliptical projections for twenty-five source and detector points (yielding three hundred unique projections).

The next section describes the application of an existing tomographic reconstruction algorithm to data obtained from a 2D phantom by simplified forward modelling.

6.2 FORWARD MODELLING AND RECONSTRUCTION

To provide a qualitative indication of the degree of reconstruction that can be attained by elliptical projections, a simulation is described here that applies an algebraic reconstruction algorithm to a set of test data obtained from a simplified forward model of elliptical propagation through a 2D phantom.

6.2.1 FORWARD MODEL

A simplified 2D phantom was constructed as a monochrome raster graphic consisting of several discrete absorbing regions embedded in an otherwise non-absorbing medium. The pattern used is depicted in Figure 6.6. The phantom itself has no inherent scattering properties; rather the projection paths are predetermined as a function of the source and detector separation, again they are arbitrarily chosen as ellipses with a semi-minor axis to major axis ratio of 1:3.

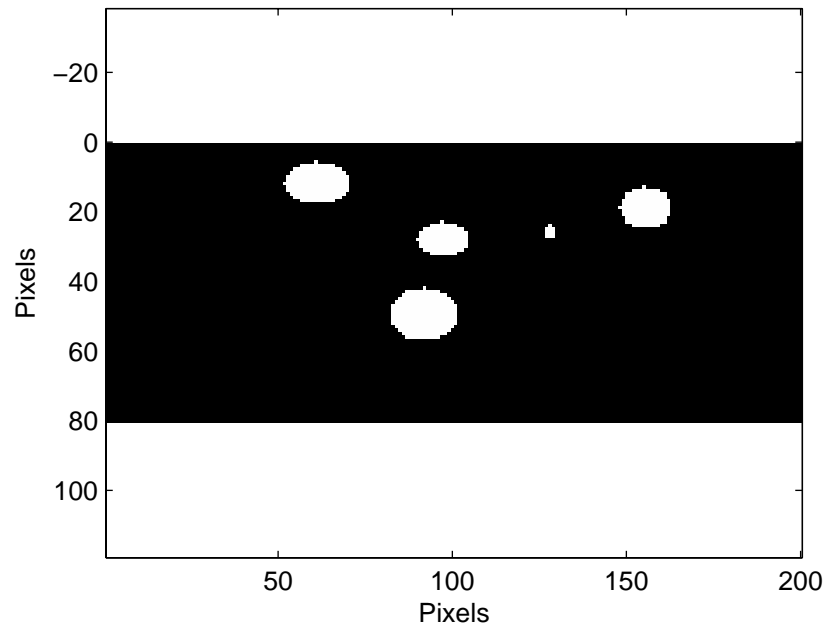


Figure 6.6 2D phantom showing absorbing regions (white) in a non-absorbing medium (black).

Prior to projection the 2D phantom is converted to a voxel format, with each voxel consisting of one or more pixels. Where a voxel consists of several pixels the binary absorbency of that voxel is determined by the fraction of absorptive pixels that it contains, with the absorbency of the voxel being set to one if half or more of its constituent pixels are absorbing. Figure 6.7 depicts the voxel representation of the phantom depicted in Figure 6.6; each voxel in Figure 6.7 has dimensions four horizontal and four vertical pixels that span the entire width of the 2D phantom. Thus the phantom is divided into fifty columns (and twenty rows) of voxels that generate 1225 projections.

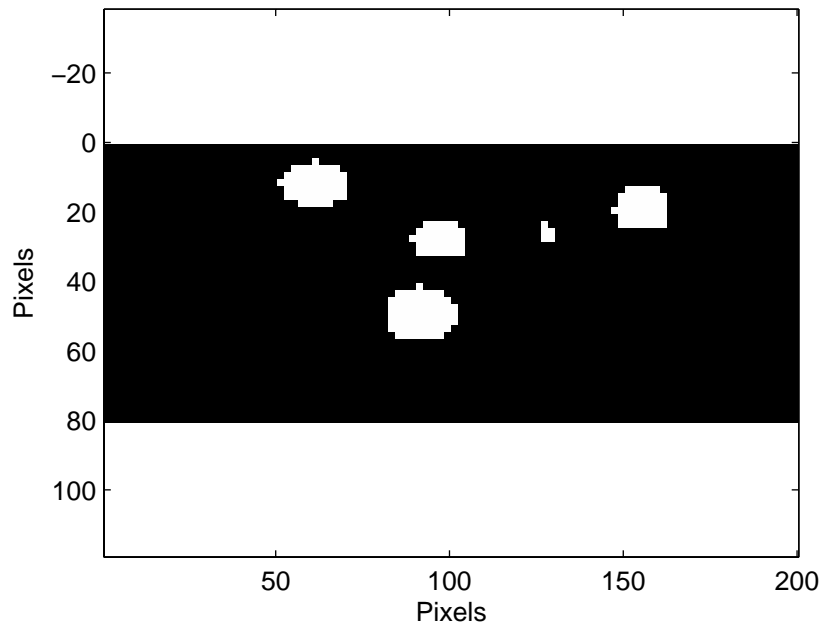


Figure 6.7 Conversion of original image so that twenty rows and fifty columns of voxels, rather than pixels, describe the absorption.

A projection is made from each source position (columns 1 to 49) to each detector position (columns 2 to 50) with an initial weight of one. Each time a projection passes through an absorbing voxel it loses half its weight (an arbitrarily chosen absorption). The source is then moved to the next position and the process is repeated noting the received weight for each source and detector position. In this way a matrix is constructed of the form depicted in Table 6.1 in which each row corresponds to a source position and each column to a detector position. This matrix represents a description of the absorptive characteristics of the medium as observed by elliptical projections through the medium.

It is now sought to evaluate the efficacy of the elliptical projection by applying a reconstruction algorithm to the matrix of absorption values.

6.2.2 ALGEBRAIC RECONSTRUCTION

Various tomographic techniques exist for reconstructing a model (both 2D and 3D) of tissue based on the observed attenuation of radiation. In general these methods can be categorised as being direct (including filtered back projections and Fourier reconstruction) or iterative. An iterative method of reconstruction is employed here based on an algebraic reconstruction technique (ART) (Brooks and Di Chiro 1976; Herman 1980).

The reconstruction algorithm begins by taking a conservatively small fraction of the absorption observed along one projection (obtained by forward modelling) and assigning that fraction to each voxel along that projection. This is repeated for each projection. Some voxels will be traversed by multiple projections and will thus accumulate a fraction of the observable absorption from each of those projections. This represents an initial guess at the voxel absorption coefficients and constitutes the first iteration.

On subsequent iterations the expected amount of absorption for a particular source and detector combination is calculated using the current absorption coefficients of the voxels that lie along that projection. A small fraction of the difference between the expected and observed absorption for that projection (which can be positive or negative) is now added to the voxel coefficients along that projection. The process is repeated for many iterations (typically several hundred). While many voxels are erroneously attributed a small level of absorption, over many iterations bright spots emerge at the intersection of projections that experienced absorption.

Figure 6.8 displays a reconstruction of the phantom depicted in Figure 6.7. The reconstruction can be seen to display each of the components of the phantom though they appear smeared. The deeper regions of the phantom are less well determined since fewer projections traverse these regions.

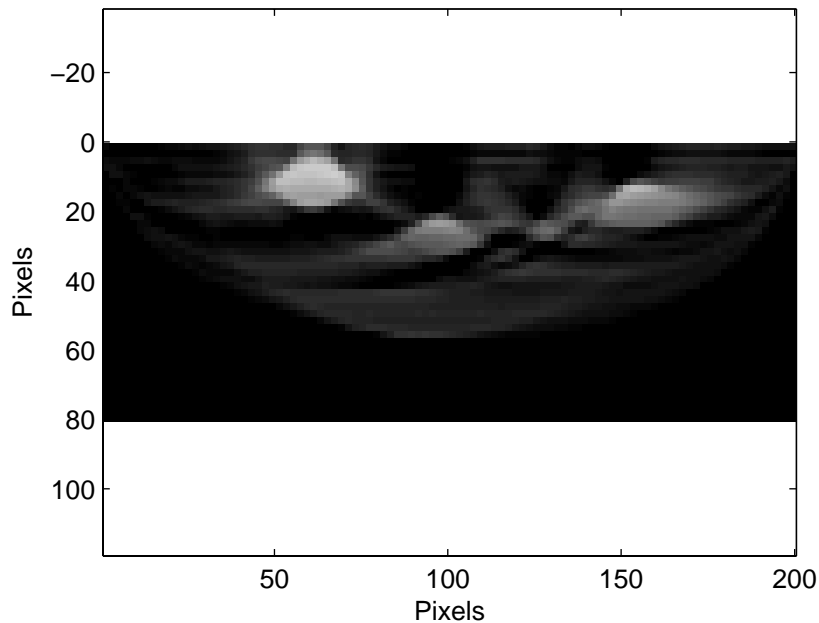


Figure 6.8 ART reconstruction based on elliptical line projections.

The algorithm employed here inherently gives rise to false positives—that is many voxels are falsely attributed an absorption because of absorptive regions that lie elsewhere along a projection. However since a projection cannot traverse an absorbing region without suffering some absorption, the image can be improved by zeroing all voxels along projections that registered no absorption—effectively discounting reports of absorption where there exists evidence to the contrary. Figure 6.9 displays the effect on the reconstruction of zeroing the identifiable false positives.

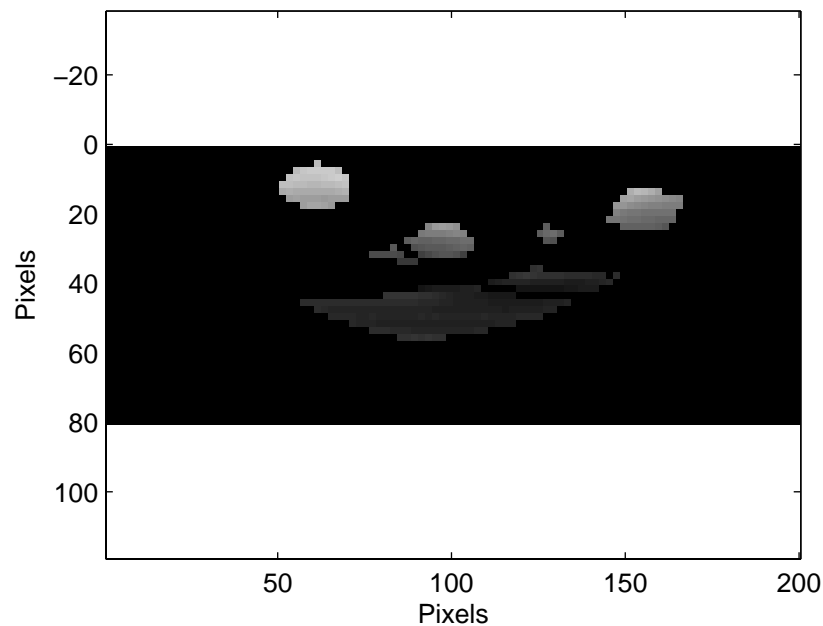


Figure 6.9 Reconstruction by elliptical line projection after zeroing of false positives.

The reconstructions depicted in Figure 6.8 and Figure 6.9 are the result of projections along elliptical lines—a gross simplification of the distribution of light in tissue. A more realistic approach is to assume that the projections form elliptical beams. To test the efficacy of reconstruction under this condition the forward modelling was repeated replacing the elliptical lines with beams. Each beam is formed of several elliptical paths, again with a major axis defined between the current source and detector position, however the semi-minor axis is now chosen to be one third of the major axis plus a small normally distributed random number with a magnitude proportional to the current length of the major axis. For each constituent elliptical line in the beam, a small amount of noise (proportional to the length of the major axis) is added to the y -coordinate of each point. The resulting beams are depicted in Figure 6.10 for five columns of voxels (for clarity only the

projections corresponding to the first source position are illustrated). This mimics crudely the migration of photons between source and detector that is known from photon modelling studies.

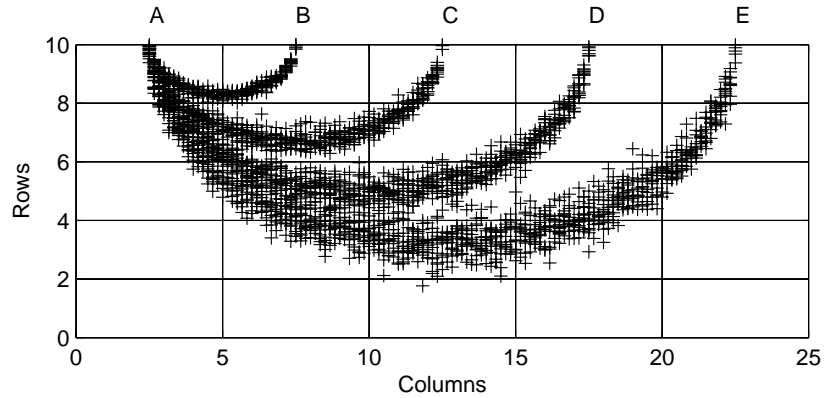


Figure 6.10 Elliptical beam projections corresponding to source position A.

The reconstruction that results from elliptical beam projections is depicted in Figure 6.11. The reconstruction can be seen to incorporate the large features of the 2D phantom, though the small detail is less well defined and the lower voxels are under determined compared to both the phantom and the reconstruction based on elliptical line projections.

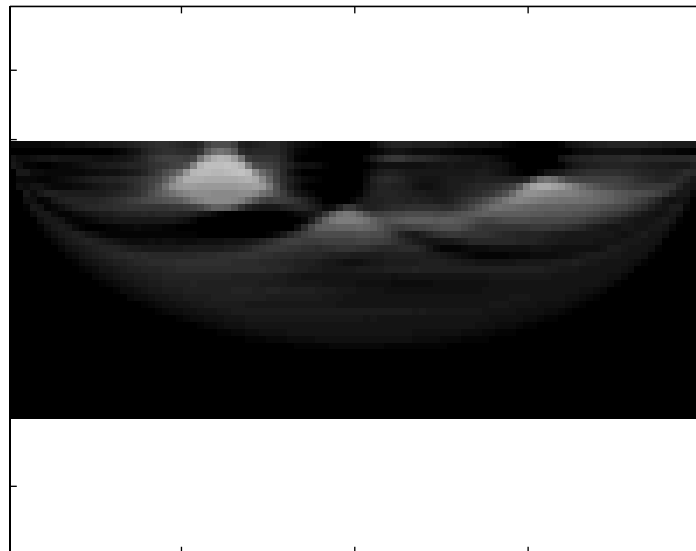


Figure 6.11 ART reconstruction based on elliptical beam projections.

False positives can again be identified and zeroed, which produces the reconstruction depicted in Figure 6.12.

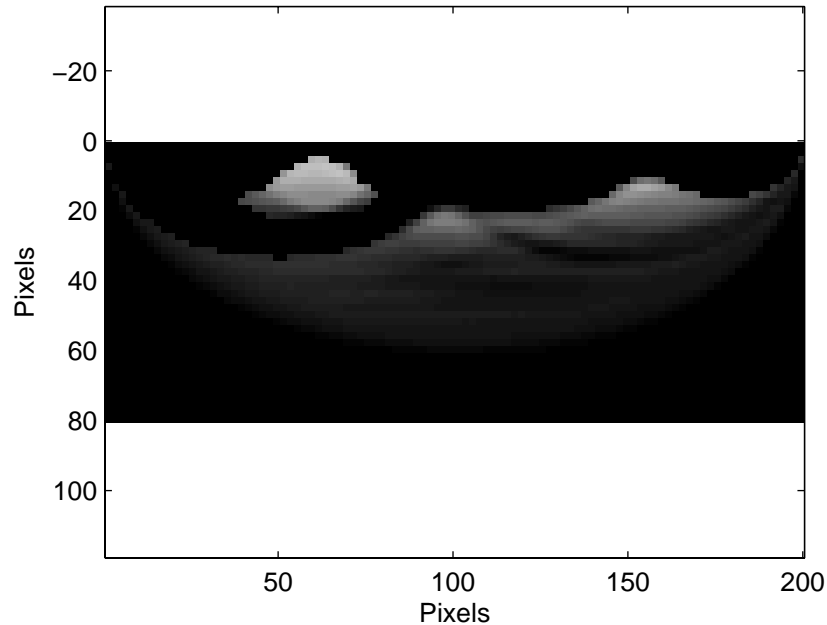


Figure 6.12 Reconstruction by elliptical beam projection after zeroing of false positives.

6.3 DISCUSSION

The description that is provided here is deliberately succinct and is intended firstly to illustrate the concept, and secondly to illustrate the level of reconstruction that might be achieved in ideal circumstances (with elliptical line projections) and under more realistic circumstances (elliptical beam projections). That an ART algorithm (intended for rectilinear X-ray projection) is suited to this form of projection is not at all obvious and no attempt is made here to identify or develop an optimal reconstruction algorithm.

The reconstructions based on elliptical beam projections, depicted in Figure 6.11 and Figure 6.12, represent a realistic approximation of the path of light in tissue, however the model inherently encompasses several important simplifications. The model assumes a point source of light and a point detector. In practice the light source would likely be a laser beam with a small elliptical cross-section. As was discussed in Section 2.3.3 in relation to Monte Carlo simulations, distribution of the photon paths in tissue resulting from a beam source is obtained by

convolving the distribution due to a point source with the shape of the beam. This would enlarge the projections. A further complication is the detector, which will not be a single point. In the case of a camera the detector will be defined as either a single rectangular pixel, a rectangular group of pixels, or a pixel approximation of an elliptical (including circular) detector region—adding further to the three dimensional broadening of the projection.

Nonetheless a device based on this concept could be constructed from a Galvo-scanner (capable of projecting laser spot on a specified location or in a specified pattern) and camera. The requirements of the camera would differ markedly from those of a camera intended for pulse oximetry and photoplethysmography, sensitivity (SNR and dynamic range) being paramount and frame rate being comparatively unimportant.

CHAPTER 7

DISCUSSION AND FUTURE WORK

7.1 A SYNOPSIS OF THE CONTRIBUTIONS OF THIS THESIS

This thesis has investigated the feasibility of non-contact remote camera-based pulse oximetry. To that end this research has produced the first report of the simultaneous detection of two PPG signals at different wavelengths by a non-contact camera-based technique. The method and apparatus used have been shown to be applicable to a range of test subjects under realistic lighting and environmental conditions.

While other researchers have investigated camera-based photoplethysmography, both previously and contemporarily, those that have sought to extend camera-based photoplethysmography to pulse oximetry have made two crucial assumptions: firstly that the separate capture of PPG signals at multiple wavelengths is readily extendable to simultaneous multiplexed capture; and secondly that camera-based PPG signals are applicable to the technique of pulse oximetry. These two assumptions are important in demarcating this thesis from contemporary research by others. Having demonstrated simultaneous dual wavelength photoplethysmography, this thesis has subsequently scrutinised the assumption that the

resulting PPG signals are either directly or inherently applicable to the method of pulse oximetry.

This thesis has investigated and demonstrated the comparability of a camera-based device with a conventional contact device, as a means of obtaining a detailed plethysmogram and as a means of measuring pulse rate. As a means of determining arterial oxygen saturation by the method of pulse oximetry, this thesis has highlighted the susceptibility of camera-based devices to two detrimental phenomena that are precluded in contact devices. The first is the combined effect of low frame rates and *integrative* sampling, which collectively distort the camera-derived PPGs and introduce error into the ratio calculations from which arterial saturation is derived. The second phenomenon is the proclivity (or perhaps *ability*) of camera-based systems, when used in conjunction with an uncontrolled light source, to detect PPG signals that pertain to unwanted, different, or multiple volumes of tissue, which violates an enabling assumption of pulse oximetry—that the two detected wavelengths of light have traversed the same path.

A secondary and perhaps less tangible contribution of this thesis is in delineating the capabilities that camera-based S_pO_2 monitoring can attain as an instance of pulse oximetry—estimate S_pO_2 , measure pulse rate and display a PPG—but not provide a spatial map of arterial oxygen saturation, which should not exhibit a spatial variance. In circumstances where a camera-based device may indicate a spatial variance in the estimated value of S_pO_2 (that is greater than the precision of the device), it is hoped that the discussion throughout this thesis has highlighted the danger in attributing that variation to an actual change in the saturation of the passing arterial blood, rather than to any of the multifarious factors that may distort the locally observed PPG signals from which the saturation values have been derived. Where a camera-based device may possess additional utility, beyond that which may come from non-contact pulse oximetry, it is likely in its ability to observe spatial variation in PPG signals (with the caveat that the light source is controllable), of which more is said in the next section.

Lastly this thesis describes a concept for a camera-based tomography system comprised of a single camera and a controllable point source such as a Galvo-scanner and laser. Such a device represents a departure from camera-based haemodynamic investigations and is presented as an alternative to stereoscopic methods of imaging shallow features in tissue. While such a system would not necessarily share requirements with a camera-based pulse oximetry device it is an

indicator to the potential of camera-based NIR investigations of tissue as both a probe of blood and tissue chemistry as well as structure.

7.2 FUTURE WORK

In investigating the feasibility and practicalities of non-contact pulse oximetry, this research has identified both further unforeseen impediments as well as new potential. The objectives of future work should encompass both further research and new development and adaptation of these techniques to real-time operation.

7.2.1 FURTHER RESEARCH INTO CAMERA-BASED PULSE OXIMETRY

The inherent distortion of PPG signals resulting from camera-based capture was highlighted in Section 5.4.4, where simulation results were described that showed an error caused by the camera's *integrative* sampling and low frame rates. The simulation pertained to the *ratio of ratios* method of calculating R_{OS} , however it is worth investigating the susceptibility of the alternative *derivative* based methods of calculating R_{OS} , or indeed investigating if a method of calculating R_{OS} can be developed that is insensitive to PPG distortion by *integrative* sampling.

Since *integrative* sampling is inherent to all camera-based observations of time-varying signals, a worthwhile alternative or parallel approach would be the development of techniques to correct or mitigate the effects of *integrative* sampling. Time-domain system identification techniques may be applicable.

7.2.2 INVESTIGATION OF CAMERA-DERIVED PPG SIGNALS

Section 3.4.3 listed some of the applications to which conventional pulse oximeter devices have been put since becoming commonplace in clinical and surgical environments. Many of those applications utilise the ability of a pulse oximeter device to non-invasively measure perfusion and spatial variations in perfusion through the PPG waveform—applications that have been made possible by the development of reflectance probes and specialised application specific probes. Camera-based photoplethysmography has a great deal of potential in this regard as an investigative tool.

A further point that should be made is that a PPG signal is comprised of several components including the pulse, respiration, and Mayer waves. Pulse oximetry is concerned only with the pulse component though other clinical and experimental applications may be equally interested in the remaining components. The spectral power method of locating PPG signals in a video described in Section 5.3.3 is equally applicable to searching a video for respiration or Mayer waves. Indeed with reference to Figure 5.15 a signal that is rejected by the spectral power figure of merit as not containing a strong pulse may still contain a significant respiration or Mayer wave component.

Whichever the desired PPG component, it should be noted that the video will contain multiple instances of the signal from different areas of tissue. Where the objective is merely to monitor that signal (rather than to attribute significance to its spatial variance), a camera-based technique may offer the potential for high SNR by incorporating the signal from multiple detection sites in the frame.

The richness of a camera signal makes the notion of a non-contact vital signs monitoring device seem plausible. A device might be envisioned capable of non-contact measurement of pulse rate, S_pO_2 , respiration, and display of the peripheral arterial pressure waveform.

7.2.3 DEVELOPMENT OF A CLINICALLY USEFUL DEVICE

Perhaps the most significant step towards a clinically useful device is the development of real-time operating capabilities. A practical device would likely require dedicated hardware and software, providing the functionality described in this thesis as well as a suitable user interface and mechanism for maintaining the desired region of tissue in frame and under illumination.

CMOS is likely the camera technology of choice particularly because of its ability to produce variable frame sizes and consequently varying frame rates. One can envision a system that produces large frame sizes (and low frame rates) during a signal acquisition period or during periods of subject movement, keeping a large area of tissue in view, and smaller frame sizes (at increased frame rates) during stable monitoring.

Real-time operation would also require the development of significant ancillary functionality, for example motion artefact reduction or compensation. Efficient means of identifying regions of interest within the frame that contain a

pulse signal—or a respiration or Mayer wave if they are the sought signals—need to be developed.

A real-time device will require the development of efficient and robust image analysis and image and signal processing techniques.

The second major step in the development of a clinical device is calibration. Though the effects of *integrative* sampling and low frame rates have yet to be quantified, assuming they can be mitigated, a non-contact device should be suited to a similar in vivo calibration procedure as is currently used with conventional devices (see Section 3.3.5). If the pulse rate and saturation dependent effects of *integrative* sampling cannot be mitigated by either system identification techniques or a purposefully designed method of calculating R_{OS} , then it may fall to the calibration procedure to remove pulse rate and saturation dependent error due to *integrative* sampling.

7.2.4 INVESTIGATION OF SINGLE CAMERA-BASED TOMOGRAPHY

Camera-based backscatter tomography utilising one camera and a controlled light source is a departure from non-contact pulse oximetry and photoplethysmography. Such a system would likely achieve greater synergy with NIR tissue oxygenation measurement or as part of a multi-modality tissue morphology imaging system. The development of such a device would incorporate a large scope including instrumentation and optics design, image processing, image analysis, and reconstruction algorithm development.

7.3 CONCLUDING REMARKS

Camera-based non-contact pulse oximetry will not replace conventional devices in routine bedside monitoring applications or ambulatory monitoring. Its most likely field of initial application is as an investigative tool in research, in specialised applications and environments, or in conjunction with other modalities such as MRI.

Obstacles remain to developing a clinically useful device. Other researchers investigating camera-based photoplethysmography have pointed to camera limitations including low SNR and dynamic range, as well as motion artefacts and ambient light interference as current obstacles. While any system would doubtlessly benefit from a camera with improved SNR and dynamic range, simultaneous dual

wavelength PPG capture has been demonstrated as being achievable with currently available technology. Cameras capable of producing comparable or better SNR performance at higher frame rates will be beneficial. Motion artefacts will certainly be an issue in the future and may be a significant constraint on the applications to which a camera device may be put. Further investigation is needed on a wide range of subjects to quantify the effects of physical variation among subjects such as fat and skin pigmentation and to identify regions of the body from which signals can be reliably obtained.

Despite impediments to developing clinically useful devices the allure of non-contact pulse oximetry and photoplethysmography is strong. Collectively they represent a step towards video based vital signs monitoring and video based biometrics in general.

APPENDIX A

PUBLICATIONS ARISING FROM THIS WORK

This appendix contains a list of peer-reviewed publications that arose from this work. Papers pertaining to camera-based pulse oximetry and camera-based photoplethysmography are additionally cited, in context, in the body of this thesis and as such appear in the list of references. The full reference of each paper is reproduced here along with its published abstract as a guide to its contents.

The list is preceded by a reference to an article on medical applications of Terahertz. Though the body of this thesis reports exclusively on a near infrared investigation of pulse oximetry and photoplethysmography, this work originally began as a search for a medical application of Terahertz imaging. Terahertz refers to a band of the electromagnetic spectrum stretching from the upper microwave frequencies, through the far infrared, and into the mid infrared—encompassing wavelengths from approximately 3 mm to 10 μm . Terahertz radiation is apt to monitoring the moisture content of tissue and has been demonstrated to be capable of discerning cancerous tissue from tissue that is healthy, and also from tissue that is inflamed but otherwise normal. A dual modality imaging system was sought (utilising Terahertz and near infrared) to develop a means of objectively assessing and monitoring the progression and condition of pressure ulcers, which can result from sustained pressure and shearing force on tissue as may occur in people who are immobile. It was envisaged that Terahertz would provide structural information about a region of tissue while near infrared imaging would provide information about tissue dynamics such as perfusion, oxygenation, and hydration.

Humphreys K., J. Loughran, M. Gradziel, W. Lanigan, T. Ward, J.A. Murphy and C. O'Sullivan, Medical applications of terahertz imaging: a review of current technology and potential applications in biomedical engineering, *In proceedings of the IEEE Engineering in Medicine and Biology Society Conference*, 2004.

Terahertz (THz) imaging is in its early stages of development but already the potential clinical impact of this new imaging modality is clear. From cancer research to DNA analysis THz technology is improving or even making possible imaging of hitherto inaccessible phenomena. In this paper we present a short review of THz imaging from the point of view of biomedical engineering. We discuss the current state of the art in terms of THz imaging systems; describe current applications, future potential and our own approaches to harnessing this novel technology. We draw attention to open problems in the area with respect to the limitations of the technology before concluding with descriptions of our future work in the area.

Humphreys K., C. Markham and T. Ward, A CMOS camera-based system for clinical photoplethysmographic applications, *In proceedings of SPIE*, 5823, 88-95, 2005.

In this work an-image based photoplethysmography (PPG) system is developed and tested against a conventional finger-based system as commonly used in clinical practise. A PPG is essentially an optical instrument consisting of a near infrared (NIR) source and detector that is capable of tracking blood flow changes in body tissue. When used with a number of wavelengths in the NIR band blood oxygenation changes as well as other blood chemical signatures can be ascertained yielding a very useful device in the clinical realm. Conventionally such a device requires direct contact with the tissue under investigation which eliminates the possibility of its use for applications like wound management where the tissue oxygenation measurement could be extremely useful. To circumnavigate this shortcoming we have developed a CMOS camera-based system, which can successfully extract the PPG signal without contact with the tissue under investigation. A comparison of our results with conventional techniques has yielded excellent results.

Humphreys K., T. Ward and C. Markham, A CMOS camera-based pulse oximetry imaging system, *In proceedings of the IEEE Engineering in Medicine and Biology Society Conference*, 2005.

In this paper a CMOS camera-based system for non-contact pulse oximetry imaging in transmission mode is described. Attention is drawn to the current uses of conventional pulse oximetry and the potential application of pulse oximetry imaging to developing objective wound assessment systems.

Humphreys K., T. Ward and C. Markham, A CMOS camera-based system for non-contact pulse oximetry imaging, *In proceedings of the International Federation for Medical and Biological Engineering Conference*, 11, 2005.

In this paper a non-contact pulse oximetry imaging system is described. The system utilises a CMOS digital camera and near infrared (NIR) light emitting diodes operating in a reflection mode to simultaneously capture photoplethysmograph (PPG) signals at two wavelengths. The Modified Beer-Lambert law is used to extrapolate tissue oxygenation from the PPG signals. Attention is drawn to the system's potential in applications such as the assessment and management of wounds.

Humphreys K., T. Ward and C. Markham, Noncontact simultaneous dual wavelength photoplethysmography: A further step toward noncontact pulse oximetry, *Review of Scientific Instruments*, 78, (4), 2007.

We present a camera-based device capable of capturing two photoplethysmographic (PPG) signals at two different wavelengths simultaneously, in a remote noncontact manner. The system comprises a complementary metal-oxide semiconductor camera and dual wavelength array of light emitting diodes [760 and 880 nm]. By alternately illuminating a region of tissue with each wavelength of light, and detecting the backscattered photons with the camera at a rate of 16 frames/wavelengths, two multiplexed PPG wave forms are simultaneously captured. This process is the basis of pulse oximetry, and we describe how, with the inclusion of a calibration procedure, this system could be used as a noncontact pulse oximeter to measure arterial oxygen saturation (S_pO_2) remotely. Results from an experiment on ten subjects, exhibiting normal S_pO_2 readings, that demonstrate the instrument's ability to capture signals from a range of subjects under realistic lighting and environmental conditions are presented. We compare the signals captured by the noncontact system to a conventional PPG signal captured concurrently from a finger, and show by means of a J. Bland and D. Altman [Lancet 327, 307 (1986); Statistician 32, 307 (1983)] test, the noncontact device to be comparable to a contact device as a monitor of heart rate. We highlight some considerations that should be made when using camera-based "integrative" sampling methods and demonstrate through simulation, the suitability of the captured PPG signals for application of existing pulse oximetry calibration procedures.

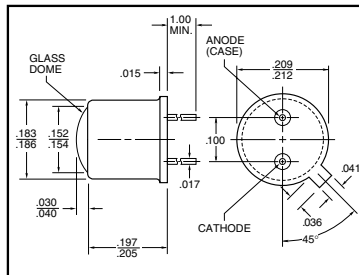
APPENDIX B

FURTHER CHARACTERISTICS OF THE LIGHT EMITTING DIODES

As a further indication of the characteristics of the light emitting diodes used in this study a sample data sheet is included here illustrating the various electrical, thermal and optical parameters of a typical device.

HIGH-POWER GaAlAs IR EMITTERS

OD-880F



FEATURES

- High reliability liquid-phase epitaxially grown GaAlAs
- 880nm peak emission for optimum matching with ODD-45W photodiode
- Wide range of linear power output
- Hermetically sealed TO-46 package
- Narrow angle for long distance applications
- OD-880F1 selected to meet minimum radiant intensity

All surfaces are gold plated. Dimensions are nominal values in inches unless otherwise specified. Window caps are welded to the case.

ELECTRO-OPTICAL CHARACTERISTICS AT 25°C

PARAMETERS	TEST CONDITIONS	MIN	TYP	MAX	UNITS
Total Power Output, P _O	OD-880F OD-880F1	15	17		mW
Radiant Intensity, I _e	OD-880F OD-880F1	120	135		mW/sr
Peak Emission Wavelength, λ _p			880		nm
Spectral Bandwidth at 50%, Δλ			80		nm
Half Intensity Beam Angle, θ			8		Deg
Forward Voltage, V _F	I _F = 100mA		1.55	1.9	Volts
Reverse Breakdown Voltage, V _R	I _R = 10μA	5	30		Volts
Capacitance, C	V _R = 0V		17		pF
Rise Time			0.5		μsec
Fall Time			0.5		μsec

ABSOLUTE MAXIMUM RATINGS AT 25°C CASE

Power Dissipation ¹	190mW
Continuous Forward Current	100mA
Peak Forward Current (10μs, 400Hz) ²	3A
Reverse Voltage	5V
Lead Soldering Temperature (1/16" from case for 10sec)	240°C

¹Derate per Thermal Derating Curve above 25°C

²Derate linearly above 25°C

THERMAL PARAMETERS

Storage and Operating Temperature Range	-55°C to 100°C
Maximum Junction Temperature	100°C
Thermal Resistance, R _{THJA} ¹	350°C/W Typical
Thermal Resistance, R _{THJA} ²	115°C/W Typical

¹Heat transfer minimized by measuring in still air with minimum heat conducting through leads

²Air circulating at a rapid rate to keep case temperature at 25°C

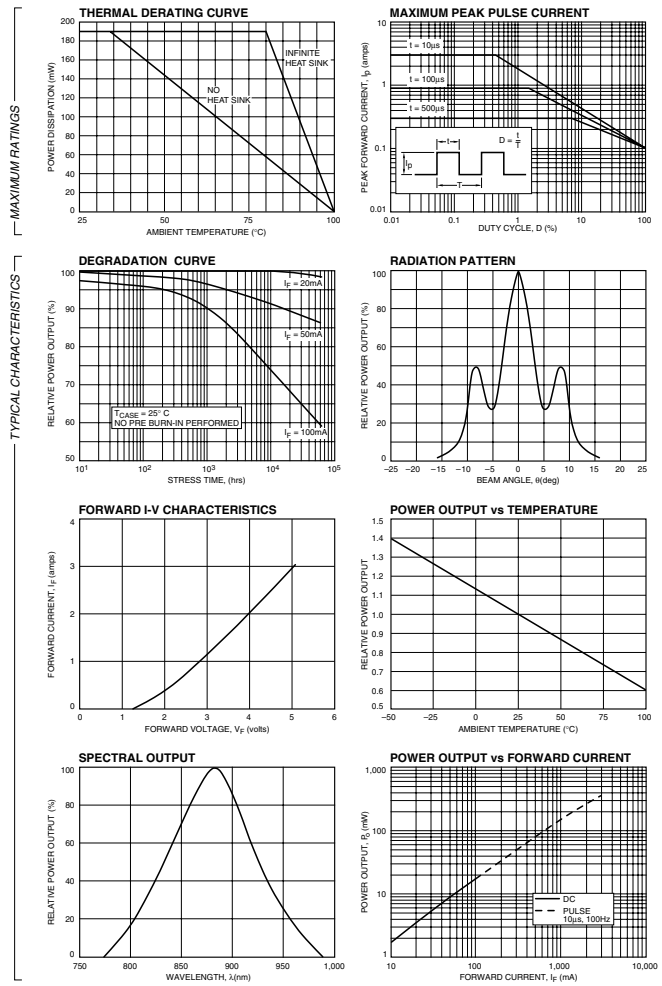


OPTO DIODE CORP.

750 Mitchell Road, Newbury Park, California 91320
Phone: (805) 499-0335 Fax: (805) 499-8108
Email: sales@optodiode.com Web Site: www.optodiode.com

HIGH-POWER GaAlAs IR EMITTERS

OD-880F



OPTO DIODE CORP.

750 Mitchell Road, Newbury Park, California 91320
 Phone: (805) 499-0335 Fax: (805) 499-8108
 Email: sales@optodiode.com Web Site: www.optodiode.com

REFERENCES

- Altman D. and J. Bland, Measurement in medicine: the analysis of method comparison studies, *The Statistician*, 32, 307-317, 1983.
- Aoyagi T., Pulse oximetry: Its origin and development, *In proceedings of IEEE Engineering in Medicine and Biology Society Conference*, 14, 1992.
- Aoyagi T., Pulse oximetry: its invention, theory, and future, *Journal of Anesthesia*, 17, (4), 259-66, 2003.
- Aoyagi T. and K. Miyasaka, Pulse oximetry: its invention, contribution to medicine, and future tasks, *Anesthesia and Analgesia*, 94, (1 Suppl), S1-3, 2002.
- Arridge S. R., M. Schweiger, M. Hiraoka and D. T. Delpy, A finite element approach for modeling photon transport in tissue, *Medical Physics*, 20, (2 Pt 1), 299-309, 1993.
- Attas M., M. Hewko, J. Pologe, T. Posthumus, M. Sowa and H. Mantsch, Visualization of cutaneous hemoglobin oxygenation and skin hydration using near-infrared spectroscopic imaging, *Skin Research and Technology*, 7, (4), 238-245, 2001.
- Barker S. and K. Tremper, Transcutaneous oxygen tension: a physiological variable for measuring oxygen tension, *Journal of Clinical Monitoring*, 1, (2), 130-134, 1984.
- Bland J. and D. Altman, Statistical methods for assessing agreement between two methods of clinical measurement, *Lancet*, 327, (8476), 307-310, 1986.

- Blazek V., T. Wu and D. Holscher, Near-infrared CCD imaging - possibilities for noninvasive and contactless 2D mapping of dermal venous hemodynamics, *Proceedings of SPIE*, 3923, 2-9, 2000.
- Bonner R. F., R. Nossal, S. Havlin and G. H. Weiss, Model for photon migration in turbid biological media, *Journal of the Optical Society of America A*, 4, (3), 423-432, 1987.
- Bourgeois B. W. J., *Design of Pulse Oximeters*, Chapter 5, Ed. J. G. Webster, Taylor and Francis Group, New York, 1997.
- Bozkurt A. and B. Onaral, Safety assessment of near infrared light emitting diodes for diffuse optical measurements, *Biomedical Engineering Online*, 3, (9), 2004.
- British Standards, BS EN 60825-1, Safety of laser products, 1994.
- Brooks R. A. and G. Di Chiro, Principles of computer assisted tomography (CAT) in radiographic and radioisotopic imaging, *Physics in Medicine and Biology*, 21, (5), 689-732, 1976.
- Bunn H. F., *Hemoglobin: molecular, genetic and clinical aspects*, Saunders, Philadelphia, 1986.
- Chan F. C., M. J. Hayes and P. R. Smith, Venous Pulse Oximetry, *United Kingdom Patent: PCT/GB2003/000427*, 2003.
- Cheung P., K. Gauglitz, S. Hunsaker, S. Prosser, D. Wagner and R. Smith, Apparatus for the automatic calibration of signal employed in pulse oximetry, *United States Patent: 5259381*, 1989a.
- Cheung P., K. Gauglitz, L. Mason, S. Prosser, R. Smith, D. Wagner and S. Hunsaker, Feedback controlled method and apparatus for processing signals used in oximetry, *United States Patent: 4819646*, 1989b.
- Chung C. and H. M. McNamara, Fetal pulse oximetry apparatus and method of use, *United States Patent: 5005573*, 1993.

- Clark S. A., *Design of Pulse Oximeters*, Chapter 1, Ed. J. G. Webster, Taylor and Francis Group, New York, 1997.
- Clayton D., R. Webb, A. Ralston, D. Duthie and W. Runciman, A comparison of the performance of 20 pulse oximeters under conditions of poor perfusion, *Anaesthesia*, 46, (1), 3-10, 1991a.
- Clayton D. G., R. K. Webb, A. C. Ralston, D. Duthie and W. B. Runciman, Pulse oximeter probes. A comparison between finger, nose, ear and forehead probes under conditions of poor perfusion, *Anaesthesia*, 46, (4), 260-5, 1991b.
- Colak S., M. van der Mark, G. Hooft, J. Hoogenraad, E. van der Linden and F. Kuijpers, Clinical optical tomography and NIR spectroscopy for breast cancer detection, *IEEE Journal of Selected Topics in Quantum Electronics*, 5, (4), 1143-1158, 1999.
- Cope M., *The development of a near infrared spectroscopy system and its application for non invasive monitoring of cerebral blood flow and tissue oxygenation in the newborn infant*, Ph.D. thesis, University College London, 1991.
- Coyle S., *Near-infrared spectroscopy for brain computer interfacing*, Ph.D. thesis, National University of Ireland, Maynooth, 2005.
- Coyle S., T. Ward, C. Markham and G. McDarby, On the suitability of near-infrared (NIR) systems for next-generation brain-computer interfaces, *Physiological Measurement*, 25, (4), 815-822, 2004.
- Coyle S., T. Ward, C. Markham, B. Roche, G. McDarby and S. McLoone, The use of near-infrared spectroscopy in measuring general autonomic arousal, *In proceedings of World Congress on Medical Physics and Biomedical Engineering*, 2003.
- Curtis H. and N. S. Barnes, *Biology*, 5th edition, Worth, New York, 1989.
- de Kock J., K. Reynolds, L. Tarassenko and J. Moyle, The effect of varying LED intensity on pulse oximetry accuracy, *Journal of Medical Engineering and Technology*, 15, (3), 111-116, 1991.

- de Kock J., L. Tarassenko, C. J. Glynn and A. R. Hill, Reflectance pulse oximetry measurements from the retinal fundus, *IEEE Transactions on Biomedical Engineering*, 40, (8), 817-823, 1993.
- Dempsey M. and B. Condon, Thermal injuries associated with MRI, *Clinical Radiology*, 56, 457-465, 2001.
- DeNobile J., P. Guzzetta and K. Patterson, Pulse oximetry as a means of assessing bowel viability, *Journal of Surgical Research*, 48, 21-23, 1990.
- Diamond J., *Guns, Germs and Steel*, Chatto and Windus, London, 1997.
- Elwell C., *A practical users guide to near infrared spectroscopy*, UCL Reprographics, London, 1995.
- Farmer J., *Design of Pulse Oximeters*, Chapter 3, Ed. J. G. Webster, Taylor and Francis Group, New York, 1997.
- Fazan V. P., C. T. Borges, J. H. Da Silva, A. G. Caetano and O. A. Filho, Superficial palmar arch: an arterial diameter study, *Journal of Anatomy*, 204, (4), 307-311, 2004.
- Fine I. and A. Wienreb, Multiple scattering effect in transmission oximetry, *Medical and Biological Engineering and Computing*, 33, 709-712, 1995.
- Fukui Y., Y. Ajichi and E. Okada, Monte Carlo prediction of near-infrared light propagation in realistic adult and neonatal head models, *Applied Optics*, 42, (16), 2881-2887, 2003.
- Heneyey L. G. and J. L. Greenstein, Diffuse radiation in the galaxy, *Astrophysical Journal*, 93, 70-83, 1941.
- Herman G. T., *Image Reconstruction from Projections: The Fundamentals of Computerized Tomography*, Academic Press, 1980.
- Hiraoka M., M. Firbank, M. Essenpreist, M. Cope, S. Arridge, P. van der Zee and D. Depty, A Monte Carlo investigation of optical pathlength in inhomogeneous

- tissue and its applications to near-infrared spectroscopy, *Physics in Medicine and Biology*, 38, 1859-1876, 1993.
- Horak W., Risk assessment of light emitting diodes, *Laser Institute of America*, 11, (1), 21-26, 1999.
- Hulsbusch M. and V. Blazek, Contactless mapping of rhythmical phenomena in tissue perfusion using PPGI, *In proceedings of SPIE*, 4683, 110-117, 2002.
- Humphreys K., C. Markham and T. Ward, A CMOS camera-based system for clinical photoplethysmographic applications, *In proceedings of SPIE*, 5823, 88-95, 2005a.
- Humphreys K., T. Ward and C. Markham, A CMOS camera-based pulse oximetry imaging system, *In proceedings of IEEE Engineering in Medicine and Biology Society Conference*, 2005b.
- Humphreys K., T. Ward and C. Markham, A CMOS camera-based system for non-contact pulse oximetry imaging, *In proceedings of International Federation for Medical and Biological Engineering Conference*, 11, 2005c.
- Humphreys K., T. Ward and C. Markham, Noncontact simultaneous dual wavelength photoplethysmography: A further step toward noncontact pulse oximetry, *Review of Scientific Instruments*, 78, (4), 2007.
- ICNIRP, Guidelines on limits of exposure to laser radiation of wavelengths between 180 nm and 1,000 microm. International Commission on Non-Ionizing Radiation Protection, *Health Physics*, 71, (5), 804-819, 1996.
- International Commission on Non-Ionizing Radiation Protection, Guidelines on limits of exposure to broad-band incoherent optical radiation (0.38 to 3 μm), 1997.
- International Commission on Non-Ionizing Radiation Protection, Revision of the guidelines on limits of exposure to laser radiation between 400 nm and 1.4 μm , 2000.

- Irwin M., M. Thorniley, C. Dore and C. Green, Near infrared spectroscopy: a non-invasive monitor of the perfusion and oxygenation within the microcirculation of limbs and flaps, *Applied Optics*, 48, (1), 14-22, 1995.
- Ito Y., R. P. Kennan, E. Watanabe and H. Koizumi, Assessment of heating effects in skin during continuous wave near infrared spectroscopy, *Journal of Biomedical Optics*, 5, (4), 383-390, 2000.
- Jobsis-vanderVliet F., Discovery of the near-infrared window into the body and the early development of near-infrared spectroscopy, *Journal of Biomedical Optics*, 4, (4), 392-396, 1999.
- Joyce W., K. Walsh, J. Gough, T. Gorey and J. Fitzpatrick, Pulse oximetry: a new non-invasive assessment of peripheral arterial occlusive disease, *British Journal of Surgery*, 77, 115-117, 1990.
- Julien C., The enigma of Mayer waves: Facts and models, *Cardiovascular Research*, 70, (1), 12-21, 2006.
- Kelleher J., Pulse oximetry, *Journal of Clinical Monitoring*, 5, 37-62, 1989.
- Kelman G. R., Digital computer subroutine for the conversion of oxygen tension into saturation, *Journal of Applied Physiology*, 21, (4), 1375-6, 1966.
- Kyriacou P. A., S. Powell, R. M. Langford and D. P. Jones, Esophageal pulse oximetry utilizing reflectance photoplethysmography, *IEEE Transactions on Biomedical Engineering*, 49, (11), 1360-1368, 2002.
- Kyriacou P. A., S. L. Powell, D. P. Jones and R. M. Langford, Evaluation of oesophageal pulse oximetry in patients undergoing cardiothoracic surgery, *Anaesthesia*, 58, (5), 422-427, 2003.
- Lerner J. M., Imaging spectrometer fundamentals for researchers in the biosciences-a tutorial, *Cytometry A*, 69, (8), 712-734, 2006.
- Liebman F., J. Pearl and S. Bango, The electrical conductance properties of blood in motion, *Physics in Medicine and Biology*, 7, 177-194, 1962.

- Lindsey L. A., J. D. Watson and A. A. Quaba, Pulse oximetry in postoperative monitoring of free muscle flaps, *British Journal of Plastic Surgery*, 44, (1), 27-29, 1991.
- Lohman B., O. Boric-Lubecke, V. M. Lubecke, P. W. Ong and M. M. Sondhi, A digital signal processor for Doppler radar sensing of vital signs, *IEEE Engineering in Medicine and Biology Magazine*, 21, (5), 161-164, 2002.
- Maguire M., *Non-invasive pulse transit time measurement - A potentially valuable medical measurant or a clinical curiosity?*, M.Eng.Sc. thesis, National University of Ireland, Maynooth, 2004.
- Mannheimer P., J. Casciana, M. Fein and S. Nierlich, Wavelength selection for low-saturation pulse oximetry, *IEEE Transactions on Biomedical Engineering*, 44, (3), 148-158, 1997.
- Marble D., D. Burns and P. Cheung, Diffusion-based model of pulse oximetry: in vitro and in vivo comparison, *Applied Optics*, 33, (7), 1279-1285, 1994.
- Matsui T., S. Gotoh, I. Arai, H. Hattori, M. Fujita, K. Obara, K. Masuoka, S. Nakamura, B. Takase, M. Ishihara and M. Kikuchi, Noncontact vital sign monitoring system for isolation unit (casualty care system), *Military Medicine*, 171, (7), 639-643, 2006.
- Mendelson Y. and J. Kent, Variations in optical absorption spectra of adult and fetal hemoglobins and its effect on pulse oximetry, *IEEE Transactions on Biomedical Engineering*, 36, (8), 844-848, 1989.
- Mendelson Y. and B. Ochs, Noninvasive pulse oximetry utilizing skin reflectance photoplethysmography, *IEEE Transactions on Biomedical Engineering*, 35, (10), 798-805, 1988.
- Millikan G., The oximeter: an instrument for measuring continuously oxygen saturation of arterial blood in man, *Review of Scientific Instruments*, 13, 434-444, 1942.

- Millikan G, J. Pappenheimer, A. Rawson and J. Hervey, Continuous measurement of oxygen saturation in man, *American Journal of Physiology*, 133, 390, 1941.
- Mower W. R., G. Myers, E. L. Nicklin, K. T. Kearin, L. J. Baraff and C. Sachs, Pulse oximetry as a fifth vital sign in emergency geriatric assessment, *Academic Emergency Medicine*, 5, (9), 858-865, 1998.
- Mower W. R., C. Sachs, E. L. Nicklin and L. J. Baraff, Pulse oximetry as a fifth pediatric vital sign, *Pediatrics*, 99, (5), 681-686, 1997.
- Moyle J., *Pulse Oximetry*, BMJ Publishing Group, London, 1994.
- Munley A., M. Sik and A. Shaw, A test object for assessing pulse oximeters, *Lancet*, i, 1048-1049, 1989.
- Nakamura T., K. Fukuda, K. Hayakawa, I. Aoki, K. Matasumoto, T. Senkine, H. Ueda and Y. Shimizu, Mechanism of burn injury during magnetic resonance imaging (MRI) - simple loops can induce heat injury, *Frontiers of Medical and Biological Engineering*, 11, (2), 117-129, 2001.
- Neff T. A., Routine oximetry. A fifth vital sign?, *Chest*, 94, (2), 227, 1988.
- New W., Pulse oximetry, *Journal of Clinical Monitoring*, 1, (2), 126-129, 1985.
- New W. and J. Corenman, Calibrated optical oximeter probe, *United States Patent: 4700708*, 1987.
- New W. and J. Corenman, Calibrated optical pulse oximeter probe, *United States Patent: 4770179*, 1988.
- Nijboer J. and J. Dorlas, Comparison of plethysmograms taken from finger and pinna during anaesthesia, *British Journal of Anaesthesia*, 57, (5), 531-534, 1985.
- Niwayama M., H. Murata and S. Shinohara, Noncontact tissue oxygenation measurement using near-infrared spectroscopy, *Review of Scientific Instruments*, 77, (7), 2006.

Nunn J. F., *Applied respiratory physiology*, 3rd edition, Butterworth, London, 1987.

Okada E., M. Firbank, M. Schweiger, S. Arridge, M. Cope and D. Delpy, Theoretical and experimental investigation of the near-infrared light propagation in a model of the adult head, *Applied Optics*, 36, 21-31, 1997.

Pallas-Areny R. and J. G. Webster, *Sensors and Signal Conditioning*, Wiley, New York, 1991.

Palreddy S., *Design of Pulse Oximeters*, Chapter 9, Ed. J. G. Webster, Taylor and Francis Group, New York, 1997.

Paranjape K. S., *Design of Pulse Oximeters*, Chapter 8, Ed. J. G. Webster, Taylor and Francis Group, New York, 1997.

Patterson M., B. Wilson and D. Wyman, The propagation of optical radiation in tissue I. Models of radiation transport and their application, *Lasers in Medical Science*, 6, 155-168, 1990.

Payne J. and J. Severinghaus, *Pulse Oximetry*, Springer, New York, 1986.

Pologe J., Pulse oximetry: technical aspects of machine design, *International Anesthesiology Clinics*, 25, (3), 137-153, 1987.

Potratz R., Condensed oximeter system with noise reduction software, *United States Patent: 5351685*, 1994.

Prahl S., M. Keijzer, S. Jacques and A. Welch, A Monte Carlo model of light propagation in tissue, *SPIE Inistitute Series*, IS 5, 102-111, 1989.

Reddy M. V. S., *Design of Pulse Oximeters*, Chapter 7, Ed. J. G. Webster, Taylor and Francis Group, New York, 1997.

Reuss J. L., Multilayer modeling of reflectance pulse oximetry, *IEEE Transactions on Biomedical Engineering*, 52, (2), 153-159, 2005.

Reynolds K., J. de Kock, L. Tarassenko and J. Moyle, Temperature dependence of LED and its theoretical effect on pulse oximetry, *British Journal of Anaesthesia*, 67, 1991.

Reynolds K., J. Moyle, L. Gale, M. Skyes and C. Hahn, In vitro performance test system for pulse oximeters, *Medical and Biological Engineering and Computing*, 30, 629-635, 1992.

Reynolds K. J., E. Palayiwa, J. T. Moyle, M. K. Sykes and C. E. Hahn, The effect of dyshemoglobins on pulse oximetry: Part I, Theoretical approach and Part II, Experimental results using an in vitro test system, *Journal of Clinical Monitoring*, 9, (2), 81-90, 1993.

Rolfe P., In vivo near-infrared spectroscopy, *Biomedical Engineering Annual Review*, 2, 715-754, 2000.

Schibli E. G., S. S. Yee and V. M. Krishnan, An electronic circuit for red/infrared oximeters, *IEEE Transactions on Biomedical Engineering*, 25, (1), 94-96, 1978.

Schmitt J. M., R. Webber, L. and E. C. Walker, Pulse oximeter for diagnosis of dental pulp pathology, *United States Patent*: 5040539, 1991.

Schowalter J. S., *Design of Pulse Oximeters*, Chapter 10, Ed. J. G. Webster, Taylor and Francis Group, New York, 1997a.

Schowalter J. S., *Design of Pulse Oximeters*, Chapter 6, Ed. J. G. Webster, Taylor and Francis Group, New York, 1997b.

Seidler D., M. M. Hirschl and G. Roeggla, Limitations of pulse oximetry, *Lancet*, 341, (8860), 1600-1, 1993.

Severinghaus J., History of blood gas analysis, *International Anesthesiology Clinics*, 25, (4), 1-225, 1987a.

Severinghaus J., History, status and future of pulse oximetry, *Advances in Experimental Medicine and Biology*, 220, 3-8, 1987b.

Severinghaus J. and P. Astrup, History of blood gas analysis. I. The development of electrochemistry, *Journal of Clinical Monitoring*, 1, (3), 180-192, 1985a.

Severinghaus J. and P. Astrup, History of blood gas analysis. II. pH and acid-base balance measurements, *Journal of Clinical Monitoring*, 1, (4), 259-277, 1985b.

Severinghaus J. and P. Astrup, History of blood gas analysis. III. Carbon dioxide tension, *Journal of Clinical Monitoring*, 2, (1), 60-73, 1986a.

Severinghaus J. and P. Astrup, History of blood gas analysis. IV. Leland Clark's oxygen electrode, *Journal of Clinical Monitoring*, 2, (2), 125-139, 1986b.

Severinghaus J. and P. Astrup, History of blood gas analysis. V. Oxygen measurement, *Journal of Clinical Monitoring*, 2, (3), 174-189, 1986c.

Severinghaus J. and P. Astrup, History of blood gas analysis. VI. Oximetry, *Journal of Clinical Monitoring*, 2, (4), 270-288, 1986d.

Severinghaus J. and Y. Honda, History of blood gas analysis. VII. Pulse oximetry, *Journal of Clinical Monitoring*, 3, (2), 135-138, 1987.

Severinghaus J., K. Naifeh and S. Koh, Errors in 14 pulse oximeters during profound hypoxia, *Journal of Clinical Monitoring*, 5, 72-81, 1989.

Shapiro B., R. Harrison, R. Cane and R. Templin, *Clinical Application of Blood Gases*, 4th edition, Year Book Medical, Chicago, 1989.

Sowa M., L. Leonardi, J. Payette, J. Fish and H. Mantsch, Near infrared spectroscopic assessment of hemodynamic changes in the early post-burn period, *Burns*, 27, 241-249, 2001.

Sowa M., J. Mansfield, G. Scarth and H. Mantsch, Noninvasive assessment of regional and temporal variations in tissue oxygenation by near-infrared spectroscopy and imaging, *Applied Spectroscopy*, 51, (2), 143-152, 1997.

Sowa M., J. Payette, M. Hewko and H. Mantsch, Visible near infrared multispectral imaging of the rat dorsal skin flap, *Journal of Biomedical Optics*, 4, (4), 474-481, 1999a.

Sowa M., J. Payette and H. Mantsch, Near-infrared spectroscopic assessment of tissue hydration following surgery, *Journal of Surgical Research*, 86, 62-69, 1999b.

Splinter R. and B. A. Hooper, *An Introduction to Biomedical Optics*, Taylor and Francis, New York, 2007.

Squire J., Instrument for measuring the quantity of blood and its degree of oxygenation in the web of the hand, *Clinical Science*, 4, 331-339, 1940.

Steinke J. and A. Shepard, Role of light scattering in whole blood oximetry, *IEEE Transactions on Biomedical Engineering*, 33, 294-301, 1986.

Stranc M. F., M. G. Sowa, B. Abdulrauf and H. H. Mantsch, Assessment of tissue viability using near-infrared spectroscopy, *British Journal of Plastic Surgery*, 51, (3), 210-217, 1998.

Strangman G., M. A. Franceschini and D. A. Boas, Factors affecting the accuracy of near-infrared spectroscopy concentration calculations for focal changes in oxygenation parameters, *NeuroImage*, 18, (4), 865-879, 2003.

Taylor M. and J. Whitman, The accuracy of pulse oximeters, *Anaesthesia*, 43, 229-232, 1988.

Tungjitkusolmun S., *Design of Pulse Oximeters*, Chapter 11, Ed. J. G. Webster, Taylor and Francis Group, New York, 1997.

Twersky V., Absorption and multiple scattering in biological suspensions, *Journal of the Optical Society of America*, 60, 1084-1093, 1970.

Uenoyama M., T. Matsui, K. Yamada, S. Suzuki, B. Takase, M. Ishihara and M. Kawakami, Non-contact respiratory monitoring system using a ceiling-attached microwave antenna, *Medical and Biological Engineering and Computing*, 44, (9), 835-840, 2006.

- United States Navy, *United States Navy Diving Manual: Volume 4*, United States Government Printing, 1994.
- Varshni Y., Temperature dependence of the energy gap in semiconductors, *Physica*, 34, 1967.
- Vegfors M., L. Lindberg, P. Oberg and C. Lennmarken, Accuracy of pulse oximetry at various haematocrits and during haemolysis in an in vitro model, *Medical and Biological Engineering and Computing*, 31, 135-41, 1993.
- Visser K., R. Lamberts, H. Korsten and W. Zijlstra, Observations of blood flow related to impedance changes, *Pflügers Archiv : European Journal of Physiology*, 366, 289-291, 1976.
- Webb R. K., A. C. Ralston and W. B. Runciman, Potential errors in pulse oximetry. II. Effects of changes in saturation and signal quality, *Anaesthesia*, 46, (3), 207-12, 1991.
- Wieben O., *Design of Pulse Oximeters*, Chapter 4, Ed. J. G. Webster, Taylor and Francis Group, New York, 1997.
- Wieringa F., F. Mastik and A. Van Der Steen, Contactless multiple wavelength photoplethysmographic imaging: a first step toward "S_pO₂ Camera" technology, *Annals of Biomedical Engineering*, 33, (8), 1034-1041, 2005.
- Wieringa F. P., F. Mastik, F. J. Cate, H. A. Neumann and A. F. van der Steen, Remote non-invasive stereoscopic imaging of blood vessels: first in-vivo results of a new multispectral contrast enhancement technology, *Annals of Biomedical Engineering*, 34, (12), 1870-1878, 2006.
- Wood E. and J. Geraci, Photoelectric determination of arterial saturation in man, *The Journal of Laboratory and Clinical Medicine*, 34, 387-401, 1949.
- Wukitsch M., Pulse oximetry: Historical review of Ohmeda functional analysis, *Journal of Clinical Monitoring and Computing*, 4, 161-166, 1987.

Wukitsch M., M. Petterson, D. Tobler and J. Pologe, Pulse oximetry: analysis of theory, technology and practice, *Journal of Clinical Monitoring*, 1988, (4), 290-301, 1988.

Young D., C. Jewkes, M. Spittal, C. Blogg, J. Weissman and D. Gradwell, Response time of pulse oximeters assessed using acute decompression, *Anesthesia and Analgesia*, 74, (2), 189-195, 1992.

Yount J., Device and procedures for in vitro calibration of pulse oximetry monitors, *United States Patent*: 4834532, 1989.

Yuanqing L., G. Lech, S. Nioka, X. Intes and B. Chance, Noninvasive, low-noise, fast imaging of blood volume and deoxygenation changes in muscles using light-emitting diode continuous-wave imager, *Review of Scientific Instruments*, 73, (8), 3065-3074, 2002.

Zeman H., G. Lovhoiden and C. Vrancken, The clinical evaluation of vein contrast enhancement, *In proceedings of IEEE Engineering in Medicine and Biology Society Conference*, 2004.

Zijlstra W., *Fundamentals and applications of oximetry*, 2nd edition, Van Gorcum, Assen, 1953.

Zijlstra W., *A Manual of Reflection Oximetry*, Van Gorcum, Assen, 1958.

Zwart A., A. Buursma, B. Oeseburg and W. Zijlstra, Determination of hemoglobin derivatives with the IL-282 CO-oximeter as compared with a manual spectrophotometric five wavelength method, *Clinical Chemistry*, 27, (11), 1903-1906, 1981.